

Weight-Adjusted Nonlinearly Stable Flux Reconstruction High-Order Methods for Compressible Flows in Curvilinear Coordinates

Alexander Cicchino

Doctor of Philosophy

Department of Mechanical Engineering

McGill University
Montreal, Quebec

April, 2024

A thesis submitted to McGill University in partial fulfillment of the requirements of the degree of Doctor of Philosophy in Mechanical Engineering

©Alexander Cicchino 2024

Abstract

To achieve genuine predictive capability, an algorithm must consistently deliver accurate results over prolonged temporal integration periods, avoiding the unwarranted proliferation of aliasing errors that compromise the discrete solution. Provable nonlinear stability bounds the discrete approximation and ensures that the discretization does not diverge. Nonlinear stability is accomplished by satisfying a secondary conservation law, namely for compressible flows; the second law of thermodynamics. For high-order methods, discrete nonlinear stability and entropy stability, have been successfully implemented for discontinuous Galerkin (DG) and residual distribution schemes, where the stability proofs depend on properties of L2-norms. Alternatively, the flux reconstruction method has gained popularity in the research community as it recovers promising high-order methods, such as DG, through a modally filtered correction field. Specific correction functions, defined by a class of energy stable flux reconstruction (ESFR) schemes, allow for larger timesteps than DG while preserving the orders of convergence. These correction functions require stability proofs to be evaluated in dense broken Sobolev-norms. This thesis develops nonlinearly stable flux reconstruction (NSFR) schemes for scalar and vector-valued conservation laws by proving discrete nonlinear stability in dense broken Sobolev-norms. NSFR differs from ESFR schemes in the literature since it incorporates the flux reconstruction correction functions on the volume terms through the use of a modified mass matrix. To arrive at this result, this thesis first derives NSFR for Burgers' equation in split form, then linear advection in split form in three-dimensional curvilinear coordinates, and finally the Euler equations using uncollocated, modal skew-symmetric operators with entropy conserving two-point fluxes in curvilinear coordinates. This thesis also focuses on efficiently scalable and low-storage implementations. The NSFR modified mass matrix is derived in a weight-adjusted form. This form reduces the computational cost in curvilinear coordinates because the dense matrix inversion is approximated by a pre-computed projection

operator and the inverse of a diagonal matrix on-the-fly. NSFR makes use of tensor product basis functions to exploit sum-factorization. Additionally, a sum-factorized Hadamard product is developed allowing the entropy stable two-point flux framework to scale at order $\mathcal{O}(n^{d+1})$, where $n = p + 1$, with p being the polynomial degree, and d the physical dimension of the problem. The nonlinear stability properties of the scheme are verified for the unsteady Burgers' equation with a shock wave, unsteady linear advection on curvilinear grids, and the Taylor-Green vortex problem on a coarse non-symmetric curvilinear grid. On a linear grid, the orders of convergence were obtained for a manufactured solution to the Burgers' equation. On nonsymmetric, heavily warped curvilinear grids, the orders of convergence were attained for manufactured solutions to linear advection and the Euler equations. Lastly, we perform a computational cost comparison between conservative DG, overintegrated DG, and our proposed entropy conserving NSFR scheme. We find that our proposed scheme is computationally competitive with the conservative nodal DG scheme per residual evaluation, and it can take larger timesteps than DG.

Résumé

Pour obtenir une véritable capacité prédictive, un algorithme doit fournir systématiquement des résultats précis sur des périodes d'intégration temporelle prolongées, évitant ainsi la prolifération injustifiée d'erreurs d'alias qui compromettent la solution discrète. La stabilité non linéaire prouvable limite l'approximation discrète et garantit que la discrétisation ne diverge pas. La stabilité non linéaire est obtenue en satisfaisant une loi de conservation secondaire, notamment pour les écoulements compressibles ; la deuxième loi de la thermodynamique. Pour les méthodes d'ordre élevé, la stabilité non linéaire discrète et la stabilité entropique ont été implémentées avec succès pour les schémas Galerkin discontinue (DG) et de distribution résiduelle, où les preuves de stabilité dépendent des propriétés des normes-L2. Alternativement, la méthode de reconstruction de flux a gagné en popularité dans la communauté des chercheurs car elle récupère des méthodes prometteuses d'ordre élevé, telles que DG, via un champ de correction filtré modalement. Des fonctions de correction spécifiques, définies par une classe de schémas de reconstruction de flux stable en énergie (ESFR), permettent des pas de temps plus grands que DG tout en préservant les ordres de convergence. Ces fonctions de correction nécessitent que les preuves de stabilité soient évaluées dans des normes-Sobolev brisées qui sont denses. Cette thèse développe des schémas de reconstruction de flux non linéairement stable (NSFR) pour les lois de conservation scalaires et vectorielles en prouvant la stabilité non linéaire discrète dans des normes de Sobolev denses et brisées. Le NSFR diffère des schémas ESFR de la littérature car il intègre les fonctions de correction de reconstruction de flux sur les termes de volume grâce à l'utilisation d'une matrice de masse modifiée. Pour arriver à ce résultat, cette thèse dérive d'abord le NSFR pour l'équation de Burgers sous forme divisée, puis l'advection linéaire sous forme divisée en coordonnées curvilignes tridimensionnelles, et enfin les équations d'Euler utilisant des opérateurs antisymétriques modaux non colocalisés avec le flux à deux pointes conservation de l'entropie en coordonnées curvilignes. Cette thèse

se concentre également sur des implémentations efficacement évolutives et à faible stockage. La matrice de masse modifiée NSFR est dérivée sous une forme ajustée en fonction du poids. Cette forme réduit le coût de calcul en coordonnées curvilignes car l'inversion de matrice dense est approximée par un opérateur de projection pré-calculé et l'inverse d'une matrice diagonale à la volée. NSFR utilise des fonctions de base de produit tensoriel pour exploiter la factorisation par somme. De plus, un produit Hadamard factorisé en somme est développé permettant au cadre de flux à deux points stable en tropie d'évoluer à l'ordre $\mathcal{O}(n^{d+1})$, où $n = p + 1$, avec p étant le degré polynomial, et d la dimension physique du problème. Les propriétés de stabilité non linéaire du schéma sont vérifiées pour l'équation de Burgers instationnaire avec onde de choc, l'advection linéaire instationnaire sur des grilles curvilignes et le problème du vortex de Taylor-Green sur une grille curviligne grossière non symétrique. Sur une grille linéaire, les ordres de convergence ont été obtenus pour une solution fabriquée de l'équation de Burgers. Sur des grilles curvilignes non symétriques et fortement déformées, les ordres de convergence ont été atteints pour les solutions fabriquées à l'advection linéaire et aux équations d'Euler. Enfin, nous effectuons une comparaison des coûts de calcul entre un DG conservateur, un DG surintégré et notre schéma NSFR proposé pour conserver l'entropie. Nous constatons que le schéma proposé est compétitif sur le plan informatique avec le schéma DG nodal conservateur par évaluation résiduelle, et qu'il peut prendre des pas de temps plus longs que DG.

Acknowledgements

Firstly, I would like to wholeheartedly thank my supervisor Professor Siva Nadarajah for his mentorship, support, guidance, and the creative freedom he allowed me to take throughout my years within his group. Thank you for challenging me to go beyond my comfort zone, for sharing your knowledge and enthusiasm with me—energetically working through concepts and proofs on the whiteboard. Your leadership has inspired me greatly to try to find the deeper, fundamental research questions to be asked, and to search for elegant solutions.

I would like to thank my labmates for the creative discussions and support. The group has pushed my understanding of all aspects in the code, from the theory, to the coding best practices. The group somehow made late night debugging enjoyable. I would also like to thank my late friend and labmate Philip Zwanenburg, he acted as a mentor for me when I first joined the group and I really looked up to him.

I would like to thank Professor David C. Del Rey Fernández. I have been fortunate to write two excellent papers with you and I am very thankful for our discussions on high-order methods. Your insight has pushed and strengthened my understanding.

I would like to thank Professor Charles Roth and his wife Ira for their wisdom and guidance. They have both positively influenced me both academically, by instilling my passion for PDEs, and spiritually. They have strengthened my attitude of gratitude and it is a blessing to have them in my life.

I am thankful for my close friends both in the city and abroad. They have made my McGill experience one filled with laughter and joy.

I am eternally grateful for the love and support from my family. Special thanks to my sisters Michelle and Amanda who have always been there for me. Papy and Nanou, thank you for the countless stories and traditions that guide me to make the right choices. Papy, mon petit, you are my greatest role model. Mom, thank you for encouraging me to be an independent thinker and to pursue my dreams.

I would also like to thank Bart Oldeman and Daniel Stubbs from Calcul-Québec for help with various aspects of the compute clusters and boosting the priority of test cases to finish before important deadlines.

Lastly, I would like to gratefully acknowledge the financial support from the Natural Sciences and Engineering Research Council of Canada - Postgraduate Scholarships Doctoral Award, McGill University - McGill Engineering Doctoral Award, and the Greville Smith Fellowship.

Contents

Abstract	i
Resumé	iii
Acknowledgements	v
Table of Contents	vii
List of Figures	xii
List of Tables	xiv
Nomenclature	xv
1 Introduction	1
1.1 High-Order Methods	1
1.1.1 Discontinuous Galerkin	2
1.1.2 Flux Reconstruction	3
1.1.3 ESFR as a Filtered DG Scheme	5
1.1.4 Summation-by-Parts Discretization	6
1.2 Nonlinear Problems	7
1.2.1 Curvilinear Meshes	7
1.2.2 Nonlinear Stability and Entropy Stability	8
1.2.3 Nonlinearly Stable Flux Reconstruction (NSFR)	12
1.3 Scalable Implementation	13
1.3.1 Sum-Factorization	13
1.3.2 Low-Storage Weight-Adjusted Approximations	15

1.3.3	Research Objectives	16
1.3.4	Thesis Contributions	16
1.3.5	Contribution of Authors	17
2	Nonlinearly Stable Flux Reconstruction for Scalar Problems	19
2.1	Introduction	22
2.2	Preliminaries	24
2.2.1	DG Formulation	24
2.2.2	Corresponding ESFR Scheme	27
2.3	SBP-ESFR Split Forms for Burgers' Equation	28
2.3.1	Proposed Splitting with Respect to the Stiffness Operator	31
2.3.1.1	Discrete Conservation	35
2.3.1.2	Discrete Energy Stability	37
2.4	Numerical Results	39
2.4.1	Energy Verification	40
2.4.2	Orders of Accuracy (OOA)	40
2.5	Conclusion	43
2.6	Acknowledgements	43
	References	43
3	Provably Stable Flux Reconstruction on Curvilinear Elements	49
3.1	Introduction	53
3.2	Math Notation and Definitions	56
3.3	Discontinuous Galerkin	60
3.3.1	DG - Conservative Strong Form	60
3.3.2	DG - Non-Conservative Strong Form	63
3.3.3	DG - Split-Form	65
3.4	Energy Stable Flux Reconstruction	66

3.4.1	ESFR - Classical Formulation	66
3.4.2	ESFR - Proposed Nonlinearly Stable Flux Reconstruction	74
3.4.3	ESFR - Accuracy of Metric Dependent ESFR Schemes	75
3.5	Discrete GCL	78
3.6	Free-Stream Preservation, Conservation and Stability	80
3.6.1	Free-Stream Preservation	80
3.6.2	Conservation	82
3.6.3	Stability	83
3.7	Results	84
3.7.1	ESFR Derivative Test	84
3.7.2	Nonsymmetric Grid	87
3.7.3	Skew-Symmetric Grid	92
3.8	Conclusion	97
3.9	Acknowledgements	98
	Appendices	98
3.A	Summation-by-Parts	98
3.A.1	SBP - Strong Form FR Split	99
3.B	Stability Proof - Operator Form	100
	References	101
4	Scalable Evaluations	112
4.1	Introduction	114
4.2	Hadamard Product	115
4.3	Results	120
4.4	Conclusion	121
4.5	Acknowledgements	121
	References	121

5	Systems of Nonlinear Conservation Laws in Curvilinear Coordinates	124
5.1	Introduction	129
5.2	Preliminaries	131
5.2.1	Systems of Equations	132
5.2.2	Computational Space	134
5.3	Nonlinearly Stable Flux Reconstruction	137
5.3.1	Discontinuous Galerkin	137
5.3.2	Energy Stable Flux Reconstruction	139
5.3.3	Nonlinearly Stable Flux Reconstruction	142
5.4	Weight-Adjusted Inverse of Flux Reconstruction Mass Matrix	145
5.5	Scalable Evaluations	147
5.6	Conserved Properties of NSFR	150
5.6.1	Free-stream Preservation	150
5.6.2	Global Conservation	151
5.6.3	Nonlinear Stability	152
5.7	Results	156
5.7.1	Manufactured Solution Convergence	158
5.7.2	Maximum CFL	160
5.7.3	Inviscid Taylor Green Vortex	163
5.7.4	NSFR versus DG Conservative with and without Overintegration	167
5.8	Conclusion	171
5.9	Acknowledgements	171
	References	172
6	General Discussion	182
6.1	NSFR Modified Mass Matrix	182
6.2	NSFR Performance - Extension	185
6.2.1	Viscous Problems: The Navier-Stokes Equations	186

7 Conclusion **194**

 7.1 Future Work 195

 7.1.1 Natural Extensions 195

 7.1.2 Limitations 196

Bibliography **198**

List of Figures

3.1	3D Warped Grid	85
3.2	3D c vs OOA for $p = 2$	87
3.3	3D c vs OOA for $p = 3$	87
3.4	3D c vs OOA for $p = 4$	87
3.5	3D c vs OOA for $p = 5$	87
3.6	Warped Grid $p = 3$	88
3.7	Second Warped Grid $p = 3$	93
4.1	CPU time versus polynomial degree	120
5.1	3D Nonsymmetrically Warped Curvilinear Grid Cross-Section.	157
5.2	3D Manufactured Solution Orders of Convergence	159
5.3	Change in Entropy. Red line c_{HU} with weight-adjusted, black line c_+ with weight-adjusted, and blue line c_+ without weight-adjusted mass matrix. . . .	165
5.4	Volume Change in Kinetic Energy without Pressure Work for LGL and GL Nodes.	166
5.5	Change in Kinetic Energy without Pressure Work.	167
5.6	CPU time versus polynomial degree TGV.	168
6.1	Viscous TGV at $Re_\infty = 1600$ using c_{DG} NSFR with 256^3 DOFs.	190
6.2	Viscous TGV at $Re_\infty = 1600$ using c_{DG} and c_+ NSFR with 96^3 DOFs.	192

List of Tables

2.1	Energy Results $p = 4,5$ Collocated Schemes $N_{vp} = p + 1$	40
2.2	Energy Results $p = 4,5$ Uncollocated Schemes $N_{vp} = p + 1$	41
2.3	Energy Results $p = 4,5$ Uncollocated Schemes Overintegrated $N_{vp} = p + 3$	41
2.4	Convergence Table $p = 4$ $N_{vp} = p + 1$	42
2.5	Convergence Table $p = 5$ $N_{vp} = p + 1$	42
2.6	Convergence Table $p = 4$ Overintegrated $N_{vp} = p + 3$	42
2.7	Convergence Table $p = 5$ Overintegrated $N_{vp} = p + 3$	43
3.1	L_2 Convergence Table $p = 3$	86
3.2	L_∞ Convergence Table $p = 3$	86
3.3	L_2 Convergence Table $p = 4$	86
3.4	L_∞ Convergence Table $p = 4$	87
3.5	Energy Results $p = 3,4$ Uncollocated $N_{vp} = (p + 1)^2$ Grid 1	89
3.6	Energy Results $p = 3,4$ Uncollocated $N_{vp} = (p + 3)^2$ Grid 1	89
3.7	L_2 Convergence Table $p = 3$ $N_{vp} = (p + 1)^2$ Upwind Numerical Flux Grid 1	90
3.8	L_∞ Convergence Table $p = 3$ $N_{vp} = (p + 1)^2$ Upwind Numerical Flux Grid 1	90
3.9	L_2 Convergence Table $p = 4$ $N_{vp} = (p + 1)^2$ Upwind Numerical Flux Grid 1	91
3.10	L_∞ Convergence Table $p = 4$ $N_{vp} = (p + 1)^2$ Upwind Numerical Flux Grid 1	91
3.11	L_2 Convergence Table $p = 3$ $N_{vp} = (p + 3)^2$ Upwind Numerical Flux Grid 1	91
3.12	L_∞ Convergence Table $p = 3$ $N_{vp} = (p + 3)^2$ Upwind Numerical Flux Grid 1	92
3.13	L_2 Convergence Table $p = 4$ $N_{vp} = (p + 3)^2$ Upwind Numerical Flux Grid 1	92

3.14	L_∞ Convergence Table $p = 4$ $N_{vp} = (p + 3)^2$ Upwind Numerical Flux Grid 1	92
3.15	Energy Results $p = 3, 4$ Uncollocated $N_{vp} = (p + 1)^2$ Grid 2	94
3.16	Energy Results $p = 3, 4$ Uncollocated $N_{vp} = (p + 3)^2$ Grid 2	94
3.17	L_2 Convergence Table $p = 3$ $N_{vp} = (p + 1)^2$ Upwind Numerical Flux Grid 2 .	94
3.18	L_∞ Convergence Table $p = 3$ $N_{vp} = (p + 1)^2$ Upwind Numerical Flux Grid 2	95
3.19	L_2 Convergence Table $p = 4$ $N_{vp} = (p + 1)^2$ Upwind Numerical Flux Grid 2 .	95
3.20	L_∞ Convergence Table $p = 4$ $N_{vp} = (p + 1)^2$ Upwind Numerical Flux Grid 2	95
3.21	L_2 Convergence Table $p = 3$ $N_{vp} = (p + 3)^2$ Upwind Numerical Flux Grid 2 .	96
3.22	L_∞ Convergence Table $p = 3$ $N_{vp} = (p + 3)^2$ Upwind Numerical Flux Grid 2	96
3.23	L_2 Convergence Table $p = 4$ $N_{vp} = (p + 3)^2$ Upwind Numerical Flux Grid 2 .	96
3.24	L_∞ Convergence Table $p = 4$ $N_{vp} = (p + 3)^2$ Upwind Numerical Flux Grid 2	97
5.1	Max CFL for $p = 3$, $p = 4$ and $p = 5$, 4^3 elements.	161
5.2	Change in Entropy Results $p = 4, 5$ Cartesian Mesh.	164
5.3	Change in Entropy Results $p = 4, 5$ Curvilinear Mesh.	164
5.4	TGV Comparison for CPU and Wall Clock Times.	170

Nomenclature

χ	Basis functions.
ϕ	Flux basis functions collocated on the volume cubature nodes.
Π	Projection operator.
Θ	Mapping shape functions.
ξ_v^r	Volume cubature nodes in the reference element.
$\xi_{f,k}^r$	Facet cubature node in the reference element corresponding to face f , node k .
C_m	The cofactor matrix for the metric Jacobian.
f	The physical flux.
f^r	The reference flux.
J_m	A diagonal matrix strong the determinant of the metric Jacobian at the volume cubature nodes in the element m .
K	Energy stable flux reconstruction correction matrix.
M	Mass matrix.
S_ξ	Stiffness matrix with differentiation in the reference direction ξ .
u_m	Conservative variables in the element m .

\mathbf{v}	Entropy variables.
$\hat{\mathbf{n}}$	The physical unit normal.
$\hat{\mathbf{n}}^r$	The reference unit normal.
$\hat{\mathbf{u}}_m$	Modal coefficients of the conservative variables in the element m .
∇	Physical gradient/divergence operator.
∇^r	Reference gradient/divergence operator.
p	Polynomial degree.

Chapter 1

Introduction

The goal of this dissertation is to develop numerical tools that can solve nonlinear partial differential equations (PDEs) on complex geometry for computational predictive science applications with large-scale data. A computational tool is truly predictive when it can accurately measure the impact that initial small perturbations have in the long-term. This imposes three focuses: accuracy, robustness, and efficiency. Accuracy is achieved with high-order accurate finite element methods, robustness is guaranteed through discrete nonlinear stability, and efficiency is optimized through scalable techniques coupled with high arithmetic intensity and minimum memory strategies.

1.1 High-Order Methods

High-order accurate methods such as discontinuous Galerkin (DG) and flux reconstruction (FR), result in efficient computations via high solution accuracy and dense computational kernels, making them an attractive approach for the exascale concurrency on next-generation hardware. Generally, high-order methods are known to be more efficient than low-order methods for linear hyperbolic problems [1, 2]. However, despite a prolonged development effort, their application to industrially relevant simulations of nonlinear PDEs has been limited due to the absence of nonlinear stability among classes of DG and FR high-order methods.

The following subsections provide a comprehensive assessment of current advancements in this field and where applicable research gaps are identified.

1.1.1 Discontinuous Galerkin

The DG method, first proposed by Reed and Hill to solve the neutron transport equation [3], combines both the key properties of finite volume and finite element schemes. As explained in the book by Hesthaven and Warburton [4], the high-order scheme provides stability through a numerical flux function and utilizes high-order shape functions to represent the solution. There are several attractive qualities of a DG scheme for industrial applications. Firstly, the scheme allows for arbitrary high-order, endowed with a compact stencil, and easily discretized over complex geometry. This makes it a very attractive algorithm to use local *hp*-adaptation in conjunction with high-order meshes to accurately capture more complicated designs. Also, its compact stencil allows for the scheme to be effortlessly parallelized making it well-suited for next generation hardware. Secondly, it can be recast in operator and quadrature-free form [5] that resembles finite difference and spectral difference schemes, creating efficient residual solves. Thirdly, the stability of the scheme is controlled by a surface numerical flux function similar to that used in finite volume codes. A piece-wise constant first-order DG scheme recovers Godunov’s method [6, 7], while its higher-order DG counterparts preserve the essence of the Riemann solver across the interfaces. For the convective term, a few common choices for the surface numerical flux are: to scale the jump in the solution by the maximum wavespeed for example Lax-Friedrichs [8], to use flux-difference splitting, for example Roe’s flux [9], or to use flux-vector splitting, for example the convective upwind split pressure flux [10]. Particularly for the diffusion equation, many numerical flux functions such as the interior penalty (IP) [11], the Bassi and Rebay II (BR2) [12], the local discontinuous Galerkin (LDG) [13], the compact discontinuous Galerkin (CDG) [14], and the compact discontinuous Galerkin 2 (CDG2) [15] have been developed with the use of a penalty term to account for the discontinuous jump across cells or control volumes, in order to maintain conservation.

There are several alternative high-order schemes to the DG method. Firstly, there is the spectral volume (SV) approach proposed by Wang *et al.* [16] which was derived by subdividing each cell into smaller control volumes in order to have a high-order, finite volume-type stencil. There are also finite difference-like schemes based on implementing higher-order operators mimetic of the differential form. The most promising was that developed by Kopriva and Kolas [17] where they introduced a staggered grid spectral method. For the staggered grid, there were two sets of nodes: solution and flux nodes. The solution was interpolated to the flux nodes and a collocated DG-like spectral element method was implemented on the flux nodes. Liu, Vinokur and Wang [18] extended it to triangular meshes. These schemes were proven to be stable by Jameson [19] as they are specific cases of FR. In [20], Wang published a review of these alternative high-order methods.

1.1.2 Flux Reconstruction

The FR framework, originally proposed by Huynh [21], has emerged as a popular finite element approach. It is simple since it can be cast in differential collocated form and it affords design flexibility through the choice of correction functions that alter the properties of the scheme. Its main attraction is that it allows for the largest timesteps of all high-order methods for the same polynomial degree. The centralized idea for FR is to “correct” the flux across the surface with correction functions of one-degree order higher than the scheme, which makes the approximate flux have both a discontinuous and continuous component. This results in the ability to take larger time steps while maintaining the correct orders of convergence [21–25].

Wang and Gao [22] later presented an alternate approach to the FR scheme. Deemed the Lifting Collocation Penalty (LCP) approach, they considered a “correction field” applied to the surface integral; instead of reconstructing the flux across the surface of the element [22]. In addition, they considered a collocated Lagrange basis for the volume flux, alike the FR discontinuous flux. Thus, the authors merged both the FR and LCP in a common framework called Correction Procedure via Reconstruction (CPR) [26, 27]. Now FR and CPR are loosely

interchangeable since Yu and Wang [28] proved that the FR surface reconstruction is identical to the CPR correction field.

Importantly, subsets of FR schemes, also known as Vincent-Castonguay-Jameson-Huynh (VCJH) schemes or Energy Stable Flux Reconstruction (ESFR), have been identified as provably linearly stable for linear advection [22, 23, 25, 29–35]. This was accomplished by proving energy stability with respect to a p -th order broken Sobolev-norm. The choice to prove stability within a dense p -th order broken Sobolev-norm for FR schemes originates from Jameson’s [19] stability proof for the spectral difference scheme. The spectral difference scheme, in the FR framework, differs from DG through the lifting operator. To prove stability, Jameson [19] added a term that is orthogonal to the divergence of the volume flux to the L2-norm. Then, by scaling the norm by a free parameter, the ESFR stability condition is realized relating the inner product of the p -th order derivative and the surface lifting correction functions [24]. The free parameter is the ESFR correction parameter c ; with values of c_{DG} , c_{SD} , c_{HU} , c_- , and c_+ . Each parameter results in the scheme having different properties, where c_{DG} recovers a DG scheme exactly; while c_{SD} recovers a spectral difference scheme, and c_{HU} recovers the Hunyh g_2 scheme [24]. The stability of the scheme is ensured through the minimum value c_- . Lastly, the value of c_+ does not have an analytical value but has numerically been shown to be the upper limit in a von Neumann analysis of the correction parameter before the scheme loses an order of accuracy [29] with an L2-error bound obtained by Lambert and Nadarajah [36]. It is to be noted, that as c increases, the maximum time step increases up until the value of c_+ . ESFR exists within a broader class of correction functions using weighted Jacobi polynomials [37] and that of general stable flux reconstruction [38] which incorporates all polynomial components for the full Sobolev-norm.

A stability proof was later developed for the diffusion equation in Castonguay *et al.* [39] where they showed that stability was ensured for the LDG scheme with a positive correction parameter. The proof was extended for the BR2, IP, CDG and CDG2 numerical fluxes in Quaegebeur *et al.* [40], where it was shown that stability was ensured by choosing a positive

correction parameter for the primary equation and that it was independent of the correction parameter used in the auxiliary equation. This proof was later developed for linear triangular elements [41], where it was also proven that the correction parameter for the primary equation had to be positive, and an arbitrary correction parameter was needed for the auxiliary equation to ensure stability using the IP and BR2 numerical fluxes. For Cartesian meshes, Sheshadri and Jameson [42] showed stability of the ESFR scheme, with the LDG numerical flux, for the same positive correction parameter used for both the primary and auxiliary equations. Quaegebeur *et al.* [43] extended the two-dimensional Cartesian proof for the BR2, IP, CDG and CDG2 numerical fluxes.

As discussed, the ESFR discretization recovers several popular high-order schemes, specifically DG. Thus, it was imperative to develop a relationship between ESFR and DG such that: ESFR is easily implemented into pre-existing DG codes and future ESFR research can refer to the DG literature.

1.1.3 ESFR as a Filtered DG Scheme

Through the close relationship between the ESFR correction field and a DG surface lifting operator, ESFR has been proven to be equivalent to a filtered DG scheme [44–46]. This allows for a seamless implementation of ESFR into pre-existing, modal, uncollocated DG codes through the addition of a symmetric filter matrix to the mass matrix [44–46]. Although the ESFR filter was originally derived based on the relationship between the ESFR and DG facet correction fields [44, 45], the filter operator has also been proven to arise naturally from the norm in which the scheme is stable [46]. The latter formulation allows for the ESFR filter to be implemented in an arbitrarily modal uncollocated basis [46] without the need to compute a reference basis alike [44, 45]. Viewing ESFR as a filtered DG scheme allows the possibility of ensuring nonlinear stability in arbitrarily dense norms.

1.1.4 Summation-by-Parts Discretization

A discretization agnostic approach for the design and analysis of arbitrarily high-order and provably stable numerical methods for linear variable coefficient problems is provided by the Summation-by-Parts (SBP) framework [47–49]. A way of viewing the SBP framework is through the lens of a quadrature-free DG scheme, alike that presented by Cockburn and Shu [13]. Then, the SBP differential operator is the derivative of the basis functions, and the SBP property is equivalent to the p -th order basis functions satisfying discrete integration-by-parts for quadrature rules of at least $2p - 1$ strength. This viewpoint directly allows for a relationship between the variational DG framework and the SBP community. Thus, similar to the DG surface lifting operator, the SBP community considers simultaneous approximation terms (SATs) [47, 49–59] to represent the surface integral. Moreover, discretizations having the SBP property are straightforward to transition to nonlinearly stable (entropy stable) schemes for nonlinear conservation laws [47, 49, 56–58, 60–71].

In the SBP literature, the extension of stability proofs for dense-norm SBP operators, to variable coefficient problems—particularly curvilinear coordinate transformations, has received little attention as a result of Svård [72]. In that paper, Svård proved that, in general, for such problems a dense-norm, \mathbf{P} , when multiplied against the diagonal matrix containing the metric Jacobian on the mesh nodes, \mathbf{J} , does not result in a norm and therefore provable stability is lost, i.e., \mathbf{PJ} is not a norm. However, by recasting dense-norm SBP operators in staggered form and constructing metrics on the staggered grid, stability can be reestablished for PDEs in curvilinear coordinates [63]. The incorporation of the metric Jacobian on the flux nodes in a staggered approach for dense-norm SBP operators [63] is equivalent to considering the DG discretization in variational form and having the metric Jacobian appear by transforming the differential volume element within the integral. Alternatively, Ranocha *et al.* [73] constructed a dense matrix \mathbf{J} , such that $\mathbf{PJ} = (\mathbf{PJ})^T$, which resulted in \mathbf{PJ} being a norm for modal based operators. The approach in [73] proved to be stable since the authors only considered a nodal DG scheme. In a similar fashion, the extension of nonlinear stability proofs to

curvilinear coordinates for ESFR schemes—to take advantage of larger timesteps, has alluded the research community as the ESFR norm is dense.

1.2 Nonlinear Problems

Unsteady, discontinuous, and chaotic turbulent flows are common in computational fluid dynamics (CFD). These properties are the result of the nonlinearity within the PDE. To tackle the problem of robustness, there exists a discrete nonlinear stability framework [74] to prove that numerical entropy monotonically decreases. Nonlinear stability proofs ensure that instabilities do not manifest themselves during long-time integration. Nonlinearities present themselves both through the governing equation’s flux and the mapping of the space itself for curvilinear coordinates.

1.2.1 Curvilinear Meshes

Curvilinear meshes are of interest for high-order schemes since they allow for body-fitted grids [75, 76]. Firstly, since the curvilinear transformation and the mesh itself are nonlinear polynomials, then the complete discretization is nonlinear; even for a linear flux. For example, consider a linear covariant flux \mathbf{f} transformed to the contravariant basis by the nonlinear mapping ψ , then the contravariant flux $\mathbf{f}^r = \psi \mathbf{f}$ is nonlinear. It has been proven that for curvilinear elements, the polynomial representation of the grid must be at least the same order of the scheme [77, 78]. In [77, 78], to demonstrate the correct orders of convergence for curvilinear meshes, only a polynomial approximation on the contravariant (reference) flux was considered since the covariant (physical) flux was never explicitly represented as a polynomial. This also resulted in two different forms for DG schemes on curvilinear grids; conservative (considering the divergence of the contravariant flux) and non-conservative (considering the contravariant transformation of the divergence of the flux) [63, 79, 80]. Thus, when the metric terms are nonlinear, the discretization is fundamentally different from the continuous formulation. Careful treatment is required for free-stream preservation, conservation, and

stability.

First presented by Thomas and Lombard [81], then later extended by Kopriva [82] for DG/high-order spectral schemes, the metric terms for the contravariant transformation must be computed *a priori* to satisfy free-stream preservation. The *a priori* computation recasts the metric terms in curl form, which results in the Geometric Conservation Law (GCL) discretely being equivalent to the divergence of the curl. Abe *et al.* [83] extended the work by considering two separate sets of points. The first is a continuous set of grid points, or mapping support points, that ensure well-posed elements [75]. Then, the centralized idea in [83] was to perform the curl interpolation at the flux points; thus the authors ensured consistent normals on each element's surface. Although the metric terms have been derived to satisfy free-stream preservation, they inherently add nonlinearity to the scheme which requires careful treatment for stability proofs [63, 70, 79, 84].

1.2.2 Nonlinear Stability and Entropy Stability

Consider a system of conservation laws

$$\begin{aligned} \frac{\partial u}{\partial t} + \nabla \cdot \mathbf{f}(u) &= 0, \quad \forall t \geq 0, \quad x \in [x_L, x_R], \\ u(x, 0) &= g(x), \end{aligned} \tag{1.1}$$

with appropriate boundary conditions, for example, Dirichlet, Neumann, Robin, mixed or Cauchy. *Smooth* solutions of Eq. (1.1) satisfy the entropy equality,

$$\frac{\partial U}{\partial t} + \nabla \cdot \mathbf{F} = 0, \quad \mathbf{F} = \mathbf{F}(u), \tag{1.2}$$

where U is a convex function of u , while *weak* solutions satisfy the entropy inequality,

$$\frac{\partial U}{\partial t} + \nabla \cdot \mathbf{F} \leq 0. \tag{1.3}$$

The foundational step from Lax and Wendroff [85] showed that if the approximation is

convergent, then for *smooth* problems, it converges to *the strong* solution; but for *non-smooth* problems, it converges to *a weak* solution. To identify the physically relevant weak solution, based on the interpretations from Lax [86] and Harten *et al.* [87], discontinuous solutions satisfy Oleinik’s Condition E [88],

$$\frac{f(u) - f(u_L)}{u - u_L} \geq s \geq \frac{f(u_R) - f(u)}{u_R - u}, \quad (1.4)$$

for all u between u_L and u_R , and s is the speed of the shock. Oleinik’s Condition E [88] is an abstraction of the Rankine-Hugoniot condition. Independently, Hopf [89] and, based on the interpretation of Lax [90], Kruřkov [91], showed that if the weak solution u is the limit of solutions to the parabolic equation,

$$\frac{\partial u}{\partial t} + \nabla \cdot \mathbf{f}(u) = \alpha \nabla \cdot (\beta(u) \nabla(u)), \quad \beta > 0, \quad \alpha \rightarrow 0, \quad (1.5)$$

then the entropy inequality in Eq. (1.3) is satisfied. Eq. (1.5) is known as the vanishing viscosity mechanism. Hopf [89] recovered Oleinik’s Condition E (Eq. (1.4)) from the entropy inequality (Eq. (1.3)) for a special set of increasing functions. For general systems of hyperbolic equations, Lax [90] proved that satisfying the entropy inequality (Eq. (1.3)) through a vanishing viscosity mechanism implies that Oleinik’s Condition E is recovered—resulting in the physically relevant weak solution.

Discretely, we can mimic the continuous vanishing viscosity mechanism by adding upwind numerical dissipation alike von Neumann and Richtmeyer [92]. For linear problems, Godunov and Bohachevsky [7] explored the concept of *monotonicity*. Then, Godunov and Bohachevsky [7] arrived at the minimum artificial viscosity needed to ensure a monotonic discretization for the linear PDE. Following from the proofs by Hopf [89] and Kruřkov [91, 93], Harten and coauthors [87] were able to show that the monotonicity condition implies that the entropy inequality is satisfied, and thus conservative monotone finite difference schemes satisfy Oleinik’s Condition E. Unfortunately, monotone schemes can be at most first-order [87], since

the monotonicity constraint limits the discretization through Godunov’s barrier theorem [7]. To extend beyond first-order, the monotonicity condition was relaxed and the focus was on discretely satisfying the entropy inequality.

The physically relevant weak solution satisfies the entropy inequality, thus a crucial first step is for the numerical scheme to discretely satisfy the entropy inequality. This motivated the research and development of admissible entropy functions and their properties therein. Friedrichs and Lax [94] proved that if a purely hyperbolic PDE can be put in symmetric hyperbolic form, where the conserved entropy function is a convex function of the original variables and satisfies the entropy equality in Eq. (1.2), then the initial value problem is well-posed. Godunov [95] showed that if there exists a set of variables that symmetrize the governing equations, then there exists a convex entropy function with corresponding entropy fluxes. For nonlinear systems of PDEs of mixed type, Mock [96] proved the converse of Godunov [95]—if there exists a convex entropy function $U(u)$, then the entropy variables $v = U_u$ symmetrize the governing equation (1.1). Harten [97] then provided a review of the general structure of conservation laws with entropy, and their symmetrizability, and laid the foundation of admissible entropy functions for Euler’s gas dynamics. After analyzing an entropy stable upper bound on the viscosity coefficient from Enquist and Osher [98], Osher [99] was the first to use the cell entropy condition to solve for the numerical flux, resulting in the E schemes. The limiting case for the E schemes was Godunov’s viscosity coefficient [7], resulting in a first-order restriction on the E schemes. Motivated to expand beyond first-order for general systems of conservation laws, in the context of finite volume schemes, Tadmor [100] proved that if the numerical flux satisfies the entropy condition from Harten [97], then the discretization is entropy stable—this was accomplished by introducing a weak condition on the numerical flux commonly referred to as the *Tadmor shuffle condition*. These notions were extended by LeFloch [101, 102] in the context of high-order finite difference stencils. In the last decade, these ideas were expanded to bounded domains by Fisher and co-authors [60], who combined the SBP framework with Tadmor’s two-point flux functions to achieve entropy

conservation. Extending the *flux differencing* connection made by Fisher *et al.* [60] between the SBP framework and Tadmor’s shuffle condition, entropy conservative and stable methods have been successfully implemented in DG [70, 103–105], FR [106, 107] for only the DG case, unstructured methods [47, 67, 69], and extended high-order SBP forms [57, 60, 62, 67, 71]. Unfortunately, for high-order numerical approximations to nonlinear PDEs, entropy stability only guarantees that the numerical scheme does not diverge, it does not imply convergence.

An alternative to the *flux differencing* approach to ensure entropy conservation is to add a design order Laplacian term to correct for the entropy production of the base scheme. This *correction term*, developed by Abgrall [108] for residual distribution (RD) schemes, is numerically obtained from the system’s entropy residual—it adds exactly sufficient diffusion or anti-diffusion to ensure entropy conservation [108]. The entropy conserving RD framework allows for extensions to many key finite element frameworks, including DG, FR, continuous Galerkin with jump stabilization, and streamline upwind Petrov-Galerkin [108, 109] while preserving the flavour of finite volume schemes. It has been successful for entropy conservation for the finite element methods [108, 110] and FR in the L2-norm [111]. Through the general form of the correction term, the framework allows for conservation across multiple constraints [110]. Concerning its extension for FR, in order for the RD-FR scheme to maintain the characteristics of larger timesteps by increasing the ESFR correction parameter c , it is imperative to establish its stability within the p -th order broken Sobolev-norm [21, 24, 29]. The p -th order broken Sobolev-norm allows for oscillations within the L2-norm. To investigate an equivalent nonlinearly stable RD-FR scheme, the entropy correction term would need to be envisioned to demonstrate stability in norms other than the L2-norm.

While convergence proofs for unsteady weak solutions are yet to be solved for the high-order methods considered [4], entropy and nonlinear stability is a great starting point to lead toward a convergent discretization. Thus, for FR schemes to be adopted for computational predictive science, it is imperative to develop a provably discrete nonlinearly stable form.

1.2.3 Nonlinearly Stable Flux Reconstruction (NSFR)

One driving topic developed in this thesis is to prove nonlinear stability for the FR scheme with entropy stable two-point fluxes. For linear advection, the ESFR stability proof depends on the p -th order derivative (broken Sobolev-norm) vanishing on the divergence of the discontinuous flux (order $p - 1$) [23, 24, 46]. For nonlinear problems, this is not the case since the volume is a nonlinear polynomial of an order greater than p . For example, consider the chain rule expression within Burgers' equation, where u represents the velocity: $u \frac{\partial u}{\partial x}$ is order $2p - 1$ since u is approximated by order p and $\frac{\partial u}{\partial x}$ is approximated by order $p - 1$. Thus, $\frac{\partial^p}{\partial x^p}(u \frac{\partial u}{\partial x}) \neq 0$. This issue was first raised on linear grids for Burgers' equation by Ranocha *et al.* [106]. Unfortunately, Ranocha *et al.* [106] were able to demonstrate stable solutions only when the ESFR contribution was set to zero; which resulted in the same DG scheme presented in [103]. Ranocha *et al.* [73] presented a second paper on ESFR in split forms, where they considered curvilinear elements. Again, similar to the Burgers' problem, a non-vanishing term arose due to the contribution of the dense norm on the nonlinear volume terms. Although the authors [73] solved the curvilinear problem by setting the ESFR contribution to zero, again, they illustrated that for a vast range of nonlinear problems, the component that prevents a stability claim is the p -th derivative not vanishing on the nonlinear volume terms, for example in Burgers' equation, $\frac{\partial^p}{\partial x^p}(u \frac{\partial u}{\partial x})$. Abe *et al.* [107] numerically demonstrated stability for the “ g_2 lumped-Lobatto” ESFR scheme, which is identical to the collocated DG scheme on Gauss-Lobatto-Legendre quadrature nodes, and is the same scheme proven stable by Gassner *et al.* [104].

The literature lacked a unifying framework for the SBP and ESFR communities. Similar to how Del Rey Fernández *et al.* [63] formulated the curvilinear staggered grid approach to solve the metric Jacobian issue raised by Svård [72], the future of nonlinearly stable ESFR schemes lies in deriving a class of FR schemes for nonlinear problems. Ranocha *et al.* [73, 106] and Abe *et al.* [107] were unable to demonstrate nonlinear stability because they employed the same ESFR scheme derived for linear problems. The first step is to understand the essence of

the stability proofs from entropy conserving DG schemes, and then design the FR scheme to preserve the key property. This step is taken in Chapter 2 to derive nonlinearly stable flux reconstruction (NSFR) for Burgers' equation, where the key property is embedding the split form within the stiffness operator to discretely satisfy integration-by-parts. Then, the resulting NSFR scheme incorporates the influence of the ESFR correction functions on the nonlinear volume term. This realization served as the foundation for the fully developed NSFR solver extending to curvilinear elements in Chapter 3, and the Euler equations in Chapter 5.

1.3 Scalable Implementation

An important property for exascale computing is that the algorithm scales efficiently and its performance is not bounded by memory. For high-order solvers, the bulk of the computational cost is in the evaluation of matrix-vector products.

1.3.1 Sum-Factorization

Sum-factorization, initially proposed by Orszag [112], exploits the tensor product structure to reduce the computational cost of matrix-vector products. Consider we have a three-dimensional matrix $\mathbf{A}(x, y, z) = \mathbf{A}(x) \otimes \mathbf{A}(y) \otimes \mathbf{A}(z)$, which is constructed by the tensor product of one-dimensional basis $\mathbf{A}(x)$ of size n . $\mathbf{A}(x, y, z)$ is of size n^d . Evaluating $\mathbf{w}^T = \mathbf{A}\mathbf{u}^T$ takes n^{2d} flops. Instead, sum-factorization performs each direction independently through pivoting to compute $\mathbf{w}^T = \mathbf{A}\mathbf{u}^T$ in dn^{d+1} flops. This is seen by expanding out $\mathbf{w}(x_i, y_j, z_k) = \sum_{r=0}^n A_r(z_k) \left\{ \sum_{q=0}^n A_q(y_j) \left\{ \sum_{p=0}^n A_p(x_i) u_{pqr} \right\} \right\}$ [113], where we let x run the fastest, then y , and z the slowest. We notice in the expansion that each direction is applied independently. Thus, we have n^2 flops in the innermost brackets for the x -direction, times n flops by the middle y -direction, and multiplied by n flops in the z -direction. For all nodal values, (x_i, y_j, z_k) , this is performed d -times, giving dn^{d+1} total flops. As prescribed by the roofline model [114], for arithmetic intensity, $\text{A.I.} = \frac{\text{flops}}{\text{bytes}}$, with sum-factorization, we do

not need to load the full matrix, but rather one-dimensional matrices of size $n \times n$. Thus the memory traffic is loading dn^2 for the d one-dimensional matrices, loading n^d for the vector, writing n^d output, and loading/writing dn^d vectors within the algorithm. Therefore, $\text{A.I.}_{\text{sum-factorization}} = \frac{dn^{d+1}}{(d+2)n^d + dn^2}$. This is compared to the arithmetic intensity of a matrix-vector product without sum-factorization $\text{A.I.}_{\text{without sum-factorization}} = \frac{n^{2d}}{n^{2d} + 2n^d} < 1$. This yields the added incentive to use sum-factorization for large data since we can push matrix-vector multiplications to be computationally bound instead of memory bound.

As extensively detailed in Karniadakis and Sherwin [115, Chapters 3, 4], by using quadrilateral and hexahedral reference elements, the basis operations can straightforwardly use sum-factorization. For triangular, tetrahedral, prismatic, and pyramidal-based elements, Karniadakis and Sherwin [115, Chapters 3, 4] derived orthogonal tensor product basis functions to exploit sum-factorization in high-order codes. Also, for triangular elements, there are different choices for the location of solution and quadrature points, for example, the α -optimized nodes [4] are found by minimizing the Lebesgue constant, and further nodal sets are derived in Witherden and Vincent[116]. Only quadrilateral and hexahedral-based elements are used in this thesis.

Unfortunately, sum-factorization is only applied for matrix-vector multiplications, and to achieve discrete nonlinear stability, such as Chan [70], a dense Hadamard product is introduced. A Hadamard product costs n^{2d} flops to directly evaluate. In Chapter 4, the tensor product sparsity structure is exploited to derive an algorithm that evaluates Hadamard products in $\mathcal{O}(n^{d+1})$ flops, recovering the sum-factorization result. This novel sum-factorized Hadamard product allows for entropy conserving/stable high-order methods to be computationally competitive with nodal conservative discontinuous Galerkin, and in Chapter 5 it is shown that on average, there is an 12% computational wall-time increase per residual evaluation for discrete nonlinear stability between our NSFR- c_{DG} solver as compared to a conservative nodal DG scheme.

1.3.2 Low-Storage Weight-Adjusted Approximations

In curvilinear coordinates, the mass matrix is fully dense in each element, it needs to be inverted and applied on each residual. There are three approaches: first, build and invert the dense local mass matrix on-the-fly, which costs $\mathcal{O}(n^{3d})$. Second, in the pre-computation stage, build and invert the dense local mass matrices and store a global mass matrix inverse. This requires the most memory for large test cases. Third, approximate the mass matrix inverse with weight-adjusted forms and apply sum-factorization on-the-fly without ever building or inverting a matrix. In Chapter 5, the third option is chosen. In the work from Chan and coauthors [117, 118], they approximated the inverse of the dense Galerkin mass matrix in curvilinear coordinates by L2-projection operators and a diagonal matrix storing the determinant of the metric Jacobian multiplied by the quadrature weights. This allowed for the projection operator in the reference element to be pre-computed, and applied on-the-fly along with the inverse of a diagonal matrix. For NSFR, we follow a similar approach in Chapter 5, but we derive the projection operator to project onto the broken Sobolev-space. This projection operator stores all of the influence of the ESFR correction functions, and it is numerically shown to preserve the orders of convergence up to c_+ . We exploit the tensor product structure of the projection operator by only storing its one-dimensional counterpart. Then, it is applied on-the-fly with a diagonal matrix storing the determinant of the metric Jacobian multiplied to the quadrature weights, to obtain a high-order approximation to the inverse of the mass matrix. This implementation capitalizes the use of sum-factorization and dramatically reduces the computational cost. Comparing the cost of the three options, letting $n = p + 1$, with p the polynomial degree, the first option's cost would be: having to assemble an $n^d \times n^d$ sized dense matrix, invert it at $\mathcal{O}(n^{3d})$ flops, and then perform a matrix-vector multiplication at n^{2d} flops per element. With the weight-adjusted form, we only store an n^2 sized matrix in the pre-computation stage, fetching only an n^2 size matrix and n^d sized vector on-the-fly, and performing dn^{d+1} flops with the transpose of the projection operator, followed by n^d flops multiplying the vector with the inverse of the determinant of the metric Jacobian

with quadrature weights, and then another dn^{d+1} flops applying the projection operator. For three-dimensions, inverting the mass matrix on-the-fly requires $\mathcal{O}(n^9)$, then, the general inverse no longer has a tensor product structure so it requires an additional $\mathcal{O}(n^6)$ flops to apply it to the residual. Conversely, if the global inverse is pre-computed, then there would be $\mathcal{O}(n^9)$ flops in the pre-computation stage, and $\mathcal{O}(n^6)$ applied on-the-fly while having to fetch n^6 terms from memory. Comparatively, in our proposed weight-adjusted form, only n^2 values for the one-dimensional projection operator and n^3 values for the vector storing the quadrature weights and determinant of the Jacobian need to be fetched from memory, and $\mathcal{O}(n^4)$ flops are performed in its application to the residual on-the-fly.

1.3.3 Research Objectives

There are two overarching objectives for this thesis.

1. To have discrete nonlinear stability without upwind dissipation for general, modal, uncollocated, flux reconstruction schemes, with any choice of ESFR correction function, applied to compressible flows in arbitrary curvilinear coordinates.
2. To have the implementation be low-storage and efficiently scalable.

1.3.4 Thesis Contributions

The first contribution is the derivation of nonlinearly stable flux reconstruction high-order schemes. The role of entropy conservation for DG and residual distribution schemes has been well documented, but its extension to general spaces with dense norms as seen in the FR framework was unclear. This thesis introduces the novel concept of incorporating the FR correction functions on the nonlinear volume terms to achieve stability, whereas, in the literature, the correction functions have only been used on the surface integral. This concept was successfully extended from Burgers' equation to the Euler equations, guaranteeing provable discrete nonlinear stability in broken Sobolev-norms.

This thesis develops NSFR for curvilinear elements. In curvilinear elements, it is proven that the DG conservative and non-conservative forms are inherently different, even under exact integration and analytically exact metric terms. This novel result deems the metric split form essential for developing provably stable high-order methods, and necessitates metric-dependent ESFR correction functions. Rigorous attention is also given to the evaluation of the metric Jacobian and cofactor matrix by following the work from Kopriva [82] to ensure free-stream preservation, conservation, and stability for the NSFR context.

Lastly, this thesis presents implementation strategies for FR high-order methods to attain low-storage and efficient scaling. A novel sum-factorized Hadamard product is derived. By using the sum-factorized Hadamard product with sum-factorization for matrix-vector products, the proposed entropy stable discretization from this thesis is computationally competitive with conservative DG schemes. For curvilinear coordinates, a weight-adjusted mass matrix for the broken Sobolev-space is also derived in a way that preserves the orders of convergence and stability properties of the full system. With all of the considerations taken, the global memory footprint of the scheme is in storing a global vector for the solution, the updated solution, and the residual. All local operations are performed in $\mathcal{O}(n^{d+1})$ flops with the local memory footprint fetching an n^d sized local vector and one-dimensional basis functions of size n^2 , with $n = p + 1$ and p the local polynomial degree.

1.3.5 Contribution of Authors

My supervisor, Prof. Siva Nadarajah, supervised and guided all the research completed in this thesis, contributed to the formal analysis, conceptualization, writing and reviewing, software review and provided valuable insights at all steps. I contributed to the formal analysis, conceptualization, methodology, software development, validation, numerical validation, writing and reviewing of all material included in this thesis. David C. Del Rey Fernández contributed to the validation and writing/review for Chapter 2, and the conceptualization, formal analysis, methodology, validation and writing/review for Chapter 3. Jesse Chan and

Mark H. Carpenter both contributed to the validation and writing/review for Chapter 3.

Chapter 2

Nonlinearly Stable Flux Reconstruction for Scalar Problems

The first step to developing NSFR is to consider a scalar nonlinear conservation law. Particularly, this section considers the one-dimensional Burgers' equation. For Burgers' equation, the entropy function and the energy function are the same, $\frac{1}{2}u^2$, and it has a unique analytical entropy conserving flux. This makes it an excellent first step to understanding the problem of ESFR with split forms proposed in the literature [1–3], and the novelty of the NSFR scheme by incorporating the correction functions on the nonlinear volume terms.

Nonlinearly Stable Flux Reconstruction High-Order Methods in Split Form

Alexander Cicchino, Siva Nadarajah, and David C. Del Rey Fernández

From: Cicchino, Alexander, Siva Nadarajah, and David C. Del Rey Fernández. “Nonlinearly stable flux reconstruction high-order methods in split form.” *Journal of Computational Physics* 458 (2022): 111094.

Contribution of authors: Alexander Cicchino: Conceptualization, Formal analysis, Methodology, Software, Validation, Writing – original draft, Writing – review & editing. Siva Nadarajah: Conceptualization, Formal analysis, Methodology, Software, Supervision, Validation, Writing – original draft, Writing – review & editing. David C. Del Rey Fernández: Validation, Writing – review & editing.

Abstract

The flux reconstruction (FR) method has gained popularity in the research community as it recovers promising high-order methods through modally filtered correction fields, such as the discontinuous Galerkin method, amongst others, on unstructured grids over complex geometries. Moreover, FR schemes, specifically energy stable FR (ESFR) schemes also known as Vincent-Castonguay-Jameson-Huynh schemes, have proven attractive as they allow for design flexibility as well as stability proofs for the linear advection problem on affine elements. Additionally, split forms have recently seen a resurgence in research activity due to their resultant nonlinear (entropy) stability proofs. This paper derives for the first time nonlinearly stable ESFR schemes in split form that enable nonlinear stability proofs for, uncollocated, modal, ESFR split forms with different volume and surface cubature nodes. The critical enabling technology is applying the splitting to the discrete stiffness operator. This naturally leads to appropriate surface and numerical fluxes, enabling both entropy stability and conservation proofs. When these schemes are recast in strong form, they differ from schemes found in the ESFR literature as the ESFR correction functions are incorporated on the volume integral. Furthermore, numerical experiments are conducted for Burgers' equation verifying that the new class of proposed ESFR split forms is nonlinearly stable in contrast to the standard split form ESFR approach. Lastly, the new ESFR split form is shown to obtain the correct orders of accuracy.

2.1 Introduction

High-order methods such as discontinuous Galerkin (DG) and flux reconstruction (FR), result in efficient computations via high solution accuracy and dense computational kernels, making them an attractive approach for the exascale concurrency on current and next generation hardware. Generally, high-order methods are known to be more efficient than low-order methods for linear hyperbolic time-dependent problems (e.g., see [4, 5]). However, despite vigorous efforts by the research community, their application to real world complex problems governed by nonlinear partial differential equations (PDEs) has been limited due to a lack of robustness.

FR schemes, first presented by Huynh [6], have proven attractive as they allow for design flexibility as well as stability proofs for the linear advection problem on affine elements. Wang and Gao [7] later presented an alternate approach to the FR scheme. Deemed the Lifting Collocation Penalty (LCP) approach, they considered a “correction field” applied to the surface integral; instead of reconstructing the flux across the surface of the element [7]. The authors merged both the FR and LCP in a common framework called Correction Procedure via Reconstruction (CPR) [8, 9]. Now, FR and CPR are loosely interchangeable since Jameson *et al.* [10] proved that the FR surface reconstruction is identical to the CPR correction field. FR and CPR were merged into a unified framework of provably linearly stable schemes, in the form of energy stable flux reconstruction (ESFR) schemes [7, 11], also known as Vincent-Castonguay-Jameson-Huynh (VCJH) schemes. Moreover, ESFR schemes expressed in a filtered DG form [12, 13], recover other high-order schemes, such as the DG, spectral difference (SD) [14] and spectral volume, by the use of appropriate correction functions. By relating the ESFR correction functions to a DG lifting operator, Allaneau and Jameson [12] presented one-dimensional ESFR schemes as a filtered DG scheme. This was extended and generalized by Zwanenburg and Nadarajah [13] for up to three-dimensional elements, and allowed ESFR to be presented in an arbitrarily modal, uncollocated framework in both weak

and strong forms.

Recently, there has been a concerted research effort to extend classical entropy stability arguments to high-order methods. The original work of Tadmor [15] laid a foundation enabling high-order extensions, where Tadmor [15] constructed entropy conservative or stable low-order finite volume schemes. These notions were extended by LeFloch [16, 17] in the context of high-order finite difference stencils. In the last decade, these ideas were expanded to bounded domains by Fisher and co-authors [18], who combined the Summation-by-parts (SBP) framework with Tadmor’s two-point flux functions. The core notion behind the SBP framework is to account for discrete integration and construct operators that discretely mimic integration by parts (see the two review papers [19, 20]). The SBP framework has seen rapid development and extensions to various schemes including DG [21, 22], FR [1, 3], unstructured methods [19, 23, 24], as well as extensions enabling entropy stability proofs [15, 18, 22, 23, 25–27]. In the context of FR, the first paper to merge a collocated DG split form and ESFR was presented by Ranocha *et al.* [1], for the one-dimensional Burgers’ equation, where they proved stability for the DG case. The methodology was further expanded for the Euler equations by Abe *et al.* [3], where stability with ESFR in split forms was only achieved for a specific ESFR discretization; Huynh’s g_2 lumped-Lobatto scheme [6], which was equivalent to a collocated DG scheme on Gauss-Lobatto-Legendre nodes [28]. Neither Ranocha *et al.* [1] nor Abe *et al.* [3] have provided a general, nonlinearly stable ESFR scheme.

In this paper we take the first critical step towards developing provably entropy stable schemes for hyperbolic conservation laws that are broadly applicable to FR schemes, *i.e.* they account for discretization design decisions such as: modal or nodal basis, uncollocated integration, different volume and surface nodes, *etc.* Specifically, the development of ESFR schemes in split form that result in entropy stability proofs for Burgers’ equation is considered. Although the derivation is presented in one-dimension, its extension for three-dimensional ESFR split forms is straightforward. The first main result is to perform the split form for uncollocated DG schemes within the discrete stiffness operator, rather than inverting the

mass matrix and performing chain rule with respect to the differential operator. This allows the scheme to utilize the summation-by-parts property with dense norms, and results in the schemes presented by Chan [22]. In Section 2.3, we demonstrate that nonlinearly stable ESFR split forms are naturally derived when constructing ESFR as a filtered DG scheme alike Allaneau and Jameson [12], and Zwanenburg and Nadarajah [13]. We propose a new class of provably nonlinearly stable, uncollocated ESFR schemes in split form by incorporating the ESFR filter on the non-conservative volume term. We also prove that, in general, no nonlinear stability claim can be made if the ESFR filter, *i.e.* the influence of the ESFR correction functions, is only applied to the surface; differentiating our proposed schemes from the literature [1, 3, 6, 7, 9–13, 29–31]. The proposed ESFR split form is proven to be nonlinearly stable (Section 2.3.1.2) and conservative (Section 2.3.1.1). The theoretical proofs are numerically verified in Section 2.4. The results demonstrate that a split form with the ESFR correction functions solely applied to the face is divergent, whereas incorporating the correction functions on the non-conservative volume term ensures entropy stability. Lastly, the schemes proposed by this paper are shown to achieve the correct orders of accuracy in the context of grid refinement.

2.2 Preliminaries

2.2.1 DG Formulation

The formulation of ESFR used in this paper follows that shown in [12, 13, 32]. The analysis is done in one-dimension, but we preserve some of the structure of multi-dimensional curvilinear approximations to allow a seamless extension to future works. Consider the scalar 1D conservation law,

$$\begin{aligned} \frac{\partial}{\partial t} u(x^c, t) + \frac{\partial}{\partial x} f(u(x^c, t)) &= 0, t \geq 0, x^c \in \Omega, \\ u(x^c, 0) &= u_0(x^c), \end{aligned} \tag{2.1}$$

where $f(u(x^c, t))$ stores the flux, while the c superscript refers to the Cartesian coordinates.

For the rest of the article, row vector notation will be used. The computational domain is partitioned into M non-overlapping elements, denoted by Ω^h ,

$$\Omega \simeq \Omega^h := \bigcup_{m=1}^M \Omega_m. \quad (2.2)$$

The global solution can then be taken as the direct sum of each approximation within each element,

$$u(x^c, t) \simeq u^h(x^c, t) = \bigoplus_{m=1}^M u_m^h(x^c, t). \quad (2.3)$$

On each element, we represent the solution with N_p linearly independent modal or nodal polynomial basis of a maximum order of p ; where $N_p = (p + 1)$,

$$u_m^h(x^c, t) = \sum_{i=1}^{N_p} \chi_{m,i}(x^c) \hat{u}_{m,i}(t) = \boldsymbol{\chi}_m(x^c) \hat{\mathbf{u}}_m(t)^T, \quad (2.4)$$

and

$$\boldsymbol{\chi}_m(x^c) := [\chi_{m,1}(x^c) \ \chi_{m,2}(x^c) \ \dots \ \chi_{m,N_p}(x^c)] \quad (2.5)$$

holds the basis functions for the element. The elementwise residual is,

$$R_m^h(x^c, t) = \frac{\partial}{\partial t} u_m^h(x^c, t) + \frac{\partial}{\partial x} f(u_m^h(x^c, t)). \quad (2.6)$$

The physical coordinates are mapped through an affine mapping to the reference element $\xi^r \in [-1, 1]$ by

$$x_m^c(\xi^r) := \Theta_m(\xi^r) = \boldsymbol{\Theta}_m(\xi^r) (\hat{\mathbf{x}}_m^c)^T, \quad (2.7)$$

where $\boldsymbol{\Theta}_m(\xi^r) := [\Theta_{m,1}(\xi^r) \ \dots \ \Theta_{m,N_{t,m}}(\xi^r)]$ are the mapping shape functions of the $N_{t,m}$ physical mapping control points $\hat{\mathbf{x}}_m^c := [\hat{x}_{m,1}^c \ \dots \ \hat{x}_{m,N_{t,m}}^c]$. Thus, the elementwise reference residual is,

$$R_m^{h,r}(\xi^r, t) := R_m^h(\Theta_m(\xi^r), t) = \frac{\partial}{\partial t} u_m^h(\Theta_m(\xi^r), t) + \frac{1}{J_m^\Omega} \frac{\partial}{\partial \xi} f^r(u_m^h(\Theta_m(\xi^r), t)), \quad (2.8)$$

where the addition of the r superscript denotes evaluation in the reference space and J_m^Ω represents the determinant of the metric Jacobian; for one-dimension J_m^Ω is the volume of cell m . Following a DG framework, we left multiply the residual by an orthogonal test function, and integrate over the computational domain. Choosing the test function to be the same as the basis function, applying integration by parts twice, and evaluating bilinear forms using cubature rules, we arrive at the following strong form:

$$\mathbf{M}_m \frac{d}{dt} \hat{\mathbf{u}}_m(t)^T + \mathbf{S}_\xi \hat{\mathbf{f}}_m^r(t)^T + \sum_{f=1}^{N_f} \boldsymbol{\chi}(\boldsymbol{\xi}_f^r)^T \mathbf{W}_f \text{diag}(\hat{\mathbf{n}}^r) \mathbf{f}_m^{C,r^T} = \mathbf{0}^T, \quad (2.9)$$

where the derivation is not restricted to one-dimension. The mass and stiffness matrices are defined as,

$$\begin{aligned} (\mathbf{M}_m)_{ij} &\approx \int_{\Omega_r} J_m^\Omega \chi_i(\xi^r) \chi_j(\xi^r) d\Omega_r \rightarrow \mathbf{M}_m = \boldsymbol{\chi}(\boldsymbol{\xi}_v^r)^T \mathbf{W} \mathbf{J}_m \boldsymbol{\chi}(\boldsymbol{\xi}_v^r), \\ (\mathbf{S}_\xi)_{ij} &= \int_{\Omega_r} \chi_i(\xi^r) \frac{\partial}{\partial \xi} \chi_j(\xi^r) d\Omega_r \rightarrow \mathbf{S}_\xi = \boldsymbol{\chi}(\boldsymbol{\xi}_v^r)^T \mathbf{W} \frac{\partial \boldsymbol{\chi}(\boldsymbol{\xi}_v^r)}{\partial \xi}. \end{aligned}$$

We also explicitly express the mass matrix without Jacobian dependence for later reference,

$$\mathbf{M} = \boldsymbol{\chi}(\boldsymbol{\xi}_v^r)^T \mathbf{W} \boldsymbol{\chi}(\boldsymbol{\xi}_v^r). \quad (2.10)$$

$\boldsymbol{\xi}_v^r$ and $\boldsymbol{\xi}_f^r$ refers to the reference coordinate at the N_{vp} volume and N_{fp} facet cubature nodes respectively; with N_f being the number of faces on the element. Here \mathbf{W} and \mathbf{W}_f are diagonal operators storing the quadrature weights of integration at the volume and facet cubature nodes respectively. \mathbf{J}_m is a diagonal operator storing the determinant of the metric Jacobian evaluated at the volume cubature nodes; while, $\text{diag}(\hat{\mathbf{n}}^r) = \text{diag}(\hat{\mathbf{n}}^r) = \text{diag}(\hat{\mathbf{n}}^\xi)$ represents the diagonal matrix of the outward pointing normal on the face at the facet cubature nodes in the one-dimensional reference element. In addition, the modal coefficients of the reference flux, $\hat{\mathbf{f}}_m^r(t)$, are equivalent to the discrete L_2 projection of the reference flux constructed at the cubature nodes, \mathbf{f}_m^r ; ie $\hat{\mathbf{f}}_m^r(t)^T = \boldsymbol{\Pi}(\mathbf{f}_m^r)^T$, where $\boldsymbol{\Pi} = \mathbf{M}^{-1} \boldsymbol{\chi}(\boldsymbol{\xi}_v^r)^T \mathbf{W}$.

Lastly, $\mathbf{f}_m^{C,r^T} := \mathbf{f}_m^{*,r^T} - \chi(\boldsymbol{\xi}_f^r) \hat{\mathbf{f}}_m^r(t)^T$ is the reference numerical flux minus the reference flux across the face f .

After discrete integration by parts once more, provided the cubature rule is exact for at least $2p - 1$, the corresponding weak form is established,

$$\mathbf{M}_m \frac{d}{dt} \hat{\mathbf{u}}_m(t)^T - \mathbf{S}_\xi^T \hat{\mathbf{f}}_m^r(t)^T + \sum_{f=1}^{N_f} \chi(\boldsymbol{\xi}_f^r)^T \mathbf{W}_f \text{diag}(\hat{\mathbf{n}}^r) \mathbf{f}_m^{*,r^T} = \mathbf{0}^T. \quad (2.11)$$

2.2.2 Corresponding ESFR Scheme

The ESFR scheme is derived using $p + 1$ correction functions, $g^{f,k}(\boldsymbol{\xi}^r)$, specific to face f , facet cubature node k , such that,

$$g^{f,k}(\boldsymbol{\xi}_{f_i,k_j}^r) \hat{n}^\xi = \begin{cases} 1 & \text{if } f_i = f, \text{ and } k_j = k \\ 0 & \text{otherwise.} \end{cases} \quad (2.12)$$

The one-dimensional correction functions are defined by the symmetry condition $g^L(\boldsymbol{\xi}^r) = -g^R(-\boldsymbol{\xi}^r)$ to satisfy Eq. (2.12), and the fundamental assumption of ESFR [11, Eqs. (3.31), (3.32)],

$$\int_{\Omega_r} \frac{\partial \chi_i(\boldsymbol{\xi}^r)}{\partial \xi} g^{f,k}(\boldsymbol{\xi}^r) d\Omega_r - c \frac{\partial^p \chi_i(\boldsymbol{\xi}^r)^T}{\partial \xi^p} \frac{\partial^{p+1} g^{f,k}(\boldsymbol{\xi}^r)}{\partial \xi^{p+1}} = 0, \quad \forall i = 1, \dots, N_p. \quad (2.13)$$

Here, c represents the correction parameter, with values of c_{DG} , c_{SD} , c_{HU} , and c_+ . Each parameter results in the scheme having different properties; where, c_{DG} recovers a DG scheme, c_{SD} recovers a spectral difference scheme, and c_{HU} recovers Huynh's g_2 scheme [11]. Lastly, the value of c_+ does not have an analytical value, but has numerically been shown to be the upper limit in a von Neumann analysis of the correction parameter before the scheme loses an order of accuracy [33]. Note that as c increases, the maximum time step increases.

As illustrated in [12, 13, 32] the corresponding ESFR strong form is,

$$(\mathbf{M}_m + \mathbf{K}_m) \frac{d}{dt} \hat{\mathbf{u}}_m(t)^T + \mathbf{S}_\xi \hat{\mathbf{f}}_m^r(t)^T + \sum_{f=1}^{N_f} \chi(\xi_f^r)^T \mathbf{W}_f \text{diag}(\hat{\mathbf{n}}^r) \mathbf{f}_m^{C,r^T} = \mathbf{0}^T, \quad (2.14)$$

while the corresponding weak form is,

$$(\mathbf{M}_m + \mathbf{K}_m) \frac{d}{dt} \hat{\mathbf{u}}_m(t)^T - \mathbf{S}_\xi^T \hat{\mathbf{f}}_m^r(t)^T + \sum_{f=1}^{N_f} \chi(\xi_f^r)^T \mathbf{W}_f \text{diag}(\hat{\mathbf{n}}^r) \mathbf{f}_m^{*,r^T} = \mathbf{0}^T. \quad (2.15)$$

The entire influence of the ESFR correction functions are stored in \mathbf{K}_m , which we define as

$$(\mathbf{K}_m)_{ij} = c \int_{\Omega_r} J_m^\Omega \frac{\partial^p \chi_i(\xi^r)}{\partial \xi^p} \frac{\partial^p \chi_j(\xi^r)}{\partial \xi^p} d\Omega_r \rightarrow \mathbf{K}_m = c(\mathbf{D}^p)^T \mathbf{M}_m (\mathbf{D}^p), \quad (2.16)$$

where the p^{th} degree strong form differential operator [32] is construed as

$$\mathbf{D}^p = \left(\mathbf{M}^{-1} \mathbf{S}_\xi \right)^p. \quad (2.17)$$

Remark 2.2.1. *Unlike in [1, 12, 13] where \mathbf{K}_m was constructed using the Legendre differential operator then transformed to the basis of the scheme, here, \mathbf{K}_m in Eq. (3.39) is computed directly with the differential operator of the scheme; where c must take the value from a normalized Legendre reference basis [32]. This was proven in [32, Sec. 3.1]*

2.3 SBP-ESFR Split Forms for Burgers' Equation

In this section we analyze a new proposed splitting that enables nonlinear stability proofs for general FR schemes, where the modal or nodal basis functions can be evaluated on uncollocated volume and surface cubature nodes. We will consider the Burgers' equation,

$$\frac{\partial}{\partial t} u + \frac{\partial}{\partial x} \left(\frac{u^2}{2} \right) = 0. \quad (2.18)$$

As demonstrated in [1, 21], for a collocated DG strong form scheme, entropy and energy stability was ensured if the differential operator is split into a linear combination of the conservative and chain rule forms. This was achieved by observing that the strong form differential operator satisfies the SBP property with respect to the metric Jacobian independent mass matrix,

$$\mathbf{M}_{\text{GLL}}\mathbf{D} + \mathbf{D}^T\mathbf{M}_{\text{GLL}} = \mathbf{B}, \quad (2.19)$$

where $\mathbf{B} = \text{diag}[-1, 0, \dots, 0, 1]$, with Gauss-Lobatto-Legendre (GLL) quadrature points or Gauss-Legendre (GL) quadrature points in one-dimension. The proposed splitting in [21] was,

$$\frac{d}{dt}\mathbf{u}_m^T = \frac{1}{J_m^\Omega} \left[-\alpha\mathbf{D}\left(\frac{1}{2}\mathbf{U}\mathbf{u}_m^T\right) - (1-\alpha)\mathbf{U}\mathbf{D}(\mathbf{u}_m^T) - \mathbf{M}_{\text{GLL}}^{-1} \sum_{f=1}^{N_f} \boldsymbol{\chi}(\boldsymbol{\xi}_f^r)^T \mathbf{W}_f \text{diag}(\hat{\mathbf{n}}^r) \mathbf{f}_m^{C,r^T} \right], \quad (2.20)$$

which was achieved using a collocated nodal Lagrange basis, with $\mathbf{U} = \text{diag}(\mathbf{u}_m)$. This was further expanded for a classical ESFR scheme in [1] as,

$$\begin{aligned} & \frac{d}{dt}\mathbf{u}_m^T \\ &= \frac{1}{J_m^\Omega} \left[-\alpha\mathbf{D}\left(\frac{1}{2}\mathbf{U}\mathbf{u}_m^T\right) - (1-\alpha)\mathbf{U}\mathbf{D}(\mathbf{u}_m^T) - (\mathbf{M}_{\text{GLL}} + \mathbf{K})^{-1} \sum_{f=1}^{N_f} \boldsymbol{\chi}(\boldsymbol{\xi}_f^r)^T \mathbf{W}_f \text{diag}(\hat{\mathbf{n}}^r) \mathbf{f}_m^{C,r^T} \right], \end{aligned} \quad (2.21)$$

where \mathbf{K} is the metric Jacobian independent ESFR correction operator.

To demonstrate stability, the following broken Sobolev-norm was proposed by [34] for

ESFR schemes:

$$\begin{aligned}
& \text{Continuous Broken Sobolev-norm: } \int_{\Omega_r} \left(\boldsymbol{\chi}(\xi^r) \hat{\mathbf{u}}_m(t)^T \right)^T J_m^\Omega \left(\boldsymbol{\chi}(\xi^r) \frac{d}{dt} \hat{\mathbf{u}}_m(t)^T \right) d\Omega_r + \\
& \int_{\Omega_r} c \left(\frac{\partial^p}{\partial \xi^p} \left(\boldsymbol{\chi}(\xi^r) \hat{\mathbf{u}}_m(t)^T \right) \right)^T J_m^\Omega \left(\frac{\partial^p}{\partial \xi^p} \left(\boldsymbol{\chi}(\xi^r) \frac{d}{dt} \hat{\mathbf{u}}_m(t)^T \right) \right) d\Omega_r \\
\implies & \text{Discrete Broken Sobolev-norm: } \frac{1}{2} \frac{d}{dt} \|\mathbf{u}\|_{M_m + K_m}^2 = \hat{\mathbf{u}}_m(t) (\mathbf{M}_m + \mathbf{K}_m) \frac{d}{dt} \hat{\mathbf{u}}_m(t)^T.
\end{aligned} \tag{2.22}$$

Applying the discrete broken Sobolev-norm to Eq. (2.21), and using the property that $\mathbf{K}\mathbf{D} = 0$ since it is the $p + 1$ derivative of a p^{th} order basis function, results in,

$$\begin{aligned}
\frac{1}{2} \frac{d}{dt} \|\mathbf{u}\|_{M_m + K_m}^2 = & \left[-\alpha \mathbf{u}_m \mathbf{M}_{GLL} \mathbf{D} \left(\frac{1}{2} \mathbf{U} \mathbf{u}_m^T \right) - (1 - \alpha) \mathbf{u}_m \mathbf{M}_{GLL} \mathbf{U} \mathbf{D} (\mathbf{u}_m^T) \right. \\
& \left. - (1 - \alpha) \mathbf{u}_m \mathbf{K} \mathbf{U} \mathbf{D} (\mathbf{u}_m^T) - \sum_{f=1}^{N_f} \mathbf{u}_m \mathbf{W}_f \text{diag}(\hat{\mathbf{n}}^r) \mathbf{f}_m^{C,rT} \right].
\end{aligned} \tag{2.23}$$

Both [1, 21] used the property that for a collocated nodal Lagrange basis, the mass matrix is a diagonal operator and therefore commutes with \mathbf{U} in the second volume term. This then allows the use of the SBP property to relate the two volume terms to a face term. The issue that was illustrated in Ranocha *et al.* [1] was that for an ESFR scheme, $\mathbf{K}\mathbf{U}\mathbf{D} \neq \mathbf{0}$, nor is it in general positive semi-definite. Thus, when the split form (chain rule) is applied on the differential operator, no stability claim can be made for an ESFR scheme, unless $\mathbf{K} = \mathbf{0}$ as used by Ranocha *et al.* [1] or \mathbf{K} is a diagonal operator. In Abe *et al.* [3], they used Huynh's g_2 lumped-Lobatto scheme [6] which was equivalent to formulating $\mathbf{M} + \mathbf{K}$ on uncollocated Gauss-Legendre nodes, with a value of c_{HU} . By design, \mathbf{K}_{HU} (\mathbf{K} evaluated with a value of c_{HU} on GL nodes) was chosen such that $\mathbf{M}_{GL} + \mathbf{K}_{HU} = \mathbf{M}_{GLL}$, the collocated lumped DG mass matrix on Gauss-Lobatto-Legendre nodes [6, 11, 28]. Then, the crucial step was to evaluate the flux on GLL nodes, which results in an equivalent DG collocated GLL scheme [3, 6, 11, 28]. In a sense, the g_2 lumped-Lobatto scheme operates on mixed nodes (with regards to the volume flux on GLL and correction functions on GL), since in the

original FR framework [6] no concept of quadrature integration was introduced.

Remark 2.3.1. *For consistency, since the ESFR formulation used in this work is completely general, there is no assumption on the nodes the volume flux is integrated on, other than being exact for at least $2p - 1$. Thus, in the ESFR strong and weak forms presented in Equations (2.14) and (2.15), Huynh's g_2 lumped-Lobatto scheme is equivalent to using a collocated basis on GLL nodes and a value of c_{DG} , or using a value of c_{HU} with $\mathbf{M} + \mathbf{K}$ evaluated with an integration strength of at least $2p$, and the volume flux on GLL nodes. Huynh's g_2 lumped-Lobatto scheme is not equivalent to computing both $\mathbf{M} + \mathbf{K}$ and the volume flux on the same set of nodes, with a value of c_{HU} . We numerically verify this in Section 2.4.*

2.3.1 Proposed Splitting with Respect to the Stiffness Operator

The stiffness operator satisfies a discrete integration by parts rule, *i.e.* an SBP property, for quadrature rules exact for at least $2p - 1$,

$$\begin{aligned} \int_{\Omega_r} \chi_i(\xi^r) \frac{\partial}{\partial \xi} \chi_j(\xi^r) d\Omega_r + \int_{\Omega_r} \frac{\partial}{\partial \xi} \chi_i(\xi^r) \chi_j(\xi^r) d\Omega_r &= \int_{\Gamma_r} \chi_i(\xi^r) \chi_j(\xi^r) \hat{n}^\xi d\Gamma_r \\ &\Leftrightarrow \mathbf{S}_\xi + \mathbf{S}_\xi^T = \sum_{f=1}^{N_f} \boldsymbol{\chi}(\boldsymbol{\xi}_f^r)^T \mathbf{W}_f \text{diag}(\hat{\mathbf{n}}^\xi) \boldsymbol{\chi}(\boldsymbol{\xi}_f^r). \end{aligned} \quad (2.24)$$

Since the underlying SBP property results from the fact that the stiffness operator satisfies discrete integration by parts, Eq. (2.24), and observing the ESFR strong and weak forms (Eq. (2.14) and (2.15) respectively), we propose to construct the split form based upon the stiffness operator rather than the differential operator, in contrast to previous works [1, 3, 21, 22].

Returning to the continuous analog of Eq. (2.14), writing it in variational form results in,

$$\begin{aligned} &\int_{\Omega_r} \left(\chi_i(\xi^r) J_m^\Omega \boldsymbol{\chi}(\xi^r) + c \frac{\partial^p \chi_i(\xi^r)}{\partial \xi^p} J_m^\Omega \frac{\partial^p \boldsymbol{\chi}(\xi^r)}{\partial \xi^p} \right) \frac{d}{dt} \hat{\mathbf{u}}_m(t)^T d\Omega_r \\ &= - \int_{\Omega_r} \chi_i(\xi^r) \frac{\partial}{\partial \xi} \left(\frac{1}{2} u_m^2 \right) d\Omega_r - \int_{\Gamma_r} \chi_i(\xi^r) \hat{n}^r f_m^{C,r} d\Gamma_r, \quad \forall i = 1, \dots, N_p. \end{aligned} \quad (2.25)$$

Performing chain rule with respect to the reference coordinate gives,

$$\begin{aligned}
& \int_{\Omega_r} \left(\chi_i(\xi^r) J_m^\Omega \boldsymbol{\chi}(\xi^r) + c \frac{\partial^p \chi_i(\xi^r)}{\partial \xi^p} J_m^\Omega \frac{\partial^p \boldsymbol{\chi}(\xi^r)}{\partial \xi^p} \right) \frac{d}{dt} \hat{\mathbf{u}}_m(t)^T d\Omega_r \\
&= -\alpha \int_{\Omega_r} \chi_i(\xi^r) \frac{\partial}{\partial \xi} \left(\frac{1}{2} u_m^2 \right) d\Omega_r - (1 - \alpha) \int_{\Omega_r} \chi_i(\xi^r) u_m \frac{\partial}{\partial \xi} (u_m) d\Omega_r \\
& \quad - \int_{\Gamma_r} \chi_i(\xi^r) \hat{n}^r f_m^{C,r} d\Gamma_r, \quad \forall i = 1, \dots, N_p.
\end{aligned} \tag{2.26}$$

Here, alike [21], $\alpha \in [0, 1]$. After evaluating at the appropriate cubature nodes, we invert the ESFR filter operator on the left hand side, and present it in discretized form,

$$\begin{aligned}
\frac{d}{dt} \hat{\mathbf{u}}_m(t)^T &= -\alpha (\mathbf{M}_m + \mathbf{K}_m)^{-1} \mathbf{S}_\xi \hat{\mathbf{f}}_m^r(t)^T - (1 - \alpha) (\mathbf{M}_m + \mathbf{K}_m)^{-1} \boldsymbol{\chi}(\boldsymbol{\xi}_v^r)^T \mathbf{U} \mathbf{W} \frac{\partial \boldsymbol{\chi}(\boldsymbol{\xi}_v^r)}{\partial \xi} \hat{\mathbf{u}}_m(t)^T \\
& \quad - (\mathbf{M}_m + \mathbf{K}_m)^{-1} \sum_{f=1}^{N_f} \boldsymbol{\chi}(\boldsymbol{\xi}_f^r)^T \mathbf{W}_f \text{diag}(\hat{\mathbf{n}}^r) \mathbf{f}_m^{C,rT}.
\end{aligned} \tag{2.27}$$

Unless GLL is employed as the volume cubature nodes, the nonlinear flux interpolated to the face does not generally equal the flux on the face evaluated using the solution interpolated to the face. Therefore, we also split the flux on the face using $\boldsymbol{\chi}(\boldsymbol{\xi}_f^r) \hat{\mathbf{f}}_m^r(t)^T$ as the interpolation of the modal coefficients of the volume flux to the face, and $\mathbf{f}_f^{rT} = \frac{1}{2} \text{diag} \left(\boldsymbol{\chi}(\boldsymbol{\xi}_f^r) \hat{\mathbf{u}}_m(t)^T \right) \left(\boldsymbol{\chi}(\boldsymbol{\xi}_f^r) \hat{\mathbf{u}}_m(t)^T \right)$ as the flux on face f evaluated using the solution interpolated to the face. The final ESFR strong split form is thus,

$$\begin{aligned}
\frac{d}{dt} \hat{\mathbf{u}}_m(t)^T &= -\alpha (\mathbf{M}_m + \mathbf{K}_m)^{-1} \mathbf{S}_\xi \hat{\mathbf{f}}_m^r(t)^T - (1 - \alpha) (\mathbf{M}_m + \mathbf{K}_m)^{-1} \boldsymbol{\chi}(\boldsymbol{\xi}_v^r)^T \mathbf{U} \mathbf{W} \frac{\partial \boldsymbol{\chi}(\boldsymbol{\xi}_v^r)}{\partial \xi} \hat{\mathbf{u}}_m(t)^T \\
& \quad - (\mathbf{M}_m + \mathbf{K}_m)^{-1} \sum_{f=1}^{N_f} \boldsymbol{\chi}(\boldsymbol{\xi}_f^r)^T \mathbf{W}_f \text{diag}(\hat{\mathbf{n}}^r) \left(\mathbf{f}_m^{*,rT} - \alpha \boldsymbol{\chi}(\boldsymbol{\xi}_f^r) \hat{\mathbf{f}}_m^r(t)^T - (1 - \alpha) \mathbf{f}_f^{rT} \right).
\end{aligned} \tag{2.28}$$

If one were to consider the general differential operator applied to the entropy conservative two-point flux in Chan [22], then the face splitting, as used in [1, 2, 35], appears naturally when grouping the face lifting terms and the DG result of Eq. (2.28) is equivalent to A.14

in [22]. Additionally, note that for a collocated DG scheme at Gauss-Lobatto-Legendre nodes, $\boldsymbol{\chi}(\boldsymbol{\xi}_f^r) \hat{\mathbf{f}}_m^r(t)^T = \mathbf{f}_f^{r^T}$, and hence no interpolation of the flux to the face was required, and thus face splitting did not appear in [21].

To convert Eq. (2.28) to the weak form, we perform discrete integration by parts, Eq. (2.24), on the two volume terms. For the first volume term we directly substitute Eq. (2.24). For the second volume term we first substitute $\frac{\partial \boldsymbol{\chi}(\boldsymbol{\xi}_v^r)}{\partial \boldsymbol{\xi}} = \boldsymbol{\chi}(\boldsymbol{\xi}_v^r) \mathbf{M}^{-1} \mathbf{S}_\xi$, then introduce the discrete L_2 projection operator $\boldsymbol{\Pi}$ and finally Eq. (2.24),

$$\begin{aligned} \frac{d}{dt} \hat{\mathbf{u}}_m(t)^T &= \alpha (\mathbf{M}_m + \mathbf{K}_m)^{-1} \mathbf{S}_\xi^T \hat{\mathbf{f}}_m^r(t)^T + (1 - \alpha) (\mathbf{M}_m + \mathbf{K}_m)^{-1} \boldsymbol{\chi}(\boldsymbol{\xi}_v^r)^T \mathbf{U} \boldsymbol{\Pi}^T \mathbf{S}_\xi^T \hat{\mathbf{u}}_m(t)^T \\ &\quad - (\mathbf{M}_m + \mathbf{K}_m)^{-1} \sum_{f=1}^{N_f} \boldsymbol{\chi}(\boldsymbol{\xi}_f^r)^T \mathbf{W}_f \text{diag}(\hat{\mathbf{r}}^r) \mathbf{f}_m^{*,r^T}. \end{aligned} \quad (2.29)$$

Remark 2.3.2. *Eq. (2.29) is not equivalent to performing integration by parts on the continuous form in Eq. (2.26), and then discretizing.*

We will now demonstrate that the proposed ESFR split form is equivalent to the DG split form with additional volume and surface terms. For this purpose, the following lemma is necessary.

Lemma 2.3.1. *The additional filter term applied to the split form volume term is exactly equal to $(\mathbf{M}_m + \mathbf{K}_m)^{-1} = \mathbf{M}_m^{-1} - \frac{1}{1+c(2p+1)(p!c_p)^2} \mathbf{M}_m^{-1} \mathbf{K}_m \mathbf{M}_m^{-1}$ for linear elements.*

Proof. After factoring out the Jacobian dependence, consider transforming $(\mathbf{M} + \mathbf{K})^{-1}$ to a normalized Legendre reference basis, $\boldsymbol{\chi}_{ref}(\boldsymbol{\xi}^r)$, by use of the transformation operator $\mathbf{T} = \boldsymbol{\Pi}_{ref} \boldsymbol{\chi}(\boldsymbol{\xi}_v^r)$, where $\boldsymbol{\Pi}_{ref} = \mathbf{M}_{ref}^{-1} \boldsymbol{\chi}_{ref}(\boldsymbol{\xi}_v^r)^T \mathbf{W}$ is the L_2 projection operator for a normalized Legendre reference basis.

$$(\mathbf{M} + \mathbf{K})^{-1} = \mathbf{T}^{-1} (\mathbf{M}_{ref} + \mathbf{K}_{ref})^{-1} \mathbf{T}^{-T}. \quad (2.30)$$

To use the Sherman-Morrison formula, we consider $\mathbf{K}_{ref} = c \mathbf{r}^T \mathbf{s}$, where

$\mathbf{r} = [0 \dots 0 \frac{\partial^p \chi_{ref,p}(\xi)}{\partial \xi^p}]$ and $\mathbf{s} = [0 \dots 0 \frac{\partial^p \chi_{ref,p}(\xi)}{\partial \xi^p} \sum_{i=1}^{N_{vp}} W(\xi_{v,i}^r)]$, with $\chi_{ref,p}(\xi) = \sqrt{\frac{2p+1}{2} \frac{(2p)!}{2^p (p!)^2}} \xi^p + \dots + c_0 = \sqrt{\frac{2p+1}{2}} c_p \xi^p + \dots + c_0$ is the p^{th} order normalized Legendre polynomial. Thus, $\frac{\partial^p \chi_{ref,p}(\xi)}{\partial \xi^p} = \sqrt{\frac{2p+1}{2}} c_p p!$. Utilizing that the mass matrix of a normalized Legendre reference basis is an identity matrix, and the Sherman-Morrison formula,

$$\begin{aligned} (\mathbf{M} + \mathbf{K})^{-1} &= \mathbf{T}^{-1} \left(\mathbf{I} - \frac{1}{1 + \mathbf{c} \mathbf{s} \mathbf{r}^T} \mathbf{K}_{ref} \right) \mathbf{T}^{-T} \\ &= \mathbf{M}^{-1} - \frac{1}{1 + c(2p+1)(p!c_p)^2} \mathbf{M}^{-1} \mathbf{K} \mathbf{M}^{-1}. \end{aligned} \quad (2.31)$$

Including Jacobian dependence results in,

$$(\mathbf{M}_m + \mathbf{K}_m)^{-1} = \mathbf{M}_m^{-1} - \frac{1}{1 + c(2p+1)(p!c_p)^2} \mathbf{M}_m^{-1} \mathbf{K}_m \mathbf{M}_m^{-1}. \quad (2.32)$$

□

Note that $\mathbf{K}_m \mathbf{M}_m^{-1} \mathbf{S}_\xi = 0$ for linear grids, provided that the flux is not projected to a higher order basis [13, Appendix A]. If the flux is not projected to a higher order basis, we can fully express Eq. (2.28) as,

$$\begin{aligned} \frac{d}{dt} \hat{\mathbf{u}}_m(t)^T &= -\alpha \mathbf{M}_m^{-1} \mathbf{S}_\xi \hat{\mathbf{f}}_m^r(t)^T - (1 - \alpha) \mathbf{M}_m^{-1} \boldsymbol{\chi}(\boldsymbol{\xi}_v^r)^T \mathbf{U} \mathbf{W} \frac{\partial \boldsymbol{\chi}(\boldsymbol{\xi}_v^r)}{\partial \xi} \hat{\mathbf{u}}_m(t)^T \\ &\quad + \frac{(1 - \alpha)}{1 + c(2p+1)(p!c_p)^2} \mathbf{M}_m^{-1} \mathbf{K}_m \mathbf{M}_m^{-1} \boldsymbol{\chi}(\boldsymbol{\xi}_v^r)^T \mathbf{U} \mathbf{W} \frac{\partial \boldsymbol{\chi}(\boldsymbol{\xi}_v^r)}{\partial \xi} \hat{\mathbf{u}}_m(t)^T \\ &\quad - (\mathbf{M}_m + \mathbf{K}_m)^{-1} \sum_{f=1}^{N_f} \boldsymbol{\chi}(\boldsymbol{\xi}_f^r)^T \mathbf{W}_f \text{diag}(\hat{\mathbf{n}}^r) \left(\mathbf{f}_m^{*,rT} - \alpha \boldsymbol{\chi}(\boldsymbol{\xi}_f^r) \hat{\mathbf{f}}_m^r(t)^T - (1 - \alpha) \mathbf{f}_f^{rT} \right). \end{aligned} \quad (2.33)$$

We numerically demonstrate that this additional term is design order by obtaining the correct orders in Section 2.4.

2.3.1.1 Discrete Conservation

Following the formulation presented in [1, 21] for conservation, we demonstrate here both local and global conservation using a quadrature of exact integration of at least $2p - 1$,

Continuous:

$$\int_{\Omega_r} (\boldsymbol{\chi}(\boldsymbol{\xi}^r) \hat{\mathbf{1}}^T)^T J_m^\Omega(\boldsymbol{\chi}(\boldsymbol{\xi}^r) \frac{d}{dt} \hat{\mathbf{u}}_m(t)^T) + c \left(\frac{\partial^p}{\partial \xi^p} (\boldsymbol{\chi}(\boldsymbol{\xi}^r) \hat{\mathbf{1}}^T) \right)^T J_m^\Omega \left(\frac{\partial^p}{\partial \xi^p} (\boldsymbol{\chi}(\boldsymbol{\xi}^r) \frac{d}{dt} \hat{\mathbf{u}}_m(t)^T) \right) d\Omega_r$$

$$\implies \text{Discrete: } \hat{\mathbf{1}}(\mathbf{M}_m + \mathbf{K}_m) \frac{d}{dt} \hat{\mathbf{u}}_m(t)^T,$$
(2.34)

where $\mathbf{1} = [1, \dots, 1] = (\boldsymbol{\chi}(\boldsymbol{\xi}_v^r) \hat{\mathbf{1}}^T)^T$. Alike [1, 10, 32, 36], we prove conservation and stability in the broken Sobolev-norm, $(\mathbf{M}_m + \mathbf{K}_m)$ -norm, which bounds the L_2 -norm. In addition, the ESFR correction functions are defined in the one degree higher Raviart-Thomas space [6, 37]. First, we substitute Eq. (2.28) to show local and global conservation for the proposed split strong form.

$$\hat{\mathbf{1}}(\mathbf{M}_m + \mathbf{K}_m) \frac{d}{dt} \hat{\mathbf{u}}_m(t)^T = -\alpha \hat{\mathbf{1}} \mathbf{S}_\xi \hat{\mathbf{f}}_m^r(t)^T - (1 - \alpha) \hat{\mathbf{1}} \boldsymbol{\chi}(\boldsymbol{\xi}_v^r)^T \mathbf{U} \mathbf{W} \frac{\partial \boldsymbol{\chi}(\boldsymbol{\xi}_v^r)}{\partial \xi} \hat{\mathbf{u}}_m(t)^T$$

$$- \hat{\mathbf{1}} \sum_{f=1}^{N_f} \boldsymbol{\chi}(\boldsymbol{\xi}_f^r)^T \mathbf{W}_f \text{diag}(\hat{\mathbf{n}}^r) \left(\mathbf{f}_m^{*,r^T} - \alpha \boldsymbol{\chi}(\boldsymbol{\xi}_f^r) \hat{\mathbf{f}}_m^r(t)^T - (1 - \alpha) \mathbf{f}_f^{r^T} \right).$$
(2.35)

Discretely integrating the first term by parts yields,

$$\hat{\mathbf{1}}(\mathbf{M}_m + \mathbf{K}_m) \frac{d}{dt} \hat{\mathbf{u}}_m(t)^T = \alpha \hat{\mathbf{1}} \mathbf{S}_\xi^T \hat{\mathbf{f}}_m^r(t)^T - (1 - \alpha) \hat{\mathbf{1}} \boldsymbol{\chi}(\boldsymbol{\xi}_v^r)^T \mathbf{U} \mathbf{W} \frac{\partial \boldsymbol{\chi}(\boldsymbol{\xi}_v^r)}{\partial \xi} \hat{\mathbf{u}}_m(t)^T$$

$$- \hat{\mathbf{1}} \sum_{f=1}^{N_f} \boldsymbol{\chi}(\boldsymbol{\xi}_f^r)^T \mathbf{W}_f \text{diag}(\hat{\mathbf{n}}^r) \left(\mathbf{f}_m^{*,r^T} - (1 - \alpha) \mathbf{f}_f^{r^T} \right).$$
(2.36)

Note that for the first volume term,

$$\hat{\mathbf{1}}\mathbf{S}_\xi^T = \left(\mathbf{S}_\xi \hat{\mathbf{1}}^T\right)^T = \left(\boldsymbol{\chi}(\boldsymbol{\xi}_v^r)^T \mathbf{W} \frac{\partial \boldsymbol{\chi}(\boldsymbol{\xi}_v^r)}{\partial \xi} \hat{\mathbf{1}}^T\right)^T = \left(\boldsymbol{\chi}(\boldsymbol{\xi}_v^r)^T \mathbf{W} \frac{\partial}{\partial \xi} \mathbf{1}^T\right)^T = \mathbf{0}, \quad (2.37)$$

is the derivative of a constant, and hence eliminated. Using $\mathbf{W} \frac{\partial \boldsymbol{\chi}(\boldsymbol{\xi}_v^r)}{\partial \xi} = \boldsymbol{\Pi}^T \mathbf{S}_\xi$ on the second volume term and discretely integrating by parts we obtain,

$$\begin{aligned} \hat{\mathbf{1}}(\mathbf{M}_m + \mathbf{K}_m) \frac{d}{dt} \hat{\mathbf{u}}_m(t)^T &= (1 - \alpha) \hat{\mathbf{1}} \boldsymbol{\chi}(\boldsymbol{\xi}_v^r)^T \mathbf{U} \boldsymbol{\Pi}^T \mathbf{S}_\xi^T \hat{\mathbf{u}}_m(t)^T \\ &- (1 - \alpha) \hat{\mathbf{1}} \boldsymbol{\chi}(\boldsymbol{\xi}_v^r)^T \mathbf{U} \boldsymbol{\Pi}^T \sum_{f=1}^{N_f} \boldsymbol{\chi}(\boldsymbol{\xi}_f^r)^T \mathbf{W}_f \text{diag}(\hat{\mathbf{n}}^r) \boldsymbol{\chi}(\boldsymbol{\xi}_f^r) \hat{\mathbf{u}}_m(t)^T \\ &- \hat{\mathbf{1}} \sum_{f=1}^{N_f} \boldsymbol{\chi}(\boldsymbol{\xi}_f^r)^T \mathbf{W}_f \text{diag}(\hat{\mathbf{n}}^r) \left(\mathbf{f}_m^{*,rT} - (1 - \alpha) \mathbf{f}_f^{rT}\right). \end{aligned} \quad (2.38)$$

Adding a half of Eq. (2.36) and (2.38), and noticing that

$$\begin{aligned} \hat{\mathbf{1}} \boldsymbol{\chi}(\boldsymbol{\xi}_v^r)^T \mathbf{U} \boldsymbol{\Pi}^T \mathbf{S}_\xi^T \hat{\mathbf{u}}_m(t)^T &= (\boldsymbol{\chi}(\boldsymbol{\xi}_v^r) \hat{\mathbf{1}}^T)^T \mathbf{U} \boldsymbol{\Pi}^T \mathbf{S}_\xi^T \hat{\mathbf{u}}_m(t)^T \\ &= (\boldsymbol{\Pi} \mathbf{u}_m^T)^T \mathbf{S}_\xi^T \hat{\mathbf{u}}_m(t)^T = \hat{\mathbf{u}}_m(t) \mathbf{S}_\xi^T \hat{\mathbf{u}}_m(t)^T = \left(\hat{\mathbf{u}}_m(t) \mathbf{S}_\xi \hat{\mathbf{u}}_m(t)^T\right)^T \end{aligned} \quad (2.39)$$

is a scalar, we can drop the transpose and the volume terms cancel and hence,

$$\begin{aligned} \hat{\mathbf{1}}(\mathbf{M}_m + \mathbf{K}_m) \frac{d}{dt} \hat{\mathbf{u}}_m(t)^T &= -\frac{(1 - \alpha)}{2} \sum_{f=1}^{N_f} \hat{\mathbf{u}}_m(t) \boldsymbol{\chi}(\boldsymbol{\xi}_f^r)^T \mathbf{W}_f \text{diag}(\hat{\mathbf{n}}^r) \boldsymbol{\chi}(\boldsymbol{\xi}_f^r) \hat{\mathbf{u}}_m(t)^T \\ &- \hat{\mathbf{1}} \sum_{f=1}^{N_f} \boldsymbol{\chi}(\boldsymbol{\xi}_f^r)^T \mathbf{W}_f \text{diag}(\hat{\mathbf{n}}^r) \left(\mathbf{f}_m^{*,rT} - (1 - \alpha) \mathbf{f}_f^{rT}\right). \end{aligned} \quad (2.40)$$

Finally, if we consider the first term in Eq. (2.40) evaluated at a single facet cubature node k ,

$$\begin{aligned} \frac{1}{2} \hat{\mathbf{u}}_m(t) \boldsymbol{\chi}(\boldsymbol{\xi}_{f,k}^r)^T \mathbf{W}_{f,k} \hat{\mathbf{n}}_{f,k}^r \boldsymbol{\chi}(\boldsymbol{\xi}_{f,k}^r) \hat{\mathbf{u}}_m(t)^T &= \frac{1}{2} \left(u_{f,k} \mathbf{W}_{f,k} \hat{\mathbf{n}}_{f,k}^r u_{f,k}\right) \\ &= 1 \mathbf{W}_{f,k} \hat{\mathbf{n}}_{f,k}^r \left(\frac{1}{2} u_{f,k}^2\right) = \hat{\mathbf{1}} \boldsymbol{\chi}(\boldsymbol{\xi}_{f,k}^r)^T \mathbf{W}_{f,k} \hat{\mathbf{n}}_{f,k}^r \mathbf{f}_{f,k}^r, \end{aligned} \quad (2.41)$$

then we are left with,

$$\hat{\mathbf{1}}(\mathbf{M}_m + \mathbf{K}_m) \frac{d}{dt} \hat{\mathbf{u}}_m(t)^T = -\hat{\mathbf{1}} \sum_{f=1}^{N_f} \boldsymbol{\chi}(\boldsymbol{\xi}_f^r)^T \mathbf{W}_f \text{diag}(\hat{\mathbf{n}}^r) \mathbf{f}_m^{*,rT}, \quad (2.42)$$

which concludes the proof for the strong ESFR split form's local and global conservation.

2.3.1.2 Discrete Energy Stability

We consider the broken Sobolev-norm in Eq. (2.22) to demonstrate nonlinear stability. Analyzing the uncollocated ESFR split strong form, we insert Eq. (2.28) into the energy balance, and notice that $(\mathbf{M}_m + \mathbf{K}_m)(\mathbf{M}_m + \mathbf{K}_m)^{-1} = \mathbf{I}$, the identity matrix. That is, when incorporating the ESFR filter on the nonlinear volume integral, the dense ESFR norm cancels off, and we obtain,

$$\begin{aligned} \frac{1}{2} \frac{d}{dt} \|\mathbf{u}\|_{M_m+K_m}^2 &= -\alpha \hat{\mathbf{u}}_m(t) \mathbf{S}_\xi \hat{\mathbf{f}}_m^r(t)^T - (1-\alpha) \hat{\mathbf{u}}_m(t) \boldsymbol{\chi}(\boldsymbol{\xi}_v^r)^T \mathbf{U} \mathbf{W} \frac{\partial \boldsymbol{\chi}(\boldsymbol{\xi}_v^r)}{\partial \xi} \hat{\mathbf{u}}_m(t)^T \\ &\quad - \hat{\mathbf{u}}_m(t) \sum_{f=1}^{N_f} \boldsymbol{\chi}(\boldsymbol{\xi}_f^r)^T \mathbf{W}_f \text{diag}(\hat{\mathbf{n}}^r) \left(\mathbf{f}_m^{*,rT} - \alpha \boldsymbol{\chi}(\boldsymbol{\xi}_f^r) \hat{\mathbf{f}}_m^r(t)^T - (1-\alpha) \mathbf{f}_f^{rT} \right). \end{aligned} \quad (2.43)$$

Using discrete integration by parts, Eq. (2.24), on the first volume term results in,

$$\begin{aligned} \frac{1}{2} \frac{d}{dt} \|\mathbf{u}\|_{M_m+K_m}^2 &= \alpha \hat{\mathbf{u}}_m(t) \mathbf{S}_\xi^T \hat{\mathbf{f}}_m^r(t)^T - (1-\alpha) \hat{\mathbf{u}}_m(t) \boldsymbol{\chi}(\boldsymbol{\xi}_v^r)^T \mathbf{U} \mathbf{W} \frac{\partial \boldsymbol{\chi}(\boldsymbol{\xi}_v^r)}{\partial \xi} \hat{\mathbf{u}}_m(t)^T \\ &\quad - \hat{\mathbf{u}}_m(t) \sum_{f=1}^{N_f} \boldsymbol{\chi}(\boldsymbol{\xi}_f^r)^T \mathbf{W}_f \text{diag}(\hat{\mathbf{n}}^r) (\mathbf{f}_m^{*,rT} - (1-\alpha) \mathbf{f}_f^{rT}). \end{aligned} \quad (2.44)$$

Note that $\hat{\mathbf{u}}_m(t) \mathbf{S}_\xi^T \hat{\mathbf{f}}_m^r(t)^T = \hat{\mathbf{f}}_m^r(t) \mathbf{S}_\xi \hat{\mathbf{u}}_m(t)^T = \left(\boldsymbol{\chi}(\boldsymbol{\xi}_v^r) \hat{\mathbf{u}}_m(t)^T \right)^T \mathbf{U} \boldsymbol{\Pi}^T \mathbf{S}_\xi \hat{\mathbf{u}}_m(t)^T$ is a scalar

and thus,

$$\begin{aligned}
\frac{1}{2} \frac{d}{dt} \|\mathbf{u}\|_{M_m+K_m}^2 &= \frac{1}{2} \alpha \left(\boldsymbol{\chi}(\boldsymbol{\xi}_v^r) \hat{\mathbf{u}}_m(t)^T \right)^T \mathbf{U} \boldsymbol{\Pi}^T \mathbf{S}_\xi \hat{\mathbf{u}}_m(t)^T \\
&\quad - (1 - \alpha) \hat{\mathbf{u}}_m(t) \boldsymbol{\chi}(\boldsymbol{\xi}_v^r)^T \mathbf{U} \boldsymbol{\Pi}^T \mathbf{S}_\xi \hat{\mathbf{u}}_m(t)^T \\
&\quad - \hat{\mathbf{u}}_m(t) \sum_{f=1}^{N_f} \boldsymbol{\chi}(\boldsymbol{\xi}_f^r)^T \mathbf{W}_f \text{diag}(\hat{\mathbf{n}}^r) (\mathbf{f}_m^{*,rT} - (1 - \alpha) \mathbf{f}_f^{rT}).
\end{aligned} \tag{2.45}$$

Choosing $\alpha = \frac{2}{3}$ has the volume terms vanish, and we are left with,

$$\frac{1}{2} \frac{d}{dt} \|\mathbf{u}\|_{M_m+K_m}^2 = -\hat{\mathbf{u}}_m(t) \sum_{f=1}^{N_f} \boldsymbol{\chi}(\boldsymbol{\xi}_f^r)^T \mathbf{W}_f \text{diag}(\hat{\mathbf{n}}^r) (\mathbf{f}_m^{*,rT} - \frac{1}{3} \mathbf{f}_f^{rT}). \tag{2.46}$$

Since our energy balance Eq. (2.46) only incorporates terms evaluated on the surface, we reuse observations from Gassner [21]. After considering an edge term, assuming all interior (left) cells' outward pointing normal is 1, letting w_0 represent the solution at the right of the edge, and v_p represent the solution at the left of the face, the surface contribution for Eq. (2.46) is,

$$\text{surface contribution} = (w_0 - v_p)^2 \left(\frac{1}{12} (w_0 - v_p) - \lambda \right), \tag{2.47}$$

where the following numerical flux is used,

$$f_m^{*,r} = \frac{1}{2} \left(\frac{w_0^2}{2} + \frac{v_p^2}{2} \right) - \lambda (w_0 - v_p). \tag{2.48}$$

This directly leads to the stability criterion of,

$$\lambda \geq \frac{1}{12} (w_0 - v_p). \tag{2.49}$$

The local Lax-Friedrichs numerical flux ensures energy and entropy stability, since,

$$\lambda_{LLF} = \frac{1}{2} \max(|w_0|, |v_p|) \geq \frac{1}{12} (w_0 - v_p). \tag{2.50}$$

As discussed by Tadmor [38] and Gassner [21], for discontinuous solutions, at the continuous level the mathematical entropy is not conserved and thus the entropy conservative approach is physically incorrect. The base entropy conservative scheme therefore necessitates some form of dissipation when considering shocks and here we utilize the above mentioned local Lax-Friedrichs interface dissipation.

2.4 Numerical Results

In this section, we use the open-source Parallel High-order Library for PDEs (PHiLiP) [39] and consider similar test cases as used in [21] and [1],

$$\frac{\partial}{\partial t}u + \frac{\partial}{\partial x}\left(\frac{u^2}{2}\right) = q(x, t), \quad x \in [0, 2], \quad (2.51)$$

with periodic boundary conditions. Using values of c_{DG} , c_+ , and $c_{10^4} = 10^4$, we first demonstrate that our proposed strong ESFR split form satisfies the energy/entropy stability criteria derived in Sec. 2.3 on collocated GLL nodes, uncollocated GL nodes, and uncollocated GL nodes with overintegration; with $q(x, t) = 0$ and $u(x, 0) = \sin(\pi x) + 0.01$. Our basis functions are Lagrange polynomials constructed on GLL nodes. Next, we verify that we observe the correct orders of accuracy for the strong ESFR split form by using $q(x, t) = \pi \sin(\pi(x - t))(1 - \cos(\pi(x - t)))$, $u(x, 0) = \cos(\pi x)$ and $u_{\text{exact}}(x, t) = \cos(\pi(x - t))$. We utilize the generality of the scheme by testing both uncollocated $N_{vp} = p + 1$ and an uncollocated overintegration scheme on $N_{vp} = p + 3$; both on GL nodes.

Since our proposed splitting includes the additional filtering of $(\mathbf{M}_m + \mathbf{K}_m)^{-1}$ on the second volume term, which does not occur in the classical ESFR scheme, we verify that it is needed for stability and that it does not effect the order of accuracy. For readability, ‘‘Cons. DG’’ refers to the conservative DG scheme Eq. (2.9), ‘‘ESFR Split’’ refers to our proposed splitting in Eq. (2.28), and ‘‘Classical ESFR Split’’ refers to the strong split form with a classical ESFR implementation, where $(\mathbf{M}_m + \mathbf{K}_m)^{-1}$ is only applied on the face terms.

Scheme	Flux	Energy Conserved $\mathcal{O}(1e-12)$	Energy Monotonically Decrease
Cons. DG	ECON	No	No
Cons. DG	LF	No	No
EFSR Split c_{DG}^{-1}	ECON	Yes	Yes
EFSR Split c_{DG}^{-1}	LF	No	Yes
EFSR Split c_+	ECON	Yes	Yes
EFSR Split c_+	LF	No	Yes
EFSR Split c_{10^4}	ECON	Yes	Yes
EFSR Split c_{10^4}	LF	No	Yes
EFSR Classical Split c_+	ECON	No	No
EFSR Classical Split c_+	LF	No	No
EFSR Classical Split c_{HU}^{-1}	ECON	No	No
EFSR Classical Split c_{HU}^{-1}	LF	No	No
EFSR Classical Split c_{HU} Lumped-Lobatto ¹	ECON	Yes	Yes
EFSR Classical Split c_{HU} Lumped-Lobatto ¹	LF	No	Yes

Table 2.1: Energy Results $p = 4,5$ Collocated Schemes $N_{vp} = p + 1$

Note that ‘‘EFSR Split’’ with a value of c_{DG} is the same scheme presented by Chan [22], and Gassner [21] when it is collocated on Gauss-Lobatto-Legendre nodes. All schemes were conservative on the order of 1×10^{-16} .

2.4.1 Energy Verification

For the collocated results, we integrate the solution and fluxes on Gauss-Lobatto-Legendre quadrature nodes. For the uncollocated results, we integrate the solution and fluxes on Gauss-Legendre quadrature nodes. The solution is integrated in time using RK4 with a timestep of $\Delta t = 1e - 4$ until a final time of $t_f = 3$ s, well past the formation of the shock, and the grid is partitioned into $M = 8$ uniform elements. ‘‘ECON’’ refers to the energy conserving numerical flux (the equality in Eq. (2.49)) and ‘‘LF’’ refers to the Lax-Friedrichs numerical flux, using the value from Eq. (2.50). Tables 2.1, 2.2, and 2.3 present the energy results.

2.4.2 Orders of Accuracy (OOA)

To compute the L_2 -error, an overintegration of $p + 10$ was used in calculating the error to provide a sufficient strength for the purpose of accuracy.

¹Note that the g_2 lumped-Lobatto scheme presented by Huynh [6], and used by Abe *et al.* [3], is equivalent to a collocated DG scheme on GLL nodes and not equivalent to using c_{HU} with a collocated \mathbf{K}_m operator [28].

²N/A refers to ‘‘Not Available’’. The g_2 lumped-Lobatto scheme cannot be run on uncollocated volume nodes since it would not make sense lumping the mode on the boundary.

Scheme	Flux	Energy Conserved $\mathcal{O}(1e-12)$	Energy Monotonically Decrease
Cons. DG	ECON	No	No
Cons. DG	LF	No	No
EFSR Split c_{DG}	ECON	Yes	Yes
EFSR Split c_{DG}	LF	No	Yes
EFSR Split c_+	ECON	Yes	Yes
EFSR Split c_+	LF	No	Yes
EFSR Split c_{10^4}	ECON	Yes	Yes
EFSR Split c_{10^4}	LF	No	Yes
EFSR Classical Split c_+	ECON	No	No
EFSR Classical Split c_+	LF	No	No
EFSR Classical Split c_{HU}^{-1}	ECON	No	No
EFSR Classical Split c_{HU}^{-1}	LF	No	No
ESFR Classical Split c_{HU} Lumped-Lobatto ²	ECON	N/A	N/A
ESFR Classical Split c_{HU} Lumped-Lobatto ²	LF	N/A	N/A

Table 2.2: Energy Results $p = 4,5$ Uncollocated Schemes $N_{vp} = p + 1$

Scheme	Flux	Energy Conserved $\mathcal{O}(1e-12)$	Energy Monotonically Decrease
Cons. DG	ECON	No	No
Cons. DG	LF	No	No
EFSR Split c_{DG}	ECON	Yes	Yes
EFSR Split c_{DG}	LF	No	Yes
EFSR Split c_+	ECON	Yes	Yes
EFSR Split c_+	LF	No	Yes
EFSR Split c_{10^4}	ECON	Yes	Yes
EFSR Split c_{10^4}	LF	No	Yes
EFSR Classical Split c_+	ECON	No	No
EFSR Classical Split c_+	LF	No	No
EFSR Classical Split c_{HU}^{-1}	ECON	No	No
EFSR Classical Split c_{HU}^{-1}	LF	No	No
ESFR Classical Split c_{HU} Lumped-Lobatto ²	ECON	N/A	N/A
ESFR Classical Split c_{HU} Lumped-Lobatto ²	LF	N/A	N/A

Table 2.3: Energy Results $p = 4,5$ Uncollocated Schemes Overintegrated $N_{vp} = p + 3$

$$L_2 - \text{error} = \sqrt{\sum_{m=1}^M \int_{\Omega} (u_m - u)^2 d\Omega} = \sqrt{\sum_{m=1}^M (\mathbf{u}_m^T - \mathbf{u}_{exact}^T) \mathbf{W} \mathbf{J}_m (\mathbf{u}_m - \mathbf{u}_{exact})}. \quad (2.52)$$

The L_2 -errors are shown for the test case described above for Cons. DG and strong EFSR Split with c_{DG} to provide a direct comparison of the influence of splitting the volume and face terms on the OOA. Also, strong EFSR Split with c_+ , and strong EFSR Classical Split with c_+ are tested to give a direct comparison of the influence of $(\mathbf{M}_m + \mathbf{K}_m)^{-1}$ being applied on the non-conservative volume term for accuracy. We use a $t_f = 1$ s, $\Delta t = 1 \times 10^{-4}$, and a Lax-Friedrichs numerical flux for the OOA test. We demonstrate the OOA for $p = 4$

uncollocated $N_{vp} = p + 1$ in table 2.4 and uncollocated overintegration in table 2.6; similarly for $p = 5$ in tables 2.5 and 2.7. All schemes yield the expected convergence rates of $p + 1$. Note that “-” in the tables denote that the values have reached machine precision.

dx	Cons. DG	OOA	ESFR Split c_{DG}	OOA	ESFR Split c_+	OOA	ESFR Classical Split c_+	OOA
2.50e-02	7.82e-06	-	7.72e-06	-	2.22e-04	-	1.42e-04	-
1.25e-02	1.94e-07	5.33	1.93e-07	5.32	6.77e-06	5.04	4.18e-06	5.09
6.25e-03	5.17e-09	5.23	5.17e-09	5.23	1.98e-07	5.10	1.28e-07	5.03
3.13e-03	1.48e-10	5.12	1.48e-10	5.12	6.30e-09	4.97	4.21e-09	4.93
1.56e-03	4.55e-12	5.02	4.55e-12	5.02	1.96e-10	5.00	1.33e-10	4.98

Table 2.4: Convergence Table $p = 4$ $N_{vp} = p + 1$

dx	Cons. DG	OOA	ESFR Split c_{DG}	OOA	ESFR Split c_+	OOA	ESFR Classical Split c_+	OOA
2.08e-02	1.65e-07	-	1.57e-07	-	2.25e-05	-	1.24e-05	-
1.04e-02	2.31e-09	6.15	2.31e-09	6.09	4.24e-07	5.73	2.35e-07	5.72
5.21e-03	3.55e-11	6.02	3.56e-11	6.02	8.00e-09	5.73	4.84e-09	5.60
2.60e-03	-	-	-	-	1.54e-10	5.70	9.99e-11	5.60
1.30e-03	-	-	-	-	2.84e-12	5.76	1.88e-12	5.73

Table 2.5: Convergence Table $p = 5$ $N_{vp} = p + 1$

dx	Cons. DG	OOA	ESFR Split c_{DG}	OOA	ESFR Split c_+	OOA	ESFR Classical Split c_+	OOA
2.50e-02	7.37e-06	-	7.37e-06	-	2.21e-04	-	9.32e-05	-
1.25e-02	1.91e-07	5.27	1.91e-07	5.27	6.76e-06	5.03	1.16e-06	6.33
6.25e-03	5.15e-09	5.21	5.15e-09	5.21	1.97e-07	5.10	1.94e-08	5.90
3.13e-03	1.48e-10	5.12	1.48e-10	5.12	6.30e-09	4.97	5.05e-10	5.26
1.56e-03	4.55e-12	5.02	4.55e-12	5.02	1.96e-10	5.00	1.52e-11	5.06

Table 2.6: Convergence Table $p = 4$ Overintegrated $N_{vp} = p + 3$

dx	Cons. DG	OOA	ESFR Split c_{DG}	OOA	ESFR Split c_+	OOA	ESFR Classical Split c_+	OOA
2.08e-02	1.56e-07	-	1.56e-07	-	2.24e-05	-	1.46e-06	-
1.04e-02	2.33e-09	6.07	2.33e-09	6.07	4.23e-07	5.72	1.01e-08	7.18
5.21e-03	3.57e-11	6.03	3.57e-11	6.03	8.00e-09	5.72	1.09e-10	6.53
2.60e-03	-	-	-	-	1.54e-10	5.70	1.66e-12	6.04
1.30e-03	-	-	-	-	2.84e-12	5.76	-	-

Table 2.7: Convergence Table $p = 5$ Overintegrated $N_{vp} = p + 3$

2.5 Conclusion

This paper derived dense, modal or nodal, ESFR schemes in both strong and weak forms that resulted in provable nonlinear stability and conservation by incorporating the ESFR filter operator on both the volume and surface terms. It was shown that by considering split forms with respect to the stiffness operator rather than the differential operator, discrete integration by parts was embedded in the discretization. The stability criteria, conservation, and convergence orders were numerically verified for a wide range of general ESFR schemes.

2.6 Acknowledgements

We would like to gratefully acknowledge the financial support of the Natural Sciences and Engineering Research Council of Canada Discovery Grant Program and McGill University.

References

- [1] Hendrik Ranocha, Philipp Öffner, and Thomas Sonar. “Summation-by-parts operators for correction procedure via reconstruction”. In: *Journal of Computational Physics* 311 (2016), pp. 299–328.
- [2] Hendrik Ranocha, Philipp Öffner, and Thomas Sonar. “Extended skew-symmetric form for summation-by-parts operators and varying Jacobians”. In: *Journal of Computational Physics* 342 (2017), pp. 13–28.

- [3] Yoshiaki Abe, Issei Morinaka, Takanori Haga, Taku Nonomura, Hisaichi Shibata, and Koji Miyaji. “Stable, non-dissipative, and conservative flux-reconstruction schemes in split forms”. In: *Journal of Computational Physics* 353 (2018), pp. 193–227.
- [4] Heinz-Otto Kreiss and Joseph Oliger. “Comparison of accurate methods for the integration of hyperbolic equations”. In: *Tellus* 24.3 (1972), pp. 199–215.
- [5] Blair Swartz and Burton Wendroff. “The relative efficiency of finite difference and finite element methods. I: Hyperbolic problems and splines”. In: *SIAM Journal on Numerical Analysis* 11.5 (1974), pp. 979–993.
- [6] H. T. Huynh. “A flux reconstruction approach to high-order schemes including discontinuous Galerkin methods”. In: American Institute of Aeronautics and Astronautics, 2007.
- [7] Zhi Jian Wang and Haiyang Gao. “A unifying lifting collocation penalty formulation including the discontinuous Galerkin, spectral volume/difference methods for conservation laws on mixed grids”. In: *Journal of Computational Physics* 228.21 (2009), pp. 8161–8186.
- [8] Zhi Jian Wang. *Adaptive high-order methods in computational fluid dynamics*. Vol. 2. World Scientific, 2011.
- [9] HT Huynh, Zhi J Wang, and Peter E Vincent. “High-order methods for computational fluid dynamics: A brief review of compact differential formulations on unstructured grids”. In: *Computers & fluids* 98 (2014), pp. 209–220.
- [10] Antony Jameson, Peter E Vincent, and Patrice Castonguay. “On the non-linear stability of flux reconstruction schemes”. In: *Journal of Scientific Computing* 50.2 (2012), pp. 434–445.
- [11] Peter E Vincent, Patrice Castonguay, and Antony Jameson. “A new class of high-order energy stable flux reconstruction schemes”. In: *Journal of Scientific Computing* 47.1 (2011), pp. 50–72.

- [12] Yves Allaneau and Antony Jameson. “Connections between the filtered discontinuous Galerkin method and the flux reconstruction approach to high order discretizations”. In: *Computer Methods in Applied Mechanics and Engineering* 200.49–52 (2011), pp. 3628–3636.
- [13] Philip Zwanenburg and Siva Nadarajah. “Equivalence between the energy stable flux reconstruction and filtered discontinuous Galerkin schemes”. In: *Journal of Computational Physics* 306 (2016), pp. 343–369.
- [14] Yen Liu, Marcel Vinokur, and Zhi J. Wang. “Spectral difference method for unstructured grids I: Basic formulation”. In: *Journal of Computational Physics* 216.2 (2006), pp. 780–801.
- [15] Eitan Tadmor. “Skew-self adjoint form for systems of conservation laws”. In: *Journal of Mathematical Analysis and Applications* 103.2 (1984), pp. 428–442.
- [16] Philippe G LeFloch, Jean-Marc Mercier, and Christian Rohde. “Fully discrete, entropy conservative schemes of arbitrary order”. In: *SIAM Journal on Numerical Analysis* 40.5 (2002), pp. 1968–1992.
- [17] Philippe G LeFloch and Christian Rohde. “High-order schemes, entropy inequalities, and nonclassical shocks”. In: *SIAM Journal on Numerical Analysis* 37.6 (2000), pp. 2023–2060.
- [18] Travis Calob Fisher. “High-order L2 stable multi-domain finite difference method for compressible flows”. PhD thesis. Purdue University, 2012.
- [19] David C Del Rey Fernández, Jason E Hicken, and David W Zingg. “Review of summation-by-parts operators with simultaneous approximation terms for the numerical solution of partial differential equations”. In: *Computers & Fluids* 95 (2014), pp. 171–196.

- [20] Magnus Svärd and Jan Nordström. “Review of summation-by-parts schemes for initial–boundary-value problems”. In: *Journal of Computational Physics* 268 (2014), pp. 17–38.
- [21] Gregor J Gassner. “A skew-symmetric discontinuous Galerkin spectral element discretization and its relation to SBP-SAT finite difference methods”. In: *SIAM Journal on Scientific Computing* 35.3 (2013), A1233–A1253.
- [22] Jesse Chan. “On discretely entropy conservative and entropy stable discontinuous Galerkin methods”. In: *Journal of Computational Physics* 362 (2018), pp. 346–374.
- [23] Jared Crean, Jason E Hicken, David C Del Rey Fernández, David W Zingg, and Mark H Carpenter. “Entropy-stable summation-by-parts discretization of the Euler equations on general curved elements”. In: *Journal of Computational Physics* 356 (2018), pp. 410–438.
- [24] David C Del Rey Fernández, Jared Crean, Mark H. Carpenter, and Jason E. Hicken. “Staggered-grid entropy-stable multidimensional summation-by-parts discretizations on curvilinear coordinates”. In: *Journal of Computational Physics* 392 (2019), pp. 161–186.
- [25] Travis C Fisher and Mark H Carpenter. “High-order entropy stable finite difference schemes for nonlinear conservation laws: Finite domains”. In: *Journal of Computational Physics* 252 (2013), pp. 518–557.
- [26] Lucas Friedrich, Gero Schnücker, Andrew R Winters, David C Del Rey Fernández, Gregor J Gassner, and Mark H Carpenter. “Entropy stable space–time discontinuous Galerkin schemes with summation-by-parts property for hyperbolic conservation laws”. In: *Journal of Scientific Computing* 80.1 (2019), pp. 175–222.
- [27] Matteo Parsani, Mark H Carpenter, and Eric J Nielsen. “Entropy stable wall boundary conditions for the three-dimensional compressible Navier–Stokes equations”. In: *Journal of Computational Physics* 292 (2015), pp. 88–113.

- [28] D De Grazia, G Mengaldo, D Moxey, PE Vincent, and SJ Sherwin. “Connections between the discontinuous Galerkin method and high-order flux reconstruction schemes”. In: *International journal for numerical methods in fluids* 75.12 (2014), pp. 860–877.
- [29] D. M. Williams and A. Jameson. “Energy stable flux reconstruction schemes for advection–diffusion problems on tetrahedra”. In: *Journal of Scientific Computing* 59.3 (2014), pp. 721–759.
- [30] Abhishek Sheshadri and Antony Jameson. “On the stability of the flux reconstruction schemes on quadrilateral elements for the linear advection equation”. In: *Journal of Scientific Computing* 67.2 (2016), pp. 769–790.
- [31] Patrice Castonguay, David M Williams, Peter E. Vincent, and Antony Jameson. “Energy stable flux reconstruction schemes for advection–diffusion problems”. In: *Computer Methods in Applied Mechanics and Engineering* 267 (2013), pp. 400–417.
- [32] Alexander Cicchino and Siva Nadarajah. “A new norm and stability condition for tensor product flux reconstruction schemes”. In: *Journal of Computational Physics* (2020), p. 110025.
- [33] Patrice Castonguay. “High-order energy stable flux reconstruction schemes for fluid flow simulations on unstructured grids”. In: *Diss. Stanford University* (2012).
- [34] Antony Jameson. “A proof of the stability of the spectral difference method for all orders of accuracy”. In: *Journal of Scientific Computing* 45.1-3 (2010), pp. 348–358.
- [35] Sigrun Ortleb. “A Kinetic Energy Preserving DG Scheme Based on Gauss-Legendre Points.” In: *J. Sci. Comput.* 71.3 (2017), pp. 1135–1168.
- [36] Peter E Vincent, Patrice Castonguay, and Antony Jameson. “Insights from von Neumann analysis of high-order flux reconstruction schemes”. In: *Journal of Computational Physics* 230.22 (2011), pp. 8134–8154.

- [37] Patrice Castonguay, Peter E Vincent, and Antony Jameson. “A new class of high-order energy stable flux reconstruction schemes for triangular elements”. In: *Journal of Scientific Computing* 51.1 (2012), pp. 224–256.
- [38] Eitan Tadmor. “The numerical viscosity of entropy stable schemes for systems of conservation laws. I”. In: *Mathematics of Computation* 49.179 (1987), pp. 91–103.
- [39] Doug Shi-Dong and Siva Nadarajah. “Full-Space Approach to Aerodynamic Shape Optimization”. In: *Computers & Fluids* (2021), p. 104843.

Chapter 3

Provably Stable Flux Reconstruction on Curvilinear Elements

With the goal of discrete nonlinear stability on complex curvilinear geometries, we first need to assess the nonlinearity introduced by the curvilinear coordinates. This section considers linear advection in curvilinear coordinates to derive a provably stable FR scheme. Since the metric terms are nonlinear, for linear advection, the reference flux becomes a nonlinear function. Importantly, for curvilinear coordinates, the physical flux is not assumed to be a polynomial, but rather, for the strong form of the equations, the reference flux is approximated by a p -th order polynomial in the reference space. This distinction prevents integration-by-parts from being satisfied in the physical space, which leads to differences between the conservative and non-conservative DG strong forms—even with analytically exact metric terms. Thus, a split form for the curvilinear coordinates is necessary to achieve provable stability in general curvilinear elements. This section also develops metric-dependent FR correction functions, and similarly to Chapter 2, this section incorporates the correction functions on the nonlinear volume metric terms to achieve stability. Lastly, this section summarizes the formulation of the metric Jacobian and cofactor matrix to discretely satisfy the geometric conservation law that allows for free-stream preservation. We numerically verify free-stream preservation,

global conservation, stability, and $p + 1$ orders of convergence on nonsymmetric curvilinear elements. After resolving the nonlinearities associated with the curvilinear mesh, then we can generalize to vector-valued systems of nonlinear PDEs in curvilinear coordinates in Chapter 5.

Provably Stable Flux Reconstruction High-Order Methods on Curvilinear Elements

Alexander Cicchino, David C. Del Rey Fernández, Siva Nadarajah, Jesse Chan, and Mark H.
Carpenter

From: Cicchino, Alexander, et al. “Provably stable flux reconstruction high-order methods on curvilinear elements.” *Journal of Computational Physics* 463 (2022): 111259.

Contribution of authors: Alexander Cicchino: Conceptualization, Formal analysis, Methodology, Software, Validation, Writing – original draft, Writing – review & editing. David C. Del Rey Fernández: Conceptualization, Formal analysis, Methodology, Supervision, Validation, Writing – review & editing. Siva Nadarajah: Conceptualization, Formal analysis, Methodology, Software, Supervision, Validation, Writing – original draft, Writing – review & editing. Jesse Chan: Validation, Writing – review & editing. Mark H. Carpenter: Validation, Writing – review & editing

Abstract

Provably stable flux reconstruction (FR) schemes are derived for partial differential equations cast in curvilinear coordinates. Specifically, energy stable flux reconstruction (ESFR) schemes are considered as they allow for design flexibility as well as stability proofs for the linear advection problem on affine elements. Additionally, the curvilinear metric split-form for a linear physical flux is examined as it enables the development of energy stability proofs. The first critical step proves, that in curvilinear coordinates, the discontinuous Galerkin (DG) conservative and non-conservative forms are inherently different—even under exact integration and analytically exact metric terms. This analysis demonstrates that the split form is essential to developing provably stable DG schemes on curvilinear coordinates and motivates the construction of metric dependent ESFR correction functions in each element. Furthermore, the provably stable FR schemes differ from schemes in the literature that only apply the ESFR correction functions to surface terms or on the conservative form, and instead incorporate the ESFR correction functions on the full split form of the equations. It is demonstrated that the scheme is divergent when the correction functions are only used for surface reconstruction in curvilinear coordinates. We numerically verify the stability claims for our proposed FR split forms and compare them to ESFR schemes in the literature. Lastly, the newly proposed provably stable FR schemes are shown to obtain optimal orders of convergence. The scheme loses the orders of accuracy at the equivalent correction parameter value c as that of the one-dimensional ESFR scheme.

3.1 Introduction

The Flux Reconstruction (FR) framework, originally proposed by Huynh [1] (also referred to as lifting collocation penalty [2] or correction procedure via reconstruction (CPR) [3, 4]), has emerged as a popular FEM approach that is both simple as it can be cast in a differential collocated form and affords design flexibility, where through a choice of the correction functions, the properties of the scheme can be altered. Importantly, subsets of FR schemes have been identified as provably linearly stable (see Refs. [5–9]) also known as Vincent-Castonguay-Jameson-Huynh (VCJH) schemes or Energy Stable Flux Reconstruction (ESFR). Unfortunately, these proofs are limited to affine elements and hence do not apply to general curvilinear meshes.

A discretization agnostic approach for the design and analysis of arbitrarily high-order and provably stable numerical methods for linear variable coefficient problems is provided by the summation-by-parts (SBP) framework [10–12]. SBP operators are matrix difference operators that are mimetic to high-order integration by parts and when combined with appropriate interface coupling procedures, for example simultaneous approximation terms (SATs) [13–20], lead to provably stable and conservative methods. FR has been cast in SBP form [21–23] as well in residual distribution schemes [24–27] paving the way for a common framework to analyze high-order schemes. Moreover, discretizations having the SBP property form the foundations for nonlinearly stable schemes for nonlinear conservation laws [19, 20, 28–39].

The focus of this article is on the construction of provably stable flux reconstruction schemes in curvilinear coordinates. Since the publication by Svärd [40], the extension of stability proofs for dense-norm SBP operators, to variable coefficient problems—particularly curvilinear coordinate transformations, has received little attention in the SBP literature. Svärd [40] proved that when dense-norms, \mathbf{M} , are multiplied against a diagonal matrix containing the metric Jacobian on the mesh nodes, \mathbf{J} , the result is not a norm, i.e., \mathbf{MJ} is not in general a norm, and therefore provable stability is lost. However, by recasting dense-norm

SBP operators in staggered form and constructing metrics on the staggered grid, stability can be recovered for partial differential equations (PDE) in curvilinear coordinates discretized using dense-norm SBP operators [41]. Alternatively, Ranocha *et al.* [22] demonstrated in one-dimension, that for modal based operators the issue with dense-norms can be overcome by using a dense-matrix, $\tilde{\mathbf{J}}$, such that $\mathbf{M}\tilde{\mathbf{J}} = (\mathbf{M}\tilde{\mathbf{J}})^T$. In a somewhat analogous way, the extension of stability proofs of ESFR schemes to curvilinear coordinates has been unclear since the ESFR norm is dense. In this paper, taking inspiration from the developments in the SBP literature and starting from the variational form, we demonstrate how to incorporate metric Jacobian dependence in dense-norms, specifically those arising in ESFR schemes. In variational form, it is immediately seen that including metric Jacobian dependence does not merely correspond to right multiplying the norm matrix, but instead having the determinant of the Jacobian embedded within the integral; since the metric Jacobian is always built on the quadrature nodes and arises in the integral by transforming from the physical to the reference domain. This allows us to formulate the metric Jacobian dependent ESFR filter and the metric dependent ESFR correction functions.

The overarching objective of this paper is to develop provably stable FR discretizations on curvilinear coordinates for systems of partial differential equations. As highlighted by the SBP community [41–43], discrete integration by parts is not satisfied in the physical space for curvilinear coordinates. This is due to the physical flux never explicitly being represented by an interpolating polynomial in the physical space [44]. This distinction, to the authors’ knowledge, has not been investigated within the ESFR and DG communities [45–48]. In the CPR community [49–51] it is common for both the metric Jacobian scaled solution and physical fluxes to be represented by an interpolating polynomial in the computational space. This allowed for efficient computations of the Navier-Stokes and Euler equations, but the drawbacks were that the orders of accuracy in the physical domain suffered. In addition, the scheme was not provably stable in the dense-norm in the sense of Svård [40] unless the physical flux is projected on a sufficiently high polynomial order and the scheme makes use

of both polynomial exactness and exact integration. In this paper, we consider a linear physical flux to focus solely on the effect of the nonlinear metric terms. In the curvilinear split-form literature [41–43, 52], our proposed split-form can be derived through chain rule on the Geometric Conservation law. We take a more rigorous approach to generalize the difference between two different ways of deriving the DG strong form. The DG strong form in reference space can be derived by either an application of integration by parts on the DG weak form in reference space or in physical space. Since the two strong DG discretizations are not equivalent [53], we present the split-form in order to mimic integration by parts in the physical space. A critical result that has not been shown in the SBP literature [41, 42, 52], is that the two DG strong forms are not equivalent even under exact integration and analytically exact metric terms, making the split-form essential for curvilinear high-order schemes.

In this article, we derive provably stable FR schemes on curvilinear coordinates and consider various design decisions: modal or nodal basis, uncollocated integration, different ESFR correction functions, and different volume and surface quadrature nodes. The first main insight is that the ESFR stability condition [6, 54–56] must contain metric dependence in curvilinear coordinates. This result is a consequence of our choice to represent the solution \mathbf{u} as a polynomial rather than the metric Jacobian scaled solution $\mathbf{J}\mathbf{u}$ as a polynomial. When choosing the latter, as shown by Yu *et al.* [51], the FR scheme needs to be overintegrated by the order of the solution and mesh to achieve desired results. Then, we demonstrate that stability cannot be achieved when the ESFR correction functions are solely used to reconstruct the flux on the surface. This issue has been presented on linear grids for Burgers’ equation by Ranocha *et al.* [21] and for Euler’s equations by Abe *et al.* [57], although neither have found a solution to satisfy stability for general ESFR in split form. In [21], the authors investigated the issue of the dense ESFR contribution to the split forms, where they proved stability only for the DG case. In [57], the authors’ numerically demonstrated stability for the “ g_2 lumped-Lobatto” ESFR scheme, which is equivalent to a collocated DG scheme on Gauss-Lobatto-Legendre nodes [58] and previously shown to be stable in split form by

Gassner [59]. Following the general nonlinearly stable FR framework developed in Cicchino *et al.* [60] for Burgers' equation, the ESFR filter/divergence of the correction functions is incorporated on the nonlinear volume terms to ensure nonlinear stability within the broken Sobolev-norm. This differs from the literature where the ESFR correction functions were only used to reconstruct the flux on the surface [1–3, 6, 54, 57, 61–63]. In addition, the proposed scheme is in contrast from schemes where the ESFR norm¹ was applied to the conservative discretization; either filtering the strong form surface integral [21, 48, 56, 64], or filtering the entire weak form [23]; since such stated schemes are only linearly stable.

The remainder of this article is organized as follows: In Section 2, we introduce the mathematical notations, definitions of metrics, and establish the relationships between the physical and reference spaces. In Section 3, the DG scheme is derived in both conservative and non-conservative strong forms. We subsequently prove that the two forms are inherently different under exact integration and metric terms, and introduce the DG split-form. In Section 4, the classical ESFR scheme is established, and the proposed novel nonlinearly stable FR scheme is derived. In subsequent Sections 5 and 6, we provide proofs of the free-stream preservation, local and global conservation, and stability of the proposed stable FR split-form. The theoretical results are numerically verified in Sec. 3.7, where the classical ESFR scheme in split-form (ESFR filter only applied to the facet terms) diverges while, our proposed ESFR split-form (ESFR filter applied to facet and volume terms) remains stable and maintains the correct orders of accuracy.

3.2 Math Notation and Definitions

Consider the scalar 3D conservation law,

$$\begin{aligned} \frac{\partial}{\partial t} u(\mathbf{x}^c, t) + \nabla \cdot \mathbf{f}(u(\mathbf{x}^c, t)) &= 0, \quad t \geq 0, \quad \mathbf{x}^c := [x \ y \ z] \in \Omega, \\ u(\mathbf{x}^c, 0) &= u_0(\mathbf{x}^c), \end{aligned} \tag{3.1}$$

¹By ESFR norm, we refer to the $(\mathbf{M} + \mathbf{K})$ modified Mass matrix form in Allaneau and Jameson [64, Eq.(13)]

where $\mathbf{f}(u(\mathbf{x}^c, t)) \in \mathbb{R}^{1 \times d}$ stores the fluxes in each of the d directions, and the superscript c refers to Cartesian coordinates. In this paper row vector notation will be used. For the purpose of focusing solely on the effect of the curvilinear metric terms, we will consider linear advection. Although the flux is linear in the physical space, it is soon shown that the nonlinear metric terms make the flux nonlinear in the reference space. The computational domain Ω^h is partitioned into M non-overlapping elements, Ω_m , where the domain is represented by the union of the elements, *i.e.*

$$\Omega \simeq \Omega^h := \bigcup_{m=1}^M \Omega_m.$$

Each element m has a surface denoted by Γ_m . The global approximation, $u^h(\mathbf{x}^c, t)$, is constructed from the direct sum of each local approximation, $u_m^h(\mathbf{x}^c, t)$, *i.e.*

$$u(\mathbf{x}^c, t) \simeq u^h(\mathbf{x}^c, t) = \bigoplus_{m=1}^M u_m^h(\mathbf{x}^c, t).$$

Throughout this paper, all quantities with a subscript m are specifically unique to the element m . On each element, we represent the solution with N_p linearly independent modal or nodal basis functions of a maximum order of p ; where, $N_p := (p + 1)^d$. The solution representation is, $u_m^h(\mathbf{x}^c, t) := \sum_{i=1}^{N_p} \chi_{m,i}(\mathbf{x}^c) \hat{u}_{m,i}(t)$, where $\hat{u}_{m,i}(t)$ are the modal coefficients for the solution. The elementwise residual for the governing equation (3.1) is,

$$R_m^h(\mathbf{x}^c, t) = \frac{\partial}{\partial t} u_m^h(\mathbf{x}^c, t) + \nabla \cdot \mathbf{f}(u_m^h(\mathbf{x}^c, t)). \quad (3.2)$$

The basis functions in each element are defined as,

$$\boldsymbol{\chi}(\mathbf{x}^c) := [\chi_1(\mathbf{x}^c), \chi_2(\mathbf{x}^c), \dots, \chi_{N_p}(\mathbf{x}^c)] = \boldsymbol{\chi}(x) \otimes \boldsymbol{\chi}(y) \otimes \boldsymbol{\chi}(z) \in \mathbb{R}^{1 \times N_p}, \quad (3.3)$$

where \otimes is the tensor product.

The physical coordinates are mapped to the reference element

$\boldsymbol{\xi}^r := \{[\xi, \eta, \zeta] : -1 \leq \xi, \eta, \zeta \leq 1\}$ by

$$\mathbf{x}_m^c(\boldsymbol{\xi}^r) := \boldsymbol{\Theta}_m(\boldsymbol{\xi}^r) = \sum_{i=1}^{N_{t,m}} \Theta_{m,i}(\boldsymbol{\xi}^r) \hat{\mathbf{x}}_{m,i}^c, \quad (3.4)$$

where $\Theta_{m,i}$ are the mapping shape functions of the $N_{t,m}$ physical mapping control points $\hat{\mathbf{x}}_{m,i}^c$.

To transform Eq. (3.2) to the reference basis, as in refs [65–69], we introduce the physical

$$\mathbf{a}_j := \frac{\partial \mathbf{x}^c}{\partial \xi^j}, \quad j = 1, 2, 3$$

and reference

$$\mathbf{a}^j := \nabla \xi^j, \quad j = 1, 2, 3$$

vector bases. We then introduce the determinant of the metric Jacobian as

$$J^\Omega := |\mathbf{J}^\Omega| = \mathbf{a}_1 \cdot (\mathbf{a}_2 \times \mathbf{a}_3), \quad (3.5)$$

and the metric Jacobian cofactor matrix as [48, 65, 66, 70],

$$\mathbf{C}^T := J^\Omega (\mathbf{J}^\Omega)^{-1} = \begin{bmatrix} J^\Omega \mathbf{a}^1 \\ J^\Omega \mathbf{a}^2 \\ J^\Omega \mathbf{a}^3 \end{bmatrix} = \begin{bmatrix} J^\Omega \mathbf{a}^\xi \\ J^\Omega \mathbf{a}^\eta \\ J^\Omega \mathbf{a}^\zeta \end{bmatrix}. \quad (3.6)$$

The metric cofactor matrix is formulated by the ‘‘conservative curl’’ form from [67, Eq. 36] so as to discretely satisfy the Geometric Conservation Law (GCL)

$$\sum_{i=1}^3 \frac{\partial (J^\Omega (\mathbf{a}^i)_n)}{\partial \xi^i} = 0, \quad n = 1, 2, 3 \Leftrightarrow \sum_{i=1}^3 \frac{\partial}{\partial \xi^i} (\mathbf{C})_{ni} = 0, \quad n = 1, 2, 3 \Leftrightarrow \nabla^r \cdot (\mathbf{C}) = \mathbf{0}, \quad (3.7)$$

which is detailed in Sec. 3.5 for a fixed mesh, where $()_{ni}$ represents the n^{th} row, i^{th} column component of a matrix.

Having established the transformations mapping the physical to the reference coordinates

on each element, the differential volume and surface elements can be defined as,

$$d\Omega_m = J_m^\Omega d\Omega_r, \text{ similarly } d\Gamma_m = J_m^\Gamma d\Gamma_r. \quad (3.8)$$

The reference flux for each element m is defined as

$$\mathbf{f}_m^r = \mathbf{C}_m^T \cdot \mathbf{f}_m \Leftrightarrow \mathbf{f}_{m,j}^r = \sum_{i=1}^d (\mathbf{C}_m^T)_{ji} \mathbf{f}_{m,i} \Leftrightarrow \mathbf{f}_m^r = \mathbf{f}_m \mathbf{C}_m, \quad (3.9)$$

where the dot product notation for tensor-vector operations is introduced. The relationship between the physical and reference unit normals is given as [48, Appendix B.2],

$$\hat{\mathbf{n}}_m = \frac{1}{J_m^\Gamma} \mathbf{C}_m \cdot \hat{\mathbf{n}}^r = \frac{1}{J_m^\Gamma} \hat{\mathbf{n}}^r \mathbf{C}_m^T, \quad (3.10)$$

for a water-tight mesh. Additionally, the definition of the divergence operator derived from divergence theorem in curvilinear coordinates can be expressed as [65, Eq. (2.22) and (2.26)],

$$\nabla \cdot \mathbf{f}_m = \frac{1}{J_m^\Omega} \nabla^r \cdot (\mathbf{f}_m \mathbf{C}_m) = \frac{1}{J_m^\Omega} \nabla^r \cdot \mathbf{f}_m^r, \quad (3.11)$$

and the gradient of a scalar as [65, Eq. (2.21)],

$$\nabla \chi = \frac{1}{J_m^\Omega} \mathbf{C}_m \cdot \nabla^r \chi = \frac{1}{J_m^\Omega} (\nabla^r \chi) \mathbf{C}_m^T. \quad (3.12)$$

Thus, substituting Eq. (3.11) into Eq. (3.2), the reference elementwise residual is,

$$R_m^{h,r}(\boldsymbol{\xi}^r, t) := R_m^h(\boldsymbol{\Theta}_m(\boldsymbol{\xi}^r), t) = \frac{\partial}{\partial t} u_m^h(\boldsymbol{\Theta}_m(\boldsymbol{\xi}^r), t) + \frac{1}{J_m^\Omega} \nabla^r \cdot \mathbf{f}^r(u_m^h(\boldsymbol{\Theta}_m(\boldsymbol{\xi}^r), t)). \quad (3.13)$$

3.3 Discontinuous Galerkin

In this section we present a provably stable DG discretization for curvilinear coordinates [41, 42, 52] to act as the cornerstone for our provably stable FR schemes. We derive the DG strong form for both “conservative” and “non-conservative” formulations, and prove that they are inherently different for curvilinear coordinates; even with analytically exact metric terms and exact integration. This difference necessitates a split-form to ensure nonlinear stability on curvilinear coordinates. Specifically we cover:

1. Deriving the conservative DG strong form by transforming the physical DG weak form to reference space. Then, projecting the reference flux onto the reference polynomial basis, and finally, integrating the volume terms by parts in the reference space.
2. Deriving the non-conservative DG strong form by projecting the physical flux onto a physical basis in the physical DG weak form. Then integrating the volume terms by parts in the physical space, and finally, transforming the physical DG non-conservative strong form to the reference space.
3. Comparing the two forms, prove that they are inherently different, even under exact integration with analytically exact metric terms, and that discrete integration by parts in the physical space is not satisfied for either form. Then, combining the two forms to discretely “mimic” integration by parts in the physical space.

3.3.1 DG - Conservative Strong Form

In a Galerkin framework, we left multiply the physical residual Eq. (3.2) by an orthogonal test function. Choosing the test function to be the same as the basis function, integrating in physical space, and applying integration by parts in physical space, we arrive at the weak

form,

$$\begin{aligned} & \int_{\Omega_m} \chi_{m,i}(\mathbf{x}^c) \frac{\partial}{\partial t} u_m^h(\mathbf{x}^c, t) d\Omega_m - \int_{\Omega_m} \nabla \chi_{m,i}(\mathbf{x}^c) \cdot \mathbf{f}(u_m^h(\mathbf{x}^c, t)) d\Omega_m \\ & + \int_{\Gamma_m} \chi_{m,i}(\mathbf{x}^c) \hat{\mathbf{n}}_m \cdot \mathbf{f}^*(u_m^h(\mathbf{x}^c, t)) d\Gamma_m = 0, \forall i = 1, \dots, N_p \end{aligned} \quad (3.14)$$

where $\mathbf{f}^*(u_m^h(\mathbf{x}^c, t))$ represents the physical numerical flux.

Now, we transform the physical DG weak form, Eq. (3.14), to the reference space, by using the definitions of the differential volume and surface elements, physical gradient operator and physical unit normals (Equations (3.8), (3.10), (3.12)),

$$\begin{aligned} & \int_{\Omega_r} \chi_i(\boldsymbol{\xi}^r) J_m^\Omega \frac{\partial}{\partial t} u_m^h(\Theta_m(\boldsymbol{\xi}^r), t) d\Omega_r - \int_{\Omega_r} \left(\frac{1}{J_m^\Omega} \nabla^r \chi_i(\boldsymbol{\xi}^r) \mathbf{C}_m^T \right) J_m^\Omega \cdot \mathbf{f}(u_m^h(\Theta_m(\boldsymbol{\xi}^r), t)) d\Omega_r \\ & + \int_{\Gamma_r} \chi_i(\boldsymbol{\xi}^r) J_m^\Gamma \frac{1}{J_m^\Gamma} \hat{\mathbf{n}}^r \mathbf{C}_m^T \cdot \mathbf{f}^*(u_m^h(\Theta_m(\boldsymbol{\xi}^r), t)) d\Gamma_r = 0, \forall i = 1, \dots, N_p. \end{aligned} \quad (3.15)$$

Notice the change of variables since $\chi_m(\mathbf{x}^c) := \boldsymbol{\chi}(\Theta_m^{-1}(\mathbf{x}^c))$ are implicitly defined through polynomial basis functions in the reference space. That is, $\boldsymbol{\chi}(\boldsymbol{\xi}^r)$ are a polynomial basis in the reference space and the physical basis functions are not polynomial as the physical coordinates \mathbf{x}^c are nonlinear functions of $\boldsymbol{\xi}^r$, and vice versa for $\boldsymbol{\xi}^r$. From the definition Eq. (3.9), the reference flux is substituted for $\mathbf{C}_m^T \cdot \mathbf{f}(u_m^h(\Theta_m(\boldsymbol{\xi}^r), t))$ in the volume integral. We then project the reference flux in Eq. (3.15) onto the reference polynomial basis functions, and substitute the basis expansion for the solution. The variational DG weak form in reference space is thus,

$$\begin{aligned} & \int_{\Omega_r} \chi_i(\boldsymbol{\xi}^r) J_m^\Omega \boldsymbol{\chi}(\boldsymbol{\xi}^r) \frac{d}{dt} \hat{\mathbf{u}}_m(t)^T d\Omega_r - \int_{\Omega_r} \nabla^r \chi_i(\boldsymbol{\xi}^r) \cdot \boldsymbol{\chi}(\boldsymbol{\xi}^r) \hat{\mathbf{f}}_m^r(t)^T d\Omega_r \\ & + \int_{\Gamma_r} \chi_i(\boldsymbol{\xi}^r) \hat{\mathbf{n}}^r \mathbf{C}_m^T \cdot \mathbf{f}^*(u_m^h(\Theta_m(\boldsymbol{\xi}^r), t)) d\Gamma_r = 0, \forall i = 1, \dots, N_p. \end{aligned} \quad (3.16)$$

Next Eq. (3.16), the reference DG weak form, is integrated by parts in the reference space

resulting in,

$$\begin{aligned} & \int_{\Omega_r} \chi_i(\boldsymbol{\xi}^r) J_m^\Omega \boldsymbol{\chi}(\boldsymbol{\xi}^r) \frac{d}{dt} \hat{\mathbf{u}}_m(t)^T d\Omega_r + \int_{\Omega_r} \chi_i(\boldsymbol{\xi}^r) \left(\sum_{j=1}^{N_p} \nabla^r \chi_j(\boldsymbol{\xi}^r) \cdot \hat{\mathbf{f}}_{m,j}^r(t) \right) d\Omega_r \\ & + \int_{\Gamma_r} \chi_i(\boldsymbol{\xi}^r) \left[\hat{\mathbf{n}}^r \mathbf{C}_m^T \cdot \mathbf{f}_m^* - \hat{\mathbf{n}}^r \cdot \boldsymbol{\chi}(\boldsymbol{\xi}^r) \hat{\mathbf{f}}_m^r(t)^T \right] d\Gamma_r = 0, \forall i = 1, \dots, N_p. \end{aligned} \quad (3.17)$$

In the general case, the interpolation of the nonlinear reference flux to the face does not equal the metric terms evaluated at the face multiplied with the flux on the face.

Next, we introduce N_{vp} volume and N_{fp} facet cubature nodes, $\boldsymbol{\xi}_v^r$ and $\boldsymbol{\xi}_{f,k}^r$ respectively. We also introduce \mathbf{W} and \mathbf{J}_m as diagonal operators storing the quadrature weights and the determinant of the metric Jacobian at the volume cubature nodes. We present the discretization of Eq. (3.17), the discrete conservative DG strong form, as

$$\begin{aligned} & \mathbf{M}_m \frac{d}{dt} \hat{\mathbf{u}}_m(t)^T + \mathbf{S}_\xi \hat{\mathbf{f}}_{1m}^r(t)^T + \mathbf{S}_\eta \hat{\mathbf{f}}_{2m}^r(t)^T + \mathbf{S}_\zeta \hat{\mathbf{f}}_{3m}^r(t)^T \\ & + \sum_{f=1}^{N_f} \sum_{k=1}^{N_{fp}} \boldsymbol{\chi}(\boldsymbol{\xi}_{f,k}^r)^T W_{f,k} [\hat{\mathbf{n}}^r \mathbf{C}_m(\boldsymbol{\xi}_{f,k}^r)^T \cdot \mathbf{f}_m^* - \hat{\mathbf{n}}^r \cdot \boldsymbol{\chi}(\boldsymbol{\xi}_{f,k}^r) \hat{\mathbf{f}}_m^r(t)^T] = \mathbf{0}^T, \end{aligned} \quad (3.18)$$

where N_f represents the number of faces on the element. The discrete mass and stiffness matrices are defined as,

$$\begin{aligned} (\mathbf{M}_m)_{ij} & \approx \int_{\Omega_r} J_m^\Omega \chi_i(\boldsymbol{\xi}^r) \chi_j(\boldsymbol{\xi}^r) d\Omega_r \rightarrow \mathbf{M}_m = \boldsymbol{\chi}(\boldsymbol{\xi}_v^r)^T \mathbf{W} \mathbf{J}_m \boldsymbol{\chi}(\boldsymbol{\xi}_v^r), \\ (\mathbf{S}_\xi)_{ij} & = \int_{\Omega_r} \chi_i(\boldsymbol{\xi}^r) \frac{\partial}{\partial \xi} \chi_j(\boldsymbol{\xi}^r) d\Omega_r \rightarrow \mathbf{S}_\xi = \boldsymbol{\chi}(\boldsymbol{\xi}_v^r)^T \mathbf{W} \boldsymbol{\chi}_\xi(\boldsymbol{\xi}_v^r), \end{aligned}$$

and similarly for the other reference directions. The equality for the stiffness matrices holds for quadrature rules of at least $2p - 1$ in strength. Note, that since we start at $p = 0$, Gauss-Lobatto-Legendre quadrature is exact for polynomials of up to $2p - 1$ and Gauss-Legendre quadrature is exact for polynomials of up to $2p + 1$. Furthermore, we introduce the L_2 projection operator as $\boldsymbol{\Pi} := \mathbf{M}^{-1} \boldsymbol{\chi}(\boldsymbol{\xi}_v^r)^T \mathbf{W}$, where the metric independent mass matrix is $\mathbf{M} = \boldsymbol{\chi}(\boldsymbol{\xi}_v^r)^T \mathbf{W} \boldsymbol{\chi}(\boldsymbol{\xi}_v^r)$. Thus, the modal coefficients of the reference flux are the L_2 projection

of the reference flux, $\hat{\mathbf{f}}_m^r(t)^T = \mathbf{\Pi}(\mathbf{f}_m^{rT})$.

3.3.2 DG - Non-Conservative Strong Form

Returning to the physical DG weak form, Eq. (3.14), as discussed in [44, 71], there is no claim that the physical flux has a polynomial basis function expansion for curvilinear elements. We term the scheme “non-conservative” because it does not recover the definition of the reference divergence operator in Eq. (3.11) [41, 52]. Following the approach in [46, 47], we substitute the solution expansion and project the physical flux onto the basis functions. Eq. (3.14) is integrated by parts in physical space and yields the “non-conservative” DG strong form in physical space,

$$\begin{aligned} & \int_{\Omega_m} \chi_{m,i}(\mathbf{x}^c) \boldsymbol{\chi}_m(\mathbf{x}^c) \frac{d}{dt} \hat{\mathbf{u}}_m(t)^T d\Omega_m + \int_{\Omega_m} \chi_{m,i}(\mathbf{x}^c) \left(\sum_{j=1}^{N_p} \nabla \chi_{m,j}(\mathbf{x}^c) \cdot \hat{\mathbf{f}}_{m,j}(t) \right) d\Omega_m \\ & + \int_{\Gamma_m} \chi_{m,i}(\mathbf{x}^c) \hat{\mathbf{n}}_m \cdot (\mathbf{f}_m^* - \mathbf{f}_m) d\Gamma_m = 0, \quad \forall i = 1, \dots, N_p. \end{aligned} \quad (3.19)$$

To discretely represent the derivative of the physical flux in the physical space, it must be represented by the derivative of a basis expansion in the physical space multiplied by its modal coefficients. Although in the continuous sense the physical divergence operator could be recovered by commuting the basis functions across the dot product in Eq. (3.19); doing so would remove the claim that the physical flux has a basis function expansion. Only in the reference space can the basis function be brought across the dot product since the derivative of a polynomial basis function on the reference element exists. Thus, discretely applying integration by parts in the physical space to arrive at Eq. (3.19) would necessitate that $\boldsymbol{\chi}_m(\mathbf{x}^c) = \boldsymbol{\chi}(\boldsymbol{\Theta}_m^{-1}(\mathbf{x}^c))$ is a polynomial basis, which cannot be the case since $\boldsymbol{\xi}^r$ is a nonlinear function of \mathbf{x}^c . It is clear when transforming Eq. (3.19) to the reference space, and substituting the definition of the gradient for curvilinear elements, Eq. (3.12), that it is

inconsistent with the previous formulation in Eq. (3.17),

$$\begin{aligned} & \int_{\Omega_r} \chi_i(\boldsymbol{\xi}^r) J_m^\Omega \boldsymbol{\chi}(\boldsymbol{\xi}^r) \frac{d}{dt} \hat{\mathbf{u}}_m(t)^T d\Omega_r + \int_{\Omega_r} \chi_i(\boldsymbol{\xi}^r) \left(\sum_{j=1}^{N_p} \left(\nabla^r \chi_j(\boldsymbol{\xi}^r) \mathbf{C}_m^T \right) \cdot \hat{\mathbf{f}}_{m,j}(t) \right) d\Omega_r \\ & + \int_{\Gamma_r} \chi_i(\boldsymbol{\xi}^r) \hat{\mathbf{n}}^r \mathbf{C}_m^T \cdot (\mathbf{f}_m^* - \mathbf{f}_m) d\Gamma_r = 0, \quad \forall i = 1, \dots, N_p. \end{aligned} \quad (3.20)$$

Explicitly, the metric cofactor matrix appears on the outside of the reference divergence/gradient operator. Only if the mesh is linear, skew-symmetric, or symmetric with uniform constant wave speeds for linear advection, will the volume integrals in Equations (3.17) and (3.20) be equivalent in discrete form.

Lemma 3.3.1. *The volume terms in Eq. (3.17) and Eq. (3.20) are inherently different for a curvilinear mesh; even with exact integration and exact metric terms.*

Proof.

Consider just one of the divergence terms in the volume integral,

$$\begin{aligned} \text{Conservative DG: } & \sum_{k=1}^d \int_{\Omega_r} \chi_i(\boldsymbol{\xi}^r) \sum_{j=1}^{N_p} \frac{\partial \chi_j(\boldsymbol{\xi}^r)}{\partial \xi_k} \left[\mathbf{\Pi} \left(J_m^\Omega \frac{\partial \xi_k}{\partial x} \mathbf{f}_x(u_m^h) \right) \right]_j d\Omega_r, \\ \text{Non-Conservative DG: } & \sum_{k=1}^d \int_{\Omega_r} \chi_i(\boldsymbol{\xi}^r) J_m^\Omega \frac{\partial \xi_k}{\partial x} \sum_{j=1}^{N_p} \frac{\partial \chi_j(\boldsymbol{\xi}^r)}{\partial \xi_k} \left[\mathbf{\Pi} \left(\mathbf{f}_x(u_m^h) \right) \right]_j d\Omega_r. \end{aligned} \quad (3.21)$$

If we are to consider both exact integration and exact metric terms ($J_m^\Omega \frac{\partial \xi_k}{\partial x}$), then the two forms cannot be equivalent for a general $\mathbf{f}_x(u_m^h)$.

□

Remark 3.3.1. *Only for the specific case of linear advection with a polynomial representation of the mesh can the two forms be equivalent through polynomial exactness; provided they are both exactly integrated and the nonlinear term in the conservative form is projected onto a sufficiently high polynomial space.*

3.3.3 DG - Split-Form

For the objective of developing provably stable schemes, alike [42, 52, 72], we introduce the split-form by adding a half of the conservative DG Strong form Eq. (3.17) with the non-conservative DG Strong form Eq. (3.20) to discretely satisfy integration by parts,

$$\begin{aligned}
& \int_{\Omega_r} \chi_i(\boldsymbol{\xi}^r) J_m^\Omega \boldsymbol{\chi}(\boldsymbol{\xi}^r) \frac{d}{dt} \hat{\mathbf{u}}_m(t)^T d\Omega_r + \frac{1}{2} \int_{\Omega_r} \chi_i(\boldsymbol{\xi}^r) \left(\sum_{j=1}^{N_p} \nabla^r \chi_j(\boldsymbol{\xi}^r) \cdot \hat{\mathbf{f}}_{m,j}^r(t) \right) d\Omega_r \\
& + \frac{1}{2} \int_{\Omega_r} \chi_i(\boldsymbol{\xi}^r) \left(\sum_{j=1}^{N_p} \left(\nabla^r \chi_j(\boldsymbol{\xi}^r) \mathbf{C}_m^T \right) \cdot \hat{\mathbf{f}}_{m,j}^r(t) \right) d\Omega_r \\
& + \int_{\Gamma_r} \chi_i(\boldsymbol{\xi}^r)^T \left[\hat{\mathbf{n}}^r \mathbf{C}_m^T \cdot (\mathbf{f}_m^* - \frac{1}{2} \mathbf{f}_m) - \hat{\mathbf{n}}^r \cdot \frac{1}{2} \boldsymbol{\chi}(\boldsymbol{\xi}^r) \hat{\mathbf{f}}_m^r(t)^T \right] d\Gamma_r = 0, \quad \forall i = 1, \dots, N_p.
\end{aligned} \tag{3.22}$$

Note that the surface splitting naturally accommodates arbitrary sets of volume and facet cubature nodes. Recasting Eq. (3.22) into discrete form by evaluating at volume and facet cubature nodes, we have the DG split-form,

$$\begin{aligned}
& \mathbf{M}_m \frac{d}{dt} \hat{\mathbf{u}}_m(t)^T + \frac{1}{2} \boldsymbol{\chi}(\boldsymbol{\xi}_v^r)^T \mathbf{W} \nabla^r \boldsymbol{\chi}(\boldsymbol{\xi}_v^r) \cdot \hat{\mathbf{f}}_m^r(t)^T + \frac{1}{2} \boldsymbol{\chi}(\boldsymbol{\xi}_v^r)^T \mathbf{W} \tilde{\nabla}^r \boldsymbol{\chi}(\boldsymbol{\xi}_v^r) \cdot \hat{\mathbf{f}}_m^r(t)^T \\
& + \sum_{f=1}^{N_f} \sum_{k=1}^{N_{fp}} \boldsymbol{\chi}(\boldsymbol{\xi}_{f,k}^r)^T W_{f,k} [\hat{\mathbf{n}}^r \cdot \mathbf{f}_m^{C,r}] = \mathbf{0}^T,
\end{aligned} \tag{3.23}$$

where we introduced $\tilde{\nabla}^r \boldsymbol{\chi}(\boldsymbol{\xi}_v^r) = \begin{pmatrix} \nabla^r \chi_1(\boldsymbol{\xi}_{v,1}^r) \mathbf{C}_m(\boldsymbol{\xi}_{v,1}^r)^T & \dots & \nabla^r \chi_{N_p}(\boldsymbol{\xi}_{v,1}^r) \mathbf{C}_m(\boldsymbol{\xi}_{v,1}^r)^T \\ \vdots & \ddots & \vdots \\ \nabla^r \chi_1(\boldsymbol{\xi}_{v,N_{vp}}^r) \mathbf{C}_m(\boldsymbol{\xi}_{v,N_{vp}}^r)^T & \dots & \nabla^r \chi_{N_p}(\boldsymbol{\xi}_{v,N_{vp}}^r) \mathbf{C}_m(\boldsymbol{\xi}_{v,N_{vp}}^r)^T \end{pmatrix}$

to store the transformed reference gradient of the basis functions evaluated at volume cubature nodes. Also, we introduced $\mathbf{f}_m^{C,r} = \mathbf{f}_m^* \mathbf{C}_m(\boldsymbol{\xi}_{f,k}^r) - \frac{1}{2} \mathbf{f}_m \mathbf{C}_m(\boldsymbol{\xi}_{f,k}^r) - \frac{1}{2} \boldsymbol{\chi}(\boldsymbol{\xi}_{f,k}^r) \hat{\mathbf{f}}_m^r(t)^T$ as the difference between the reference transformation of the physical numerical flux, the physical flux and the interpolated reference flux on the face. We note that the rigorously derived split-form in Eq. (3.23) recovers the metric split-form in [35, 41] by considering chain rule on the GCL.

3.4 Energy Stable Flux Reconstruction

3.4.1 ESFR - Classical Formulation

Following an ESFR framework, the reference flux is composed of a discontinuous and a corrected component,

$$\mathbf{f}^r(u_m^h(\Theta_m(\boldsymbol{\xi}^r), t)) := \mathbf{f}^{D,r}(u_m^h(\Theta_m(\boldsymbol{\xi}^r), t)) + \sum_{f=1}^{N_f} \sum_{k=1}^{N_{fp}} \mathbf{g}^{f,k}(\boldsymbol{\xi}^r) [\hat{\mathbf{n}}^r \cdot (\mathbf{f}_m^{*,r} - \mathbf{f}_m^r)]. \quad (3.24)$$

The vector correction functions $\mathbf{g}^{f,k}(\boldsymbol{\xi}^r) \in \mathbb{R}^{1 \times d}$ associated with face f , facet cubature node k in the reference element, are defined as the tensor product of the $p+1$ order one-dimensional correction functions (ϕ stores a basis of order $p+1$), with the corresponding p -th order basis functions in the other reference directions.

$$\begin{aligned} & \mathbf{g}^{f,k}(\boldsymbol{\xi}^r) \\ &= \left[\left(\phi(\xi) \otimes \chi(\eta) \otimes \chi(\zeta) \right) \left(\hat{\mathbf{g}}_1^{f,k} \right)^T, \left(\chi(\xi) \otimes \phi(\eta) \otimes \chi(\zeta) \right) \left(\hat{\mathbf{g}}_2^{f,k} \right)^T, \left(\chi(\xi) \otimes \chi(\eta) \otimes \phi(\zeta) \right) \left(\hat{\mathbf{g}}_3^{f,k} \right)^T \right] \\ &= \left[g_1^{f,k}(\boldsymbol{\xi}^r), g_2^{f,k}(\boldsymbol{\xi}^r), g_3^{f,k}(\boldsymbol{\xi}^r) \right], \end{aligned} \quad (3.25)$$

such that

$$\mathbf{g}^{f,k}(\boldsymbol{\xi}_{f_i, k_j}^r) \cdot \hat{\mathbf{n}}_{f_i, k_j}^r = \begin{cases} 1, & \text{if } f_i = f, \text{ and } k_j = k \\ 0, & \text{otherwise.} \end{cases} \quad (3.26)$$

Coupled with the symmetry condition $g^L(\boldsymbol{\xi}^r) = -g^R(-\boldsymbol{\xi}^r)$ to satisfy Eq. (3.26), the one-dimensional ESFR fundamental assumption from [54] is,

$$\int_{-1}^1 \nabla^r \chi_i(\boldsymbol{\xi}^r) g^{f,k}(\boldsymbol{\xi}^r) d\xi - c \frac{\partial^p \chi_i(\boldsymbol{\xi}^r)^T}{\partial \xi^p} \frac{\partial^{p+1} g^{f,k}(\boldsymbol{\xi}^r)}{\partial \xi^{p+1}} = 0, \quad \forall i = 1, \dots, N_p, \quad (3.27)$$

and similarly for the other reference directions.

Akin to [6, 55], consider introducing the differential operator,

$$\begin{aligned}
2\text{D:} \quad \partial^{(s,v)} &= \frac{\partial^{s+v}}{\partial \xi^s \partial \eta^v}, \text{ such that } s = \{0, p\}, v = \{0, p\}, s + v \geq p, \\
3\text{D:} \quad \partial^{(s,v,w)} &= \frac{\partial^{s+v+w}}{\partial \xi^s \partial \eta^v \partial \zeta^w}, \text{ such that } s = \{0, p\}, v = \{0, p\}, w = \{0, p\}, s + v + w \geq p,
\end{aligned} \tag{3.28}$$

with its corresponding correction parameter

$$\begin{aligned}
2\text{D:} \quad c_{(s,v)} &= c_{1D}^{\binom{s+v}{p}}, \\
3\text{D:} \quad c_{(s,v,w)} &= c_{1D}^{\binom{s+v+w}{p}}.
\end{aligned} \tag{3.29}$$

Note that the total degree is $\dim \times p$ for a tensor-product basis that is of order p in each direction.

For example,

$$\partial^{(0,p,0)} = \frac{\partial^p}{\partial \eta^p}, c_{(0,p,0)} = c_{1D}, \partial^{(p,0,p)} = \frac{\partial^{2p}}{\partial \xi^p \partial \zeta^p}, c_{(p,0,p)} = c_{1D}^2, \partial^{(p,p,p)} = \frac{\partial^{3p}}{\partial \xi^p \partial \eta^p \partial \zeta^p}, c_{(p,p,p)} = c_{1D}^3.$$

Since $\int_{\Omega_r} \partial^{(s,v,w)} \chi(\boldsymbol{\xi}^r)^T \partial^{(s,v,w)} \left(\nabla^r \chi(\boldsymbol{\xi}^r) \right) d\Omega_r$ composes of the complete broken Sobolev-norm for each s, v, w [56, 63], the tensor product ESFR fundamental assumption, that recovers the VCJH schemes exactly for linear elements is defined as,

$$\int_{\Omega_r} \nabla^r \chi_i(\boldsymbol{\xi}^r) \cdot \mathbf{g}^{f,k}(\boldsymbol{\xi}^r) d\Omega_r - \sum_{s,v,w} c_{(s,v,w)} \partial^{(s,v,w)} \chi_i(\boldsymbol{\xi}^r) \partial^{(s,v,w)} \left(\nabla^r \cdot \mathbf{g}^{f,k}(\boldsymbol{\xi}^r) \right) = 0, \forall i = 1, \dots, N_p, \tag{3.30}$$

where $\sum_{s,v,w}$ sums over all possible s, v, w combinations in Eq. (3.28).

To discretely represent the divergence of the correction functions, we introduce the correction field

$h^{f,k}(\boldsymbol{\xi}^r) \in P_{3p}(\boldsymbol{\Omega}_r)$ associated with the face f cubature node k as,

$$h^{f,k}(\boldsymbol{\xi}^r) = \boldsymbol{\chi}(\boldsymbol{\xi}^r) \left(\hat{\mathbf{h}}^{f,k} \right)^T = \nabla^r \cdot \mathbf{g}^{f,k}(\boldsymbol{\xi}^r). \quad (3.31)$$

To arrive at the ESFR strong form, we substitute the ESFR reference flux, Eq. (3.24), into the elementwise reference residual, Eq. (3.13), project it onto the polynomial basis, and evaluate at cubature nodes,

$$\boldsymbol{\chi}(\boldsymbol{\xi}_v^r) \frac{d}{dt} \hat{\mathbf{u}}_m(t)^T + \mathbf{J}_m^{-1} \nabla^r \boldsymbol{\chi}(\boldsymbol{\xi}_v^r) \cdot \hat{\mathbf{f}}_m^{D,r}(t)^T + \mathbf{J}_m^{-1} \sum_{f=1}^{N_f} \sum_{k=1}^{N_{fp}} \boldsymbol{\chi}(\boldsymbol{\xi}_v^r) \left(\hat{\mathbf{h}}^{f,k} \right)^T [\hat{\mathbf{n}}^r \cdot (\mathbf{f}_m^{*,r} - \mathbf{f}_m^r)] = \mathbf{0}^T. \quad (3.32)$$

Since Eq. (3.32) does not mimic integration by parts in the physical domain, as previously demonstrated in Sections 3.3.2 and 3.3.3, we introduce the split-form in compact form,

$$\begin{aligned} & \boldsymbol{\chi}(\boldsymbol{\xi}_v^r) \frac{d}{dt} \hat{\mathbf{u}}_m(t)^T + \frac{1}{2} \mathbf{J}_m^{-1} \nabla^r \boldsymbol{\chi}(\boldsymbol{\xi}_v^r) \cdot \hat{\mathbf{f}}_m^{D,r}(t)^T + \frac{1}{2} \mathbf{J}_m^{-1} \tilde{\nabla}^r \boldsymbol{\chi}(\boldsymbol{\xi}_v^r) \cdot \hat{\mathbf{f}}_m^D(t)^T \\ & + \mathbf{J}_m^{-1} \sum_{f=1}^{N_f} \sum_{k=1}^{N_{fp}} \boldsymbol{\chi}(\boldsymbol{\xi}_v^r) \left(\hat{\mathbf{h}}^{f,k} \right)^T [\mathbf{n}^r \cdot \mathbf{f}_m^{C,r}] = \mathbf{0}^T. \end{aligned} \quad (3.33)$$

Unfortunately, Eq. (3.33), which we will coin as the ‘‘Classical ESFR split-form’’ is not energy stable since the nonlinearity introduced by both the metric cofactor matrix and determinant of the Jacobian prevents the volume terms from vanishing within the broken Sobolev-norm introduced in [73]. Fortunately, there is a modified form of Eq. (3.33) which is provably stable and recovers the Classical ESFR scheme for linear problems. We will term the proposed split-form, which we now derive, as the ‘‘ESFR split-form’’.

To derive the proposed ESFR split-form, we recast ESFR as a filtered DG scheme. To do so, as shown in [48, 56, 64], we integrate Eq. (3.33) with respect to the basis function as the test function in the physical domain. Using the definitions of the differential volume and

surface elements, Eq. (3.8), we integrate the divergence of the correction functions by parts,

$$\begin{aligned}
& \int_{\Omega_r} \chi_i(\boldsymbol{\xi}^r) J_m^\Omega \boldsymbol{\chi}(\boldsymbol{\xi}^r) \frac{d}{dt} \hat{\mathbf{u}}_m(t)^T d\Omega_r + \frac{1}{2} \int_{\Omega_r} \chi_i(\boldsymbol{\xi}^r) \nabla^r \boldsymbol{\chi}(\boldsymbol{\xi}^r) \cdot \hat{\mathbf{f}}_m^{D,r}(t)^T d\Omega_r \\
& + \frac{1}{2} \int_{\Omega_r} \chi_i(\boldsymbol{\xi}^r) \tilde{\nabla}^r \boldsymbol{\chi}(\boldsymbol{\xi}^r) \cdot \hat{\mathbf{f}}_m^D(t)^T d\Omega_r + \int_{\Gamma_r} \chi_i(\boldsymbol{\xi}^r) \left(\hat{\mathbf{n}}^r \cdot \mathbf{g}^{f,k}(\boldsymbol{\xi}^r) \right) [\hat{\mathbf{n}}^r \cdot \mathbf{f}_m^{C,r}] d\Gamma_r \\
& - \int_{\Omega_r} \nabla^r \chi_i(\boldsymbol{\xi}^r) \cdot \mathbf{g}^{f,k}(\boldsymbol{\xi}^r) [\hat{\mathbf{n}}^r \cdot \mathbf{f}_m^{C,r}] d\Omega_r = 0, \quad \forall i = 1, \dots, N_p.
\end{aligned} \tag{3.34}$$

From the ESFR correction functions' surface condition, Eq. (3.26), the facet integral in Eq. (3.34) is the exact same as the facet integral in the DG strong split-form Eq. (3.22). Also, the reference discontinuous flux for the ESFR scheme is the same as the reference flux for a DG scheme (from definition). Thus, we will drop the D superscript for the flux.

Next, as in the ESFR literature, we apply the differential operator $\partial^{(s,v,w)}$ on Eq. (3.33), then left multiply and integrate with respect to the $\partial^{(s,v,w)}$ derivative of the basis function as the test function in the physical domain [1, 5, 8, 48, 56, 73]. Then a scalar $c_{(s,v,w)}$ is incorporated and the expression is summed over all (s, v, w) combinations. The order of those steps is extremely important as it ensures a positive-definite broken Sobolev-norm, which solves the issue presented in [22, 40]. This results in,

$$\begin{aligned}
& \sum_{s,v,w} c_{(s,v,w)} \int_{\Omega_r} J_m^\Omega \partial^{(s,v,w)} \chi_i(\boldsymbol{\xi}^r) \partial^{(s,v,w)} \boldsymbol{\chi}(\boldsymbol{\xi}^r) \frac{d}{dt} \hat{\mathbf{u}}_m(t)^T d\Omega_r \\
& + \sum_{s,v,w} c_{(s,v,w)} \int_{\Omega_r} J_m^\Omega \partial^{(s,v,w)} \chi_i(\boldsymbol{\xi}^r) \partial^{(s,v,w)} \left(\frac{1}{J_m^\Omega} \nabla^r \cdot \mathbf{g}^{f,k}(\boldsymbol{\xi}^r) \right) [\hat{\mathbf{n}}^r \cdot \mathbf{f}_m^{C,r}] d\Omega_r \\
& + \sum_{s,v,w} \frac{c_{(s,v,w)}}{2} \int_{\Omega_r} J_m^\Omega \partial^{(s,v,w)} \chi_i(\boldsymbol{\xi}^r) \partial^{(s,v,w)} \left[\frac{1}{J_m^\Omega} \nabla^r \boldsymbol{\chi}(\boldsymbol{\xi}^r) \cdot \hat{\mathbf{f}}_m^r(t)^T + \frac{1}{J_m^\Omega} \tilde{\nabla}^r \boldsymbol{\chi}(\boldsymbol{\xi}^r) \cdot \hat{\mathbf{f}}_m(t)^T \right] d\Omega_r = 0, \\
& \forall i = 1, \dots, N_p.
\end{aligned} \tag{3.35}$$

Adding Eqs. (3.34) and (3.35) together results in,

$$\begin{aligned}
& \int_{\Omega_r} \left(\chi_i(\boldsymbol{\xi}^r) J_m^\Omega \boldsymbol{\chi}(\boldsymbol{\xi}^r) + \sum_{s,v,w} c_{(s,v,w)} J_m^\Omega \partial^{(s,v,w)} \chi_i(\boldsymbol{\xi}^r) \partial^{(s,v,w)} \boldsymbol{\chi}(\boldsymbol{\xi}^r) \right) \frac{d}{dt} \hat{\mathbf{u}}_m(t)^T d\Omega_r \\
& + \frac{1}{2} \int_{\Omega_r} \chi_i(\boldsymbol{\xi}^r) \nabla^r \boldsymbol{\chi}(\boldsymbol{\xi}^r) \cdot \hat{\mathbf{f}}_m^r(t)^T d\Omega_r + \frac{1}{2} \int_{\Omega_r} \chi_i(\boldsymbol{\xi}^r) \tilde{\nabla}^r \boldsymbol{\chi}(\boldsymbol{\xi}^r) \cdot \hat{\mathbf{f}}_m(t)^T d\Omega_r \\
& + \int_{\Gamma_r} \chi_i(\boldsymbol{\xi}^r) [\hat{\mathbf{n}}^r \cdot \mathbf{f}_m^{C,r}] d\Gamma_r \\
& + \sum_{s,v,w} \frac{c_{(s,v,w)}}{2} \int_{\Omega_r} J_m^\Omega \partial^{(s,v,w)} \chi_i(\boldsymbol{\xi}^r) \partial^{(s,v,w)} \left[\frac{1}{J_m^\Omega} \nabla^r \boldsymbol{\chi}(\boldsymbol{\xi}^r) \cdot \hat{\mathbf{f}}_m^r(t)^T + \frac{1}{J_m^\Omega} \tilde{\nabla}^r \boldsymbol{\chi}(\boldsymbol{\xi}^r) \cdot \hat{\mathbf{f}}_m(t)^T \right] d\Omega_r \\
& - \left(\int_{\Omega_r} \nabla^r \chi_i(\boldsymbol{\xi}^r) \cdot \mathbf{g}^{f,k}(\boldsymbol{\xi}^r) d\Omega_r \right. \\
& \quad \left. - \sum_{s,v,w} c_{(s,v,w)} \int_{\Omega_r} J_m^\Omega \partial^{(s,v,w)} \chi_i(\boldsymbol{\xi}^r) \partial^{(s,v,w)} \left(\frac{1}{J_m^\Omega} \nabla^r \cdot \mathbf{g}^{f,k}(\boldsymbol{\xi}^r) \right) d\Omega_r \right) [\hat{\mathbf{n}}^r \cdot \mathbf{f}_m^{C,r}] \\
& = 0, \quad \forall i = 1, \dots, N_p.
\end{aligned} \tag{3.36}$$

Note that $[\hat{\mathbf{n}}^r \cdot \mathbf{f}_m^{C,r}]$ is a constant evaluated on the surface, so it can be factored out of the last volume integrals [54, 55].

The root of the instability of the classical ESFR in split-form is demonstrated in the third line of Eq. (3.36). On linear grids, the determinant of the Jacobian and the metric cofactor matrix are both constants, and render the $\partial^{(s,v,w)}$ derivative of the divergence of the discontinuous flux to be skew-symmetric [63]. However, for curvilinear elements, the determinant of the Jacobian and the metric cofactor matrix are both nonlinear polynomials. Thus, the $\partial^{(s,v,w)}$ derivative of the volume terms does not vanish in Eq. (3.36). Ranocha *et al.* in [21] circumvented the issue by setting the ESFR contribution to zero and solving for the DG case ($c_{(s,v,w)} = 0$). In the case of Abe *et al.* [57], the authors showed stability for Huynh's g_2 lumped-Lobatto scheme. This was expected since Huynh's g_2 lumped-Lobatto scheme is equivalent to a collocated DG scheme on LGL nodes [58].

An additional issue introduced by ESFR on curvilinear grids is that the aforementioned ESFR stability condition (fundamental assumption) in Eq. (3.30) (or the 1D analogous

Eq. (3.27)) only holds true on linear grids. That is, because in Eq. (3.36), if the determinant of the Jacobian was constant, then it would be factored off in the last integral and the $\partial^{(s,v,w)}$ derivative of the corresponding mode of the correction functions would then be factored out of the integral [5, 7–9, 56, 74, 75]. On general curvilinear coordinates, this is not true, even for analytically exact metric terms and exact integration as per Theorem 3.3.1, and the complete ESFR fundamental assumption for three-dimensional tensor product curvilinear elements should be,

$$\int_{\Omega_r} \nabla^r \chi_i(\boldsymbol{\xi}^r) \cdot \mathbf{g}^{f,k}(\boldsymbol{\xi}^r) d\Omega_r - \sum_{s,v,w} c_{(s,v,w)} \int_{\Omega_r} J_m^\Omega \partial^{(s,v,w)} \chi_i(\boldsymbol{\xi}^r) \partial^{(s,v,w)} \left(\frac{1}{J_m^\Omega} \nabla^r \cdot \mathbf{g}^{f,k}(\boldsymbol{\xi}^r) \right) d\Omega_r = 0,$$

$$\forall i = 1, \dots, N_p. \quad (3.37)$$

If the grid is constant/linear then Eq. (3.37) simplifies to Eq. (3.30) with a constant scaling of the volume of the reference element on $c_{(s,v,w)}$. To extend Eq. (3.37) for triangular and prismatic curvilinear grids, one should change the $\partial^{(s,v,w)}$ derivative with the operator $\mathbf{D}^{p,v,w}$ presented in [8, 48, 55], and the analysis/result is the same.

Therefore, using the metric dependent ESFR stability criteria, Eq. (3.37) in Eq. (3.36), and evaluating bilinear forms at cubature nodes results in,

$$\begin{aligned} & \left(\mathbf{M}_m + \mathbf{K}_m \right) \frac{d}{dt} \hat{\mathbf{u}}_m(t)^T + \frac{1}{2} \boldsymbol{\chi}(\boldsymbol{\xi}_v^r)^T \mathbf{W} \nabla^r \boldsymbol{\chi}(\boldsymbol{\xi}_v^r) \cdot \hat{\mathbf{f}}_m^r(t)^T + \frac{1}{2} \boldsymbol{\chi}(\boldsymbol{\xi}_v^r)^T \mathbf{W} \tilde{\nabla}^r \boldsymbol{\chi}(\boldsymbol{\xi}_v^r) \cdot \hat{\mathbf{f}}_m(t)^T \\ & + \sum_{f=1}^{N_f} \sum_{k=1}^{N_{fp}} \boldsymbol{\chi}(\boldsymbol{\xi}_{f,k}^r)^T W_{f,k} [\hat{\mathbf{n}}^r \cdot \mathbf{f}_m^{C,r}] \\ & + \sum_{s,v,w} \frac{c_{(s,v,w)}}{2} \partial^{(s,v,w)} \boldsymbol{\chi}(\boldsymbol{\xi}_v^r)^T \mathbf{J}_m \mathbf{W} \partial^{(s,v,w)} \boldsymbol{\chi}(\boldsymbol{\xi}_v^r) \Pi \left[\mathbf{J}_m^{-1} \nabla^r \cdot \boldsymbol{\chi}(\boldsymbol{\xi}_v^r) \hat{\mathbf{f}}_m^r(t)^T \right. \\ & \quad \left. + \mathbf{J}_m^{-1} \tilde{\nabla}^r \boldsymbol{\chi}(\boldsymbol{\xi}_v^r) \cdot \hat{\mathbf{f}}_m(t)^T \right] = \mathbf{0}^T. \end{aligned} \quad (3.38)$$

Eq. (3.38) is the filtered DG equivalent of the Classical ESFR split-form presented in Eq. (3.33),

with

$$\begin{aligned}
(\mathbf{K}_m)_{ij} &\approx \sum_{s,v,w} c_{(s,v,w)} \int_{\Omega_r} J_m^\Omega \partial^{(s,v,w)} \chi_i(\boldsymbol{\xi}^r) \partial^{(s,v,w)} \chi_j(\boldsymbol{\xi}^r) d\Omega_r \\
\rightarrow \mathbf{K}_m &= \sum_{s,v,w} c_{(s,v,w)} \partial^{(s,v,w)} \boldsymbol{\chi}(\boldsymbol{\xi}_v^r)^T \mathbf{W} \mathbf{J}_m \partial^{(s,v,w)} \boldsymbol{\chi}(\boldsymbol{\xi}_v^r) \\
&= \sum_{s,v,w} c_{(s,v,w)} \left(\mathbf{D}_\xi^s \mathbf{D}_\eta^v \mathbf{D}_\zeta^w \right)^T \mathbf{M}_m \left(\mathbf{D}_\xi^s \mathbf{D}_\eta^v \mathbf{D}_\zeta^w \right),
\end{aligned} \tag{3.39}$$

where $\mathbf{D}_\xi^s = \left(\mathbf{M}^{-1} \mathbf{S}_\xi \right)^s$ is the strong form differential operator raised to the power s , and similarly for the other reference directions.

Remark 3.4.1. *Note the inclusion of \mathbf{J}_m within \mathbf{K}_m in Eq. (3.39). It allows the broken Sobolev-norm $\mathbf{M}_m + \mathbf{K}_m$ to be symmetric positive definite (for values of $c_{1D} > c_-$). This naturally arises from the order of applying the differential operator, then integrating in physical space in Eq. (3.35), and re-defining the resultant curvilinear ESFR fundamental assumption Eq. (3.37). This varies from the literature where the Jacobian was either a constant [8, 54, 61, 64] or for curvilinear ESFR [45, 48] where the determinant of the Jacobian was left multiplied to Eq. (3.33). The $\partial^{(s,v,w)}$ derivative was then applied to the entire discretization (to have the $\partial^{(s,v,w)}$ derivative applied directly on the reference divergence operator), which would arise in the $\partial^{(s,v,w)}$ derivative of the determinant of the metric Jacobian \mathbf{J}_m in the norm. Explicitly, $\partial^{(s,v,w)} \left(\mathbf{J}_m \frac{d}{dt} \mathbf{u}_m^T \right) \neq \mathbf{J}_m \partial^{(s,v,w)} \left(\frac{d}{dt} \mathbf{u}_m^T \right)$, and hence $\partial^{(s,v,w)} \boldsymbol{\chi}(\boldsymbol{\xi}_v^r)^T \mathbf{W} \partial^{(s,v,w)} \left(\mathbf{J}_m \right)$ is not a norm.*

Remark 3.4.2. *The stated approach is unlike what is adopted in [21, 48, 64] where \mathbf{K}_m was constructed using the Legendre differential operator then transformed to the basis of the scheme. Here $c_{(s,v,w)}$ must take the value from a normalized Legendre reference basis.*

However, Eq. (3.38) is not provably stable since the final term does not vanish in the broken Sobolev-norm.

Lemma 3.4.1. *Eq. (3.38) is equivalent to a DG scheme with the ESFR filter applied solely to the facet integral.*

Proof.

Rearranging Eq. (3.38) by substituting $\mathbf{\Pi}_m = \mathbf{M}_m^{-1} \boldsymbol{\chi}(\boldsymbol{\xi}_v^r)^T \mathbf{W} \mathbf{J}_m$, thus

$\boldsymbol{\chi}(\boldsymbol{\xi}_v^r)^T \mathbf{W} = \boldsymbol{\chi}(\boldsymbol{\xi}_v^r)^T \mathbf{W} \mathbf{J}_m \mathbf{J}_m^{-1} = \mathbf{M}_m \mathbf{\Pi}_m \mathbf{J}_m^{-1}$, and using Chan [52, Theorem 4] results in,

$$\begin{aligned} & \left(\mathbf{M}_m + \mathbf{K}_m \right) \frac{d}{dt} \hat{\mathbf{u}}_m(t)^T + \frac{1}{2} \mathbf{M}_m \mathbf{\Pi}_m \left[\mathbf{J}_m^{-1} \nabla^r \boldsymbol{\chi}(\boldsymbol{\xi}_v^r) \cdot \hat{\mathbf{f}}_m^r(t)^T + \mathbf{J}_m^{-1} \tilde{\nabla}^r \boldsymbol{\chi}(\boldsymbol{\xi}_v^r) \cdot \hat{\mathbf{f}}_m(t)^T \right] \\ & + \sum_{f=1}^{N_f} \sum_{k=1}^{N_{fp}} \boldsymbol{\chi}(\boldsymbol{\xi}_{f,k}^r)^T W_{f,k} [\hat{\mathbf{n}}^r \cdot \mathbf{f}_m^{C,r}] \\ & + \frac{1}{2} \mathbf{K}_m \mathbf{\Pi}_m \left[\mathbf{J}_m^{-1} \nabla^r \boldsymbol{\chi}(\boldsymbol{\xi}_v^r) \cdot \hat{\mathbf{f}}_m^r(t)^T + \mathbf{J}_m^{-1} \tilde{\nabla}^r \boldsymbol{\chi}(\boldsymbol{\xi}_v^r) \cdot \hat{\mathbf{f}}_m(t)^T \right] = \mathbf{0}^T, \end{aligned} \quad (3.40)$$

which simplifies to

$$\begin{aligned} & \left(\mathbf{M}_m + \mathbf{K}_m \right) \frac{d}{dt} \hat{\mathbf{u}}_m(t)^T + \frac{1}{2} \left(\mathbf{M}_m + \mathbf{K}_m \right) \mathbf{\Pi}_m \left[\mathbf{J}_m^{-1} \nabla^r \boldsymbol{\chi}(\boldsymbol{\xi}_v^r) \cdot \hat{\mathbf{f}}_m^r(t)^T + \mathbf{J}_m^{-1} \tilde{\nabla}^r \boldsymbol{\chi}(\boldsymbol{\xi}_v^r) \cdot \hat{\mathbf{f}}_m(t)^T \right] \\ & + \sum_{f=1}^{N_f} \sum_{k=1}^{N_{fp}} \boldsymbol{\chi}(\boldsymbol{\xi}_{f,k}^r)^T W_{f,k} [\hat{\mathbf{n}}^r \cdot \mathbf{f}_m^{C,r}] = \mathbf{0}^T. \end{aligned} \quad (3.41)$$

Recalling the definition of $\mathbf{\Pi}_m = \mathbf{M}_m^{-1} \boldsymbol{\chi}(\boldsymbol{\xi}_v^r)^T \mathbf{W} \mathbf{J}_m$ and solving for $\frac{d}{dt} \hat{\mathbf{u}}_m(t)^T$ in Eq. (3.41) results in,

$$\begin{aligned} & \frac{d}{dt} \hat{\mathbf{u}}_m(t)^T + \frac{1}{2} \mathbf{M}_m^{-1} \boldsymbol{\chi}(\boldsymbol{\xi}_v^r)^T \mathbf{W} \left[\nabla^r \boldsymbol{\chi}(\boldsymbol{\xi}_v^r) \cdot \hat{\mathbf{f}}_m^r(t)^T + \tilde{\nabla}^r \boldsymbol{\chi}(\boldsymbol{\xi}_v^r) \cdot \hat{\mathbf{f}}_m(t)^T \right] \\ & + \left(\mathbf{M}_m + \mathbf{K}_m \right)^{-1} \sum_{f=1}^{N_f} \sum_{k=1}^{N_{fp}} \boldsymbol{\chi}(\boldsymbol{\xi}_{f,k}^r)^T W_{f,k} [\hat{\mathbf{n}}^r \cdot \mathbf{f}_m^{C,r}] = \mathbf{0}^T, \end{aligned} \quad (3.42)$$

which concludes the proof since the ESFR filter is only applied to the facet integral in Eq. (3.42). □

The proof in Lemma 3.4.1 shows that Eq. (3.38) recovers the divergence of the correction functions applied solely to the face in Eq. (3.42), as seen in the literature [48, 64]. That is,

from Allaneau and Jameson [64], and Zwanenburg and Nadarajah [48, Eq. 2.19],

$$\Pi \mathbf{J}_m^{-1} \boldsymbol{\chi}(\boldsymbol{\xi}_v^r) \left(\hat{\mathbf{h}}^{f,k} \right)^T = \left(\mathbf{M}_m + \mathbf{K}_m \right)^{-1} \boldsymbol{\chi}(\boldsymbol{\xi}_{f,k}^r)^T W_{f,k}. \quad (3.43)$$

Explicitly, Eqs. (3.33), (3.38), and (3.42) are all equivalent expressions of ESFR.

3.4.2 ESFR - Proposed Nonlinearly Stable Flux Reconstruction

As shown by Cicchino *et al.* [60], provable nonlinear stability can be established for FR schemes by incorporating the ESFR filter/divergence of the correction functions on the volume integrals. This results in our proposed ESFR split-form,

$$\begin{aligned} \frac{d}{dt} \hat{\mathbf{u}}_m(t)^T + \frac{1}{2} \left(\mathbf{M}_m + \mathbf{K}_m \right)^{-1} \boldsymbol{\chi}(\boldsymbol{\xi}_v^r)^T \mathbf{W} \left[\nabla^r \boldsymbol{\chi}(\boldsymbol{\xi}_v^r) \cdot \hat{\mathbf{f}}_m^r(t)^T + \tilde{\nabla}^r \boldsymbol{\chi}(\boldsymbol{\xi}_v^r) \cdot \hat{\mathbf{f}}_m(t)^T \right] \\ + \left(\mathbf{M}_m + \mathbf{K}_m \right)^{-1} \sum_{f=1}^{N_f} \sum_{k=1}^{N_{fp}} \boldsymbol{\chi}(\boldsymbol{\xi}_{f,k}^r)^T W_{f,k} [\hat{\mathbf{n}}^r \cdot \mathbf{f}_m^{C,r}] = \mathbf{0}^T. \end{aligned} \quad (3.44)$$

Or in equivalent form which simplifies the stability and conservation analysis,

$$\begin{aligned} \left(\mathbf{M}_m + \mathbf{K}_m \right) \frac{d}{dt} \hat{\mathbf{u}}_m(t)^T + \frac{1}{2} \boldsymbol{\chi}(\boldsymbol{\xi}_v^r)^T \mathbf{W} \left[\nabla^r \boldsymbol{\chi}(\boldsymbol{\xi}_v^r) \cdot \hat{\mathbf{f}}_m^r(t)^T + \tilde{\nabla}^r \boldsymbol{\chi}(\boldsymbol{\xi}_v^r) \cdot \hat{\mathbf{f}}_m(t)^T \right] \\ + \sum_{f=1}^{N_f} \sum_{k=1}^{N_{fp}} \boldsymbol{\chi}(\boldsymbol{\xi}_{f,k}^r)^T W_{f,k} [\hat{\mathbf{n}}^r \cdot \mathbf{f}_m^{C,r}] = \mathbf{0}^T. \end{aligned} \quad (3.45)$$

Eq. (3.44) is on design order as proved in Sec. 3.4.3.

Remark 3.4.3. *We present the equivalent form of Eq. (3.44) in SBP notation in Sec. 3.A.1 based on [76].*

We note that the computational implementation of the proposed ESFR schemes differ significantly from existing FR implementations in the literature [77]. On general curved meshes and for general quadrature rules, the FR norm matrix over each element is dense. Thus, when implementing the proposed energy stable FR scheme, the FR norm matrix must be constructed and inverted over each individual element. On affine elements, the inverse of

each elemental norm matrix can be computed through a constant scaling of a single reference norm matrix, as is typically done in ESFR by solving for the correction functions [6, 55]. However, for a static curved mesh, these matrix inverses can be precomputed and stored. This increases both storage costs and the number of memory transfers necessary for the proposed schemes. With regards to the case of curved triangular meshes, a form of sum factorization for triangular meshes can be adopted based on a transformation onto a quadrilateral element on which the basis is tensorial (e.g. Proriol, Kornwinder, Dubiner, and Owen (PKDO) polynomials or Bernstein polynomials); however, the computational cost is higher. In our numerical results, we use a Gauss-Jordan algorithm to compute $(\mathbf{M}_m + \mathbf{K}_m)^{-1}$ on-the-fly.

In comparison, the most common FR schemes [1, 2, 54, 55] avoid introducing a mass/norm matrix altogether by formulating the main computational steps of the scheme as operations on the reference element. Collocated DG schemes (and the equivalent FR schemes) on curved elements yield a trivially invertible diagonal mass (norm) matrix, with values of the determinant of the metric Jacobian at collocation points appearing as weights for each diagonal entry. For dense-mass (norm) matrices appearing in high-order DG on curved meshes, it is possible to approximate the inverse in an efficient, energy stable, and high order accurate fashion using a weight-adjusted approximation to the mass matrix [52]. However, because the norm matrices constructed in this work are constructed as the sum of two matrices, it is not currently possible to directly apply such an approach.

3.4.3 ESFR - Accuracy of Metric Dependent ESFR Schemes

Following the work of [48, 56, 64], we consider a normalized, p -th order Legendre reference basis

$\chi_{ref}(\boldsymbol{\xi}^r) = \chi_{ref}(\xi) \otimes \chi_{ref}(\eta) \otimes \chi_{ref}(\zeta)$ on $\boldsymbol{\xi}^r \in [-1, 1]^3$. The motivation behind using an orthonormal reference basis rather than an orthogonal reference basis is that it allows \mathbf{K}_m to be constructed directly with the differential operator and mass matrix of the scheme [56, Sec. 3.1]. Thus, we introduce the transformation operator $\mathbf{T} = \mathbf{\Pi}_{ref}\boldsymbol{\chi}(\boldsymbol{\xi}_v^r)$, where $\mathbf{\Pi}_{ref} =$

$\mathbf{M}_{ref}^{-1} \boldsymbol{\chi}_{ref}(\boldsymbol{\xi}_v^r)^T \mathbf{W}$, such that $\mathbf{K}_m = \mathbf{T}^T \mathbf{K}_{m,ref} \mathbf{T}$.

Next, we explicitly formulate $\mathbf{K}_{m,ref}$ to derive the metric Jacobian dependent ESFR filter. To express $\mathbf{K}_{m,ref}$ we introduce the modal differential operators for a normalized Legendre reference basis $\hat{\mathbf{D}}_\xi^s = (\mathbf{M}_{ref}^{-1} \mathbf{S}_{\xi,ref})^s$, similarly for $\hat{\mathbf{D}}_\eta^v$ and $\hat{\mathbf{D}}_\zeta^w$, to result in,

$$\begin{aligned} \mathbf{K}_{m,ref} &= \sum_{s,v,w} c_{(s,v,w)} \partial^{(s,v,w)} \boldsymbol{\chi}_{ref}(\boldsymbol{\xi}_v^r)^T \mathbf{W} \mathbf{J}_m \partial^{(s,v,w)} \boldsymbol{\chi}_{ref}(\boldsymbol{\xi}_v^r) \\ &= \sum_{s,v,w} c_{(s,v,w)} \left(\hat{\mathbf{D}}_\xi^s \hat{\mathbf{D}}_\eta^v \hat{\mathbf{D}}_\zeta^w \right)^T \mathbf{M}_{m,ref} \left(\hat{\mathbf{D}}_\xi^s \hat{\mathbf{D}}_\eta^v \hat{\mathbf{D}}_\zeta^w \right) \\ \implies (\mathbf{K}_{m,ref})_{ij} &\approx \sum_{s,v,w} c_{(s,v,w)} \int_{\Omega_r} J_m^\Omega \partial^{(s,v,w)} \chi_{ref,i}(\boldsymbol{\xi}^r) \partial^{(s,v,w)} \chi_{ref,j}(\boldsymbol{\xi}^r) d\Omega_r \end{aligned} \quad (3.46)$$

Typically when deriving the correction functions [54, 55, 75] or ESFR filter [48, 56, 64], we would utilize the orthogonality of the reference basis functions. However, for curvilinear coordinates, the reference basis functions are not orthogonal on $d\Omega_m = J_m^\Omega d\Omega_r$. That is,

$$\int_{\Omega_r} \chi_{ref,i}(\boldsymbol{\xi}^r) \chi_{ref,j}(\boldsymbol{\xi}^r) d\Omega_r = \delta_{ij}, \quad (3.47)$$

but,

$$\int_{\Omega_r} J_m^\Omega \chi_{ref,i}(\boldsymbol{\xi}^r) \chi_{ref,j}(\boldsymbol{\xi}^r) d\Omega_r \neq \alpha \delta_{ij}, \text{ where } \alpha = \text{const}, \text{ unless } J_m^\Omega = \text{const}, \quad (3.48)$$

where the last inequality holds even under exact integration and the analytically exact J_m^Ω . An equality would be present in Eq. (3.48) if and only if $\boldsymbol{\chi}_{ref}(\boldsymbol{\Theta}_m^{-1}(\mathbf{x}^c))$ is also an orthogonal polynomial basis; but thus far there is no claim that $\boldsymbol{\chi}_{ref}(\boldsymbol{\Theta}_m^{-1}(\mathbf{x}^c))$ or $\boldsymbol{\chi}(\boldsymbol{\Theta}_m^{-1}(\mathbf{x}^c))$ are polynomial in the analysis. Using Eq. (3.48) in Eq. (3.46) directly shows that for a tensor-product basis, $\mathbf{K}_{m,ref}$ is not diagonal for curvilinear coordinates, and is diagonal only under the constant metric Jacobian case.

To prove the order of accuracy for curvilinear ESFR schemes, we demonstrate which modes the ESFR filter, $\mathbf{F}_{m,ref}$, operates on; such that $\left. \frac{d}{dt} \hat{\mathbf{u}}_{ref}(t)^T \right|_{\text{ESFR}} = \mathbf{F}_{m,ref} \left. \frac{d}{dt} \hat{\mathbf{u}}_{ref}(t)^T \right|_{\text{DG}}$.

Theorem 3.4.1. *For general curvilinear coordinates, the ESFR filter operator is applied to all modes of the discretization, not just the highest order mode; even for triangular/prismatic elements [55, 78], the 3p-th broken Sobolev-norm considered in [56], and all other cases where the corresponding $\mathbf{K}_{m,ref}$ would be diagonal with a single entry on the highest mode.*

Proof. We substitute Eq. (3.48) when constructing the metric Jacobian dependent mass matrix for a normalized Legendre reference basis,

$$(\mathbf{M}_{m,ref})_{ij} \approx \int_{\Omega_r} J_m^\Omega \chi_{ref,i}(\boldsymbol{\xi}^r) \chi_{ref,j}(\boldsymbol{\xi}^r) d\Omega_r \neq \alpha \delta_{ij}, \text{ where } \alpha = \text{const}, \quad (3.49)$$

that shows the reference mass matrix is dense, even with exact integration and analytically exact metric terms. Thus, we let $\mathbf{M}_{m,ref} = \begin{bmatrix} a & b \\ b & c \end{bmatrix}$ and $\mathbf{K}_{m,ref} = \begin{bmatrix} 0 & 0 \\ 0 & d \end{bmatrix}$ to consider the special case where the correction functions are only applied on the highest mode, *i.e.* prismatic/triangular curvilinear elements and tensor-product curvilinear elements using the

3p-th broken Sobolev-norm [56]. This implies $(\mathbf{M}_{m,ref} + \mathbf{K}_{m,ref})^{-1} = \frac{1}{a(c+d)-b^2} \begin{bmatrix} c+d & -b \\ -b & a \end{bmatrix}$.

Thus $\mathbf{F}_{m,ref} = (\mathbf{M}_{m,ref} + \mathbf{K}_{m,ref})^{-1} \mathbf{M}_{m,ref} = \begin{bmatrix} 1 & \frac{bd}{a(c+d)-b^2} \\ 0 & \frac{ac-b^2}{a(c+d)-b^2} \end{bmatrix}$. Therefore, considering the

complete case for $\mathbf{F}_{m,ref} = (\mathbf{M}_{m,ref} + \mathbf{K}_{m,ref})^{-1} \mathbf{M}_{m,ref}$ implies the filter has influence on all modes, rather than just the highest mode, which varies from the literature for linear grids [48, 56, 64]. \square

Typically in the ESFR literature [1, 2, 54, 55, 61], the scheme is shown to lose at most one order of accuracy because the divergence of the correction functions corresponds to the highest mode of the scheme. Unfortunately, this is only true for constant metric Jacobians, or non-positive-definite norms as discussed in Remark 3.4.1. Theorem 3.4.1 directly proves that ESFR schemes can lose all orders for general curvilinear coordinates; even without considering our proposed ESFR split-form and instead considering the classical VCJH schemes with or without exact integration, and/or with or without analytically exact or discrete metric

terms. This result is dependent on the metric dependence within the ESFR fundamental assumption, Eq. (3.37), in curvilinear coordinates. In Section 3.7.1, we numerically show for three-dimensions that the scheme loses all orders at the approximate location [8, Figure 3.6] that the one-dimensional ESFR/VCJH schemes lose one order of accuracy; at a value of $c \gg c_+$.

3.5 Discrete GCL

In this section we briefly review how to compute \mathbf{C}_m to ensure both the correct orders of accuracy, free-stream preservation and surface metric terms being consistent between interior and exterior cells. The main idea from Kopriva [67] was to satisfy the GCL (Eq. (3.7)) *a priori* by equivalently expressing the reference vector basis multiplied by the determinant of the Jacobian in curl form. With the interpolation being within the curl, discrete GCL is satisfied since it is the divergence of the curl. That is, by expressing the reference transformation (metric cofactor matrix) as,

$$\begin{aligned}
& \text{(Cross Product Form) } J^\Omega \mathbf{a}^i = \mathbf{a}_j \times \mathbf{a}_k, \quad i = 1, 2, 3 \quad (i, j, k) \text{ cyclic,} \\
& \Leftrightarrow \text{(Conservative Curl Form) } J^\Omega(\mathbf{a}^i)_n = -\hat{\mathbf{e}}_i \cdot \nabla^r \times \left(\mathbf{x}_l^c \nabla^r \mathbf{x}_m^c \right), \\
& \quad i = 1, 2, 3, \quad n = 1, 2, 3 \quad (n, m, l) \text{ cyclic,} \\
& \Leftrightarrow \text{(Invariant Curl Form) } J^\Omega(\mathbf{a}^i)_n = -\frac{1}{2} \hat{\mathbf{e}}_i \cdot \nabla^r \times \left(\mathbf{x}_l^c \nabla^r \mathbf{x}_m^c - \mathbf{x}_m^c \nabla^r \mathbf{x}_l^c \right), \\
& \quad i = 1, 2, 3, \quad n = 1, 2, 3 \quad (n, m, l) \text{ cyclic,}
\end{aligned}$$

where $\hat{\mathbf{e}} = [\hat{x}, \hat{y}, \hat{z}]$ is the physical unit vector ². Then for the conservative curl form, the GCL can be written as,

$$\sum_{i=1}^3 \frac{\partial (J^\Omega(\mathbf{a}^i)_n)}{\partial \xi^i} = -\nabla^r \cdot \left(\nabla^r \times \left(\mathbf{x}_l^c \nabla^r \mathbf{x}_m^c \right) \right) = 0, \quad n = 1, 2, 3 \quad (n, m, l) \text{ cyclic,}$$

²this is not to be confused with the previous definition of $\hat{\mathbf{x}}^c$ which are the mapping support points (grid points)

and similarly for the invariant curl form. Thus Kopriva [67] proved that to discretely satisfy GCL *a priori*, one must interpolate to the flux nodes (volume or facet cubature nodes) before applying the curl. That is, the discrete conservative curl form reads as,

$$J^\Omega(\mathbf{a}^i)_n = (\mathbf{C})_{ni} = -\hat{\mathbf{e}}_i \cdot \nabla^r \times \Theta(\boldsymbol{\xi}^r) \left(\mathbf{x}_l^c \nabla^r \mathbf{x}_m^c \right), \quad i = 1, 2, 3, \quad n = 1, 2, 3 \quad (n, m, l) \text{ cyclic}, \quad (3.50)$$

and similarly for the invariant curl form. For general three-dimensional curvilinear elements, Kopriva [67] also proved that the cross product form does not discretely satisfy GCL, thus the conservative or invariant curl forms should always be used.

One of the primary issues raised by Abe *et al.* [79] was that Eq. (3.50) does not ensure that the normals match at each facet cubature node. It is to be noted that Abe *et al.* [79] considered only the invariant curl form, but the methodology is also consistent for the conservative curl form. To circumvent the issue, one main result from [79] was to have two separate interpolation operators, one for the “grid points” (mapping support points) and another for the cubature (flux) nodes. This distinction was made because in high-order grid generation, it is typical to have the exact corners of the elements, making them continuous finite elements at the grid points [80, 81]. Thus, Abe *et al.* [79, Eqs. (31)-(34), (41) and (42)] evaluated $\left(\mathbf{x}_l^c \nabla^r \mathbf{x}_m^c \right)$ in Eq. (3.50) at the grid nodes, and computed the mapping shape functions at the flux nodes prior to the application of the curl operator [79, Eq. (43)]. By doing so, consistency is ensured at each face since the grid nodes are continuous; and GCL is satisfied at each quadrature point because the final interpolation is performed within the curl operator. Therefore, we have the discrete conservative curl form,

$$(\mathbf{C})_{ni} = -\hat{\mathbf{e}}_i \cdot \nabla^r \times \Theta(\boldsymbol{\xi}_{\text{flux nodes}}^r) \left[\Theta(\boldsymbol{\xi}_{\text{grid nodes}}^r) \hat{\mathbf{x}}_l^{cT} \nabla^r \Theta(\boldsymbol{\xi}_{\text{grid nodes}}^r) \hat{\mathbf{x}}_m^{cT} \right], \quad (3.51)$$

$$i = 1, 2, 3, \quad n = 1, 2, 3 \quad (n, m, l) \text{ cyclic},$$

and similarly for the discrete invariant curl form,

$$(\mathbf{C})_{ni} = -\frac{1}{2}\hat{\mathbf{e}}_i \cdot \nabla^r \times \Theta(\boldsymbol{\xi}_{\text{flux nodes}}^r) \left[\Theta(\boldsymbol{\xi}_{\text{grid nodes}}^r) \hat{\mathbf{x}}_l^{cT} \nabla^r \Theta(\boldsymbol{\xi}_{\text{grid nodes}}^r) \hat{\mathbf{x}}_m^{cT} - \Theta(\boldsymbol{\xi}_{\text{grid nodes}}^r) \hat{\mathbf{x}}_m^{cT} \nabla^r \Theta(\boldsymbol{\xi}_{\text{grid nodes}}^r) \hat{\mathbf{x}}_l^{cT} \right], \quad (3.52)$$

$$i = 1, 2, 3, n = 1, 2, 3 \text{ (} n, m, l \text{) cyclic,}$$

where we assumed the mapping shape functions are collocated on the mapping support points $\hat{\mathbf{x}}^c$. In all numerical results we used Eq. (3.51) with LGL as the grid nodes.

3.6 Free-Stream Preservation, Conservation and Stability

In this section, we prove free-stream preservation, conservation, and stability for our proposed provably stable FR split-form, Eq. (3.44). For free-stream preservation, we prove that it is essential to distinguish between grid nodes and flux nodes in Eqs. (3.51) and (3.52). Then, by satisfying GCL, we demonstrate conservation. Lastly, to illustrate the stability of the scheme, we show that it is essential to incorporate the divergence of the correction functions on the volume terms.

3.6.1 Free-Stream Preservation

We first demonstrate that the surface splitting from Eq. (3.44) satisfies free-stream preservation if the metric terms are computed via Eq. (3.51) or (3.52). We start by substituting

$$\mathbf{f}_m = \boldsymbol{\alpha} = \text{constant and } \frac{d}{dt} \hat{\mathbf{u}}_m(t)^T = \mathbf{0}^T \text{ into Eq. (3.44),}$$

$$\begin{aligned} & \frac{1}{2} \left(\mathbf{M}_m + \mathbf{K}_m \right)^{-1} \boldsymbol{\chi}(\boldsymbol{\xi}_v^r)^T \mathbf{W} \left[\nabla^r \cdot \boldsymbol{\alpha} \mathbf{C}_m(\boldsymbol{\xi}_v^r) + \tilde{\nabla}^r \cdot \boldsymbol{\alpha} \right] \\ & + \left(\mathbf{M}_m + \mathbf{K}_m \right)^{-1} \sum_{f=1}^{N_f} \sum_{k=1}^{N_{fp}} \boldsymbol{\chi}(\boldsymbol{\xi}_{f,k}^r)^T W_{f,k} [\hat{\mathbf{n}}^r \mathbf{C}_m(\boldsymbol{\xi}_{f,k}^r)^T \cdot (\boldsymbol{\alpha} - \frac{1}{2} \boldsymbol{\alpha}) - \frac{1}{2} \hat{\mathbf{n}}^r \cdot \boldsymbol{\chi}(\boldsymbol{\xi}_{f,k}^r) \boldsymbol{\Pi}(\boldsymbol{\alpha} \mathbf{C}_m(\boldsymbol{\xi}_v^r))]. \end{aligned} \quad (3.53)$$

Factoring out the constant, utilizing GCL Eq. (3.7), and the divergence of a constant is zero

we are left with,

$$\implies \left(\mathbf{M}_m + \mathbf{K}_m \right)^{-1} \sum_{f=1}^{N_f} \sum_{k=1}^{N_{fp}} \boldsymbol{\chi}(\boldsymbol{\xi}_{f,k}^r)^T W_{f,k} \left[\frac{1}{2} \hat{\mathbf{n}}^r \mathbf{C}_m(\boldsymbol{\xi}_{f,k}^r)^T \cdot \mathbf{1} - \frac{1}{2} \hat{\mathbf{n}}^r \cdot \boldsymbol{\chi}(\boldsymbol{\xi}_{f,k}^r) \boldsymbol{\Pi}(\mathbf{1} \mathbf{C}_m(\boldsymbol{\xi}_v^r)) \right]. \quad (3.54)$$

Since the metrics computed in Eq. (3.51) or (3.52) are computed at a continuous set of grid nodes (included on the boundary), with only the last interpolation performed at the flux nodes,

$$\begin{aligned} & \left(\boldsymbol{\chi}(\boldsymbol{\xi}_{f,k}^r) \boldsymbol{\Pi}(\mathbf{1} \mathbf{C}_m(\boldsymbol{\xi}_v^r)) \right)_{ni} \\ &= -\hat{e}_i \cdot \boldsymbol{\Theta}(\boldsymbol{\xi}_{f,k}^r) \boldsymbol{\Theta}(\boldsymbol{\xi}_v^r)^{-1} \boldsymbol{\Theta}(\boldsymbol{\xi}_v^r) \nabla^r \times \boldsymbol{\Theta}(\boldsymbol{\xi}_{\text{grid nodes}}^r) \left[\boldsymbol{\Theta}(\boldsymbol{\xi}_{\text{grid nodes}}^r) \hat{\mathbf{x}}_l^{cT} \nabla^r \boldsymbol{\Theta}(\boldsymbol{\xi}_{\text{grid nodes}}^r) \hat{\mathbf{x}}_m^{cT} \right], \\ & i = 1, 2, 3, \quad n = 1, 2, 3 \quad (n, m, l) \text{ cyclic,} \\ &= \left(\mathbf{1} \mathbf{C}_m(\boldsymbol{\xi}_{f,k}^r) \right)_{ni}, \end{aligned} \quad (3.55)$$

and similarly for the invariant curl formulation. Note that $\boldsymbol{\Theta}(\boldsymbol{\xi}_v^r)^{-1}$ is always true and appears from a change of basis in Eq. (3.55). Thus Eq. (3.54) becomes,

$$\implies \left(\mathbf{M}_m + \mathbf{K}_m \right)^{-1} \sum_{f=1}^{N_f} \sum_{k=1}^{N_{fp}} \boldsymbol{\chi}(\boldsymbol{\xi}_{f,k}^r)^T W_{f,k} \left[\frac{1}{2} \hat{\mathbf{n}}^r \mathbf{C}_m(\boldsymbol{\xi}_{f,k}^r)^T \cdot \mathbf{1} - \frac{1}{2} \hat{\mathbf{n}}^r \cdot (\mathbf{1} \mathbf{C}_m(\boldsymbol{\xi}_{f,k}^r)) \right] = \mathbf{0}^T, \quad (3.56)$$

which concludes the proof since free-stream is preserved. \square

3.6.2 Conservation

To prove global and local conservation, we use quadrature rules exact of at least $2p - 1$, and consider the $(\mathbf{M}_m + \mathbf{K}_m)$ -norm,

$$\begin{aligned} \hat{\mathbf{1}}(\mathbf{M}_m + \mathbf{K}_m) \frac{d}{dt} \hat{\mathbf{u}}_m(t)^T &= -\frac{1}{2} \mathbf{1} \mathbf{W} \nabla^r \chi(\boldsymbol{\xi}_v^r) \cdot \hat{\mathbf{f}}_m^r(t)^T - \frac{1}{2} \mathbf{1} \mathbf{W} \tilde{\nabla}^r \chi(\boldsymbol{\xi}_v^r) \cdot \hat{\mathbf{f}}_m(t)^T \\ &\quad - \sum_{f=1}^{N_f} \sum_{k=1}^{N_{fp}} 1W_{f,k} [\hat{\mathbf{n}}^r \cdot \mathbf{f}_m^{C,r}], \end{aligned} \quad (3.57)$$

where $\hat{\mathbf{1}}$ is implicitly defined by $\mathbf{1} = [1, \dots, 1] = \left(\chi(\boldsymbol{\xi}_v^r) \hat{\mathbf{1}}^T \right)^T$. Discretely integrating both volume terms by parts yields the following expression for the right-hand-side of Eq. (3.57),

$$\begin{aligned} &= \frac{1}{2} \nabla^r (\mathbf{1}) \mathbf{W} \cdot \chi(\boldsymbol{\xi}_v^r) \hat{\mathbf{f}}_m^r(t)^T + \frac{1}{2} (\nabla^r \cdot \mathbf{1} \mathbf{C}_m(\boldsymbol{\xi}_v^r)) \mathbf{W} \cdot \chi(\boldsymbol{\xi}_v^r) \hat{\mathbf{f}}_m(t)^T \\ &\quad - \sum_{f=1}^{N_f} \sum_{k=1}^{N_{fp}} 1W_{f,k} [\hat{\mathbf{n}}^r \mathbf{C}_m(\boldsymbol{\xi}_{f,k}^r)^T \cdot \mathbf{f}_m^*]. \end{aligned} \quad (3.58)$$

Utilizing the property of GCL from Eq. (3.7) and that the gradient of a scalar is zero, allows the volume terms to vanish and local conservation is established,

$$\therefore \hat{\mathbf{1}}(\mathbf{M}_m + \mathbf{K}_m) \frac{d}{dt} \hat{\mathbf{u}}(t)^T = - \sum_{f=1}^{N_f} \sum_{k=1}^{N_{fp}} 1W_{f,k} [\hat{\mathbf{n}}^r \mathbf{C}_m(\boldsymbol{\xi}_{f,k}^r)^T \cdot \mathbf{f}_m^*]. \quad (3.59)$$

From the assumption of a conforming, water-tight mesh, then the interior normal equals the negative of the exterior normal, provided the surface metrics are computed by Eqs. (3.51) or (3.52), which concludes the proof for global conservation with periodic boundary conditions.

□

3.6.3 Stability

We consider the broken Sobolev-norm $W_\delta^{3p,2} = \mathbf{M}_m + \mathbf{K}_m$ to demonstrate stability,

$$\begin{aligned} \hat{\mathbf{u}}_m(t) \left(\mathbf{M}_m + \mathbf{K}_m \right) \frac{d}{dt} \hat{\mathbf{u}}_m(t)^T &= \frac{1}{2} \frac{d}{dt} \|\mathbf{u}\|_{W_\delta^{3p,2}}^2 = \frac{1}{2} \frac{d}{dt} \|\mathbf{u}\|_{\mathbf{M}_m + \mathbf{K}_m}^2 \\ &= -\frac{1}{2} \mathbf{u}_m \mathbf{W} \nabla^r \chi(\boldsymbol{\xi}_v^r) \cdot \hat{\mathbf{f}}_m^r(t)^T - \frac{1}{2} \mathbf{u}_m \mathbf{W} \tilde{\nabla}^r \chi(\boldsymbol{\xi}_v^r) \cdot \hat{\mathbf{f}}_m(t)^T - \sum_{f=1}^{N_f} \sum_{k=1}^{N_{fp}} u_m W_{f,k} [\hat{\mathbf{n}}^r \cdot \mathbf{f}_m^{C,r}] \end{aligned} \quad (3.60)$$

Next, we discretely integrate the first volume term by parts in the reference space,

$$\begin{aligned} &= \frac{1}{2} \nabla^r(\mathbf{u}_m) \mathbf{W} \cdot \chi(\boldsymbol{\xi}_v^r) \hat{\mathbf{f}}_m^r(t)^T - \frac{1}{2} \mathbf{u}_m \mathbf{W} \tilde{\nabla}^r \chi(\boldsymbol{\xi}_v^r) \cdot \hat{\mathbf{f}}_m(t)^T \\ &\quad - \sum_{f=1}^{N_f} \sum_{k=1}^{N_{fp}} u_m W_{f,k} [\hat{\mathbf{n}}^r \mathbf{C}_m(\boldsymbol{\xi}_{f,k}^r)^T \cdot (\mathbf{f}_m^* - \frac{1}{2} \mathbf{f}_m)]. \end{aligned} \quad (3.61)$$

Since the two volume terms in Eq. (3.61) are equivalent,

$$\begin{aligned} \nabla^r(\mathbf{u}_m) \mathbf{W} \cdot \chi(\boldsymbol{\xi}_v^r) \hat{\mathbf{f}}_m^r(t)^T &= \nabla^r(\mathbf{u}_m) \mathbf{W} \cdot \mathbf{f}_m \mathbf{C}_m(\boldsymbol{\xi}_v^r) = \nabla^r(\mathbf{u}_m) \mathbf{W} \mathbf{C}_m(\boldsymbol{\xi}_v^r)^T \cdot \mathbf{f}_m \\ &= \mathbf{f}_m \mathbf{W} \cdot \nabla^r(\mathbf{u}_m) \mathbf{C}_m(\boldsymbol{\xi}_v^r)^T, \end{aligned} \quad (3.62)$$

$$\because \mathbf{f}_m = \mathbf{a} \mathbf{u}_m \implies \nabla^r(\mathbf{u}_m) \mathbf{W} \cdot \chi(\boldsymbol{\xi}_v^r) \hat{\mathbf{f}}_m^r(t)^T = \mathbf{u}_m \mathbf{W} \tilde{\nabla}^r \chi(\boldsymbol{\xi}_v^r) \cdot \hat{\mathbf{f}}_m(t)^T,$$

they discretely cancel for linear advection, and we are left with

$$\frac{1}{2} \frac{d}{dt} \|\mathbf{u}\|_{W_\delta^{3p,2}}^2 = - \sum_{f=1}^{N_f} \sum_{k=1}^{N_{fp}} u_m W_{f,k} [\hat{\mathbf{n}}^r \mathbf{C}_m(\boldsymbol{\xi}_{f,k}^r)^T \cdot (\mathbf{f}_m^* - \frac{1}{2} \mathbf{f}_m)], \quad (3.63)$$

which concludes the proof since it is the same stability claim as that for a linear grid. Thus energy is conserved for a central numerical flux, and energy monotonically decreases for an upwind numerical flux with periodic boundary conditions [41, 56]. \square

For completeness, we present the operator form of the above stability proof in Appendix 3.B.

3.7 Results

In this section, we use the open-source Parallel High-order Library for PDEs (PHiLiP, <https://github.com/dougshidong/PHiLiP.git>) [82], developed at the Computational Aerodynamics Group at McGill University, to numerically verify all proofs. Three tests are used: the first verifies Thm. 3.4.1 for three-dimensions, the second verifies that the ESFR filter operator (divergence of the correction functions) must be applied to the volume for stability, and the third verifies Lem. 3.3.1 and Remark 3.4.1. When we refer to “ESFR Classical Split”, we are using the split-form with the ESFR correction functions only applied to the surface, whereas “ESFR Split” refers to our proposed provably stable ESFR split-form with the correction functions applied on both the volume and surface terms.

For the order of accuracy (OOA) tests, to compute the L_2 error, an overintegration of $p + 10$ was used to provide sufficient strength,

$$L_2 - error = \sqrt{\sum_{m=1}^M \int_{\Omega} (u_m - u)^2 d\Omega} = \sqrt{\sum_{m=1}^M (\mathbf{u}_m^T - \mathbf{u}_{exact}^T) \mathbf{W}_m \mathbf{J}_m (\mathbf{u}_m - \mathbf{u}_{exact})}. \quad (3.64)$$

We additionally compute the L_{∞} error as $\max(|\mathbf{u}_m(\boldsymbol{\xi}_{v,i}^r)^T - \mathbf{u}_{exact}(\boldsymbol{\xi}_{v,i}^r)^T|)$ as the maximum pointwise error at cubature node $(\boldsymbol{\xi}_{v,i}^r)$. In all experiments, our basis functions $\boldsymbol{\chi}(\boldsymbol{\xi}^r)$ are Lagrange polynomials constructed on LGL quadrature nodes. Our “grid nodes”, or mapping-support-points, are LGL quadrature nodes. Our “flux nodes” for integration are GL quadrature nodes. Lastly, all schemes were conservative on the order of $1e - 15$. For the energy tests, schemes that diverge are indicated as non-monotonically decreasing in Tables 3.5-3.6 and 3.15-3.16.

3.7.1 ESFR Derivative Test

The first numerical test addresses Thm. 3.4.1, where we solve for the divergence of the flux, $\nabla \cdot \mathbf{f}$. In this test, we only solve for the volume terms. We take the heavily warped grid in

Fig. 3.1, defined by Eq. (3.65), and distribute the flux from Eq. (3.66). Then we solve for the volume terms in Eq. (3.44), that approximate $\nabla \cdot \mathbf{f}$, for varying values of c .

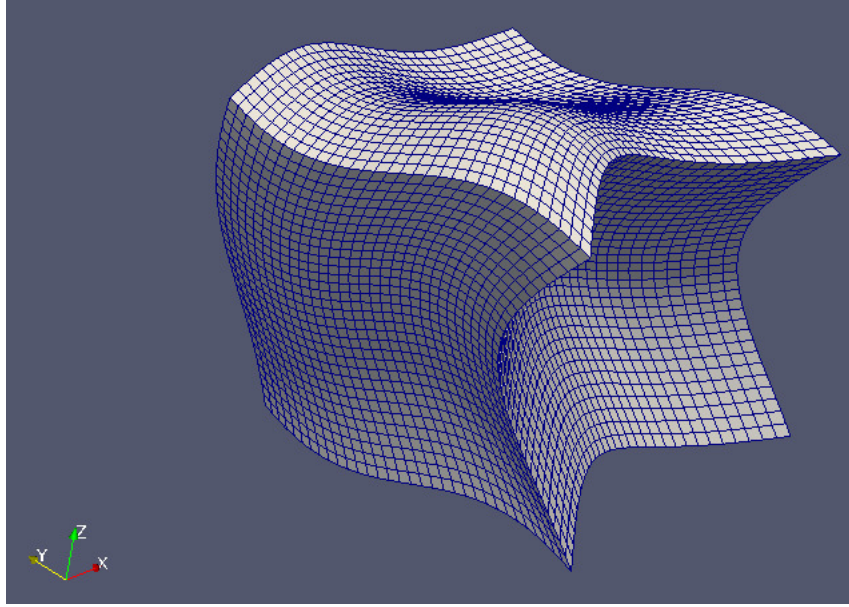


Figure 3.1: 3D Warped Grid

$$\begin{aligned}
 x &= \xi + \frac{1}{10} \left(\cos \pi \eta + \cos \pi \zeta \right), \\
 y &= \eta + \frac{1}{10} \exp(1 - \eta) \left(\sin \pi \xi + \sin \pi \zeta \right), \\
 z &= \zeta + \frac{1}{20} (\sin 2\pi \xi + \sin 2\pi \eta), \\
 [\xi, \eta, \zeta] &\in [0, 1]^3.
 \end{aligned} \tag{3.65}$$

$$\begin{aligned}
 \mathbf{f} &= [\exp(-10x^2), \exp(-10\pi y^3), \exp(-10 \sin z)], \\
 \nabla \cdot \mathbf{f}_{\text{exact}} &= -10 \left(2x \exp(-10x^2) + 3\pi y^2 \exp(-10\pi y^3) + \cos(z) \exp(-10 \sin z) \right).
 \end{aligned} \tag{3.66}$$

The maximum GCL computed for the grid was $O(1e-15)$. First, we demonstrate in Tables 3.1 through 3.4 that the error levels change as we increase c , but the orders remain unchanged until $c \gg c_+$. Next, for the polynomial order range, $p = 2$ through $p = 5$, we verify

that applying the ESFR filter operator does not affect the order of accuracy up to a certain value, and by Thm. 3.4.1, the scheme loses all orders of accuracy at this value. The black star is the location of c_+ in Figures 3.2 through 3.5. The drop off value for c closely resembles the values obtained by Castonguay [8, Figure 3.6].

dx	c_{DG}	OOA	c_+	OOA
3.125e-02	1.949e-02	-	1.860e-02	-
1.563e-02	2.587e-03	2.91	2.467e-03	2.91
7.813e-03	3.285e-04	2.98	3.133e-04	2.98
3.906e-03	4.122e-05	2.99	3.931e-05	2.99

Table 3.1: L_2 Convergence Table $p = 3$

dx	c_{DG}	OOA	c_+	OOA
3.125e-02	4.436e-01	-	3.713e-01	-
1.563e-02	7.033e-02	2.66	5.746e-02	2.69
7.813e-03	9.885e-03	2.83	8.056e-03	2.83
3.906e-03	1.309e-03	2.92	1.072e-03	2.91

Table 3.2: L_∞ Convergence Table $p = 3$

dx	c_{DG}	OOA	c_+	OOA
2.5000e-02	1.618e-03	-	1.559e-03	-
1.2500e-02	1.070e-04	3.92	1.032e-04	3.92
6.2500e-03	6.784e-06	3.98	6.542e-06	3.98
3.1250e-03	4.256e-07	3.99	4.103e-07	3.99

Table 3.3: L_2 Convergence Table $p = 4$

dx	c_{DG}	OOA	c_+	OOA
2.5000e-02	4.648e-02	-	4.085e-02	-
1.2500e-02	3.388e-03	3.78	3.033e-03	3.75
6.2500e-03	2.296e-04	3.88	2.056e-04	3.88
3.1250e-03	1.496e-05	3.94	1.341e-05	3.94

Table 3.4: L_∞ Convergence Table $p = 4$

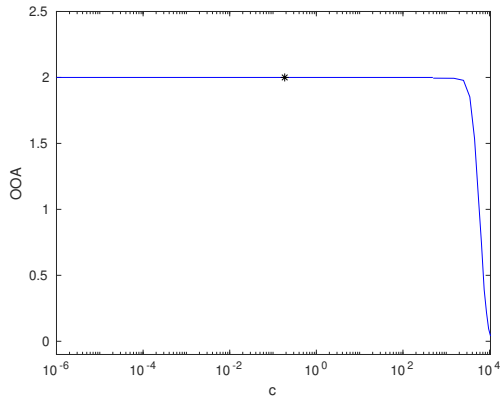


Figure 3.2: 3D c vs OOA for $p = 2$

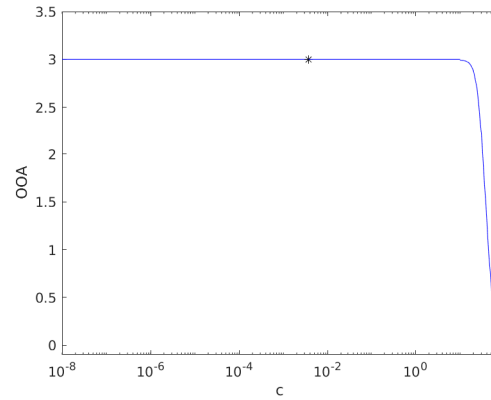


Figure 3.3: 3D c vs OOA for $p = 3$

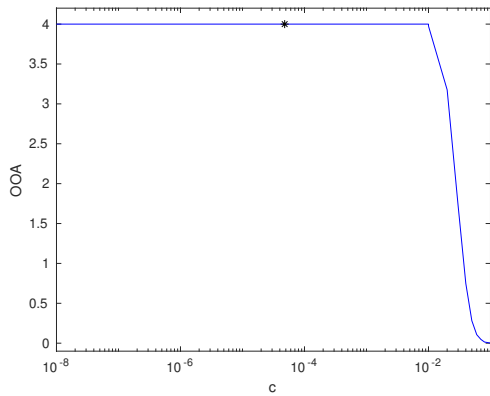


Figure 3.4: 3D c vs OOA for $p = 4$

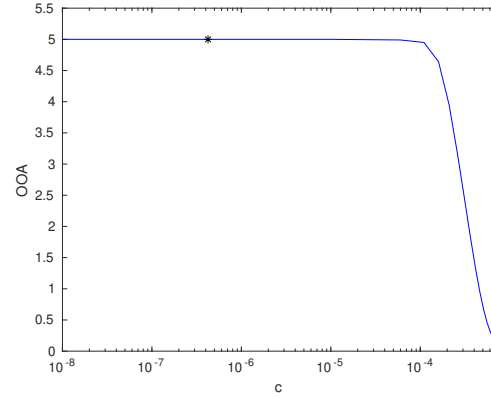


Figure 3.5: 3D c vs OOA for $p = 5$

3.7.2 Nonsymmetric Grid

As illustrated by Lem. 3.3.1, the nonlinear metric terms vanish for both symmetric and skew-symmetric grids; resulting in a false-positive stable solution. Thus, a nonsymmetric

grid was chosen to ensure that nonlinear metric terms are present. The warping for the nonsymmetric grid is similar to that used by Wu *et al.* [83], defined by Eq. (3.67), and the grid is illustrated in Fig. 3.6,

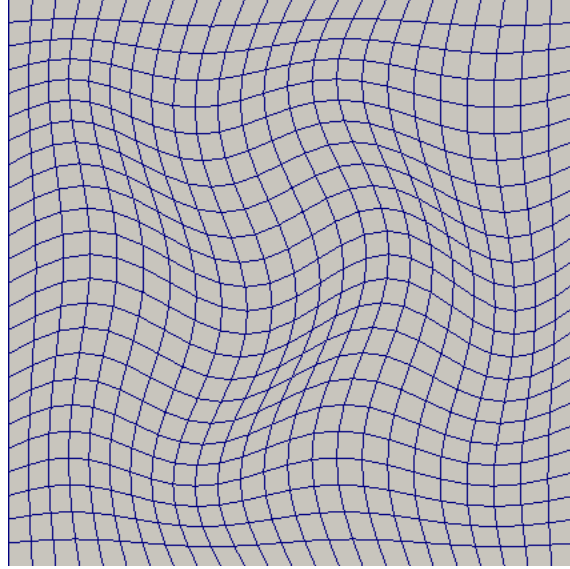


Figure 3.6: Warped Grid $p = 3$

$$\begin{aligned}
 x &= \xi + \frac{1}{10} \cos \frac{\pi}{2} \xi \cos \frac{3\pi}{2} \eta \\
 y &= \eta + \frac{1}{10} \sin 2\pi \xi \cos \frac{\pi}{2} \eta, \\
 [\xi, \eta] &\in [-1, 1]^2.
 \end{aligned} \tag{3.67}$$

We apply the following linear advection problem in Eq. (3.68),

$$\begin{aligned}
 \frac{\partial u}{\partial t} + 1.1 \frac{\partial u}{\partial x} - \frac{\pi}{e} \frac{\partial u}{\partial y} &= 0, \\
 u(x, y, 0) &= e^{-20(x^2+y^2)},
 \end{aligned} \tag{3.68}$$

with periodic boundary conditions. We integrate with a Runge-Kutta-4 integrator, using a timestep $dt = 0.05dx$, with dx being the average distance between two quadrature nodes. The grid is partitioned into 8^2 elements. All results are uncollocated, with the solution built

Scheme	Flux	Energy Conserved $\mathcal{O}(1e-12)$	Energy Monotonically Decrease
Cons. DG	Central	No	No
Cons. DG	Upwind	No	No
EFSR Split c_{DG}	Central	Yes	Yes
EFSR Split c_{DG}	Upwind	No	Yes
EFSR Split c_+	Central	Yes	Yes
EFSR Split c_+	Upwind	No	Yes
EFSR Classical Split c_+	Central	No	No
EFSR Classical Split c_+	Upwind	No	No ¹

Table 3.5: Energy Results $p = 3, 4$ Uncollocated $N_{vp} = (p + 1)^2$ Grid 1

Scheme	Flux	Energy Conserved $\mathcal{O}(1e-12)$	Energy Monotonically Decrease
Cons. DG	Central	No	No
Cons. DG	Upwind	No	No
EFSR Split c_{DG}	Central	Yes	Yes
EFSR Split c_{DG}	Upwind	No	Yes
EFSR Split c_+	Central	Yes	Yes
EFSR Split c_+	Upwind	No	Yes
EFSR Classical Split c_+	Central	No	No
EFSR Classical Split c_+	Upwind	No	No ¹

Table 3.6: Energy Results $p = 3, 4$ Uncollocated $N_{vp} = (p + 3)^2$ Grid 1

on the LGL nodes and integrated on the GL nodes. Since our metrics were computed via Eq. (3.51) and surface splitting was used, we were able to use GL nodes for both volume and surface integration without any form of optimization seen in the literature [41]. We first show energy results for uncollocated integration in Table 3.5, then uncollocated overintegration in Table 3.6.

An interesting result in Tables 3.5 and 3.6 is the false positive for the EFSR Classical split with an upwind numerical flux. From the derivation of our proposed curvilinear FR schemes in Sec. 3.4.1, specifically Eq. (3.35), there is no stability claim for the two terms $\mathbf{K}_m\left(\mathbf{J}_m^{-1}\nabla^r\chi(\xi_v^r)\right)$ and $\mathbf{K}_m\left(\mathbf{J}_m^{-1}\tilde{\nabla}^r\chi(\xi_v^r)\right)$ as they can result in either a convergent or divergent scheme. The advantage of our proposed FR schemes is that they are provably stable. In the next test case, it will be shown that the EFSR classical split is divergent for a skew-symmetric grid.

¹Although the energy did not monotonically decrease for this case, it did not diverge either. Instead it gradually decreased over time giving a false positive.

To demonstrate the orders of accuracy, we consider the linear advection problem in Eq. (3.69),

$$\begin{aligned} \frac{\partial u}{\partial t} + \frac{\partial u}{\partial x} + \frac{\partial u}{\partial y} &= 0, \\ [x, y] &\in [-1, 1]^2, \quad t \in [0, 2] \\ u(x, y, 0) &= \sin \pi x \sin \pi y, \\ u_{exact}(x, y, t) &= \sin \pi(x - t) \sin \pi(y - t). \end{aligned} \tag{3.69}$$

We used a timestep of $dt = 0.5dx$, where again dx is the average distance between two quadrature nodes. The convergence rates are shown in Tables 3.7 through 3.10 for uncollocated integration, and Tables 3.11 through 3.14 for uncollocated overintegration.

dx	c_{DG}	OOA	c_+	OOA
6.2500e-02	1.4592e-02	-	3.9628e-02	-
3.1250e-02	1.1632e-03	3.65	3.0945e-03	3.68
1.5625e-02	7.4833e-05	3.96	1.7779e-04	4.12
7.8125e-03	4.7374e-06	3.98	1.0851e-05	4.03
3.9062e-03	3.0227e-07	3.97	6.8311e-07	3.99

Table 3.7: L_2 Convergence Table $p = 3$ $N_{vp} = (p + 1)^2$ Upwind Numerical Flux Grid 1

dx	c_{DG}	OOA	c_+	OOA
6.2500e-02	4.7490e-02	-	1.1192e-01	-
3.1250e-02	5.2854e-03	3.17	1.4510e-02	2.95
1.5625e-02	3.6961e-04	3.84	1.5445e-03	3.23
7.8125e-03	2.5181e-05	3.88	8.0837e-05	4.26
3.9062e-03	1.6401e-06	3.94	5.2672e-06	3.94

Table 3.8: L_∞ Convergence Table $p = 3$ $N_{vp} = (p + 1)^2$ Upwind Numerical Flux Grid 1

dx	c_{DG}	OOA	c_+	OOA
5.0000e-02	3.7766e-03	-	8.1107e-03	-
2.5000e-02	1.4876e-04	4.67	2.5675e-04	4.98
1.2500e-02	5.1042e-06	4.87	9.2869e-06	4.79
6.2500e-03	1.6763e-07	4.93	3.1350e-07	4.89
3.1250e-03	5.4776e-09	4.94	1.0345e-08	4.92

Table 3.9: L_2 Convergence Table $p = 4$ $N_{vp} = (p + 1)^2$ Upwind Numerical Flux Grid 1

dx	c_{DG}	OOA	c_+	OOA
5.0000e-02	1.7943e-02	-	3.4934e-02	-
2.5000e-02	7.1420e-04	4.65	1.8378e-03	4.25
1.2500e-02	2.7883e-05	4.67	6.7414e-05	4.77
6.2500e-03	1.0551e-06	4.72	2.9290e-06	4.52
3.1250e-03	3.4989e-08	4.91	1.0435e-07	4.81

Table 3.10: L_∞ Convergence Table $p = 4$ $N_{vp} = (p + 1)^2$ Upwind Numerical Flux Grid 1

dx	c_{DG}	OOA	c_+	OOA
6.2500e-02	1.4539e-02	-	3.9565e-02	-
3.1250e-02	1.1594e-03	3.65	3.0883e-03	3.68
1.5625e-02	7.4762e-05	3.95	1.7771e-04	4.12
7.8125e-03	4.7363e-06	3.98	1.0849e-05	4.03
3.9062e-03	3.0074e-07	3.98	6.8243e-07	3.99

Table 3.11: L_2 Convergence Table $p = 3$ $N_{vp} = (p + 3)^2$ Upwind Numerical Flux Grid 1

dx	c_{DG}	OOA	c_+	OOA
6.2500e-02	4.7467e-02	-	1.1172e-01	-
3.1250e-02	5.2245e-03	3.18	1.4400e-02	2.96
1.5625e-02	3.6902e-04	3.82	1.5435e-03	3.22
7.8125e-03	2.5167e-05	3.87	8.0826e-05	4.26
3.9062e-03	1.6398e-06	3.94	5.2670e-06	3.94

Table 3.12: L_∞ Convergence Table $p = 3$ $N_{vp} = (p + 3)^2$ Upwind Numerical Flux Grid 1

dx	c_{DG}	OOA	c_+	OOA
5.0000e-02	3.7361e-03	-	8.0479e-03	-
2.5000e-02	1.4812e-04	4.66	2.5660e-04	4.97
1.2500e-02	5.0980e-06	4.86	9.2793e-06	4.79
6.2500e-03	1.6758e-07	4.93	3.1344e-07	4.89
3.1250e-03	5.4642e-09	4.94	1.0338e-08	4.92

Table 3.13: L_2 Convergence Table $p = 4$ $N_{vp} = (p + 3)^2$ Upwind Numerical Flux Grid 1

dx	c_{DG}	OOA	c_+	OOA
5.0000e-02	1.7408e-02	-	3.4462e-02	-
2.5000e-02	7.0797e-04	4.62	1.8335e-03	4.23
1.2500e-02	2.7798e-05	4.67	6.7391e-05	4.77
6.2500e-03	1.0549e-06	4.72	2.9288e-06	4.52
3.1250e-03	3.4983e-08	4.91	1.0434e-07	4.81

Table 3.14: L_∞ Convergence Table $p = 4$ $N_{vp} = (p + 3)^2$ Upwind Numerical Flux Grid 1

3.7.3 Skew-Symmetric Grid

For further verification, we conduct the same experiments on the skew-symmetric grid from Hennemann *et al.* [84], shown in Fig.3.7, with warping defined in Eq. (3.70),

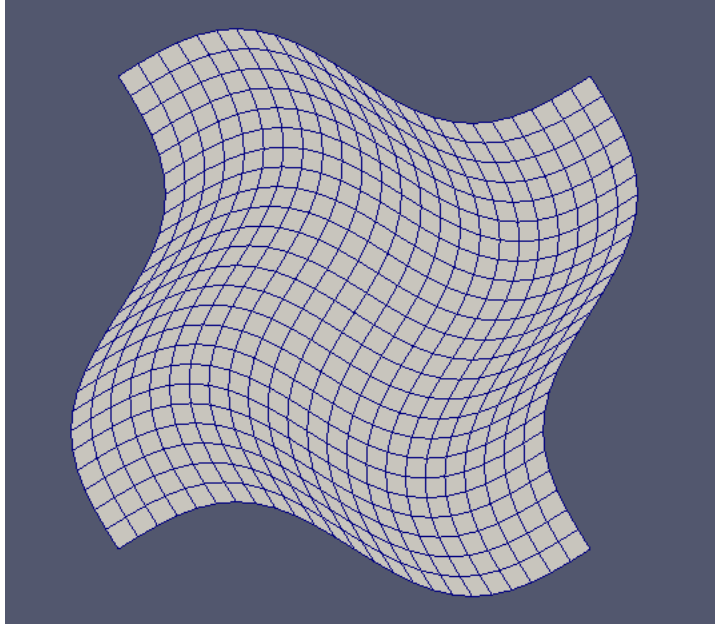


Figure 3.7: Second Warped Grid $p = 3$

$$\begin{aligned}
 x &= \xi - 0.1 \sin 2\pi\eta, \\
 y &= \eta + 0.1 \sin 2\pi\xi, \\
 [\xi, \eta] &\in [0, 1]^2.
 \end{aligned}
 \tag{3.70}$$

The sole purpose of using a skew-symmetric grid, is to show that even in the case when the grid has all the nonlinear metric terms cancel out, as per Lem. 3.3.1, Remark 3.4.1 holds because the determinant of the metric Jacobian cannot be factored out of the $\partial^{(s,v,w)}$ derivative. That is, the conservative and non-conservative forms are equivalent for this case as per Lem. 3.3.1, and this testcase showcases purely the necessity of the metric dependent correction functions. Thus, the ESFR correction functions must satisfy the metric dependent stability criteria in Eq. (3.37). We use the same initial condition described in Eq. (3.68) for the energy results, presented in Tables 3.15 and 3.16.

An interesting result from this grid is that conservative DG without the split form was stable, due to the skew-symmetry of the grid; while, ESFR classical split form was unstable.

Scheme	Flux	Energy Conserved $\mathcal{O}(1e-12)$	Energy Monotonically Decrease
Cons. DG	Central	Yes	Yes
Cons. DG	Upwind	No	Yes
EFSR Split c_{DG}	Central	Yes	Yes
EFSR Split c_{DG}	Upwind	No	Yes
EFSR Split c_+	Central	Yes	Yes
EFSR Split c_+	Upwind	No	Yes
EFSR Classical Split c_+	Central	No	No
EFSR Classical Split c_+	Upwind	No	No

Table 3.15: Energy Results $p = 3, 4$ Uncollocated $N_{vp} = (p + 1)^2$ Grid 2

Scheme	Flux	Energy Conserved $\mathcal{O}(1e-12)$	Energy Monotonically Decrease
Cons. DG	Central	Yes	Yes
Cons. DG	Upwind	No	Yes
EFSR Split c_{DG}	Central	Yes	Yes
EFSR Split c_{DG}	Upwind	No	Yes
EFSR Split c_+	Central	Yes	Yes
EFSR Split c_+	Upwind	No	Yes
EFSR Classical Split c_+	Central	No	No
EFSR Classical Split c_+	Upwind	No	No

Table 3.16: Energy Results $p = 3, 4$ Uncollocated $N_{vp} = (p + 3)^2$ Grid 2

This highlights the importance of false positives while testing curvilinear grids. To demonstrate the orders of accuracy, we consider the linear advection problem from Eq. (3.69), and present the results in Tables 3.17 to 3.24.

dx	c_{DG}	OOA	c_+	OOA
6.2500e-02	6.9001e-03	-	2.2205e-02	-
3.1250e-02	4.9929e-04	3.79	2.1666e-03	3.36
1.5625e-02	3.0374e-05	4.04	9.5947e-05	4.50
7.8125e-03	1.9340e-06	3.97	5.6723e-06	4.08
3.9062e-03	1.2339e-07	3.97	3.5426e-07	4.00

Table 3.17: L_2 Convergence Table $p = 3$ $N_{vp} = (p + 1)^2$ Upwind Numerical Flux Grid 2

dx	c_{DG}	OOA	c_+	OOA
6.2500e-02	4.0068e-02	-	1.6836e-01	-
3.1250e-02	3.7121e-03	3.43	2.7181e-02	2.63
1.5625e-02	3.0497e-04	3.61	1.2679e-03	4.42
7.8125e-03	2.1527e-05	3.82	6.7106e-05	4.24
3.9062e-03	1.4001e-06	3.94	4.0344e-06	4.06

Table 3.18: L_∞ Convergence Table $p = 3$ $N_{vp} = (p + 1)^2$ Upwind Numerical Flux Grid 2

dx	c_{DG}	OOA	c_+	OOA
5.0000e-02	1.5174e-03	-	3.7476e-03	-
2.5000e-02	4.8840e-05	4.96	1.0266e-04	5.19
1.2500e-02	1.6575e-06	4.88	3.7381e-06	4.78
6.2500e-03	5.9007e-08	4.81	1.4512e-07	4.69
3.1250e-03	2.1770e-09	4.76	5.2669e-09	4.78

Table 3.19: L_2 Convergence Table $p = 4$ $N_{vp} = (p + 1)^2$ Upwind Numerical Flux Grid 2

dx	c_{DG}	OOA	c_+	OOA
5.0000e-02	9.6178e-03	-	2.4719e-02	-
2.5000e-02	3.9077e-04	4.62	1.2826e-03	4.27
1.2500e-02	1.5061e-05	4.70	5.5561e-05	4.53
6.2500e-03	6.9115e-07	4.45	2.6736e-06	4.38
3.1250e-03	2.4981e-08	4.79	1.0379e-07	4.69

Table 3.20: L_∞ Convergence Table $p = 4$ $N_{vp} = (p + 1)^2$ Upwind Numerical Flux Grid 2

dx	c_{DG}	OOA	c_+	OOA
6.2500e-02	6.8280e-03	-	2.2131e-02	-
3.1250e-02	4.9794e-04	3.78	2.1647e-03	3.35
1.5625e-02	3.0357e-05	4.04	9.5922e-05	4.50
7.8125e-03	1.9337e-06	3.97	5.6719e-06	4.08
3.9062e-03	1.2338e-07	3.97	3.5425e-07	4.00

Table 3.21: L_2 Convergence Table $p = 3$ $N_{vp} = (p + 3)^2$ Upwind Numerical Flux Grid 2

dx	c_{DG}	OOA	c_+	OOA
6.2500e-02	3.9689e-02	-	1.6899e-01	-
3.1250e-02	3.6977e-03	3.42	2.7110e-02	2.64
1.5625e-02	3.0464e-04	3.60	1.2676e-03	4.42
7.8125e-03	2.1521e-05	3.82	6.7102e-05	4.24
3.9062e-03	1.4000e-06	3.94	4.0343e-06	4.06

Table 3.22: L_∞ Convergence Table $p = 3$ $N_{vp} = (p + 3)^2$ Upwind Numerical Flux Grid 2

dx	c_{DG}	OOA	c_+	OOA
5.0000e-02	1.5058e-03	-	3.7268e-03	-
2.5000e-02	4.8725e-05	4.95	1.0251e-04	5.18
1.2500e-02	1.6566e-06	4.88	3.7369e-06	4.78
6.2500e-03	5.8997e-08	4.81	1.4511e-07	4.69
3.1250e-03	2.1769e-09	4.76	5.2668e-09	4.78

Table 3.23: L_2 Convergence Table $p = 4$ $N_{vp} = (p + 3)^2$ Upwind Numerical Flux Grid 2

dx	c_{DG}	OOA	c_+	OOA
5.0000e-02	9.5289e-03	-	2.4636e-02	-
2.5000e-02	3.8874e-04	4.62	1.2817e-03	4.26
1.2500e-02	1.5046e-05	4.69	5.5551e-05	4.53
6.2500e-03	6.9098e-07	4.44	2.6735e-06	4.38
3.1250e-03	2.4979e-08	4.79	1.0379e-07	4.69

Table 3.24: L_∞ Convergence Table $p = 4$ $N_{vp} = (p + 3)^2$ Upwind Numerical Flux Grid 2

3.8 Conclusion

This article proved that discrete integration by parts is not satisfied in the physical space for DG conservative and non-conservative forms, as well as standard FR forms, even with analytically exact metric terms and exact integration—provided that the basis functions are polynomial in the reference space. This leads to the formulation of metric dependent FR correction functions. Through the construction of metric dependent FR correction functions, the inclusion of metric Jacobian dependence within arbitrarily dense-norms was derived and manifested through the FR broken Sobolev-norm. The resultant curvilinear expression had the correction functions filtering all modes of the discretization. The theoretical findings were numerically verified with a three-dimensional, heavily warped, non-symmetric grid, where the orders of convergence were lost at the equivalent correction parameter value c as that of the one-dimensional ESFR scheme.

We derived dense, modal or nodal, FR schemes in curvilinear coordinates that ensured provable stability and conservation. This was achieved by incorporating the FR correction functions (FR filter operator) on both the volume and surface terms. Through a suite of curvilinear test-cases, one being non-symmetric and the other being skew-symmetric, the provable stability claim was numerically verified for our proposed FR schemes. The choice of grids highlighted the importance of assessing false-positives, especially in curvilinear

coordinates where metric skew-symmetry has the metric cross-terms cancel out, as well as when metric symmetry combined with equivalent advection speeds in every physical direction results in an equivalence between the conservative and non-conservative forms. It was also numerically verified that FR schemes that solely use the correction functions to reconstruct the surface are divergent in general curvilinear coordinates—in both conservative and in split form. Lastly, we demonstrate that the proposed FR scheme retains optimal orders of accuracy in the appropriate range of c values.

3.9 Acknowledgements

We would like to gratefully acknowledge the financial support of the Natural Sciences and Engineering Research Council of Canada Discovery Grant Program and McGill University. Jesse Chan acknowledges support from the US National Science Foundation under awards DMS-1719818 and DMS-1943186.

3.A Summation-by-Parts

The proposed algorithm in this paper is inspired by developments in the SBP literature, but derived using standard techniques and arguments from both the DG and FR communities. In this section, we make the link to the SBP formalism directly by assembling the relevant SBP operators.

The stiffness operators satisfy discrete integration by parts for quadrature rules of at least $2p - 1$ strength,

$$\begin{aligned}
& \int_{\Omega_r} \chi_i(\boldsymbol{\xi}^r) \nabla^r \chi_j(\boldsymbol{\xi}^r) d\Omega_r + \int_{\Omega_r} \nabla^r \chi_i(\boldsymbol{\xi}^r) \chi_j(\boldsymbol{\xi}^r) d\Omega_r = \int_{\Gamma_r} \chi_i(\boldsymbol{\xi}^r) \chi_j(\boldsymbol{\xi}^r) \hat{\mathbf{n}}^r d\Gamma_r \\
& \Leftrightarrow \boldsymbol{\chi}(\boldsymbol{\xi}_v^r)^T \mathbf{W} \nabla^r \boldsymbol{\chi}(\boldsymbol{\xi}_v^r) + \nabla^r \boldsymbol{\chi}(\boldsymbol{\xi}_v^r)^T \mathbf{W} \boldsymbol{\chi}(\boldsymbol{\xi}_v^r) = \sum_{f=1}^{N_f} \sum_{k=1}^{N_{fp}} \boldsymbol{\chi}(\boldsymbol{\xi}_{f,k}^r)^T W_{f,k} \hat{\mathbf{n}}^r \boldsymbol{\chi}(\boldsymbol{\xi}_{f,k}^r).
\end{aligned} \tag{3.71}$$

3.A.1 SBP - Strong Form FR Split

We introduce the lifting operator,

$$\mathbf{L}_q = \mathbf{M}^{-1} \sum_{f=1}^{N_f} \boldsymbol{\chi}(\boldsymbol{\xi}_f^r)^T \mathbf{W}_f, \quad (3.72)$$

where $\boldsymbol{\chi}(\boldsymbol{\xi}_f^r)$ stores the basis functions evaluated at all facet cubature nodes on the face f , and \mathbf{W}_f is a diagonal matrix storing the quadrature weights on the face f .

We now introduce the SBP operator [76],

$$\mathbf{Q}^i = \mathbf{W}(\mathbf{M}^{-1} \mathbf{S}_\xi) \boldsymbol{\Pi},$$

to formulate the *skew-hybridized* SBP operator from Chan [76, Eq. (10)],

$$\tilde{\mathbf{Q}}_p^i = \frac{1}{2} \begin{bmatrix} \mathbf{Q}^i - (\mathbf{Q}^i)^T & \mathbf{W} \boldsymbol{\chi}(\boldsymbol{\xi}_v^r) \mathbf{L}_q \text{diag}(\hat{\mathbf{n}}_f^\xi) \\ -\sum_{f=1}^{N_f} \mathbf{W}_f \text{diag}(\hat{\mathbf{n}}_f^\xi) \boldsymbol{\chi}(\boldsymbol{\xi}_f^r) \boldsymbol{\Pi} & \sum_{f=1}^{N_f} \mathbf{W}_f \text{diag}(\hat{\mathbf{n}}_f^\xi) \end{bmatrix}. \quad (3.73)$$

Next, similar to Chan [76, Eq. (27)], we introduce the metric dependent hybridized SBP operator as,

$$\mathbf{Q}_m^i = \frac{1}{2} \sum_{j=1}^d \left(\text{diag} \begin{bmatrix} \mathbf{C}_m(\boldsymbol{\xi}_v^r)_{ji} \\ \mathbf{C}_m(\boldsymbol{\xi}_f^r)_{ji} \end{bmatrix} \tilde{\mathbf{Q}}_p^j + \tilde{\mathbf{Q}}_p^j \text{diag} \begin{bmatrix} \mathbf{C}_m(\boldsymbol{\xi}_v^r)_{ji} \\ \mathbf{C}_m(\boldsymbol{\xi}_f^r)_{ji} \end{bmatrix} \right). \quad (3.74)$$

In equivalent form, we express Eq. (3.44) as,

$$\begin{aligned} \frac{d}{dt} \hat{\mathbf{u}}_m(t)^T + \left[(\mathbf{M}_m + \mathbf{K}_m)^{-1} \boldsymbol{\chi}(\boldsymbol{\xi}_v^r)^T (\mathbf{M}_m + \mathbf{K}_m)^{-1} \sum_{f=1}^{N_f} \boldsymbol{\chi}(\boldsymbol{\xi}_f^r)^T \right] \sum_{j=1}^d \left(2\mathbf{Q}_m^i \circ \mathbf{F}_S^j \right) \mathbf{1}^T \\ + \sum_{j=1}^d (\mathbf{M}_m + \mathbf{K}_m)^{-1} \sum_{f=1}^{N_f} \text{diag}(\mathbf{n}_{m,j}) (\mathbf{f}_j^* - \mathbf{f}_j(\tilde{\mathbf{u}}_m)) = \mathbf{0}^T \quad (3.75) \\ (\mathbf{F}_S^i)_{jk} = \mathbf{f}_S^i(\tilde{\mathbf{u}}_j, \tilde{\mathbf{u}}_k), \forall 1 \leq j+k \leq N_{vp} + N_{fp}, \end{aligned}$$

where $\mathbf{n}_m = \hat{\mathbf{n}}^r \mathbf{C}_m^T$.

We would like to emphasize that incorporating the ESFR filter on the volume terms does not create a new ESFR differential operator, but instead is a modification on the norm that the DG volume is projected on. That is, we project both the volume and the surface terms to the p -th order broken Sobolev-space in the nonlinearly stable FR scheme, whereas in DG, the volume and surfaces are projected onto the L_2 -space.

3.B Stability Proof - Operator Form

Here we present the stability proof from Sec. 3.6.3 in operator form. We start by applying the $(\mathbf{M}_m + \mathbf{K}_m)$ -norm, and we quickly see that it cancels off with its respective inverse,

$$\begin{aligned}
& \hat{\mathbf{u}}_m(t) \left(\mathbf{M}_m + \mathbf{K}_m \right) \frac{d}{dt} \hat{\mathbf{u}}_m(t)^T \\
&= -\hat{\mathbf{u}}_m(t) \left(\mathbf{M}_m + \mathbf{K}_m \right) \left(\mathbf{M}_m + \mathbf{K}_m \right)^{-1} \sum_{i=1}^d \sum_{j=1}^d \boldsymbol{\chi}(\boldsymbol{\xi}_v^r)^T \mathbf{W} \left(a_i \frac{\partial \boldsymbol{\chi}(\boldsymbol{\xi}_v^r)}{\partial \xi_j} \boldsymbol{\Pi} \left(J_m^\Omega \frac{\partial \xi_j}{\partial x_i} \right) \boldsymbol{\chi}(\boldsymbol{\xi}_v^r) \hat{\mathbf{u}}_m(t)^T \right. \\
&\quad \left. + a_i \left(J_m^\Omega \frac{\partial \xi_j}{\partial x_i} \right) \frac{\partial \boldsymbol{\chi}(\boldsymbol{\xi}_v^r)}{\partial \xi_j} \boldsymbol{\Pi} \boldsymbol{\chi}(\boldsymbol{\xi}_v^r) \hat{\mathbf{u}}_m(t)^T \right) \\
&- \hat{\mathbf{u}}_m(t) \left(\mathbf{M}_m + \mathbf{K}_m \right) \left(\mathbf{M}_m + \mathbf{K}_m \right)^{-1} \sum_{f=1}^{N_f} \boldsymbol{\chi}(\boldsymbol{\xi}_f^r)^T \mathbf{W}_f \text{diag}(\hat{\mathbf{n}}_f^r) \mathbf{f}_m^{C,r^T}.
\end{aligned} \tag{3.76}$$

Next, consider the volume terms with respect to a single (i, j) -pairing, substitute $\frac{\partial \boldsymbol{\chi}(\boldsymbol{\xi}_v^r)}{\partial \xi_j} = \boldsymbol{\chi}(\boldsymbol{\xi}_v^r) \mathbf{M}^{-1} \mathbf{S}_{\xi,j}$, and swap the metric terms with the quadrature weights in the second volume term,

$$\begin{aligned}
& \hat{\mathbf{u}}_m(t) \boldsymbol{\chi}(\boldsymbol{\xi}_v^r)^T \mathbf{W} \left(a_i \frac{\partial \boldsymbol{\chi}(\boldsymbol{\xi}_v^r)}{\partial \xi_j} \boldsymbol{\Pi} \left(J_m^\Omega \frac{\partial \xi_j}{\partial x_i} \right) \boldsymbol{\chi}(\boldsymbol{\xi}_v^r) \hat{\mathbf{u}}_m(t)^T + a_i \left(J_m^\Omega \frac{\partial \xi_j}{\partial x_i} \right) \frac{\partial \boldsymbol{\chi}(\boldsymbol{\xi}_v^r)}{\partial \xi_j} \boldsymbol{\Pi} \boldsymbol{\chi}(\boldsymbol{\xi}_v^r) \hat{\mathbf{u}}_m(t)^T \right) \\
&= a_i \hat{\mathbf{u}}_m(t) \boldsymbol{\chi}(\boldsymbol{\xi}_v^r)^T \mathbf{W} \boldsymbol{\chi}(\boldsymbol{\xi}_v^r) \mathbf{M}^{-1} \mathbf{S}_{\xi,j} \boldsymbol{\Pi} \left(J_m^\Omega \frac{\partial \xi_j}{\partial x_i} \right) \boldsymbol{\chi}(\boldsymbol{\xi}_v^r) \hat{\mathbf{u}}_m(t)^T \\
&\quad + a_i \hat{\mathbf{u}}_m(t) \boldsymbol{\chi}(\boldsymbol{\xi}_v^r)^T \left(J_m^\Omega \frac{\partial \xi_j}{\partial x_i} \right) \mathbf{W} \boldsymbol{\chi}(\boldsymbol{\xi}_v^r) \mathbf{M}^{-1} \mathbf{S}_{\xi,j} \boldsymbol{\Pi} \boldsymbol{\chi}(\boldsymbol{\xi}_v^r) \hat{\mathbf{u}}_m(t)^T.
\end{aligned} \tag{3.77}$$

We continue by substituting $\mathbf{\Pi}^T = \mathbf{W}\boldsymbol{\chi}(\boldsymbol{\xi}_v^r)\mathbf{M}^{-1}$, and $\mathbf{\Pi}\boldsymbol{\chi}(\boldsymbol{\xi}_v^r) = \mathbf{M}^{-1}\mathbf{M} = \mathbf{I}$,

$$\begin{aligned}
&= a_i \hat{\mathbf{u}}_m(t) \boldsymbol{\chi}(\boldsymbol{\xi}_v^r)^T \mathbf{\Pi}^T \mathbf{S}_{\xi,j} \mathbf{\Pi} (J_m^\Omega \frac{\partial \xi_j}{\partial x_i}) \boldsymbol{\chi}(\boldsymbol{\xi}_v^r) \hat{\mathbf{u}}_m(t)^T + a_i \hat{\mathbf{u}}_m(t) \boldsymbol{\chi}(\boldsymbol{\xi}_v^r)^T (J_m^\Omega \frac{\partial \xi_j}{\partial x_i}) \mathbf{\Pi}^T \mathbf{S}_{\xi,j} \hat{\mathbf{u}}_m(t)^T \\
&= a_i \left(\mathbf{\Pi} \boldsymbol{\chi}(\boldsymbol{\xi}_v^r) \hat{\mathbf{u}}_m(t)^T \right)^T \mathbf{S}_{\xi,j} \mathbf{\Pi} (J_m^\Omega \frac{\partial \xi_j}{\partial x_i}) \boldsymbol{\chi}(\boldsymbol{\xi}_v^r) \hat{\mathbf{u}}_m(t)^T + a_i \hat{\mathbf{u}}_m(t) \boldsymbol{\chi}(\boldsymbol{\xi}_v^r)^T (J_m^\Omega \frac{\partial \xi_j}{\partial x_i}) \mathbf{\Pi}^T \mathbf{S}_{\xi,j} \hat{\mathbf{u}}_m(t)^T.
\end{aligned} \tag{3.78}$$

Lastly, we substitute $\mathbf{\Pi}\boldsymbol{\chi}(\boldsymbol{\xi}_v^r) = \mathbf{M}^{-1}\mathbf{M} = \mathbf{I}$ once more and then perform integration-by-parts on the first stiffness matrix to arrive at,

$$\begin{aligned}
&= -a_i \hat{\mathbf{u}}_m(t) \mathbf{S}_{\xi,j}^T \mathbf{\Pi} (J_m^\Omega \frac{\partial \xi_j}{\partial x_i}) \boldsymbol{\chi}(\boldsymbol{\xi}_v^r) \hat{\mathbf{u}}_m(t)^T + a_i \hat{\mathbf{u}}_m(t) \boldsymbol{\chi}(\boldsymbol{\xi}_v^r)^T (J_m^\Omega \frac{\partial \xi_j}{\partial x_i}) \mathbf{\Pi}^T \mathbf{S}_{\xi,j} \hat{\mathbf{u}}_m(t)^T \\
&\quad + \sum_{f=1}^{N_f} a_i \hat{\mathbf{u}}_m(t) \boldsymbol{\chi}(\boldsymbol{\xi}_f^r)^T \text{diag}(\hat{\mathbf{n}}^{\xi_j}) \boldsymbol{\chi}(\boldsymbol{\xi}_f) \hat{\mathbf{u}}_m(t)^T.
\end{aligned} \tag{3.79}$$

The two volume terms are the transpose of each other, thus they cancel out and the resultant stability claim is the same as Eq. (3.63) in Sec. 3.6.3. \square

References

- [1] H. T. Huynh. “A flux reconstruction approach to high-order schemes including discontinuous Galerkin methods”. In: American Institute of Aeronautics and Astronautics, 2007.
- [2] Zhi Jian Wang and Haiyang Gao. “A unifying lifting collocation penalty formulation including the discontinuous Galerkin, spectral volume/difference methods for conservation laws on mixed grids”. In: *Journal of Computational Physics* 228.21 (2009), pp. 8161–8186.
- [3] HT Huynh, Zhi J Wang, and Peter E Vincent. “High-order methods for computational fluid dynamics: A brief review of compact differential formulations on unstructured grids”. In: *Computers & fluids* 98 (2014), pp. 209–220.

- [4] Meilin Yu and Zhi Jian Wang. “On the connection between the correction and weighting functions in the correction procedure via reconstruction method”. In: *Journal of Scientific Computing* 54.1 (2013), pp. 227–244.
- [5] Peter E Vincent, Patrice Castonguay, and Antony Jameson. “Insights from von Neumann analysis of high-order flux reconstruction schemes”. In: *Journal of Computational Physics* 230.22 (2011), pp. 8134–8154.
- [6] D. M. Williams and A. Jameson. “Energy stable flux reconstruction schemes for advection–diffusion problems on tetrahedra”. In: *Journal of Scientific Computing* 59.3 (2014), pp. 721–759.
- [7] Peter E Vincent, Antony M Farrington, Freddie D Witherden, and Antony Jameson. “An extended range of stable-symmetric-conservative flux reconstruction correction functions”. In: *Computer Methods in Applied Mechanics and Engineering* 296 (2015), pp. 248–272.
- [8] Patrice Castonguay. “High-order energy stable flux reconstruction schemes for fluid flow simulations on unstructured grids”. In: *Diss. Stanford University* (2012).
- [9] Patrice Castonguay, Peter E Vincent, and Antony Jameson. “A new class of high-order energy stable flux reconstruction schemes for triangular elements”. In: *Journal of Scientific Computing* 51.1 (2012), pp. 224–256.
- [10] David C Del Rey Fernández, Jason E Hicken, and David W Zingg. “Review of summation-by-parts operators with simultaneous approximation terms for the numerical solution of partial differential equations”. In: *Computers & Fluids* 95 (2014), pp. 171–196.
- [11] Magnus Svärd and Jan Nordström. “Review of summation-by-parts schemes for initial–boundary-value problems”. In: *Journal of Computational Physics* 268 (2014), pp. 17–38.

- [12] David C Del Rey Fernández, Pieter D Boom, and David W Zingg. “A generalized framework for nodal first derivative summation-by-parts operators”. In: *Journal of Computational Physics* 266 (2014), pp. 214–239.
- [13] Mark H Carpenter, David Gottlieb, and Saul Abarbanel. “Time-stable boundary conditions for finite-difference schemes solving hyperbolic systems: Methodology and application to high-order compact schemes”. In: *Journal of Computational Physics* 111.2 (1994), pp. 220–236.
- [14] Mark H Carpenter, Jan Nordström, and David Gottlieb. “A stable and conservative interface treatment of arbitrary spatial accuracy”. In: *Journal of Computational Physics* 148.2 (1999), pp. 341–365.
- [15] Jan Nordström and Mark H Carpenter. “Boundary and interface conditions for high-order finite-difference methods applied to the Euler and Navier–Stokes equations”. In: *Journal of Computational Physics* 148.2 (1999), pp. 621–645.
- [16] Jan Nordström and Mark H Carpenter. “High-order finite difference methods, multidimensional linear problems, and curvilinear coordinates”. In: *Journal of Computational Physics* 173.1 (2001), pp. 149–174.
- [17] Mark H Carpenter, Jan Nordström, and David Gottlieb. “Revisiting and extending interface penalties for multi-domain summation-by-parts operators”. In: *Journal of Scientific Computing* 45.1-3 (2010), pp. 118–150.
- [18] Magnus Svärd and Hatice Özcan. “Entropy-stable schemes for the Euler equations with far-field and wall boundary conditions”. In: *Journal of Scientific Computing* 58.1 (2014), pp. 61–89.
- [19] Matteo Parsani, Mark H Carpenter, and Eric J Nielsen. “Entropy stable discontinuous interfaces coupling for the three-dimensional compressible Navier-Stokes equations.” In: *J. Comput. Phys.* 290.1 (2015), pp. 132–138.

- [20] Matteo Parsani, Mark H Carpenter, and Eric J Nielsen. “Entropy stable wall boundary conditions for the three-dimensional compressible Navier–Stokes equations”. In: *Journal of Computational Physics* 292 (2015), pp. 88–113.
- [21] Hendrik Ranocha, Philipp Öffner, and Thomas Sonar. “Summation-by-parts operators for correction procedure via reconstruction”. In: *Journal of Computational Physics* 311 (2016), pp. 299–328.
- [22] Hendrik Ranocha, Philipp Öffner, and Thomas Sonar. “Extended skew-symmetric form for summation-by-parts operators and varying Jacobians”. In: *Journal of Computational Physics* 342 (2017), pp. 13–28.
- [23] Tristan Montoya and David W Zingg. “A unifying algebraic framework for discontinuous Galerkin and flux reconstruction methods based on the summation-by-parts property”. In: *Journal of Scientific Computing* 92.3 (2022), p. 87.
- [24] Rémi Abgrall, Philipp Öffner, and Hendrik Ranocha. “Reinterpretation and extension of entropy correction terms for residual distribution and discontinuous Galerkin schemes: Application to structure preserving discretization”. In: *Journal of Computational Physics* 453 (2022), p. 110955.
- [25] Rémi Abgrall. “A general framework to construct schemes satisfying additional conservation relations. Application to entropy conservative and entropy dissipative schemes”. In: *Journal of Computational Physics* 372 (2018), pp. 640–666.
- [26] Rémi Abgrall, Elise le Meledo, and Phiipp Öffner. “On the connection between residual distribution schemes and flux reconstruction”. In: *arXiv preprint arXiv:1807.01261* (2018).
- [27] Rémi Abgrall, Jan Nordström, Philipp Öffner, and Svetlana Tokareva. “Analysis of the SBP-SAT stabilization for finite element methods part II: Entropy stability”. In: *Communications on Applied Mathematics and Computation* (2021), pp. 1–23.

- [28] Travis Calob Fisher. “High-order L2 stable multi-domain finite difference method for compressible flows”. PhD thesis. Purdue University, 2012.
- [29] Travis C Fisher, Mark H Carpenter, Jan Nordström, Nail K Yamaleev, and Charles Swanson. “Discretely conservative finite-difference formulations for nonlinear conservation laws in split form: Theory and boundary conditions”. In: *Journal of Computational Physics* 234 (2013), pp. 353–375.
- [30] Travis C Fisher and Mark H Carpenter. “High-order entropy stable finite difference schemes for nonlinear conservation laws: Finite domains”. In: *Journal of Computational Physics* 252 (2013), pp. 518–557.
- [31] Mark H Carpenter, Travis C Fisher, Eric J Nielsen, and Steven H Frankel. “Entropy stable spectral collocation schemes for the Navier–Stokes equations: Discontinuous interfaces”. In: *SIAM Journal on Scientific Computing* 36.5 (2014), B835–B867.
- [32] Matteo Parsani, Mark H Carpenter, Travis C Fisher, and Eric J Nielsen. “Entropy stable staggered grid discontinuous spectral collocation methods of any order for the compressible Navier–Stokes equations”. In: *SIAM Journal on Scientific Computing* 38.5 (2016), A3129–A3162.
- [33] Mark H Carpenter, Matteo Parsani, Eric J Nielsen, and Travis C Fisher. “Towards an entropy stable spectral element framework for computational fluid dynamics”. In: *54th AIAA Aerospace Sciences Meeting*. 2016, p. 1058.
- [34] Nail K Yamaleev and Mark H Carpenter. “A family of fourth-order entropy stable nonoscillatory spectral collocation schemes for the 1-D Navier–Stokes equations”. In: *Journal of Computational Physics* 331 (2017), pp. 90–107.
- [35] Jared Crean, Jason E Hicken, David C Del Rey Fernández, David W Zingg, and Mark H Carpenter. “Entropy-stable summation-by-parts discretization of the Euler equations on general curved elements”. In: *Journal of Computational Physics* 356 (2018), pp. 410–438.

- [36] Tianheng Chen and Chi-Wang Shu. “Entropy stable high order discontinuous Galerkin methods with suitable quadrature rules for hyperbolic conservation laws”. In: *Journal of Computational Physics* 345 (2017), pp. 427–461.
- [37] David C Del Rey Fernández, Jared Crean, Mark H. Carpenter, and Jason E. Hicken. “Staggered-grid entropy-stable multidimensional summation-by-parts discretizations on curvilinear coordinates”. In: *Journal of Computational Physics* 392 (2019), pp. 161–186.
- [38] Jesse Chan. “On discretely entropy conservative and entropy stable discontinuous Galerkin methods”. In: *Journal of Computational Physics* 362 (2018), pp. 346–374.
- [39] Lucas Friedrich, Gero Schnücke, Andrew R Winters, David C Del Rey Fernández, Gregor J Gassner, and Mark H Carpenter. “Entropy stable space–time discontinuous Galerkin schemes with summation-by-parts property for hyperbolic conservation laws”. In: *Journal of Scientific Computing* 80.1 (2019), pp. 175–222.
- [40] Magnus Svärd. “On coordinate transformations for summation-by-parts operators”. In: *Journal of Scientific Computing* 20.1 (2004), pp. 29–42.
- [41] David C Del Rey Fernández, Pieter D Boom, Mark H Carpenter, and David W Zingg. “Extension of tensor-product generalized and dense-norm summation-by-parts operators to curvilinear coordinates”. In: *Journal of Scientific Computing* 80.3 (2019), pp. 1957–1996.
- [42] Oskar Ålund and Jan Nordström. “Encapsulated high order difference operators on curvilinear non-conforming grids”. In: *Journal of Computational Physics* 385 (2019), pp. 209–224.
- [43] Niklas Wintermeyer, Andrew R Winters, Gregor J Gassner, and David A Kopriva. “An entropy stable nodal discontinuous Galerkin method for the two dimensional shallow water equations on unstructured curvilinear meshes with discontinuous bathymetry”. In: *Journal of Computational Physics* 340 (2017), pp. 200–242.

- [44] David Moxey, Shankar P Sastry, and Robert M Kirby. “Interpolation error bounds for curvilinear finite elements and their implications on adaptive mesh refinement”. In: *Journal of Scientific Computing* 78.2 (2019), pp. 1045–1062.
- [45] Gianmarco Mengaldo, Daniele De Grazia, Peter E Vincent, and Spencer J Sherwin. “On the connections between discontinuous Galerkin and flux reconstruction schemes: Extension to curvilinear meshes”. In: *Journal of Scientific Computing* 67.3 (2016), pp. 1272–1292.
- [46] Jan S. Hesthaven and Tim Warburton. *Nodal discontinuous Galerkin methods algorithms, analysis and applications*. Springer, 2008.
- [47] George Karniadakis and Spencer Sherwin. *Spectral/hp element methods for computational fluid dynamics*. Oxford University Press, 2013.
- [48] Philip Zwanenburg and Siva Nadarajah. “Equivalence between the energy stable flux reconstruction and filtered discontinuous Galerkin schemes”. In: *Journal of Computational Physics* 306 (2016), pp. 343–369.
- [49] ML Yu, Z J Wang, and Hui Hu. “A high-order spectral difference method for unstructured dynamic grids”. In: *Computers & Fluids* 48.1 (2011), pp. 84–97.
- [50] T. Haga, H. Gao, and Z. J. Wang. “A high-order unifying discontinuous formulation for the Navier-Stokes equations on 3D mixed grids”. In: *Mathematical Modelling of Natural Phenomena* 6.3 (2011), pp. 28–56.
- [51] Meilin Yu, Zhi Jian Wang, and Yen Liu. “On the accuracy and efficiency of discontinuous Galerkin, spectral difference and correction procedure via reconstruction methods”. In: *Journal of Computational Physics* 259 (2014), pp. 70–95.
- [52] Jesse Chan and Lucas C Wilcox. “On discretely entropy stable weight-adjusted discontinuous Galerkin methods: Curvilinear meshes”. In: *Journal of Computational Physics* 378 (2019), pp. 366–393.

- [53] Saul A Teukolsky. “Formulation of discontinuous Galerkin methods for relativistic astrophysics”. In: *Journal of Computational Physics* 312 (2016), pp. 333–356.
- [54] Peter E Vincent, Patrice Castonguay, and Antony Jameson. “A new class of high-order energy stable flux reconstruction schemes”. In: *Journal of Scientific Computing* 47.1 (2011), pp. 50–72.
- [55] Patrice Castonguay, Peter E Vincent, and Antony Jameson. “A new class of high-order energy stable flux reconstruction schemes for triangular elements”. In: *Journal of Scientific Computing* 51.1 (2012), pp. 224–256.
- [56] Alexander Cicchino and Siva Nadarajah. “A new norm and stability condition for tensor product flux reconstruction schemes”. In: *Journal of Computational Physics* (2020), p. 110025.
- [57] Yoshiaki Abe, Issei Morinaka, Takanori Haga, Taku Nonomura, Hisaichi Shibata, and Koji Miyaji. “Stable, non-dissipative, and conservative flux-reconstruction schemes in split forms”. In: *Journal of Computational Physics* 353 (2018), pp. 193–227.
- [58] D De Grazia, G Mengaldo, D Moxey, PE Vincent, and SJ Sherwin. “Connections between the discontinuous Galerkin method and high-order flux reconstruction schemes”. In: *International journal for numerical methods in fluids* 75.12 (2014), pp. 860–877.
- [59] Gregor J Gassner, Andrew R Winters, and David A Kopriva. “Split form nodal discontinuous Galerkin schemes with summation-by-parts property for the compressible Euler equations”. In: *Journal of Computational Physics* 327 (2016), pp. 39–66.
- [60] Alexander Cicchino, Siva Nadarajah, and David C. Del Rey Fernández. “Nonlinearly stable flux reconstruction high-order methods in split form”. In: *Journal of Computational Physics* (2022), p. 111094.
- [61] Antony Jameson, Peter E Vincent, and Patrice Castonguay. “On the non-linear stability of flux reconstruction schemes”. In: *Journal of Scientific Computing* 50.2 (2012), pp. 434–445.

- [62] Patrice Castonguay, David M Williams, Peter E. Vincent, and Antony Jameson. “Energy stable flux reconstruction schemes for advection–diffusion problems”. In: *Computer Methods in Applied Mechanics and Engineering* 267 (2013), pp. 400–417.
- [63] Abhishek Sheshadri and Antony Jameson. “On the stability of the flux reconstruction schemes on quadrilateral elements for the linear advection equation”. In: *Journal of Scientific Computing* 67.2 (2016), pp. 769–790.
- [64] Yves Allaneau and Antony Jameson. “Connections between the filtered discontinuous Galerkin method and the flux reconstruction approach to high order discretizations”. In: *Computer Methods in Applied Mechanics and Engineering* 200.49–52 (2011), pp. 3628–3636.
- [65] Gregor J Gassner, Andrew R Winters, Florian J Hindenlang, and David A Kopriva. “The BR1 scheme is stable for the compressible Navier–Stokes equations”. In: *Journal of Scientific Computing* 77.1 (2018), pp. 154–200.
- [66] Juan Manzanero, Gonzalo Rubio, David A Kopriva, Esteban Ferrer, and Eusebio Valero. “Entropy–stable discontinuous Galerkin approximation with summation–by–parts property for the incompressible Navier–Stokes/Cahn–Hilliard system”. In: *Journal of Computational Physics* 408 (2020), p. 109363.
- [67] David A Kopriva. “Metric identities and the discontinuous spectral element method on curvilinear meshes”. In: *Journal of Scientific Computing* 26.3 (2006), p. 301.
- [68] Patrick D Thomas and Charles K Lombard. “Geometric conservation law and its application to flow computations on moving grids”. In: *AIAA journal* 17.10 (1979), pp. 1030–1037.
- [69] Marcel Vinokur and HC Yee. “Extension of efficient low dissipation high order schemes for 3-D curvilinear moving grids”. In: *Frontiers of Computational Fluid Dynamics 2002*. World Scientific, 2002, pp. 129–164.

- [70] David A Kopriva, Florian J Hindenlang, Thomas Bolemann, and Gregor J Gassner. “Free-Stream Preservation for Curved Geometrically Non-conforming Discontinuous Galerkin Spectral Elements”. In: *Journal of Scientific Computing* 79.3 (2019), pp. 1389–1408.
- [71] Lorenzo Botti. “Influence of reference-to-physical frame mappings on approximation properties of discontinuous piecewise polynomial spaces”. In: *Journal of Scientific Computing* 52.3 (2012), pp. 675–703.
- [72] David C Del Rey Fernández, Mark H Carpenter, Lisandro Dalcin, Stefano Zampini, and Matteo Parsani. “Entropy stable h/p-nonconforming discretization with the summation-by-parts property for the compressible Euler and Navier–Stokes equations”. In: *SN Partial Differential Equations and Applications* 1.2 (2020), pp. 1–54.
- [73] Antony Jameson. “A proof of the stability of the spectral difference method for all orders of accuracy”. In: *Journal of Scientific Computing* 45.1-3 (2010), pp. 348–358.
- [74] H. T. Huynh. “A reconstruction approach to high-order schemes including discontinuous Galerkin for diffusion”. In: American Institute of Aeronautics and Astronautics, 2009.
- [75] FD Witherden, PE Vincent, and A Jameson. “High-order flux reconstruction schemes”. In: *Handbook of numerical analysis*. Vol. 17. Elsevier, 2016, pp. 227–263.
- [76] Jesse Chan. “Skew-symmetric entropy stable modal discontinuous Galerkin formulations”. In: *Journal of Scientific Computing* 81.1 (2019), pp. 459–485.
- [77] Freddie D Witherden, Antony M Farrington, and Peter E Vincent. “PyFR: An open source framework for solving advection–diffusion type problems on streaming architectures using the flux reconstruction approach”. In: *Computer Physics Communications* 185.11 (2014), pp. 3028–3040.
- [78] Freddie D Witherden and Peter E Vincent. “An analysis of solution point coordinates for flux reconstruction schemes on triangular elements”. In: *Journal of Scientific Computing* 61.2 (2014), pp. 398–423.

- [79] Yoshiaki Abe, Takanori Haga, Taku Nonomura, and Kozo Fujii. “On the freestream preservation of high-order conservative flux-reconstruction schemes”. In: *Journal of Computational Physics* 281 (2015), pp. 28–54.
- [80] Amaury Johnen, J-F Remacle, and Christophe Geuzaine. “Geometrical validity of curvilinear finite elements”. In: *Journal of Computational Physics* 233 (2013), pp. 359–372.
- [81] Michael Turner, Joaquim Peiró, and David Moxey. “Curvilinear mesh generation using a variational framework”. In: *Computer-Aided Design* 103 (2018), pp. 73–91.
- [82] Doug Shi-Dong and Siva Nadarajah. “Full-Space Approach to Aerodynamic Shape Optimization”. In: *Computers & Fluids* (2021), p. 104843.
- [83] Xinhui Wu, Ethan J Kubatko, and Jesse Chan. “High-order entropy stable discontinuous Galerkin methods for the shallow water equations: Curved triangular meshes and GPU acceleration”. In: *Computers & Mathematics with Applications* 82 (2021), pp. 179–199.
- [84] Sebastian Hennemann, Andrés M Rueda-Ramírez, Florian J Hindenlang, and Gregor J Gassner. “A provably entropy stable subcell shock capturing approach for high order split form DG for the compressible Euler equations”. In: *Journal of Computational Physics* 426 (2021), p. 109935.

Chapter 4

Scalable Evaluations

With the intent of the high-order solver being used on next-generation hardware, on both CPUs and GPUs, we wish that the solver scales at the lowest order possible, and has a low memory footprint. An approach to reduce the computational cost for matrix-vector products, with tensor product basis functions, is sum-factorization [1]. The NSFR scheme was developed with tensor product elements and basis from the beginning to capitalize on sum-factorization. With the extension of the NSFR discretization to the Euler equations, we will have to introduce a dense Hadamard product like Chan [2]. Thus, the focus of this chapter is the derivation of a novel sum-factorized Hadamard product, which allows our entropy stable NSFR discretization to scale at $\mathcal{O}(n^{d+1})$, where $n = p + 1$ and d is the dimension of the problem.

Scalable Evaluation of Hadamard Products with Tensor Product Basis for Entropy-Stable High-Order Methods

Alexander Cicchino and Siva Nadarajah

From: Cicchino, Alexander, and Siva Nadarajah. “Scalable Evaluation of Hadamard Products with Tensor Product Basis for Entropy-Stable High-Order Methods.” Accepted with Minor Modifications to the Journal of Computational Physics (2023).

Contribution of authors: Alexander Cicchino: Conceptualization, Formal analysis, Methodology, Software, Validation, Writing – original draft, Writing – review & editing. Siva Nadarajah: Conceptualization, Formal analysis, Methodology, Software, Supervision, Validation, Writing – original draft, Writing – review & editing.

4.1 Introduction

Sum-Factorization techniques were introduced by Orszag [1] to efficiently evaluate spectral methods. Orszag [1] made use of the tensor product nature of the basis functions to perform the operations in each direction independently, and result in $\mathcal{O}(n^{d+1})$ flops for interpolation, projection and differentiation operations, where n is the size of the one-dimensional basis, for example the polynomial degree. Unfortunately, a tensor product algorithm resulting in $\mathcal{O}(n^{d+1})$ flops for Hadamard products does not yet exist in the literature. The aim of this technical note is to demonstrate that Hadamard products can be computed in $\mathcal{O}(n^{d+1})$ flops with a tensor product basis, provided the basis functions have one additional property that is common in the spectral and finite element communities.

Entropy stable numerical schemes, initially proposed by Tadmor [3] for finite-volume methods, guarantee robustness on extremely coarse meshes. Through the application of summation-by-parts (SBP) operators, and introducing flux differencing techniques, Fisher *et al.* [4, 5] made the concepts from Tadmor applicable in a finite-element framework. This led to the development of provably nonlinearly stable high-order methods in a collocated split-form discontinuous Galerkin (DG) form [6, 7], collocated split-form flux reconstruction (FR) framework recovering the DG case [8–10], modal uncollocated entropy stable DG framework [2, 11–13], and modal uncollocated nonlinearly stable FR (NSFR) schemes [14, 15].

In the application of flux differencing [4, Eq. (3.9)], Ranocha *et al.* [16] numerically demonstrated that $\mathcal{O}(n^{d+1})$ flops could be recovered. For modal uncollocated schemes, the general expression requires the computation of a dense Hadamard product, as seen in Chan [2, Eq. (58)]. The focus of this short note is on efficiently evaluating a Hadamard product using a tensor product basis. Specifically, using the tensor product structure, we demonstrate that a Hadamard product can be assembled and evaluated in $\mathcal{O}(n^{d+1})$ flops and memory allocation, rather than $\mathcal{O}(n^{2d})$, where d is the dimension. We term the algorithm a “sum-factorized” Hadamard product because we recover the scaling result of sum-factorization techniques [1] by

exploiting the tensor product structure in the Hadamard product. This result is dependent on the basis operators being diagonal operators in at least $d - 1$ directions—fortunately, this is always the case for Hadamard products involving interpolation, projection, and differentiation operators of polynomial basis functions. This is the case because we can use sum-factorization techniques to project onto a collocated Lagrange basis, evaluate the Hadamard product using our proposed algorithm, and then project back onto the dense basis. In Section 4.3, we provide numerical results showing that the Hadamard product scales at $\mathcal{O}(n^{d+1})$.

4.2 Hadamard Product

Consider solving $(\mathbf{A} \otimes \mathbf{B}) \circ \mathbf{C}$, with $\mathbf{A}, \mathbf{B} \in \mathbb{R}^{n \times n}$ and $\mathbf{C} \in \mathbb{R}^{n^2 \times n^2}$.

$$(\mathbf{A} \otimes \mathbf{B}) \circ \mathbf{C} = \begin{bmatrix} A_{11} [\mathbf{B} \circ \mathbf{C}_{11}] & \dots & A_{1n} [\mathbf{B} \circ \mathbf{C}_{1n}] \\ \vdots & \vdots & \vdots \\ A_{n1} [\mathbf{B} \circ \mathbf{C}_{n1}] & \dots & A_{nn} [\mathbf{B} \circ \mathbf{C}_{nn}] \end{bmatrix}. \quad (4.1)$$

The computational cost associated with solving the Hadamard product in Eq. (4.1) is $\mathcal{O}(n^4)$. Unfortunately, unlike sum-factorization [1], it is not possible to reduce the computational cost of Eq. (4.1) by evaluating each direction independently. The Hadamard product in Eq. (4.1) requires evaluating the n^2 terms in the square brackets, then multiplying it by a scalar, and repeating the operations n^{2d-2} times.

If we add an additional condition, $\mathbf{A} = \text{diag}(\mathbf{a})$, $\mathbf{a} \in \mathbb{R}^{n \times 1}$, then

$$(\mathbf{A} \otimes \mathbf{B}) \circ \mathbf{C} = \begin{bmatrix} a_1 [\mathbf{B} \circ \mathbf{C}_{11}] & & 0 \\ & \ddots & \\ 0 & & a_n [\mathbf{B} \circ \mathbf{C}_{nn}] \end{bmatrix} = \text{diag} \left(\begin{matrix} a_1 [\mathbf{B} \circ \mathbf{C}_{11}] \\ \vdots \\ a_n [\mathbf{B} \circ \mathbf{C}_{nn}] \end{matrix} \right)_{n^2 \times n}. \quad (4.2)$$

The computational cost to evaluate Eq. (4.2) is $\mathcal{O}(n^3)$. Similarly, if $\mathbf{B} = \text{diag}(\mathbf{b})$ with \mathbf{A} dense, then $(\mathbf{A} \otimes \mathbf{B}) \circ \mathbf{C}$ costs $\mathcal{O}(n^3)$ to evaluate by changing the stride through the matrix.

This can be generalized for an arbitrary d -sized tensor product, $(\mathbf{A}_1 \otimes \mathbf{A}_2 \otimes \cdots \otimes \mathbf{A}_d) \circ \mathbf{C}$, with

$\mathbf{A}_1, \dots, \mathbf{A}_d \in \mathbb{R}^{n \times n}$ and $\mathbf{C} \in \mathbb{R}^{n^d \times n^d}$. If $\mathbf{A}_i = \text{diag}(\mathbf{a}_i)$, $\mathbf{a} \in \mathbb{R}^{n \times 1}$, $\forall i = 1, \dots, d-1$, then,

$$(\mathbf{A}_1 \otimes \mathbf{A}_2 \otimes \cdots \otimes \mathbf{A}_d) \circ \mathbf{C} = \text{diag} \left(\begin{array}{c} (\mathbf{a}_1)_1 \cdots (\mathbf{a}_{d-1})_1 [\mathbf{A}_d \circ \mathbf{C}_{11}] \\ \vdots \\ (\mathbf{a}_1)_n \cdots (\mathbf{a}_{d-1})_n [\mathbf{A}_d \circ \mathbf{C}_{n^d n^d}] \end{array} \right)_{n^d \times n^d}, \quad (4.3)$$

and similarly for the other $d-1$ directions through pivoting. Thus, in each of these d -cases, the total computational cost is $dn^{d+1} = \mathcal{O}(n^{d+1})$, $\forall n \gg d$. In the square brackets, we perform n^2 flops, then perform $d-1$ scalar multiplications, and this is repeated for n^{d-1} rows. The memory footprint for Eq. (4.3) is comprised of storing and fetching two n^{d+1} -sized matrices, and writing n^{d+1} values.

In the context of high-order entropy stable methods, the Hadamard product can always be computed with the diagonal property above, regardless of the basis functions.

Theorem 4.2.1. *If the basis function is represented as a tensor product, then the Hadamard product involving some α -th order derivative of the basis function costs dn^{d+1} flops.*

Proof.

Consider solving,

$$\left(\frac{\partial^\alpha \boldsymbol{\chi}(\boldsymbol{\xi}_v^r)}{\partial \xi_j^\alpha} \boldsymbol{\Pi} \right) \circ \mathbf{C}, \quad (4.4)$$

where $\boldsymbol{\chi}$ is some linearly independent, polynomial basis, $\boldsymbol{\xi}_v^r$ are a set of nodes that the basis are evaluated on in computational space, ξ_j is a direction that the α -th order derivative is applied in, and $\boldsymbol{\Pi}$ is the projection operator corresponding to the basis $\boldsymbol{\chi}$ such that $\boldsymbol{\Pi}\boldsymbol{\chi}(\boldsymbol{\xi}_v^r) = \mathbf{I}$. Using Zwanenburg and Nadarajah [17, Proposition 2.1 and Corollary 2.2], we can always make the substitution $\frac{\partial^\alpha \boldsymbol{\ell}(\boldsymbol{\xi}_v^r)}{\partial \xi_j^\alpha} = \frac{\partial^\alpha \boldsymbol{\chi}(\boldsymbol{\xi}_v^r)}{\partial \xi_j^\alpha} \boldsymbol{\Pi}$ where $\boldsymbol{\ell}$ is the Lagrange basis collocated on the nodes $\boldsymbol{\xi}_v^r$ —that is $\boldsymbol{\ell}(\boldsymbol{\xi}_v^r) = \mathbf{I}$. If we let $\boldsymbol{\ell}$ be a tensor product basis, then $\frac{\partial^\alpha \boldsymbol{\ell}(\boldsymbol{\xi}_v^r)}{\partial \xi_j^\alpha} = \mathbf{I}(\xi_{i < j}) \otimes \frac{d^\alpha \boldsymbol{\ell}(\xi_j)}{d \xi_j^\alpha} \otimes \mathbf{I}(\xi_{i > j})$. Therefore, $\frac{\partial^\alpha \boldsymbol{\ell}(\boldsymbol{\xi}_v^r)}{\partial \xi_j^\alpha} \circ \mathbf{C}$ recovers the form of Eq. (4.3), where $\mathbf{A}_i = \mathbf{I} \forall i = 1, \dots, d, i \neq j$.

Similarly, if we have some weight function that is a non-identity diagonal matrix multiplied to the derivative, then we have,

$$\mathbf{W}(\boldsymbol{\xi}_v^r) \left(\frac{\partial \boldsymbol{\chi}(\boldsymbol{\xi}_v^r)}{\partial \xi_j^\alpha} \boldsymbol{\Pi} \right) = \mathbf{W}(\boldsymbol{\xi}_v^r) \frac{\partial^\alpha \boldsymbol{\ell}(\boldsymbol{\xi}_v^r)}{\partial \xi_j^\alpha} = \mathbf{W}(\xi_{i < j}) \otimes \mathbf{W}(\xi_j) \frac{d^\alpha \boldsymbol{\ell}(\xi_j)}{d \xi_j^\alpha} \otimes \mathbf{W}(\xi_{i > j}). \quad (4.5)$$

Eq. 4.5 is of the same form as Eq. 4.3, and thus its Hadamard product costs dn^{d+1} flops. \square

This theorem allows us to solve Hadamard products at $\mathcal{O}(n^{d+1})$ for general uncollocated modal schemes in curvilinear coordinates since Eq. (4.5) closely resembles the stiffness matrix that appears in finite element methods.

Remark 4.2.1. *The same algorithm can be used in evaluating the Hadamard product with the surface integral terms in Chan [2, Eq. (58)] by substituting $\alpha = 0$ and the facet cubature nodes in Eq. (4.4).*

We provide a sample algorithm for implementation in three-dimensions from our in-house PDE solver PHiLiP “Operators” class that performs the subroutines within the solver. A similar structure is done for the surface Hadamard products where the one-dimensional basis matrices are of size $m \times n$, $m < n$. Let’s assume we want to compute $(\mathbf{D} \otimes \mathbf{W} \otimes \mathbf{W}) \circ \mathbf{C}_x$, $(\mathbf{W} \otimes \mathbf{D} \otimes \mathbf{W}) \circ \mathbf{C}_y$, and $(\mathbf{W} \otimes \mathbf{W} \otimes \mathbf{D}) \circ \mathbf{C}_z$, where $\mathbf{W} = \text{diag}(\mathbf{w})$ stores some weights, and \mathbf{D} is dense. This mimics the Hadamard product to be computed on the quadrature nodes for entropy conserving schemes alike in Chan [2, Eq. (58)]. For the tensor product, we let the x -direction run fastest, then the y -direction and the z -direction run slowest. We will refer to the first term as the first direction, the second term as the second direction, and subsequently the third. We evaluate it in three steps. First, we create two vectors of size $\mathbb{R}^{n^{d+1} \times d}$ storing a sparsity pattern: one stores the non-zero row indices, and the other stores the non-zero column indices for each of the d -directions. From these, we then build an $n^d \times n$ -sized matrix storing only the non-zero entries of the general $n^d \times n^d$ -sized matrix for each of the d -directions. Lastly, after the matrices of size $\mathbb{R}^{n^d \times n}$ for each direction are built, we evaluate the Hadamard product directly.

We generate the sparsity patterns by the algorithm 1, then, using the sparsity patterns, we store only the non-zero entries of the matrices $D \otimes W \otimes W$, $W \otimes D \otimes W$, and $W \otimes W \otimes D$ by algorithm 2:

Algorithm 1 Sparsity Pattern Algorithm

```

1: Result: Create rows and columns vectors of size  $n^{d+1} \times d$  storing the sparsity pattern of
   all indices that correspond to non-zero values in the dense matrices.
2: for  $i, j, k, l = 0; i, j, k, l < n; i, j, k, l++$  do ▷ Loop over the  $n^{d+1}$  indices.
3:   Let array_index be the ordering of the  $n^{d+1}$  indices.
4:   array_index  $\leftarrow i * n^3 + j * n^2 + k * n + l$ 
5:   Let row_index correspond to the row index of the non-zero value in the dense matrix.
6:   row_index  $\leftarrow i * n^2 + j * n + k$ 
7:   rows[array_index][0,1,2]  $\leftarrow$  row_index
8:   Let column_index correspond to the column index of the non-zero value in the dense
   matrix.
9:   column_index_x  $\leftarrow i * n^2 + j * n + l$  ▷ Index in x-direction
10:  columns[array_index][0]  $\leftarrow$  column_index_x
11:  column_index_y  $\leftarrow l * n + k + i * n^2$  ▷ Index in y-direction
12:  columns[array_index][1]  $\leftarrow$  column_index_y
13:  column_index_z  $\leftarrow l * n^2 + k + j * n$  ▷ Index in z-direction
14:  columns[array_index][2]  $\leftarrow$  column_index_z
15: end for

```

Algorithm 2 Basis Assembly Algorithm

```
1: Result: Store only the non-zero entries of the tensor product basis in Basis_Sparse of
   size  $d \times (n^d \times n)$ .
2: for index=0, counter=0; index <  $n^{d+1}$ ; index++, counter++ do    ▷ Loop over the  $n^{d+1}$ 
   indices.
3:   if counter == n then counter ← 0
4:   end if
5:   Extract the row and column indices of the one-dimensional basis for the given direction.
6:   x_row_index ← rows[index][0] % n    ▷ We use integer division and % as the mod
   operator.
7:   x_column_index ← columns[index][0] % n
8:   y_row_index ← (rows[index][1] / n) % n
9:   y_column_index ← (columns[index][1] / n) % n
10:  z_row_index ← rows[index][2] / n / n
11:  z_column_index ← columns[index][2] / n / n
12:  Create the matrix storing only  $n^{d+1}$  non-zero values.
13:  Basis_Sparse[0][rows[index][0]][counter] ← basis[x_row_index][x_column_index] *
   weights[y_row_index] * weights[z_row_index];    ▷ x-direction,  $\mathbf{D} \otimes \mathbf{W} \otimes \mathbf{W}$ .
14:  Basis_Sparse[1][rows[index][1]][counter] ← basis[y_row_index][y_column_index] *
   weights[x_row_index] * weights[z_row_index];    ▷ y-direction,  $\mathbf{W} \otimes \mathbf{D} \otimes \mathbf{W}$ .
15:  Basis_Sparse[2][rows[index][2]][counter] ← basis[z_row_index][z_column_index] *
   weights[x_row_index] * weights[y_row_index];    ▷ z-direction,  $\mathbf{W} \otimes \mathbf{W} \otimes \mathbf{D}$ .
16: end for
```

where “basis” refers to \mathbf{D} in the given direction, “weights” refers to \mathbf{W} , and “Basis_Sparse” refers to their tensor product storing only the n^{d+1} non-zero values. We can similarly construct \mathbf{C}_x , \mathbf{C}_y and \mathbf{C}_z using the sparsity patterns. The third step of evaluating the Hadamard product doesn’t require the sparsity patterns since it is the Hadamard product of $\mathbb{R}^{n^d \times n}$ dense

matrices and is computed directly.

4.3 Results

For numerical verification, we use the open-source Parallel High-order Library for PDEs (PHiLiP, <https://github.com/dougshidong/PHiLiP.git>) [18], developed at the Computational Aerodynamics Group at McGill University. The test is compiled in C++ with gcc 9.4.0, and executed on a single Intel i5-8600 CPU with a maximum of 1GB of DDR4 RAM. We consider three-dimensions and verify the scaling of our proposed Thm 4.2.1. We let $(\mathbf{C})_{ij} = c_i c_j$, $\mathbf{C} \in \mathbb{R}^{n^d \times n^d}$, with $\mathbf{c} = \text{rand}([1e^{-8}, 30])$. We compare the cost of evaluating the three-dimensional Hadamard product $\sum_{j=1}^3 \frac{\partial \ell(\boldsymbol{\xi}_v^r)}{\partial \xi_j} \circ \mathbf{C}$ by: directly building the three-dimensional tensor product basis and applying the Hadamard product, versus using our proposed algorithm in Thm 4.2.1. The test loops through polynomial degrees $n \in [3, 19]$, and for each polynomial degree, we perform the operations 100 times.

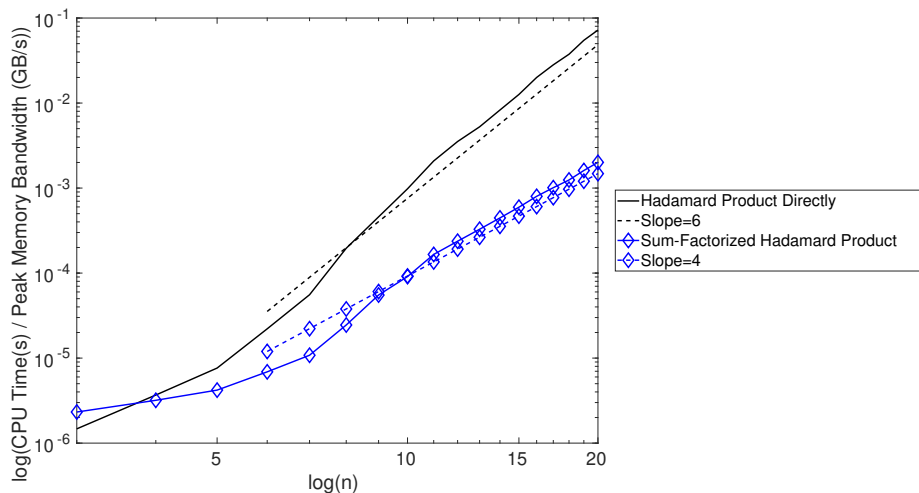


Figure 4.1: CPU time versus polynomial degree

We store the CPU time by running the test on one processor and we record the clock time before the algorithm then subtract the clock time after computing $\sum_{j=1}^3 \frac{\partial \ell(\boldsymbol{\xi}_v^r)}{\partial \xi_j} \circ \mathbf{C}$. We normalized the CPU time by the peak memory bandwidth of 347.23 GB/s. In Fig. 4.1, the conventional way of computing a Hadamard product in all three directions costs $\mathcal{O}(n^{2d})$,

whereas our proposed “sum-factorized” form that exploits the tensor product structure costs $\mathcal{O}(n^{d+1})$.

4.4 Conclusion

We derived and demonstrated a “sum-factorized” technique to build and compute Hadamard products at $\mathcal{O}(n^{d+1})$. With the fast evaluations, the computational cost of entropy conserving and stable schemes becomes computationally competitive with the classical conservative modal discontinuous Galerkin method in general three-dimensional curvilinear coordinates.

4.5 Acknowledgements

We gratefully acknowledge the financial support of the Natural Sciences and Engineering Research Council of Canada (NSERC) Discovery Grant Program, NSERC Postgraduate Scholarships – Doctoral program, and McGill University.

References

- [1] Steven A Orszag. “Spectral methods for problems in complex geometrics”. In: *Numerical methods for partial differential equations*. Elsevier, 1979, pp. 273–305.
- [2] Jesse Chan. “On discretely entropy conservative and entropy stable discontinuous Galerkin methods”. In: *Journal of Computational Physics* 362 (2018), pp. 346–374.
- [3] Eitan Tadmor. “Skew-self adjoint form for systems of conservation laws”. In: *Journal of Mathematical Analysis and Applications* 103.2 (1984), pp. 428–442.
- [4] Travis C Fisher and Mark H Carpenter. “High-order entropy stable finite difference schemes for nonlinear conservation laws: Finite domains”. In: *Journal of Computational Physics* 252 (2013), pp. 518–557.

- [5] Travis C Fisher, Mark H Carpenter, Jan Nordström, Nail K Yamaleev, and Charles Swanson. “Discretely conservative finite-difference formulations for nonlinear conservation laws in split form: Theory and boundary conditions”. In: *Journal of Computational Physics* 234 (2013), pp. 353–375.
- [6] Gregor J Gassner. “A skew-symmetric discontinuous Galerkin spectral element discretization and its relation to SBP-SAT finite difference methods”. In: *SIAM Journal on Scientific Computing* 35.3 (2013), A1233–A1253.
- [7] Gregor J Gassner, Andrew R Winters, and David A Kopriva. “Split form nodal discontinuous Galerkin schemes with summation-by-parts property for the compressible Euler equations”. In: *Journal of Computational Physics* 327 (2016), pp. 39–66.
- [8] Hendrik Ranocha, Philipp Öffner, and Thomas Sonar. “Summation-by-parts operators for correction procedure via reconstruction”. In: *Journal of Computational Physics* 311 (2016), pp. 299–328.
- [9] Hendrik Ranocha, Philipp Öffner, and Thomas Sonar. “Extended skew-symmetric form for summation-by-parts operators and varying Jacobians”. In: *Journal of Computational Physics* 342 (2017), pp. 13–28.
- [10] Yoshiaki Abe, Issei Morinaka, Takanori Haga, Taku Nonomura, Hisaichi Shibata, and Koji Miyaji. “Stable, non-dissipative, and conservative flux-reconstruction schemes in split forms”. In: *Journal of Computational Physics* 353 (2018), pp. 193–227.
- [11] Jesse Chan. “Skew-symmetric entropy stable modal discontinuous Galerkin formulations”. In: *Journal of Scientific Computing* 81.1 (2019), pp. 459–485.
- [12] Jesse Chan and Lucas C Wilcox. “On discretely entropy stable weight-adjusted discontinuous Galerkin methods: Curvilinear meshes”. In: *Journal of Computational Physics* 378 (2019), pp. 366–393.

- [13] Jesse Chan, David C Del Rey Fernández, and Mark H Carpenter. “Efficient entropy stable Gauss collocation methods”. In: *SIAM Journal on Scientific Computing* 41.5 (2019), A2938–A2966.
- [14] Alexander Cicchino, Siva Nadarajah, and David C. Del Rey Fernández. “Nonlinearly stable flux reconstruction high-order methods in split form”. In: *Journal of Computational Physics* (2022), p. 111094.
- [15] Alexander Cicchino, David C Del Rey Fernández, Siva Nadarajah, Jesse Chan, and Mark H Carpenter. “Provably stable flux reconstruction high-order methods on curvilinear elements”. In: *Journal of Computational Physics* 463 (2022), p. 111259.
- [16] Hendrik Ranocha, Michael Schlottke-Lakemper, Jesse Chan, Andrés M Rueda-Ramírez, Andrew R Winters, Florian Hindenlang, and Gregor J Gassner. “Efficient implementation of modern entropy stable and kinetic energy preserving discontinuous Galerkin methods for conservation laws”. In: *ACM Transactions on Mathematical Software* 49.4 (2023), pp. 1–30.
- [17] Philip Zwanenburg and Siva Nadarajah. “Equivalence between the energy stable flux reconstruction and filtered discontinuous Galerkin schemes”. In: *Journal of Computational Physics* 306 (2016), pp. 343–369.
- [18] Doug Shi-Dong and Siva Nadarajah. “Full-Space Approach to Aerodynamic Shape Optimization”. In: *Computers & Fluids* (2021), p. 104843.

Chapter 5

Systems of Nonlinear Conservation Laws in Curvilinear Coordinates

After successfully establishing a provable nonlinearly stable scheme, implemented within a scalable numerical architecture, we proceed to expand the framework to accommodate vector-valued functions. Similar to Chan [1, 2] we formulate the general system with volume-surface skew-symmetric operators, coupled with Tadmor’s two-point flux [3], to ensure nonlinear stability with flux differencing [4, 5]. Following the steps to achieve stability in Chapters 2 and 3, we achieve nonlinear stability for general FR schemes by incorporating the ESFR correction functions on all nonlinear terms in the discretization. From Chapter 3, we incorporate the metric split form within the two-point flux, through the transformation from physical to reference space. This form of the reference flux allows us to exploit the tensor product structure and use the sum-factorized Hadamard product in Chapter 4. In addition, this section introduces a weight-adjusted inverse approximation for the NSFR modified mass matrix, alike the DG form from Chan and Wilcox [6]. The weight-adjusted approximation allows the scheme to avoid the need to compute and invert a dense matrix, but rather invert a diagonal operator and use sum-factorization with one-dimensional pre-computed projection operators on-the-fly. This section proves free-stream preservation, global

conservation, and discrete nonlinear stability for the weight-adjusted NSFR discretization, for the Euler equations—with the properties numerically verified. The orders of convergence are verified with a manufactured solution on a nonsymmetrically warped curvilinear grid. Lastly, this section demonstrates a computational performance comparison between the proposed NSFR discretization as opposed to the conservative nodal DG scheme with and without overintegration. We find that all schemes scale at order $\mathcal{O}(n^{d+1})$, and the proposed general NSFR scheme is computationally competitive with the nodal DG scheme.

Discretely Nonlinearly Stable Weight-Adjusted Flux Reconstruction High-Order Method for Compressible Flows on Curvilinear Grids

Alexander Cicchino and Siva Nadarajah

From: Cicchino, Alexander, and Siva Nadarajah. “Discretely Nonlinearly Stable Weight-Adjusted Flux Reconstruction High-Order Method for Compressible Flows on Curvilinear Grids.” Accepted with Minor Modifications to the Journal of Computational Physics (2023).

Contribution of authors: Alexander Cicchino: Conceptualization, Formal analysis, Methodology, Software, Validation, Writing – original draft, Writing – review & editing. Siva Nadarajah: Conceptualization, Formal analysis, Methodology, Software, Supervision, Validation, Writing – original draft, Writing – review.

Abstract

To achieve genuine predictive capability, an algorithm must consistently deliver accurate results over prolonged temporal integration periods, avoiding the unwarranted growth of aliasing errors that compromise the discrete solution. Provable nonlinear stability bounds the discrete approximation and ensures that the discretization does not diverge. Nonlinear stability is accomplished by satisfying a secondary conservation law, namely for compressible flows; the second law of thermodynamics. For high-order methods, discrete nonlinear stability and entropy stability, have been successfully implemented for discontinuous Galerkin (DG) and residual distribution schemes, where the stability proofs depend on properties of L2-norms. In this paper, nonlinearly stable flux reconstruction (NSFR) schemes are developed for three-dimensional compressible flow in curvilinear coordinates. NSFR is derived by merging the energy stable flux reconstruction (ESFR) framework with entropy stable DG schemes. NSFR is demonstrated to use larger time-steps than DG due to the ESFR correction functions, at the cost of larger error levels at design order convergence for equivalent degrees of freedom, while preserving discrete nonlinear stability. NSFR differs from ESFR schemes in the literature since it incorporates the FR correction functions on the volume terms through the use of a modified mass matrix. We also prove that discrete kinetic energy stability cannot be preserved to machine precision for quadrature rules where the surface quadrature is not a subset of the volume quadrature. This result stems from the inverse mapping from the kinetic energy variables to the conservative variables not existing for the kinetic energy projected variables. This paper also presents the NSFR modified mass matrix in a weight-adjusted form. This form reduces the computational cost in curvilinear coordinates because the dense matrix inversion is approximated by a pre-computed projection operator and the inverse of a diagonal matrix on-the-fly and exploits the tensor product basis functions to utilize sum-factorization. The nonlinear stability properties of the scheme are verified on a nonsymmetric curvilinear grid for

the inviscid Taylor-Green vortex problem and the correct orders of convergence were obtained on a curvilinear mesh for a manufactured solution. Lastly, we perform a computational cost comparison between conservative DG, overintegrated DG, and our proposed entropy conserving NSFR scheme, and find that our proposed entropy conserving NSFR scheme is computationally competitive with the conservative DG scheme.

5.1 Introduction

High-order methods such as discontinuous Galerkin (DG) and flux reconstruction (FR), result in efficient computations via high solution accuracy and dense computational kernels, making them an attractive approach for the exascale concurrency on current and next generation hardware. Generally, high-order methods are known to be more efficient than low-order methods for linear hyperbolic time-dependent problems (e.g., see [7, 8]). However, despite vigorous efforts by the research community, their application to real world complex problems governed by nonlinear partial differential equations (PDEs) has been limited due to a lack of robustness.

The DG method, proposed by Reed and Hill [9], combines both the key properties of finite volume and finite element schemes. As explained in the book of Hesthaven and Warburton [10], the high-order scheme provides stability through a numerical flux function, and utilizes high-order shape functions to represent the solution. Another variation of the DG method is FR, initially proposed by H.T. Huynh [11] and later presented as a class of energy stable flux reconstruction (ESFR) schemes [12–14]. Through the introduction of correction functions, which is equivalently viewed as a filtered DG correction field [15–17], ESFR recovers various high-order schemes alike the spectral difference [18] and spectral volume.

There has been a concerted research effort to extend classical entropy stability arguments to high-order methods. The original work of Tadmor [19] laid a foundation enabling high-order extensions, where Tadmor [20] proved that if the numerical flux satisfies the entropy condition from Harten [21], then the discretization is entropy stable—this was accomplished by introducing a weak condition on the numerical flux commonly referred to as the *Tadmor shuffle condition*. These notions were extended by LeFloch [22, 23] in the context of high-order finite difference stencils. In the last decade, these ideas were expanded to bounded domains by Fisher and co-authors [4], who combined the Summation-by-parts (SBP) framework with Tadmor’s two-point flux functions to achieve entropy conservation. Extending the connection

made by Fisher *et al.* [4] between the SBP framework and Tadmor’s shuffle condition, entropy conservative and stable methods have been successfully implemented in DG [1, 2, 5, 24], FR [25, 26] for only the DG case, unstructured methods [27–29], extended high-order SBP forms [4, 28, 30–32], and residual distribution schemes [33–36].

Recent developments by Cicchino *et al.* [37, 38] proved that nonlinear stability for FR schemes can only be satisfied if the FR correction functions are applied to the nonlinear volume terms. This paper derives a general nonlinearly stable flux reconstruction (NSFR) framework for three-dimensional vector-valued problems in curvilinear coordinates. Specifically, we consider Euler’s equations in this work. The first main contribution follows the works by Chan [1, 2, 6] and Cicchino *et al.* [37, 38] to derive NSFR that is free-stream preserving, globally conservative, and entropy conserving for general modal basis functions evaluated on quadrature rules with at least $2p - 1$ strength, for any ESFR correction function. This is accomplished by formulating NSFR with the general modal skew-symmetric operators from Chan [2], then incorporating the ESFR correction functions on both the volume and surface hybrids terms through the modified mass matrix alike Cicchino and coauthors [37, 38]. Apart from entropy conservation, kinetic energy conservation is also sought. Unfortunately, the inverse mapping from the kinetic energy variables to the conservative variables does not exist. This consequence leads to our proof that discrete kinetic energy stability cannot be preserved to machine precision for quadrature rules where the surface quadrature is not a subset of the volume quadrature.

We first introduce the notation used in this paper in Sec. 5.2, where Sec. 5.2.1 presents entropy conservation and Sec. 5.2.2 presents notation pertaining to computational quantities. Then, in Sec. 5.3.1 we derive the DG scheme, followed by ESFR in Sec. 5.3.2, and lastly, we merge the concepts in Sec. 5.3.3. In Sec. 5.6 we prove that NSFR is free-stream preserving, globally conservative, and entropy conserving. In Sec. 5.6.3 we prove that kinetic energy cannot be discretely conserved if the surface quadrature is not a subset of the volume quadrature. In Sec. 5.7.3 we numerically verify all conserved quantities to machine precision for different FR

correction functions on a non-symmetrically warped curvilinear grid. Lastly, in Sec. 5.7.1, we verify the orders of convergence for a manufactured solution on a three-dimensional, nonsymmetrically warped curvilinear grid.

As shown in Cicchino *et al.* [38], for curvilinear coordinates, the scheme requires that a dense matrix is inverted for every element. Motivated by the work by Chan and Wilcox [6, 39], we present NSFR in a low-storage, weight-adjusted inverse form. This is achieved in Sec. 5.4 by introducing an ESFR projection operator, that projects onto the broken Sobolev-space, and deriving the weight-adjusted mass inverse through it. Then, we demonstrate that the operation can be further improved through sum-factorization techniques [40] by introducing an FR projection operator. In Sec. 5.7.1 we numerically verify that NSFR with a weight-adjusted mass inverse preserves the orders of convergence in curvilinear coordinates for a manufactured solution. Also, in Sec. 5.7.3, we numerically demonstrate that the weight-adjusted inverse preserves the stability properties for the weight-adjusted system. In Sec. 5.7.4, we compare a conservative nodal DG scheme, and overintegrated nodal DG scheme, and our proposed algorithm. We find that our proposed algorithm is computationally competitive with the nodal DG scheme, as compared to the overintegrated scheme. This result is dependent on the weight-adjusted mass matrix inversion, sum-factorization, and the novel sum-factorized Hadamard product evaluation from Cicchino and Nadarajah [41].

5.2 Preliminaries

In this section, we present the notation that is used throughout the paper. First, we review concepts on entropy conservation. Then, we introduce notation pertaining to the computational setup.

5.2.1 Systems of Equations

Consider the system of 3D conservation laws,

$$\begin{aligned} \frac{\partial}{\partial t} u_i(\mathbf{x}^c, t) + \nabla \cdot \mathbf{f}_i(\mathbf{u}(\mathbf{x}^c, t)) &= 0, \quad \forall i \in [1, n_{\text{state}}], \quad t \geq 0, \quad \mathbf{x}^c := [x \ y \ z] \in \Omega, \\ u_i(\mathbf{x}^c, 0) &= u_{i,0}(\mathbf{x}^c), \end{aligned} \quad (5.1)$$

where $\mathbf{f}_i(\mathbf{u}(\mathbf{x}^c, t)) \in \mathbb{R}^{1 \times d}$ stores the fluxes in each of the d directions for the i -th equation of state, n_{state} represents the number of state variables, and the superscript c refers to Cartesian coordinates. In this paper row vector notation will be used.

Smooth solutions of Eq. (5.1) satisfy the entropy equality,

$$\frac{\partial U}{\partial t} + \nabla \cdot \mathbf{F} = 0, \quad \mathbf{F} = \mathbf{F}(u), \quad (5.2)$$

where U is a convex function of u , while *weak* solutions satisfy the entropy inequality,

$$\frac{\partial U}{\partial t} + \nabla \cdot \mathbf{F} \leq 0. \quad (5.3)$$

In the context of entropy conservative numerical schemes, from Mock [42] and Harten [21], it was shown that the symmetrization of the PDE by the entropy variables $\mathbf{v} = U'(\mathbf{u})$, $\mathbf{v} \in \mathbb{R}^{1 \times n_{\text{state}}}$, along with the convexity of the entropy function U , leads to the existence of an entropy flux function $\mathbf{F}(\mathbf{u})$ such that in each physical direction $k \in [1, d]$,

$$\mathbf{v} \frac{\partial \mathbf{f}^{kT}}{\partial \mathbf{u}} = \frac{dF^k(\mathbf{u})}{d\mathbf{u}}, \quad \text{where,} \quad \left(\frac{\partial \mathbf{f}^{kT}}{\partial \mathbf{u}} \right)_{ij} = \frac{\partial f_i^k(\mathbf{u})}{\partial u_j}, \quad \forall i, j \in [1, n_{\text{state}}], \quad (5.4)$$

Integrating Eq. (5.4) with respect to the conservative variables, and introducing the entropy potential $\psi(\mathbf{v})$ such that $\frac{d\psi^k(\mathbf{v})}{d\mathbf{v}} = \mathbf{f}^k(\mathbf{u}(\mathbf{v}))$, we have [21, Eq. 1.13b],

$$\psi^k(\mathbf{v}) = \mathbf{v} \mathbf{f}^{kT} - F^k(\mathbf{u}), \quad \forall k \in [1, d]. \quad (5.5)$$

Tadmor [20, Eq. 4.5a] demonstrated that a numerical scheme is entropy conservative if,

$$\mathbf{v} \Delta (\mathbf{f}^{kT}) = \Delta (F^k). \quad (5.6)$$

Unfortunately, Eq. (5.6) is a strong condition on the flux. To satisfy Eq. (5.6) in a weak sense, Tadmor [20] applied the Δ operator on Eq. (5.5) to retrieve $\Delta (\psi^k) = \Delta (\mathbf{v}) \mathbf{f}^{kT} + \mathbf{v} \Delta (\mathbf{f}^{kT}) - \Delta (F^k)$, resulting in the equivalent condition [20, Eq. 4.5b],

$$\Delta (\mathbf{v}) \mathbf{f}^{kT} = \Delta (\psi^k). \quad (5.7)$$

Eq. (5.7) is known as the *Tadmor shuffle condition*. We introduce $[[\mathbf{v}]] = \mathbf{v}_i - \mathbf{v}_j$ as the jump, and it has been shown that the two-point flux $\mathbf{f}_s^k(\mathbf{v}_i, \mathbf{v}_j)$,

$$[[\mathbf{v}]] \mathbf{f}_s^k(\mathbf{v}_i, \mathbf{v}_j)^T = [[\psi^k]], \quad \forall k \in [1, d] \quad (5.8)$$

is entropy conserving [1, 20] in the sense that the numerical discretization conserves the equality

$$\int_{\Omega} \frac{\partial U}{\partial t} d\Omega + \int_{\Gamma} (\mathbf{v} \mathbf{f}^T - \psi) \cdot \hat{\mathbf{n}} d\Gamma = 0 \text{ exactly.}$$

In this paper, we consider the three-dimensional unsteady Euler equations,

$$\begin{aligned} \frac{\partial \mathbf{W}^T}{\partial t} + \nabla \cdot \mathbf{f}(\mathbf{W})^T &= \mathbf{0}^T, \\ \mathbf{W} &= \begin{bmatrix} \rho, & \rho u, & \rho v, & \rho w, & \rho e \end{bmatrix}, \\ \mathbf{f}_1 &= \begin{bmatrix} \rho u, & \rho u^2 + p, & \rho uv, & \rho uw, & (\rho e + p) u \end{bmatrix}, \\ \mathbf{f}_2 &= \begin{bmatrix} \rho v, & \rho uv, & \rho v^2 + p, & \rho vw, & (\rho e + p) v \end{bmatrix}, \\ \mathbf{f}_3 &= \begin{bmatrix} \rho w, & \rho uw, & \rho vw, & \rho w^2 + p, & (\rho e + p) w \end{bmatrix}, \end{aligned} \quad (5.9)$$

where $\rho e = \frac{p}{\gamma-1} + \frac{1}{2}\rho(u^2 + v^2 + w^2)$, and $\rho, u, v, w, p, e, \gamma$ are the density, velocity, pressure,

specific total energy, and adiabatic coefficient respectively.

5.2.2 Computational Space

To discretely solve Eq. (5.1), we need to introduce notations with respect to the computational space and basis functions. Since we discretely represent each equation of state separately, we will remove the boldface on u to indicate that it is for a single state variable.

The computational domain Ω^h is partitioned into M non-overlapping elements, Ω_m , where the domain is represented by the union of the elements, *i.e.*

$$\Omega \simeq \Omega^h := \bigcup_{m=1}^M \Omega_m.$$

Each element m has a surface denoted by Γ_m . The global approximation, $u^h(\mathbf{x}^c, t)$, is constructed from the direct sum of each local approximation, $u_m^h(\mathbf{x}^c, t)$, *i.e.*

$$u(\mathbf{x}^c, t) \simeq u^h(\mathbf{x}^c, t) = \bigoplus_{m=1}^M u_m^h(\mathbf{x}^c, t).$$

Throughout this paper, all quantities with a subscript m are specifically unique to the element m . On each element, we represent the solution with N_p linearly independent modal or nodal basis functions of a maximum order of p ; where, $N_p := (p + 1)^d$. The solution representation is, $u_m^h(\mathbf{x}^c, t) := \sum_{i=1}^{N_p} \chi_{m,i}(\mathbf{x}^c) \hat{u}_{m,i}(t)$, where $\hat{u}_{m,i}(t)$ are the modal coefficients for the solution. The elementwise residual for the governing equation (5.1) is,

$$R_m^h(\mathbf{x}^c, t) = \frac{\partial}{\partial t} u_m^h(\mathbf{x}^c, t) + \nabla \cdot \mathbf{f}(u_m^h(\mathbf{x}^c, t)). \quad (5.10)$$

The basis functions in each element are defined as,

$$\boldsymbol{\chi}(\mathbf{x}^c) := [\chi_1(\mathbf{x}^c), \chi_2(\mathbf{x}^c), \dots, \chi_{N_p}(\mathbf{x}^c)] = \boldsymbol{\chi}(x) \otimes \boldsymbol{\chi}(y) \otimes \boldsymbol{\chi}(z) \in \mathbb{R}^{1 \times N_p}, \quad (5.11)$$

where \otimes is the tensor product. Importantly, in curvilinear elements, the basis functions are not polynomial in physical space, but the basis functions are polynomial in reference space. This concept was explored in great detail in Cicchino *et al.* [38, Sec. 3], as well as proofs for rate of convergence in Botti [43] and Moxey *et al.* [44].

The physical coordinates are mapped to the reference element $\boldsymbol{\xi}^r := \{[\xi, \eta, \zeta] : -1 \leq \xi, \eta, \zeta \leq 1\}$ by

$$\mathbf{x}_m^c(\boldsymbol{\xi}^r) := \boldsymbol{\Theta}_m(\boldsymbol{\xi}^r) = \sum_{i=1}^{N_{t,m}} \Theta_{m,i}(\boldsymbol{\xi}^r) \hat{\mathbf{x}}_{m,i}^c, \quad (5.12)$$

where $\Theta_{m,i}$ are the mapping shape functions of the $N_{t,m}$ physical mapping control points $\hat{\mathbf{x}}_{m,i}^c$.

To transform Eq. (5.10) to the reference basis, as in refs [45–49], we introduce the physical

$$\mathbf{a}_j := \frac{\partial \mathbf{x}^c}{\partial \xi^j}, \quad j = 1, 2, 3$$

and reference

$$\mathbf{a}^j := \nabla_{\xi^j}, \quad j = 1, 2, 3$$

vector bases. We then introduce the determinant of the metric Jacobian as

$$J := |\mathbf{J}| = \mathbf{a}_1 \cdot (\mathbf{a}_2 \times \mathbf{a}_3), \quad (5.13)$$

and the metric Jacobian cofactor matrix as [15, 45, 46, 50],

$$\mathbf{C}^T := J(\mathbf{J})^{-1} = \begin{bmatrix} J\mathbf{a}^1 \\ J\mathbf{a}^2 \\ J\mathbf{a}^3 \end{bmatrix} = \begin{bmatrix} J\mathbf{a}^\xi \\ J\mathbf{a}^\eta \\ J\mathbf{a}^\zeta \end{bmatrix}. \quad (5.14)$$

The metric cofactor matrix is formulated by the ‘‘conservative curl’’ form from [47, Eq. 36]

so as to discretely satisfy the Geometric Conservation Law (GCL)

$$\sum_{i=1}^3 \frac{\partial(J(\mathbf{a}^i)_n)}{\partial \xi^i} = 0, \quad n = 1, 2, 3 \Leftrightarrow \sum_{i=1}^3 \frac{\partial}{\partial \xi^i} (\mathbf{C})_{ni} = 0, \quad n = 1, 2, 3 \Leftrightarrow \nabla^r \cdot (\mathbf{C}) = \mathbf{0}, \quad (5.15)$$

for a fixed mesh, where $(\)_{ni}$ represents the n^{th} row, i^{th} column component of a matrix. The exact implementation of the metric cofactor matrix is extensively detailed in Cicchino *et al.* [38, Sec. 5]

Having established the transformations mapping the physical to the reference coordinates on each element, the differential volume and surface elements can be defined as,

$$d\Omega_m = J_m^\Omega d\Omega_r, \quad \text{similarly } d\Gamma_m = J_m^\Gamma d\Gamma_r, \quad (5.16)$$

where J_m^Ω and J_m^Γ are the determinants of the metric Jacobian in the volume Ω and surface Γ for the element m respectively. The reference flux for each element m is defined as

$$\mathbf{f}_m^r = \mathbf{C}_m^T \cdot \mathbf{f}_m \Leftrightarrow \mathbf{f}_{m,j}^r = \sum_{i=1}^d (\mathbf{C}_m^T)_{ji} \mathbf{f}_{m,i} \Leftrightarrow \mathbf{f}_m^r = \mathbf{f}_m \mathbf{C}_m, \quad (5.17)$$

where the dot product notation for tensor-vector operations is introduced. The relationship between the physical and reference unit normals is given as [15, Appendix B.2],

$$\hat{\mathbf{n}}_m = \frac{1}{J_m^\Gamma} \mathbf{C}_m \cdot \hat{\mathbf{n}}^r = \frac{1}{J_m^\Gamma} \hat{\mathbf{n}}^r \mathbf{C}_m^T, \quad (5.18)$$

for a water-tight mesh. Additionally, the definition of the divergence operator derived from divergence theorem in curvilinear coordinates can be expressed as [45, Eq. (2.22) and (2.26)],

$$\nabla \cdot \mathbf{f}_m = \frac{1}{J_m^\Omega} \nabla^r \cdot (\mathbf{f}_m \mathbf{C}_m) = \frac{1}{J_m^\Omega} \nabla^r \cdot \mathbf{f}_m^r, \quad (5.19)$$

and the gradient of a scalar as [45, Eq. (2.21)],

$$\nabla \chi = \frac{1}{J_m^\Omega} \mathbf{C}_m \cdot \nabla^r \chi = \frac{1}{J_m^\Omega} (\nabla^r \chi) \mathbf{C}_m^T. \quad (5.20)$$

Thus, substituting Eq. (5.19) into Eq. (5.10), the reference elementwise residual can be expressed as,

$$R_m^{h,r}(\boldsymbol{\xi}^r, t) := R_m^h(\boldsymbol{\Theta}_m(\boldsymbol{\xi}^r), t) = \frac{\partial}{\partial t} u_m^h(\boldsymbol{\Theta}_m(\boldsymbol{\xi}^r), t) + \frac{1}{J_m^\Omega} \nabla^r \cdot \mathbf{f}^r(u_m^h(\boldsymbol{\Theta}_m(\boldsymbol{\xi}^r), t)). \quad (5.21)$$

Lastly, since the basis functions are polynomial in the reference space, we introduce $\boldsymbol{\chi}(\boldsymbol{\xi}^r)$, and they discretely satisfy discrete integration-by-parts for quadrature rules exact for at least $2p - 1$ polynomials,

$$\int_{\Omega_r} \nabla^r \chi_i(\boldsymbol{\xi}^r) \chi_j(\boldsymbol{\xi}^r) d\Omega_r + \int_{\Omega_r} \chi_i(\boldsymbol{\xi}^r) \nabla^r \chi_j(\boldsymbol{\xi}^r) d\Omega_r = \int_{\Gamma_r} \chi_i(\boldsymbol{\xi}^r) \chi_j(\boldsymbol{\xi}^r) \hat{\mathbf{n}}^r d\Gamma_r, \forall i, j \in [1, N_p]. \quad (5.22)$$

Eq. (5.22) is commonly referred to as the summation-by-parts (SBP) property.

5.3 Nonlinearly Stable Flux Reconstruction

In this section, we will present our nonlinearly stable FR scheme. To arrive at it, we first present DG, then ESFR. Following the motivation from [37, 38], we then incorporate the entropy stable framework within the stiffness operator to arrive at NSFR.

5.3.1 Discontinuous Galerkin

The discontinuous Galerkin approach is obtained by multiplying the reference residual Eq. (3.13) by a test function which is chosen to be the basis function and integrating in physical space. Then, we apply integration-by-parts in the reference space on the divergence of the flux. Since the solution and flux are both discontinuous across the face, we introduce a numerical surface flux \mathbf{f}_m^* to treat the resulting Riemann problem. The continuous weak DG

is,

$$\begin{aligned}
& \int_{\Omega_r} \chi_i(\boldsymbol{\xi}^r) J_m^\Omega \boldsymbol{\chi}(\boldsymbol{\xi}^r) \frac{d}{dt} \hat{\mathbf{u}}_m(t)^T d\Omega_r - \int_{\Omega_r} \nabla^r \chi_i(\boldsymbol{\xi}^r) \cdot \mathbf{f}_m^r d\Omega_r \\
& + \int_{\Gamma_r} \chi_i(\boldsymbol{\xi}^r) \hat{\mathbf{n}}^r \mathbf{C}_m^T \cdot \mathbf{f}_m^*(u_m^h(\boldsymbol{\Theta}_m(\boldsymbol{\xi}^r), t)) d\Gamma_r = 0, \quad \forall i = 1, \dots, N_p.
\end{aligned} \tag{5.23}$$

The nonlinear reference flux \mathbf{f}_m^r is computed through Eq. (5.17), where the physical flux $\mathbf{f}_m = f(\mathbf{u}(\boldsymbol{\xi}_v^r, t))$ is evaluated directly from the solution at the integration points $\boldsymbol{\xi}_v^r$. Discretely, to evaluate the integrals in Eq. (5.23), we utilize quadrature rules, where $\boldsymbol{\xi}_v^r$ represents the volume quadrature nodes, and $\boldsymbol{\xi}_{f,k}^r$ represents the surface quadrature node on the face $f \in [1, N_f]$ with facet cubature node $k \in [1, N_{fp}]$. To arrive at the equivalent strong form, we first need to pay special attention to the nonlinear flux. Since the reference flux is evaluated directly on the volume cubature nodes, we need to project it onto a polynomial basis with the order of the number of quadrature nodes. For example, if \mathbf{u}^h is order p , and it is integrated on $p + 4$ quadrature nodes, the flux basis $\phi(\boldsymbol{\xi}^r)$ needs to be of at least order $p + 3$ to avoid aliasing errors when representing the flux. The easiest choice of basis functions for the flux basis is to use Lagrange polynomials collocated on the quadrature nodes since a collocated Lagrange basis has an identity projection operator. By collocated, we mean that the Lagrange polynomial is evaluated on the same nodes, the quadrature nodes, as the polynomial it is constructed from, making $l_{ij} = \delta_{ij}$, where i is the polynomial basis number and j the nodal number.

Thus, applying discrete integration by parts on Eq. (5.23) results in,

$$\begin{aligned}
& \mathbf{M}_m \frac{d}{dt} \hat{\mathbf{u}}_m(t)^T + \boldsymbol{\chi}(\boldsymbol{\xi}_v^r)^T \mathbf{W} \nabla^r \phi(\boldsymbol{\xi}_v^r) \cdot \hat{\mathbf{f}}_m^r(t)^T \\
& + \sum_{f=1}^{N_f} \sum_{k=1}^{N_{fp}} \boldsymbol{\chi}(\boldsymbol{\xi}_{fk}^r)^T W_{fk} \hat{\mathbf{n}}^r \cdot \left[\mathbf{f}_m^{*,r} - \phi(\boldsymbol{\xi}_{fk}^r) \hat{\mathbf{f}}_m^r(t)^T \right] = \mathbf{0}^T,
\end{aligned} \tag{5.24}$$

where \mathbf{W} is a diagonal matrix storing the quadrature weights and the discrete mass matrix is,

$$(\mathbf{M}_m)_{ij} \approx \int_{\Omega_r} J_m^\Omega \chi_i(\boldsymbol{\xi}^r) \chi_j(\boldsymbol{\xi}^r) d\Omega_r \rightarrow \mathbf{M}_m = \boldsymbol{\chi}(\boldsymbol{\xi}_v^r)^T \mathbf{W} \mathbf{J}_m \boldsymbol{\chi}(\boldsymbol{\xi}_v^r), \quad (5.25)$$

with \mathbf{J}_m as a diagonal matrix storing the determinant of the metric Jacobian at quadrature nodes.

5.3.2 Energy Stable Flux Reconstruction

As initially proposed by H.T. Huynh [11], in an ESFR framework, the reference flux is composed of a discontinuous and a corrected component,

$$\mathbf{f}^r(u_m^h(\boldsymbol{\Theta}_m(\boldsymbol{\xi}^r), t)) := \mathbf{f}^{D,r}(u_m^h(\boldsymbol{\Theta}_m(\boldsymbol{\xi}^r), t)) + \sum_{f=1}^{N_f} \sum_{k=1}^{N_{fp}} \mathbf{g}^{f,k}(\boldsymbol{\xi}^r) [\hat{\mathbf{n}}^r \cdot (\mathbf{f}_m^{*,r} - \mathbf{f}_m^r)]. \quad (5.26)$$

For three-dimensions, the vector correction functions $\mathbf{g}^{f,k}(\boldsymbol{\xi}^r) \in \mathbb{R}^{1 \times d}$ associated with face f , facet cubature node k in the reference element, are defined as the tensor product of the $p+1$ order one-dimensional correction functions ($\boldsymbol{\chi}_{p+1}$ stores a basis of order $p+1$), with the corresponding p -th order basis functions in the other reference directions.

$$\begin{aligned} & \mathbf{g}^{f,k}(\boldsymbol{\xi}^r) \\ &= \left[\left(\phi(\xi) \otimes \boldsymbol{\chi}(\eta) \otimes \boldsymbol{\chi}(\zeta) \right) \left(\hat{\mathbf{g}}_1^{f,k} \right)^T, \left(\boldsymbol{\chi}(\xi) \otimes \phi(\eta) \otimes \boldsymbol{\chi}(\zeta) \right) \left(\hat{\mathbf{g}}_2^{f,k} \right)^T, \left(\boldsymbol{\chi}(\xi) \otimes \boldsymbol{\chi}(\eta) \otimes \phi(\zeta) \right) \left(\hat{\mathbf{g}}_3^{f,k} \right)^T \right] \\ &= \left[g_1^{f,k}(\boldsymbol{\xi}^r), g_2^{f,k}(\boldsymbol{\xi}^r), g_3^{f,k}(\boldsymbol{\xi}^r) \right], \end{aligned} \quad (5.27)$$

such that

$$\mathbf{g}^{f,k}(\boldsymbol{\xi}_{f_i, k_j}^r) \cdot \hat{\mathbf{n}}_{f_i, k_j}^r = \begin{cases} 1, & \text{if } f_i = f, \text{ and } k_j = k \\ 0, & \text{otherwise.} \end{cases} \quad (5.28)$$

Coupled with the symmetry condition $g^L(\boldsymbol{\xi}^r) = -g^R(-\boldsymbol{\xi}^r)$ to satisfy Eq. (3.26), the

one-dimensional ESFR fundamental assumption from [12] is,

$$\int_{-1}^1 \nabla^r \chi_i(\xi^r) g^{f,k}(\xi^r) d\xi - c \frac{\partial^p \chi_i(\xi^r)^T}{\partial \xi^p} \frac{\partial^{p+1} g^{f,k}(\xi^r)}{\partial \xi^{p+1}} = 0, \forall i = 1, \dots, N_p, \quad (5.29)$$

and similarly for the other reference directions. Here, c is the ESFR correction parameter.

Akin to [38, 51, 52], consider introducing the differential operator,

$$\begin{aligned} \text{2D: } \quad \partial^{(s,v)} &= \frac{\partial^{s+v}}{\partial \xi^s \partial \eta^v}, \text{ such that } s = \{0, p\}, v = \{0, p\}, s + v \geq p, \\ \text{3D: } \quad \partial^{(s,v,w)} &= \frac{\partial^{s+v+w}}{\partial \xi^s \partial \eta^v \partial \zeta^w}, \text{ such that } s = \{0, p\}, v = \{0, p\}, w = \{0, p\}, s + v + w \geq p, \end{aligned} \quad (5.30)$$

with its corresponding correction parameter

$$\begin{aligned} \text{2D: } \quad c_{(s,v)} &= c_{1D}^{\left(\frac{s+v}{p}\right)}, \\ \text{3D: } \quad c_{(s,v,w)} &= c_{1D}^{\left(\frac{s+v+w}{p}\right)}. \end{aligned} \quad (5.31)$$

Note that the total degree is $d \times p$ for a tensor product basis that is of order p in each direction.

For example,

$$\partial^{(0,p,0)} = \frac{\partial^p}{\partial \eta^p}, c_{(0,p,0)} = c_{1D}, \partial^{(p,0,p)} = \frac{\partial^{2p}}{\partial \xi^p \partial \zeta^p}, c_{(p,0,p)} = c_{1D}^2, \partial^{(p,p,p)} = \frac{\partial^{3p}}{\partial \xi^p \partial \eta^p \partial \zeta^p}, c_{(p,p,p)} = c_{1D}^3.$$

Since $\int_{\Omega_r} \partial^{(s,v,w)} \chi(\boldsymbol{\xi}^r)^T \partial^{(s,v,w)} (\nabla^r \chi(\boldsymbol{\xi}^r)) d\Omega_r$ composes of the complete broken Sobolev-norm for each s, v, w [38, 53], the tensor product ESFR fundamental assumption, that recovers the VCJH [54] schemes exactly for linear elements is defined as,

$$\int_{\Omega_r} \nabla^r \chi_i(\boldsymbol{\xi}^r) \cdot \mathbf{g}^{f,k}(\boldsymbol{\xi}^r) d\Omega_r - \sum_{s,v,w} c_{(s,v,w)} \partial^{(s,v,w)} \chi_i(\boldsymbol{\xi}^r) \partial^{(s,v,w)} (\nabla^r \cdot \mathbf{g}^{f,k}(\boldsymbol{\xi}^r)) = 0, \forall i = 1, \dots, N_p, \quad (5.32)$$

where $\sum_{s,v,w}$ sums over all possible s, v, w combinations in Eq. (5.30).

To discretely represent the divergence of the correction functions, we introduce the

correction field

$h^{f,k}(\boldsymbol{\xi}^r) \in P_{3p}(\boldsymbol{\Omega}_r)$ associated with the face f cubature node k as,

$$h^{f,k}(\boldsymbol{\xi}^r) = \boldsymbol{\chi}(\boldsymbol{\xi}^r) \left(\hat{\mathbf{h}}^{f,k} \right)^T = \nabla^r \cdot \mathbf{g}^{f,k}(\boldsymbol{\xi}^r). \quad (5.33)$$

To arrive at the ESFR strong form, we substitute the ESFR reference flux, Eq. (5.26), into the elementwise reference residual, Eq. (5.21), project it onto the polynomial basis, and evaluate at cubature nodes,

$$\boldsymbol{\chi}(\boldsymbol{\xi}_v^r) \frac{d}{dt} \hat{\mathbf{u}}_m(t)^T + \mathbf{J}_m^{-1} \nabla^r \boldsymbol{\chi}(\boldsymbol{\xi}_v^r) \cdot \hat{\mathbf{f}}_m^{D,r}(t)^T + \mathbf{J}_m^{-1} \sum_{f=1}^{N_f} \sum_{k=1}^{N_{fp}} \boldsymbol{\chi}(\boldsymbol{\xi}_v^r) \left(\hat{\mathbf{h}}^{f,k} \right)^T [\hat{\mathbf{n}}^r \cdot (\mathbf{f}_m^{*,r} - \mathbf{f}_m^r)] = \mathbf{0}^T. \quad (5.34)$$

For implementation in a pre-existing DG framework, Allaneau and Jameson [16] showed that ESFR can be expressed as a filtered DG scheme in one-dimension. Zwanenburg and Nadarajah [15] proved that ESFR can be expressed as a filtered DG scheme for general three-dimensional curvilinear coordinates on mixed element types. Expanding the reference ESFR filter in Zwanenburg and Nadarajah [15] allows ESFR schemes to be seen as a DG-type scheme with a modified norm [17]. Only by viewing ESFR as DG with a modified norm can a nonlinearly stable form be achieved [37, 38] since the determinant of the metric Jacobian gets embedded in the norm, and the entropy stability application is embedded in the stiffness operator. The equivalence to view ESFR through a modified norm is dependent on [38, Lemma 2], where it was proven that the ESFR correction operator has no influence on the conservative volume term when the inverse of the mass matrix is applied. To present ESFR

as a DG scheme with a modified mass matrix, we introduce the ESFR correction operator as,

$$\begin{aligned}
(\mathbf{K}_m)_{ij} &\approx \sum_{s,v,w} c_{(s,v,w)} \int_{\Omega_r} J_m^\Omega \partial^{(s,v,w)} \chi_i(\boldsymbol{\xi}^r) \partial^{(s,v,w)} \chi_j(\boldsymbol{\xi}^r) d\Omega_r \\
\rightarrow \mathbf{K}_m &= \sum_{s,v,w} c_{(s,v,w)} \partial^{(s,v,w)} \boldsymbol{\chi}(\boldsymbol{\xi}_v^r)^T \mathbf{W} \mathbf{J}_m \partial^{(s,v,w)} \boldsymbol{\chi}(\boldsymbol{\xi}_v^r) \\
&= \sum_{s,v,w} c_{(s,v,w)} \left(\mathbf{D}_\xi^s \mathbf{D}_\eta^v \mathbf{D}_\zeta^w \right)^T \mathbf{M}_m \left(\mathbf{D}_\xi^s \mathbf{D}_\eta^v \mathbf{D}_\zeta^w \right),
\end{aligned} \tag{5.35}$$

where $\mathbf{D}_\xi^s = \left(\mathbf{M}^{-1} \mathbf{S}_\xi \right)^s$ is the strong form differential operator raised to the power s , and similarly for the other reference directions.

Therefore, recasting Eq. (5.24) as an ESFR scheme through the modified-norm framework [37, 38] results in,

$$\begin{aligned}
&(\mathbf{M}_m + \mathbf{K}_m) \frac{d}{dt} \hat{\mathbf{u}}_m(t)^T + \boldsymbol{\chi}(\boldsymbol{\xi}_v^r)^T \mathbf{W} \nabla^r \phi(\boldsymbol{\xi}_v^r) \cdot \hat{\mathbf{f}}_m^r(t)^T \\
&+ \sum_{f=1}^{N_f} \sum_{k=1}^{N_{fp}} \boldsymbol{\chi}(\boldsymbol{\xi}_{fk}^r)^T W_{fk} \hat{\mathbf{n}}^r \cdot \left[\mathbf{f}_m^{*,r} - \phi(\boldsymbol{\xi}_{fk}^r) \hat{\mathbf{f}}_m^r(t)^T \right] = \mathbf{0}^T.
\end{aligned} \tag{5.36}$$

Comparing Eq. (5.36) with Eq. (5.24), we note that all of the FR contributions arise from the modified mass matrix.

5.3.3 Nonlinearly Stable Flux Reconstruction

As in Chan [1, 2, 6], we utilize the general differential operator to recast Eq. (5.36) in a skew-symmetric two-point flux differencing form [2, Eq. (15)],

$$\begin{aligned}
&(\mathbf{M}_m + \mathbf{K}_m) \frac{d}{dt} \hat{\mathbf{u}}_m(t)^T + [\boldsymbol{\chi}(\boldsymbol{\xi}_v^r)^T \boldsymbol{\chi}(\boldsymbol{\xi}_f^r)^T] \left[(\tilde{\mathbf{Q}} - \tilde{\mathbf{Q}}^T) \odot \mathbf{F}_m^r \right] \mathbf{1}^T \\
&+ \sum_{f=1}^{N_f} \sum_{k=1}^{N_{fp}} \boldsymbol{\chi}(\boldsymbol{\xi}_{fk}^r)^T W_{fk} \hat{\mathbf{n}}^r \cdot \mathbf{f}_m^{*,r} = \mathbf{0}^T,
\end{aligned} \tag{5.37}$$

where,

$$\tilde{\mathbf{Q}} - \tilde{\mathbf{Q}}^T = \begin{bmatrix} \mathbf{W} \nabla^r \phi(\boldsymbol{\xi}_v^r) - \nabla^r \phi(\boldsymbol{\xi}_v^r)^T \mathbf{W} & \sum_{f=1}^{N_f} \phi(\boldsymbol{\xi}_f^r)^T \mathbf{W}_f \text{diag}(\hat{\mathbf{n}}_f^r) \\ - \sum_{f=1}^{N_f} \mathbf{W}_f \text{diag}(\hat{\mathbf{n}}_f^r) \phi(\boldsymbol{\xi}_f^r) & \mathbf{0} \end{bmatrix} \in \mathbb{R}^{(N_v + N_{fp}) \times (N_v + N_{fp}) \times d} \quad (5.38)$$

is the general hybridized skew-symmetric stiffness operator involving both volume and surface quadrature evaluations [2] that has each $\tilde{\mathbf{Q}}$ satisfying the SBP-like property

$$\tilde{\mathbf{Q}} + \tilde{\mathbf{Q}}^T = \begin{bmatrix} \mathbf{0} & \mathbf{0} \\ \mathbf{0} & \mathbf{W}_f \text{diag}(\hat{\mathbf{n}}_f^r) \end{bmatrix}. \quad (5.39)$$

The hybrid skew-symmetric stiffness operator is constructed solely from the flux basis since the flux basis discretely satisfies the SBP property on the quadrature nodes. Here, $\phi(\boldsymbol{\xi}_f^r)$ be the matrix storing the flux basis evaluated at all surface quadrature nodes on the surface f . We let \odot represent a Hadamard product with a component-wise dot product on the d -dimensional tensors. This is accomplished by performing a Hadamard product of size $(N_v + N_{fp}) \times (N_v + N_{fp})$ in each of the d directions, then performing the summation on each d direction from the dot product. Also, \mathbf{F}_m^r is the matrix storing the reference two-point flux values,

$$(\mathbf{F}_m^r)_{ij} = \mathbf{f}_s(\tilde{\mathbf{u}}_m(\boldsymbol{\xi}_i^r), \tilde{\mathbf{u}}_m(\boldsymbol{\xi}_j^r)) \left(\frac{1}{2} (\mathbf{C}_m(\boldsymbol{\xi}_i^r) + \mathbf{C}_m(\boldsymbol{\xi}_j^r)) \right), \quad \forall 1 \leq i, j \leq N_v + N_{fp}. \quad (5.40)$$

We chose to incorporate the splitting of the metric cofactor matrix [38] within forming the reference two-point flux rather than incorporating it within a “physical” skew-symmetric stiffness operator [2, 6]. Although both forms are mathematically equivalent, the former allows us to exploit the tensor product structure of the reference basis stiffness operator to perform the Hadamard product at order $\mathcal{O}(n^{d+1})$ [41] whereas the latter does not. We provide a detailed report on evaluations of Hadamard products at $\mathcal{O}(n^{d+1})$ using tensor product basis in the technical report [41].

The choice of two-point flux $\mathbf{f}_s(\tilde{\mathbf{u}}_m(\boldsymbol{\xi}_i^r), \tilde{\mathbf{u}}_m(\boldsymbol{\xi}_j^r))$ dictates the physically relevant conserving properties of the scheme. For an entropy conserving scheme, we choose a two-point flux that satisfies the Tadmor shuffle condition Eq. (5.7),

$$(\mathbf{v}(\boldsymbol{\xi}_i^r) - \mathbf{v}(\boldsymbol{\xi}_j^r)) \mathbf{f}_s(\tilde{\mathbf{u}}_m(\boldsymbol{\xi}_i^r), \tilde{\mathbf{u}}_m(\boldsymbol{\xi}_j^r))^T = \psi(\mathbf{v}(\boldsymbol{\xi}_i^r)) - \psi(\mathbf{v}(\boldsymbol{\xi}_j^r)), \quad \forall 1 \leq i, j \leq N_v + N_{fp}, \quad (5.41)$$

with the entropy-projected conservative variables $\tilde{\mathbf{u}}_m(\boldsymbol{\xi}^r)$ [1]. The entropy projected conservative variables are computed by interpolating the conservative solution to the volume quadrature nodes, and evaluating the entropy variables on the quadrature nodes. Then the entropy variables are projected onto the solution basis to obtain the p -th order modal coefficients. Lastly, the modal coefficients are then interpolated to the volume and surface quadrature nodes where the entropy-projected conservative variables are obtained by doing the inverse of the mapping. This process is critical because, in Eq. (5.41), the entropy potential ψ is a function of the entropy variables, not of the conservative variables. Thus, we need to discretely satisfy it with the entropy variables at the quadrature nodes. Also, for the stability condition, the residual is left multiplied by the modal coefficients of the entropy variables—thus we need the entropy variables projected on the solution basis. The entropy projected variables are summarized by,

$$\tilde{\mathbf{u}}(\boldsymbol{\xi}^r) = \mathbf{u}(\boldsymbol{\chi}(\boldsymbol{\xi}^r) \hat{\mathbf{v}}^T), \quad \hat{\mathbf{v}}^T = \mathbf{\Pi}(\mathbf{v}(\boldsymbol{\chi}(\boldsymbol{\xi}_v^r) \hat{\mathbf{u}}^T)). \quad (5.42)$$

For Burgers' equation, there is a unique flux that satisfies the Tadmor shuffle equation [19], but for the Euler equations, there are different possibilities depending on the variables chosen for expressing the jumps [55, Sec. 4.5]. Ismail and Roe [56] were the first to introduce a change of variables to arrive at an explicit form for an entropy conserving flux. Motivated to conserve both entropy and kinetic energy, Chandrashekar [55] derived an entropy conserving and kinetic energy preserving flux by considering the variables ρ , u , and $\beta = \frac{\rho}{2p} = \frac{1}{2RT}$, where R is the universal gas constant and T is the temperature. Importantly noted by both Ismail

and Roe [56] and Chandrashekar [55], for an entropy dissipative flux, the jump in the entropy variables must be recovered. If the jump in the conservative variables is employed, then for the Euler equations, the scheme is not purely entropy dissipative [55, Sec. 5]. Lastly, Ranocha [57] presented a systematic framework to constructing an entropy conserving and kinetic energy preserving flux from different combinations of thermodynamic variables for the Euler equations.

5.4 Weight-Adjusted Inverse of Flux Reconstruction Mass Matrix

By immediate inspection, inverting $\mathbf{M}_m + \mathbf{K}_m$ on-the-fly is costly since they are both fully dense matrices in curvilinear coordinates. Instead, our goal is to make use of the tensor product structure and use sum-factorization [40] techniques for efficient, low storage evaluations on-the-fly.

Similar to Chan and Wilcox [6, Eq. (27)], we let \mathbf{u}_J represent the weight-adjusted polynomial's modal coefficients. We need to solve the matrix system,

$$(\mathbf{M}_{1/J} + \mathbf{K}_{1/J})\mathbf{u}_J^T = (\mathbf{M} + \mathbf{K})\mathbf{u}^T, \quad (5.43)$$

where

$$\begin{aligned} \mathbf{M}_{1/J} &= \boldsymbol{\chi}(\boldsymbol{\xi}_v^r)^T \mathbf{W} \mathbf{J}_m^{-1} \boldsymbol{\chi}(\boldsymbol{\xi}_v^r), \\ \mathbf{K}_{1/J} &= \sum_{s,v,w} c_{(s,v,w)} (\mathbf{D}_\xi^s \mathbf{D}_\eta^v \mathbf{D}_\zeta^w)^T \mathbf{M}_{1/J} (\mathbf{D}_\xi^s \mathbf{D}_\eta^v \mathbf{D}_\zeta^w), \end{aligned} \quad (5.44)$$

are both dense for the uncollocated case, symmetric and positive definite. Thus, we can express the respective weight-adjusted system FR mass matrix and inverse of the FR mass

matrix as,

$$\begin{aligned} (\mathbf{M}_m + \mathbf{K}_m) &\approx (\mathbf{M} + \mathbf{K}) (\mathbf{M}_{1/J} + \mathbf{K}_{1/J})^{-1} (\mathbf{M} + \mathbf{K}), \\ (\mathbf{M}_m + \mathbf{K}_m)^{-1} &\approx (\mathbf{M} + \mathbf{K})^{-1} (\mathbf{M}_{1/J} + \mathbf{K}_{1/J}) (\mathbf{M} + \mathbf{K})^{-1}. \end{aligned} \quad (5.45)$$

It is important to note that $(\mathbf{M} + \mathbf{K})^{-1}$ has the same local value for each element. Therefore, computing $(\mathbf{M}_m + \mathbf{K}_m)^{-1}$ via Eq. (5.45) only depends on inverting the diagonal matrix storing the determinant of the Jacobian on-the-fly.

As detailed by Chan and Wilcox [6], the accuracy of the weight-adjusted inverse approximation is solely dependent on the accuracy of the projection. In Cicchino *et al.* [38], the ESFR projection operator was demonstrated to maintain the orders of convergence up to the upper limit found by Castonguay [58, Fig. 3.6]. Thus, we can make further improvements by introducing the ESFR projection operator in reference space,

$$\begin{aligned} \tilde{\mathbf{\Pi}}(\boldsymbol{\xi}_v^r) &= \tilde{\mathbf{\Pi}}(\xi_v) \otimes \tilde{\mathbf{\Pi}}(\eta_v) \otimes \tilde{\mathbf{\Pi}}(\zeta_v), \\ \tilde{\mathbf{\Pi}}(\xi_v) &= (\mathbf{M}(\xi_v) + \mathbf{K}(\xi_v))^{-1} \boldsymbol{\chi}(\xi_v)^T \mathbf{W}(\xi_v), \end{aligned} \quad (5.46)$$

where $\mathbf{M}(\xi_v) + \mathbf{K}(\xi_v)$ is the one-dimensional modified mass matrix, $\boldsymbol{\chi}(\xi_v)$ is the one-dimensional basis function, and $\mathbf{W}(\xi_v)$ stores the 1D quadrature weights.

Therefore, using the reference ESFR projection operator in Eq. (5.46), the weight-adjusted inverse to the ESFR modified mass matrix is,

$$(\mathbf{M}_m + \mathbf{K}_m)^{-1} \approx \tilde{\mathbf{\Pi}}(\boldsymbol{\xi}_v^r) (\mathbf{W} \mathbf{J}_m)^{-1} \tilde{\mathbf{\Pi}}(\boldsymbol{\xi}_v^r)^T. \quad (5.47)$$

Using Eq. (5.47) reduces the computational cost to inverting a diagonal matrix, $\mathbf{W} \mathbf{J}_m$, and this form enables sum-factorized expansions through the tensor product structure of the reference ESFR projection operator. The diagonal elements $\mathbf{W} \mathbf{J}_m$ can either be pre-computed and stored or computed on-the-fly. Lastly, we need to show that the ESFR weight-adjusted inverse preserves the orders of convergence.

Theorem 5.4.1. *The weight-adjusted inverse for the ESFR mass matrix in Eq. (5.47) preserves the order of convergence $\mathcal{O}(h^{p+1})$.*

Proof. From Chan and Wilcox [6, Thm 4], the weight-adjusted inverse is of order $h^{\min(r,p+1)+1}$ for $u \in W^{r,2}(\Omega_m)$. With the choice of ESFR correction functions from Vincent *et al.* [12], and by rewriting the correction functions through a filtered DG form [15, 16], the ESFR projection operator is of the same order as the DG projection operator for values of $c \leq c_+$. This was numerically shown by Castonguay [58] for the ESFR correction functions and by Cicchino *et al.* [38] for the ESFR projection of the volume split-form divergence in curvilinear coordinates. Therefore, since the ESFR projection operator is of the same order of accuracy as the DG projection operator, the ESFR weight-adjusted inverse holds the same order of accuracy as the DG result in Chan and Wilcox [6]. \square

In Sec. 5.7.1, we demonstrate numerically that the numerical scheme with the weight-adjusted inverse for ESFR discretizations maintains the correct orders of accuracy for values $c \leq c_+$, with the same trends in the error convergence as [12, 38, 58].

5.5 Scalable Evaluations

With the intent of the high-order solver being used on next generation hardware, on both CPUs and GPUs, we wish that the solver’s flops scale at the lowest order possible, and has a low memory footprint. In this section, we briefly review sum-factorization techniques to drastically reduce the memory footprint and flop count for evaluating the NSFR discretization in Eq. (5.37). For this section, we will let $n = p + 1$ and d still represent the dimension of the operators. By observation, the flops in the NSFR discretization Eq. (5.37) are dominated by dense matrix-vector multiplications, along with a dense Hadamard product. We resolve the scaling issue for the matrix-vector multiplications with sum-factorization [40], and the Hadamard product with the sum-factorized Hadamard product from Cicchino and Nadarajah [41, Thm. 2.1]. Following the roofline model [59], all operations would ideally have

a large arithmetic intensity (A.I.), $\text{A.I.} = \frac{\text{flops}}{\text{bytes}}$, with it being a function of n .

Let's consider interpolating the modal coefficients $\hat{\mathbf{u}}$ to the volume quadrature nodes by the basis functions $\boldsymbol{\chi}(\boldsymbol{\xi}_v^r)$. Since, $\boldsymbol{\chi}(\boldsymbol{\xi}_v^r) = \boldsymbol{\chi}(\xi_v^r) \otimes \boldsymbol{\chi}(\eta_v^r) \otimes \boldsymbol{\chi}(\zeta_v^r) \in \mathbf{M}_{n^d \times n^d}(\mathbb{R})$ is the tensor product of the n -sized one-dimensional basis function matrices $\boldsymbol{\chi}(\xi_v^r)$, then $\mathbf{u}_v^T = \boldsymbol{\chi}(\boldsymbol{\xi}_v^r) \hat{\mathbf{u}}^T$ is evaluated directly in n^{2d} flops. Orszag [40] observed that the tensor product structure can be exploited, and the matrix-vector multiplication can be evaluated in each direction independently. The flop count for sum-factorization is dn^{d+1} . As extensively detailed in Karniadakis and Sherwin [60, Chapters 3, 4], by using quadrilateral and hexahedral reference elements, the basis operations can straightforwardly use sum-factorization. For triangular, tetrahedral, prismatic, and pyramidal-based elements, Karniadakis and Sherwin [60, Chapters 3, 4] derived orthogonal tensor product basis functions to exploit sum-factorization in high-order codes.

We will present the sum-factorization operations as a sequence of matrix-matrix multiplications alike Cantwell *et al.* [61] to leverage optimizations in the BLAS subsystem. We let the ξ -direction run the fastest, then η , and ζ running the slowest. First, we rearrange the modal coefficient's of $\hat{\mathbf{u}} \rightarrow \hat{\mathbf{u}}^{n_\xi:n_\eta n_\zeta} \in \mathbf{M}_{n_\xi \times n_\eta n_\zeta}(\mathbb{R})$, where n_ξ is the one-dimensional basis size in the ξ -direction, similarly for n_η and n_ζ . The transformation makes $\hat{\mathbf{u}}^{n_\xi:n_\eta n_\zeta}$ a matrix where its rows vary in the ξ -direction, and its columns vary in η and ζ . This allows us to perform a one-dimensional matrix-vector multiplication in ξ , at n^2 flops, and perform it n^{d-1} times for the η and ζ combinations in the columns. Alike Cantwell *et al.* [61, Sec. 2.3.1], following the same steps for the other directions arrives at,

$$\begin{aligned}
\mathbf{q}_0^{n_\xi:n_\eta n_\zeta} &= \boldsymbol{\chi}(\xi_v^r) \hat{\mathbf{u}}^{n_\xi:n_\eta n_\zeta}, \\
\mathbf{q}_1^{n_\eta:n_\zeta n_\xi} &= \boldsymbol{\chi}(\eta_v^r) \mathbf{q}_0^{n_\eta:n_\zeta n_\xi}, \\
\mathbf{q}_2^{n_\zeta:n_\xi n_\eta} &= \boldsymbol{\chi}(\zeta_v^r) \mathbf{q}_1^{n_\zeta:n_\xi n_\eta}, \\
\mathbf{u}_v &= \mathbf{q}_2^{n_\xi n_\eta n_\zeta:1}.
\end{aligned} \tag{5.48}$$

Each line in Eq. (5.48) has $n^2 n^{d-1} = n^{d+1}$ flops, and then it is repeated for the d -

lines, arriving at dn^{d+1} flops. The memory footprint involves loading the d one-dimensional basis operator matrices of size n^2 , loading the n^d vector, writing the final n^d vector, and writing/loading the n^d sub-vectors d -times. Thus, the arithmetic intensity for Eq. (5.48) is $\text{A.I.} = \frac{dn^{d+1}}{(d+2)n^d + dn^2}$. A detailed analysis of the strong scaling and roofline model for high-order methods, such as continuous Galerkin, DG, and hybrid DG, while exploiting sum-factorization on quadrilateral/hexahedral meshes is found in Kronbichler and Wall [62] and Moxey *et al.* [63] for triangular based elements.

For the evaluation of the mass inverse, and other multi-step operators, each step is evaluated consecutively. For example, let's consider applying the weight-adjusted mass matrix inverse approximation, Eq. (5.47), on the right-hand-side. We would first use sum-factorization on multiplying $\tilde{\mathbf{\Pi}}(\boldsymbol{\xi}_v^r)^T$ to the right-hand-side at dn^{d+1} flops. Then we multiply the inverse of a diagonal operator storing the determinant of the Jacobian multiplied with the quadrature weights at n^d flops. Lastly, we use sum-factorization to multiply $\tilde{\mathbf{\Pi}}(\boldsymbol{\xi}_v^r)$ for an additional dn^{d+1} flops. Rather than building a mass matrix at n^{2d} flops, inverting it at n^{3d} flops, and performing one matrix-vector operation at n^{2d} flops, we used the *matrix-free* sum-factorization approach to evaluate it in three separate steps, at a total of $2dn^{d+1} + n^d$ flops.

For the Hadamard product in Eq. (5.37), we use the sum-factorized Hadamard product from Cicchino and Nadarajah [41, Thm. 2.1]. The volume-volume Hadamard product from the upper left block of Eq. (5.38) is evaluated in dn^{d+1} flops. The surface-volume Hadamard products from the upper right and lower left blocks in Eq. (5.38) are each evaluated in dn^d flops. Since sum-factorization evaluates a matrix-vector product in dn^{d+1} flops, the computational cost difference between the divergence of the flux in conservative strong DG and the Hadamard product in NSFR is in the evaluation of the two-point flux.

In Sec. 5.7.4, for the Taylor-Green vortex problem on a nonsymmetrically warped curvilinear mesh, we numerically verify the scaling at order $\mathcal{O}(n^{d+1})$ for the NSFR discretization in Eq. (5.37) as compared to the conservative DG scheme in Eq. (5.24) with and without overintegration. We also numerically compare the wall clock time for the flow simulation.

5.6 Conserved Properties of NSFR

In this section we provide the three main theorems of this work: free-stream preservation, global conservation, and entropy stability for NSFR in a weight-adjusted framework.

5.6.1 Free-stream Preservation

The first conserved quantity that NSFR preserves is free-stream preservation. If the free-stream is not preserved, then the nonlinear metric terms would introduce cross-wind into the flow that drastically destroy the fidelity of the solver [47, 64]. Thus, for curvilinear coordinates, it is necessary that the discretization is provably free-stream preserving.

Theorem 5.6.1. *The NSFR discretization in Eq. (5.37) with the weight-adjusted low-storage mass matrix inverse from Eq. (5.47) is free-stream preserving.*

Proof. Similar to Cicchino *et al.* [38, Sec. 5.1], we substitute $\mathbf{f}_m = \boldsymbol{\alpha} = \text{constant}$ and $\frac{d\hat{\mathbf{u}}_m(t)}{dt} = \mathbf{0}$ into Eq. (5.37),

$$[\boldsymbol{\chi}(\boldsymbol{\xi}_v^r)^T \boldsymbol{\chi}(\boldsymbol{\xi}_f^r)^T] \left[(\tilde{\mathbf{Q}} - \tilde{\mathbf{Q}}^T) \odot \mathbf{F}_m^r \right] \mathbf{1}^T + \sum_{f=1}^{N_f} \sum_{k=1}^{N_{fp}} \boldsymbol{\chi}(\boldsymbol{\xi}_{fk}^r)^T W_{fk} \hat{\mathbf{n}}^r \cdot \boldsymbol{\alpha} \mathbf{C}_m(\boldsymbol{\xi}_{fk}^r). \quad (5.49)$$

Substituting the SBP property Eq. (5.39) for $\tilde{\mathbf{Q}}^T$ into Eq. (5.49) results in,

$$[\boldsymbol{\chi}(\boldsymbol{\xi}_v^r)^T \boldsymbol{\chi}(\boldsymbol{\xi}_f^r)^T] \left[2\tilde{\mathbf{Q}} \odot \mathbf{F}_m^r \right] \mathbf{1}^T + \sum_{f=1}^{N_f} \sum_{k=1}^{N_{fp}} \boldsymbol{\chi}(\boldsymbol{\xi}_{fk}^r)^T W_{fk} \hat{\mathbf{n}}^r \cdot [\boldsymbol{\alpha} \mathbf{C}_m(\boldsymbol{\xi}_{fk}^r) - \boldsymbol{\alpha} \mathbf{C}_m(\boldsymbol{\xi}_{fk}^r)], \quad (5.50)$$

where the surface integral cancels off. For the Hadamard product, we note that the physical flux is constant, rendering the reference flux $(\mathbf{F}_m^r)_{ij} = \frac{1}{2} \boldsymbol{\alpha} (\mathbf{C}_m(\boldsymbol{\xi}_i^r) + \mathbf{C}_m(\boldsymbol{\xi}_j^r))$ equal to the central flux with respect to the metric cofactor matrix. Using Fisher and Carpenter [4, Thm

3.1 and 3.2] and Gassner *et al.* [5, Eq. (3.5)], we can expand the Hadamard product as,

$$\begin{aligned}
& [\boldsymbol{\chi}(\boldsymbol{\xi}_v^r)^T \boldsymbol{\chi}(\boldsymbol{\xi}_f^r)^T] \left[2\tilde{\mathbf{Q}} \odot \mathbf{F}_m^r \right] \mathbf{1}^T = \boldsymbol{\chi}(\boldsymbol{\xi}_v^r)^T \mathbf{W} \nabla^r \boldsymbol{\phi}(\boldsymbol{\xi}_v^r) \cdot (\boldsymbol{\alpha} \mathbf{C}_m(\boldsymbol{\xi}_v^r)) \\
& - \boldsymbol{\chi}(\boldsymbol{\xi}_v^r)^T \sum_{f=1}^{N_f} \sum_{k=1}^{N_{fp}} \left[\boldsymbol{\phi}(\boldsymbol{\xi}_{fk}^r)^T W_{fk} \hat{\mathbf{n}}^r \cdot \boldsymbol{\phi}(\boldsymbol{\xi}_{fk}^r) (\boldsymbol{\alpha} \mathbf{C}_m(\boldsymbol{\xi}_v^r)) - \frac{1}{2} \boldsymbol{\phi}(\boldsymbol{\xi}_{fk}^r)^T W_{fk} \hat{\mathbf{n}}^r \cdot (\boldsymbol{\alpha} \mathbf{C}_m(\boldsymbol{\xi}_{f,k}^r)) \right] \\
& + \frac{1}{2} \sum_{f=1}^{N_f} \sum_{k=1}^{N_{fp}} \boldsymbol{\chi}(\boldsymbol{\xi}_{f,k}^r)^T W_{fk} \hat{\mathbf{n}}^r \cdot \boldsymbol{\phi}(\boldsymbol{\xi}_{fk}^r) (\boldsymbol{\alpha} \mathbf{C}_m(\boldsymbol{\xi}_v^r)).
\end{aligned} \tag{5.51}$$

The volume term on the right-hand side vanishes if the GCL in Eq. (3.7) is satisfied discretely. In Cicchino *et al.* [38, Sec. 5], we provided a detailed review to construct the metric terms to discretely satisfy GCL with consistent surface normals. The review in Cicchino *et al.* [38, Sec. 5] first summarized Kopriva's [47] derivation of the conservative and invariant curl forms, then followed the work by Abe *et al.* [65] to ensure consistency on the surfaces for different flux and grid nodes. By using the consistency condition from the mapping shape functions from the grid nodes to the flux nodes, then $\boldsymbol{\phi}(\boldsymbol{\xi}_{fk}^r) (\boldsymbol{\alpha} \mathbf{C}_m(\boldsymbol{\xi}_v^r)) = \boldsymbol{\alpha} \mathbf{C}_m(\boldsymbol{\xi}_{f,k}^r)$, and $\boldsymbol{\phi}(\boldsymbol{\xi}_{fk}^r) \boldsymbol{\chi}(\boldsymbol{\xi}_v^r) = \boldsymbol{\chi}(\boldsymbol{\xi}_{fk}^r)$, which sees the surface terms eliminated. Therefore, the NSFR discretization is free-stream preserving for vector-valued conservation laws. □

5.6.2 Global Conservation

A crucial property for discretizations that approximate weak solutions to conservation laws is that they discretely satisfy conservation. Continuously, the conservation property is obtained by performing divergence theorem on the flux, $\int_{\Omega} \frac{\partial u}{\partial t} d\Omega = - \int_{\Omega} \nabla \cdot \mathbf{f} d\Omega = - \int_{\Gamma} \mathbf{f} \cdot \hat{\mathbf{n}} d\Gamma$.

Theorem 5.6.2. *The NSFR discretization in Eq. (5.37) with the weight-adjusted low-storage mass matrix inverse from Eq. (5.47) is locally conserving.*

Proof. For each equation of state we left multiply Eq. (5.37) by $\hat{\mathbf{1}}$, such that $\chi(\xi_v^r)\hat{\mathbf{1}}^T = \mathbf{1}^T$,

$$\hat{\mathbf{1}} (\mathbf{M}_m + \mathbf{K}_m) \frac{d}{dt} \hat{\mathbf{u}}_m(t)^T + \mathbf{1} \left[(\tilde{\mathbf{Q}} - \tilde{\mathbf{Q}}^T) \odot \mathbf{F}_m^r \right] \mathbf{1}^T + \sum_{f=1}^{N_f} \sum_{k=1}^{N_{fp}} W_{fk} \hat{\mathbf{n}}^r \cdot \mathbf{f}_m^{*,r}. \quad (5.52)$$

Akin to [1, 2, 5, 24, 28, 31, 66–70], $(\tilde{\mathbf{Q}} - \tilde{\mathbf{Q}}^T) \odot \mathbf{F}_m^r$ is skew-symmetric, so the volume terms vanish. Also, we substitute $\hat{\mathbf{1}} \mathbf{K}_m \frac{d}{dt} \hat{\mathbf{u}}_m(t)^T = 0$ because $\hat{\mathbf{1}} \mathbf{K}_m = \mathbf{0}$. Therefore,

$$\hat{\mathbf{1}} (\mathbf{M}_m + \mathbf{K}_m) \frac{d}{dt} \hat{\mathbf{u}}_m(t)^T = \hat{\mathbf{1}} \mathbf{M}_m \hat{\mathbf{u}}_m(t)^T = - \sum_{f=1}^{N_f} \sum_{k=1}^{N_{fp}} W_{fk} \hat{\mathbf{n}}^r \cdot \mathbf{f}_m^{*,r}, \quad (5.53)$$

recovers the local conservation result for discontinuous Galerkin schemes and the scheme is locally conservative. \square

After summing across all of the elements and using a telescopic flux, the scheme is globally conservative.

5.6.3 Nonlinear Stability

The last theorem of this section pertains to nonlinear stability. When a scheme is provably discretely nonlinearly stable, then, based from the work of Lyapunov, the approximate solution is bounded within a norm to the true solution. Hence, the discrete solution remains stable provided the positivity of density and pressure. It is important to note that stability does not imply convergence.

Theorem 5.6.3. *The NSFR discretization in Eq. (5.37) with the weight-adjusted low-storage mass matrix inverse from Eq. (5.47) is discretely entropy conserving if the two-point flux satisfies the Tadmor shuffle condition. Thus, the NSFR discretization in Eq. (5.37) is nonlinearly stable.*

Proof. We left multiply Eq. (5.37) by the modal coefficients of the entropy variables evaluated at the quadrature nodes, and sum over all of the states,

$$\begin{aligned} \sum_{n=1}^{n_{\text{state}}} \left[\hat{\mathbf{v}}_n (\mathbf{M}_m + \mathbf{K}_m) \frac{d}{dt} \hat{\mathbf{u}}_{m,n}(t)^T + \hat{\mathbf{v}}_n [\boldsymbol{\chi}(\boldsymbol{\xi}_v^r)^T \boldsymbol{\chi}(\boldsymbol{\xi}_f^r)^T] \left[(\tilde{\mathbf{Q}} - \tilde{\mathbf{Q}}^T) \odot \mathbf{F}_{m,n}^r \right] \mathbf{1}^T \right. \\ \left. + \hat{\mathbf{v}}_n \sum_{f=1}^{N_f} \sum_{k=1}^{N_{fp}} \boldsymbol{\chi}(\boldsymbol{\xi}_{fk}^r)^T W_{fk} \hat{\mathbf{n}}^r \cdot \mathbf{f}_{m,n}^{*,r} \right]. \end{aligned} \quad (5.54)$$

It is important to note that Eq. (5.54) is not the same as only applying the $(\mathbf{M}_m + \mathbf{K}_m)^{-1}$ on the surface as commonly used in the FR literature [12, 15, 16, 25, 26, 71–73]. To demonstrate this, consider comparing the stability condition for NSFR,

NSFR Stability:

$$\begin{aligned} \sum_{n=1}^{n_{\text{state}}} \left[\hat{\mathbf{v}}_n (\mathbf{M}_m + \mathbf{K}_m) \frac{d}{dt} \hat{\mathbf{u}}_{m,n}(t)^T \right. \\ \left. + \hat{\mathbf{v}}_n (\mathbf{M}_m + \mathbf{K}_m) (\mathbf{M}_m + \mathbf{K}_m)^{-1} [\boldsymbol{\chi}(\boldsymbol{\xi}_v^r)^T \boldsymbol{\chi}(\boldsymbol{\xi}_f^r)^T] \left[(\tilde{\mathbf{Q}} - \tilde{\mathbf{Q}}^T) \odot \mathbf{F}_{m,n}^r \right] \mathbf{1}^T \right. \\ \left. + \hat{\mathbf{v}}_n (\mathbf{M}_m + \mathbf{K}_m) (\mathbf{M}_m + \mathbf{K}_m)^{-1} \sum_{f=1}^{N_f} \sum_{k=1}^{N_{fp}} \boldsymbol{\chi}(\boldsymbol{\xi}_{fk}^r)^T W_{fk} \hat{\mathbf{n}}^r \cdot \mathbf{f}_{m,n}^{*,r} \right], \end{aligned} \quad (5.55)$$

versus a classical ESFR scheme in a flux differencing form,

ESFR Flux Differencing Stability:

$$\begin{aligned} \sum_{n=1}^{n_{\text{state}}} \left[\hat{\mathbf{v}}_n (\mathbf{M}_m + \mathbf{K}_m) \frac{d}{dt} \hat{\mathbf{u}}_{m,n}(t)^T \right. \\ \left. + \hat{\mathbf{v}}_n (\mathbf{M}_m + \mathbf{K}_m) (\mathbf{M}_m)^{-1} [\boldsymbol{\chi}(\boldsymbol{\xi}_v^r)^T \boldsymbol{\chi}(\boldsymbol{\xi}_f^r)^T] \left[(\tilde{\mathbf{Q}} - \tilde{\mathbf{Q}}^T) \odot \mathbf{F}_{m,n}^r \right] \mathbf{1}^T \right. \\ \left. + \hat{\mathbf{v}}_n (\mathbf{M}_m + \mathbf{K}_m) (\mathbf{M}_m + \mathbf{K}_m)^{-1} \sum_{f=1}^{N_f} \sum_{k=1}^{N_{fp}} \boldsymbol{\chi}(\boldsymbol{\xi}_{fk}^r)^T W_{fk} \hat{\mathbf{n}}^r \cdot \mathbf{f}_{m,n}^{*,r} \right]. \end{aligned} \quad (5.56)$$

By considering FR as DG with a modified mass matrix $\mathbf{M}_m + \mathbf{K}_m$, we directly incorporate the influence of the FR correction functions through \mathbf{K}_m on the non-conservative volume terms. This allows Eq. (5.54) to implicitly have $(\mathbf{M}_m + \mathbf{K}_m)(\mathbf{M}_m + \mathbf{K}_m)^{-1}$ cancel on the

volume-surface hybrid term as seen in Eq. (5.55). That was not observed in Ranocha *et al.* [25, 73] nor Abe *et al.* [26] since the ESFR flux differencing volume term does not have the \mathbf{K}_m operator vanish, which renders it unstable, as seen by $\mathbf{K}_m \mathbf{M}_m^{-1}$ in Eq. (5.56).

The next step highlights the importance of using the entropy-projected variables. As in, Chan [1], we will denote $\tilde{\mathbf{v}} = \boldsymbol{\chi}(\boldsymbol{\xi}^r) \hat{\mathbf{v}}^T$, then the volume-surface hybrid term becomes,

$$\begin{aligned} & \sum_{n=1}^{n_{\text{state}}} \hat{\mathbf{v}}_n [\boldsymbol{\chi}(\boldsymbol{\xi}_v^r)^T \boldsymbol{\chi}(\boldsymbol{\xi}_f^r)^T] \left[(\tilde{\mathbf{Q}} - \tilde{\mathbf{Q}}^T) \odot \mathbf{F}_{m,n}^r \right] \mathbf{1}^T \\ &= \sum_{n=1}^{n_{\text{state}}} \sum_{i,j=1}^{N_v+N_f N_{fp}} \left(\tilde{\mathbf{Q}} \right)_{ij} \cdot (\tilde{v}_{n,i} - \tilde{v}_{n,j}) \mathbf{f}_{s,n}^r(\tilde{\mathbf{u}}_m(\boldsymbol{\xi}_i^r), \tilde{\mathbf{u}}_m(\boldsymbol{\xi}_j^r)). \end{aligned} \quad (5.57)$$

Chan [1] arrived at Eq. (5.57) by expanding the volume hybrid term in a flux differencing form that sums over all quadrature nodes [1, Eq. (71)]. Then the Tadmor shuffle condition was substituted for the change of entropy variables and two-point flux to recover the entropy potential on the surface through integration-by-parts [1, Eq. (72) and (73)]. The substitution for the Tadmor shuffle condition by Chan [1, Eq. (72) and (73)] was only possible because the two-point flux was constructed by the entropy projected variables. Since the Tadmor shuffle condition is a function of the entropy variables in Eq. (5.41), the two-point flux has to satisfy $\mathbf{f}_{s,n} = \frac{\psi_{n,i} - \psi_{n,j}}{\tilde{v}_{n,i} - \tilde{v}_{n,j}}$, and thus the conservative variables used to construct \mathbf{f}_s need to be mapped from $\tilde{\mathbf{v}}$. Making the substitution renders,

$$\sum_{n=1}^{n_{\text{state}}} \hat{\mathbf{v}}_n (\mathbf{M}_m + \mathbf{K}_m) \frac{d}{dt} \hat{\mathbf{u}}_{m,n}(t)^T = \sum_{n=1}^{n_{\text{state}}} \sum_{f=1}^{N_f} \sum_{k=1}^{N_{fp}} (\psi_n(\boldsymbol{\xi}_{fk}^r) - v_n(\boldsymbol{\xi}_{fk}^r) \mathbf{f}_{m,n}^{*,r}) \cdot \hat{\mathbf{n}}^r. \quad (5.58)$$

Using appropriate boundary conditions, and the choice of $\mathbf{f}_{m,n}^{*,r}(\tilde{\mathbf{u}}_{\text{left}}(\boldsymbol{\xi}_{fk}^r), \tilde{\mathbf{u}}_{\text{right}}(\boldsymbol{\xi}_{fk}^r))$ as an entropy conserving flux based on entropy projected variables from the left and right of the face, completes the proof for discrete entropy conservation within the $(\mathbf{M}_m + \mathbf{K}_m)$ -norm. \square

To incorporate entropy dissipation, as extensively detailed by Chandrashekar [55, Sec. 5 and 6], careful treatment needs to be considered. By directly considering the jump in the conservative variables with a positive scalar does not provably guarantee entropy dissipation

because the jump in energy is not entropy dissipative [55, Sec. 5.2]. Thus, we make use of the Roe dissipation [74] which can provably be recast with the jump of the entropy variables to provably add entropy dissipation [55, 56].

An important consequence of the need for projected entropy variables to satisfy the Tadmor shuffle condition in the volume is that a scheme cannot be discretely kinetic energy preserving if the surface quadrature is not a subset of the volume quadrature. For example, if the scheme is integrated on Gauss-Legendre quadrature nodes it cannot be exactly discretely kinetic energy preserving, whereas if it is integrated on Gauss-Legendre-Lobatto volume quadrature it can be kinetic energy preserving.

Lemma 5.6.1. *An uncollocated high-order discretization cannot be exactly discretely kinetic energy preserving if the surface quadrature nodes are not a subset of the volume quadrature nodes.*

Proof.

We begin by considering the kinetic energy as $K.E. = \frac{1}{2}\rho(u^2 + v^2 + w^2)$. Similarly to entropy, the kinetic energy variables are,

$$\mathbf{v}_{K.E.} = \frac{\partial K.E.}{\partial \mathbf{u}} = \left[-\frac{u^2 + v^2 + w^2}{2}, u, v, w, 0 \right], \quad (5.59)$$

and the kinetic energy potential is $\psi^k = 0, \forall k \in [1, d]$. Since the fifth value of $\mathbf{v}_{K.E.}$ is 0, an inverse mapping from $\mathbf{v}_{K.E.} \rightarrow \mathbf{u}$ does not exist. Considering we have a two-point flux that satisfies kinetic energy preservation, we need the surface numerical flux evaluated with the entropy projected variables on the face f facet cubature node k , $\tilde{\mathbf{u}}(\boldsymbol{\xi}_{fk}^r) = \mathbf{u}(\boldsymbol{\chi}(\boldsymbol{\xi}_{fk}^r) \hat{\mathbf{v}}_{K.E.}^T)$. Although we can evaluate the interpolation of the kinetic energy variable to the face, we cannot perform the inverse mapping to extract the conservative variables. If the surface quadrature nodes are a subset of the volume quadrature nodes, then the interpolation and projection operators become an identity, and the inverse mapping is never needed to evaluate $\tilde{\mathbf{u}}(\boldsymbol{\xi}_{fk}^r)$, allowing for discrete kinetic energy conservation only for the case when the surface quadrature

nodes are a subset of the volume quadrature nodes (for example Gauss-Lobatto-Legendre). □

We numerically verify Lemma 5.6.1 in Sec. 5.7.3, where kinetic energy is conserved to machine precision when integrated on Gauss-Lobatto-Legendre quadrature nodes, and it is dissipated when integrated on Gauss-Legendre quadrature nodes.

5.7 Results

In this section, we use the open-source Parallel High-order Library for PDEs (PHiLiP) [75]. We first perform a grid study to verify the orders of convergence with the weight-adjusted framework. Then, we numerically verify the nonlinear stability properties from Section 5.6.

For all tests, we use a 4-stage, fourth-order Runge-Kutta timestepping scheme with an adaptive timestep based on the maximum wavespeed in the domain with a CFL= 0.1. We let the adiabatic constant $\gamma = 1.4$ for all tests. For the NSFR-EC schemes, “EC” refers to entropy conserving, we use Chandrashekar’s [55] entropy conserving flux with Ranocha’s [76] pressure fix for kinetic energy preservation for the two-point flux; while “GL” refers to integrating on Gauss-Legendre nodes and “LGL” refers to integrating on Lobatto-Gauss-Legendre quadrature. All schemes have the conservative solution modal coefficients on LGL nodes. We use the weight-adjusted mass matrix inverse for all schemes except the conservative DG. For the curvilinear case, the metric terms are constructed by $p + 1$ order polynomials detailed in Cicchino *et al.* [38]. Lastly, when the scheme is “overintegrated”, the number of quadrature nodes is $(p + 1) + \text{overintegration}$.

For the curvilinear grid, it is important to use a non-symmetric mapping in every direction to ensure that none of the nonlinear metric terms implicitly factor off, as discussed in

Cicchino *et al.* [38]. The three-dimensional mapping is

$$\begin{aligned}
 [x, y, z] &\in [x_L, x_R]^3, \quad [a, b, c] \in [x_L, x_R]^3, \quad l = \frac{x_R - x_L}{2\pi}, \\
 x &= a + \beta \sin\left(\frac{a}{l}\right) \sin\left(\frac{b}{l}\right) \sin\left(\frac{2c}{l}\right), \\
 y &= b + \beta \sin\left(\frac{4a}{l}\right) \sin\left(\frac{b}{l}\right) \sin\left(\frac{3c}{l}\right), \\
 z &= c + \beta \sin\left(\frac{2a}{l}\right) \sin\left(\frac{5b}{l}\right) \sin\left(\frac{c}{l}\right).
 \end{aligned} \tag{5.60}$$

A cross-section for Eq. (5.60) is presented in Figure 5.1.

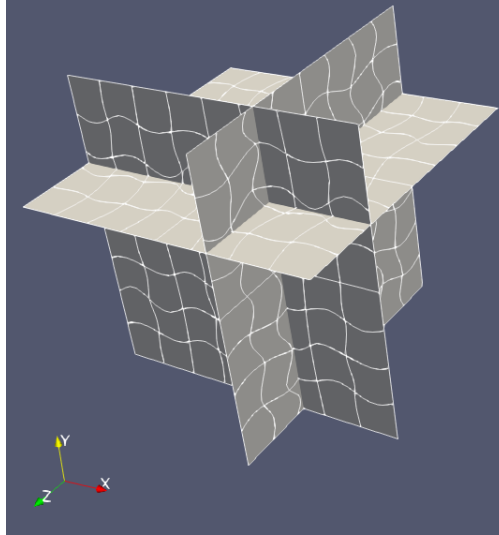


Figure 5.1: 3D Nonsymmetrically Warped Curvilinear Grid Cross-Section.

5.7.1 Manufactured Solution Convergence

In this subsection we consider the manufactured solution for Euler's equations from Gassner *et al.* [5],

$$\begin{aligned}
 \rho &= 2 + \frac{1}{10} \sin(\pi(x + y + z - 2t)), \\
 u &= 1, \\
 v &= 1, \\
 w &= 1, \\
 \rho e &= \rho^2,
 \end{aligned} \tag{5.61}$$

with the unsteady source term,

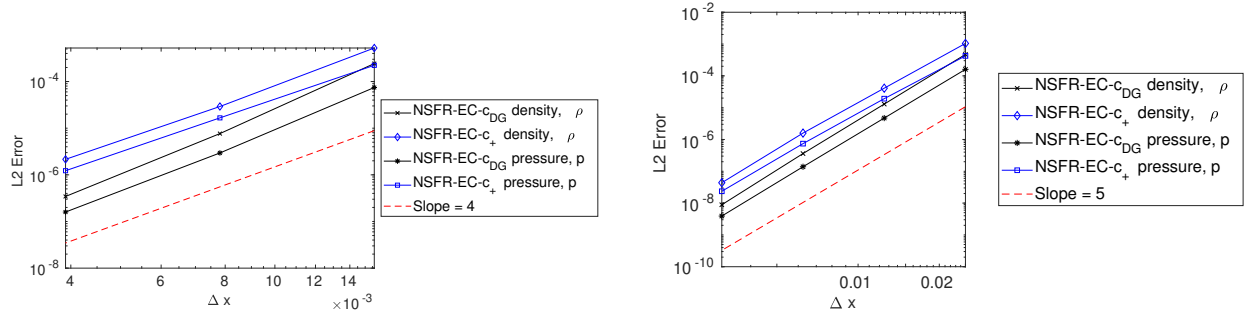
$$\mathbf{q} = \begin{bmatrix} c_1 \cos(\pi(x + y + z - 2t)) \\ c_2 \cos(\pi(x + y + z - 2t)) + c_3 \sin(2\pi(x + y + z - 2t)) \\ c_2 \cos(\pi(x + y + z - 2t)) + c_3 \sin(2\pi(x + y + z - 2t)) \\ c_2 \cos(\pi(x + y + z - 2t)) + c_3 \sin(2\pi(x + y + z - 2t)) \\ c_4 \cos(\pi(x + y + z - 2t)) + c_5 \sin(2\pi(x + y + z - 2t)) \end{bmatrix}, \tag{5.62}$$

with $c_1 = \frac{\pi}{10}$, $c_2 = -\frac{\pi}{5} + \frac{\pi}{20}(1 + 5\gamma)$, $c_3 = \frac{\pi}{100}(\gamma - 1)$, $c_4 = \frac{\pi}{20}(-7 + 15\gamma)$, and $c_5 = \frac{\pi}{100}(3\gamma - 2)$. The domain is $[x, y, z] \in [-1, 1]^3$, and we use $\beta = \frac{1}{50}$ and $l = 2$ in the warping Eq. (5.60). The Δx is taken as the average distance between two quadrature points, $\frac{l}{M_1 D^{(p+1)}}$, where $M_1 D$ is the total number of elements in one-dimension. We simulate for one cycle to a final nondimensionalized time of $t_f = 2$. For the surface numerical flux, we add Roe dissipation [74] to the entropy conserving baseline flux. We integrate on Gauss-Legendre quadrature nodes with an uncollocated Lagrange modal basis. We used the weight-adjusted mass inverse approximation from Eq. (5.47) with an adaptive timestep of $\Delta t = 0.2 \frac{\Delta x}{\lambda_{\max}}$, where λ_{\max} is the maximum eigenvalue in the domain.

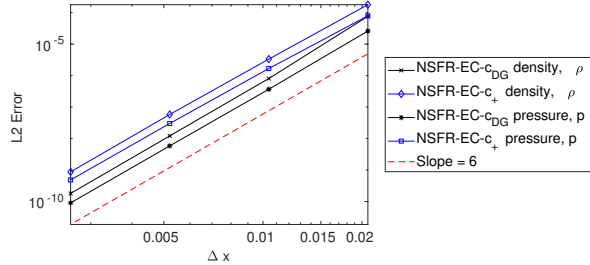
The L2-error is computed as,

$$\text{L2 - error} \approx \sqrt{\sum_{m=1}^M \int_{\Omega_m} (u_m - u)^2 d\Omega_m} = \sqrt{\sum_{m=1}^M (\mathbf{u}_m^T - \mathbf{u}_{exact}^T) \mathbf{W} \mathbf{J}_m (\mathbf{u}_m - \mathbf{u}_{exact})}. \quad (5.63)$$

The orders are presented in Fig. 5.2 for both density and pressure for the NSFR entropy conserving (EC) scheme with c_{DG} and c_+ .



(a) 3D Manufactured Solution $p = 3$ Orders of Convergence. (b) 3D Manufactured Solution $p = 4$ Orders of Convergence.



(c) 3D Manufactured Solution $p = 5$ Orders of Convergence.

Figure 5.2: 3D Manufactured Solution Orders of Convergence

From Fig. 5.2, we observe that the NSFR discretization converges at $p + 1$ for both c_{DG} and c_+ variants in curvilinear coordinates. The error levels obtained with c_+ were slightly larger than those obtained with c_{DG} for the same grid level and polynomial order as expected. The larger error levels are a trade-off for larger maximum timesteps offered by c_+ .

5.7.2 Maximum CFL

In this subsection we compare the maximum CFL numerically obtained for different NSFR schemes. We consider the manufactured solution from Sec. 5.7.1 and run it for different NSFR correction parameter choices, different integration nodes, and different polynomial degrees. The manufactured solution is integrated until a final time $t_f = 1.0$ s for each combination of parameters with a CFL= 0.1. Then, we increase the CFL by 0.01 and rerun the test until the computed pressure error at $t_f = 1.0$ exceeds seven significant digits as compared to the solution obtained with a CFL= 0.1. GL implies that the scheme was integrated on Gauss-Legendre quadrature nodes, and LGL signifies that the scheme was integrated on Gauss-Legendre-Lobatto quadrature nodes.

Scheme	Quadrature	Max CFL
NSFR c_{DG}	GL	0.18
NSFR c_+	GL	0.21
NSFR c_{HU}	GL	0.22
NSFR c_{DG}	LGL	0.16
NSFR c_+	LGL	0.24

(a) Max CFL for $p = 3$, 4^3 elements.

Scheme	Quadrature	Max CFL
NSFR c_{DG}	GL	0.17
NSFR c_+	GL	0.29
NSFR c_{HU}	GL	0.24
NSFR c_{DG}	LGL	0.14
NSFR c_+	LGL	0.28

(b) Max CFL for $p = 4$, 4^3 elements.

Scheme	Quadrature	Max CFL
NSFR c_{DG}	GL	0.17
NSFR c_+	GL	0.22
NSFR c_{HU}	GL	0.23
NSFR c_{DG}	LGL	0.16
NSFR c_+	LGL	0.20

(c) Max CFL for $p = 5$, 4^3 elements.

Table 5.1: Max CFL for $p = 3$, $p = 4$ and $p = 5$, 4^3 elements.

Table 5.1 shows an increase in CFL from c_{DG} to c_+ as that found for linear advection

by Vincent *et al.* [54], but the difference in CFL values is not as large as the linear case from Vincent *et al.* [54]. In the NSFR implementation Eq. (5.37), this increase in CFL comes without additional runtime computational cost. Unlike the results from Gassner and Kopriva [77], we did not find an increase in CFL by using LGL nodes as compared to GL nodes, except only for $p = 3$ and c_+ . We believe this was due to the loss of integration strength with LGL nodes as compared to GL nodes. Gassner and Kopriva [77] considered a linear flux on a linear grid, where LGL nodes would integrate the volume divergence of the flux exactly, whereas, for our cases, the flux is rational on a curvilinear mesh. For the nonlinear case, to replicate the filter obtained in Gassner and Kopriva [77] we also ran a value of c_{HU} . When integrated on GL nodes with a value of c_{HU} and a Lagrange basis with LGL solution nodes, the modified mass matrix is exactly the LGL collocated mass matrix [11, 12, 78]. Thus, the nonlinear extension for the CFL increase from Gassner and Kopriva [77] would be using NSFR with c_{HU} .

For $p = 3$ and $p = 5$, c_{HU} gave a slightly larger CFL than c_+ . The value of c_+ used was numerically obtained from the von Neumann analysis for linear advection by Vincent and coauthors [54]. This case considers a rational flux, and due to the nonlinearities, the c value that corresponds to the maximum timestep might be slightly lower than the c_+ value for one-dimensional linear advection. A full conclusion on the value of c_+ for nonlinear and rational fluxes cannot be drawn until a von Neumann analysis for nonlinear problems is performed for the cases.

5.7.3 Inviscid Taylor Green Vortex

We consider the inviscid Taylor-Green vortex problem, initialized on the periodic box as,

$$\begin{aligned}
 \rho &= 1, \\
 u &= \sin x \cos y \cos z, \\
 v &= -\cos x \sin y \cos z, \\
 w &= 0, \\
 p &= \frac{100}{\gamma} + \frac{1}{16} \left(\cos 2x \cos 2z + 2 \cos 2x + 2 \cos 2y + \cos 2y \cos 2z \right), \\
 \mathbf{x}^c &\in [0, 2\pi]^3, \quad t \in [0, 14].
 \end{aligned} \tag{5.64}$$

We consider both a Cartesian mesh and the heavily warped, periodic grid defined by Eq. (5.60) with $\beta = \frac{1}{5}$. We use 4 elements in each direction and verify that the discrete change in entropy, $\hat{\mathbf{v}} (\mathbf{M}_m + \mathbf{K}_m) \frac{d}{dt} \hat{\mathbf{u}}(t)^T$, is conserved on the order of 1×10^{-13} for $p = 4, 5$. These polynomial orders and mesh size correspond to 20^3 and 24^3 degrees of freedom to simulate under-resolved turbulence. This test showcases the strength of the entropy conserving framework because a conservative DG scheme, without the entropy stable framework, diverges. All schemes were globally conservative and free-stream preserving on the order of 1×10^{-16} . In Fig. 5.3, for a polynomial degree of 4, we plot the discrete change in entropy for c_{HU} and c_+ with the weight-adjusted inverse, and c_+ without using a weight-adjusted inverse on the curvilinear grid to demonstrate the discrete entropy conservation.

Scheme	Overintegration	Discrete Entropy Conserved $\mathcal{O}(1e-13)$
Cons. DG-GL	0	No
NSFR-EC-LGL c_{DG}	0	Yes
NSFR-EC-LGL c_{DG}	3	Yes
NSFR-EC-GL c_{DG}	0	Yes
NSFR-EC-GL c_{DG}	3	Yes
NSFR-EC-LGL c_+	0	Yes
NSFR-EC-LGL c_+	3	Yes
NSFR-EC-GL c_+	0	Yes
NSFR-EC-GL c_+	3	Yes

Table 5.2: Change in Entropy Results $p = 4,5$ Cartesian Mesh.

Scheme	Overintegration	Discrete Entropy Conserved $\mathcal{O}(1e-13)$
Cons. DG-GL	0	No
NSFR-EC-LGL c_{DG}	0	Yes
NSFR-EC-LGL c_{DG}	3	Yes
NSFR-EC-GL c_{DG}	0	Yes
NSFR-EC-GL c_{DG}	3	Yes
NSFR-EC-LGL c_+	0	Yes
NSFR-EC-LGL c_+	3	Yes
NSFR-EC-GL c_+	0	Yes
NSFR-EC-GL c_+	3	Yes

Table 5.3: Change in Entropy Results $p = 4,5$ Curvilinear Mesh.

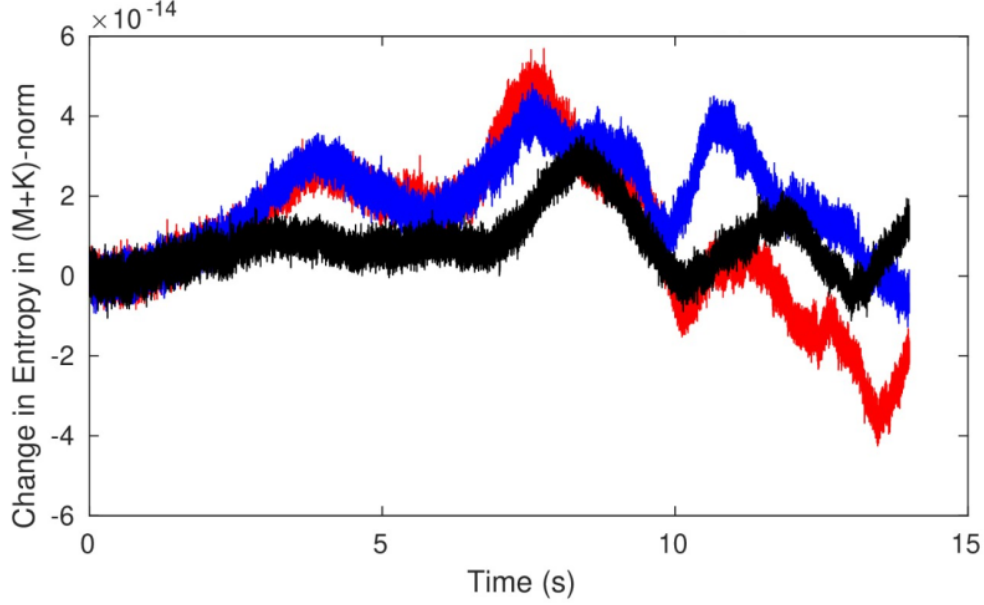


Figure 5.3: Change in Entropy. Red line c_{HU} with weight-adjusted, black line c_+ with weight-adjusted, and blue line c_+ without weight-adjusted mass matrix.

As we can see from Tables 5.2 and 5.3, for both a Cartesian and curvilinear mesh, the weight-adjusted NSFR entropy conserving discretization discretely conserves the change in entropy on the order of $1e-13$ for arbitrary quadrature integration—provided the integration strength is exact for at least $2p-1$ polynomials. The imperative of showing varying quadrature rules is that, as shown by Winter *et al.* [79], the integration strength affects the polynomial dealiasing for turbulent flows. Since the application for NSFR will be in predicting turbulent flows, Tables 5.2 and 5.3 demonstrate the promising flexibility that the scheme offers.

We additionally plot the change in kinetic energy for the LGL and GL DG cases in Fig. 5.4 to verify Lemma 5.6.1. We first verify that the kinetic energy conserving flux discretely satisfies

$$\sum_{n=1}^{n_{\text{state}}} \hat{\mathbf{v}}_{\text{K.E.,}n} \chi(\boldsymbol{\xi}_v^r)^T \left[\left(\mathbf{W} \nabla^r \phi(\boldsymbol{\xi}_v^r) - \nabla^r \phi(\boldsymbol{\xi}_v^r)^T \mathbf{W} \right) \circ \left(\tilde{\mathbf{F}}_{m,v}^r - \tilde{\mathbf{P}}_{m,v}^r \right) \right] \mathbf{1}^T = \sum_{k=1}^d \psi_{\text{K.E.}}^k = 0$$

on the volume quadrature nodes. In Fig. 5.4, this is demonstrated to machine precision for

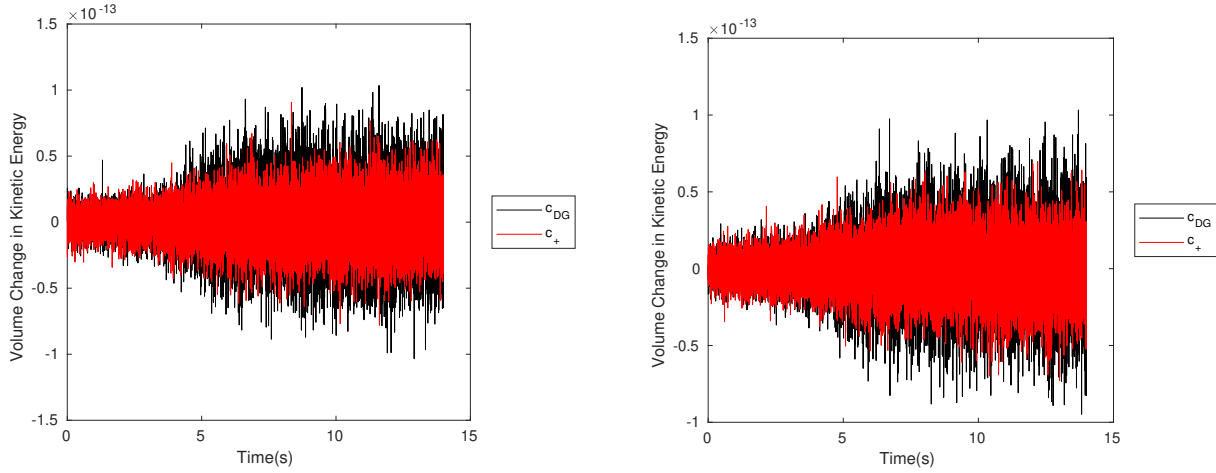
both GL and LGL nodes. Here $\tilde{\mathbf{F}}_{m,v}^r$ is the two-point flux for only the volume nodes,

$$\left(\tilde{\mathbf{F}}_{m,v}^r\right)_{ij} = \mathbf{f}_s(\tilde{\mathbf{u}}_m(\boldsymbol{\xi}_i^r), \tilde{\mathbf{u}}_m(\boldsymbol{\xi}_j^r)) \left(\frac{1}{2}(\mathbf{C}_m(\boldsymbol{\xi}_i^r) + \mathbf{C}_m(\boldsymbol{\xi}_j^r))\right), \forall 1 \leq i, j \leq N_v,$$

and $\tilde{\mathbf{P}}_{m,v}^r$ is the volume pressure work,

$$\left(\tilde{\mathbf{P}}_{m,v}^r\right)_{ij} = \frac{1}{2}(p_i + p_j) \mathbf{I}_d \left(\frac{1}{2}(\mathbf{C}_m(\boldsymbol{\xi}_i^r) + \mathbf{C}_m(\boldsymbol{\xi}_j^r))\right), \forall 1 \leq i, j \leq N_v$$

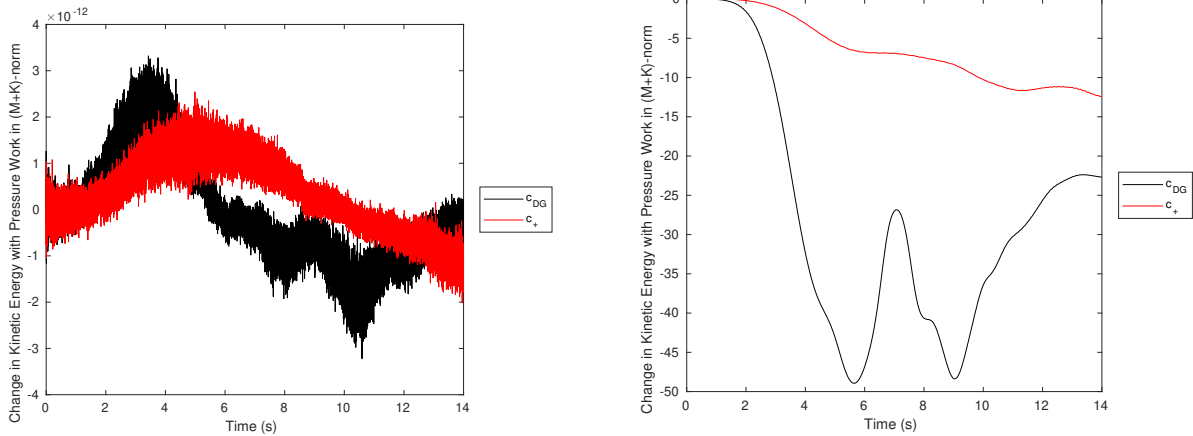
with \mathbf{I}_d the $d \times d$ identity matrix.



(a) Volume Change in Kinetic Energy without Pressure Work LGL.

(b) Volume Change in Kinetic Energy without Pressure Work GL.

Figure 5.4: Volume Change in Kinetic Energy without Pressure Work for LGL and GL Nodes.



(a) Change in Kinetic Energy without Pressure Work LGL. (b) Change in Kinetic Energy without Pressure Work GL.

Figure 5.5: Change in Kinetic Energy without Pressure Work.

Next, we compute the total change in kinetic energy by $\hat{\mathbf{v}}_{\text{K.E.}} (\mathbf{M}_m + \mathbf{K}_m) \frac{d}{dt} \hat{\mathbf{u}}(t)^T - P_{\text{work}}$, where P_{work} is the global pressure work by integrating the volume and surface terms. From Fig. 5.5a, we see for LGL nodes, the total change in kinetic energy is conserved on the order of $1e-12$ since it does not require the inverse mapping of kinetic energy variables to the surface, whereas in Fig. 5.5b, for GL nodes, it is not conserved. Although a kinetic energy conserving numerical flux was used, from Lemma 5.6.1, the LGL case discretely conserved kinetic energy to machine precision, whereas the GL case did not. This verifies Lemma 5.6.1 that global kinetic energy cannot be conserved for uncollocated schemes when the surface nodes are not a subset of the volume nodes because the inverse mapping from $\mathbf{v}_{\text{K.E.}} \rightarrow \mathbf{u}$ does not exist.

5.7.4 NSFR versus DG Conservative with and without Overintegration

Next, using our proposed sum-factorized Hadamard product from Cicchino and Nadarajah [41], we wish to compare the performance of the entropy conserving scheme with the conservative DG scheme using sum-factorization techniques. We solve the three-dimensional inviscid TGV problem, with Gauss-Legendre quadrature nodes on the curvilinear grid defined in Eq. (5.60),

with 4^3 elements and $\beta = \frac{1}{5}$. We solve it in six different ways. First, with the conservative DG scheme that does not require a Hadamard product in Eq. (5.24). Second, the conservative DG scheme overintegrated by $2(p+1)$ quadrature points, to exactly integrate polynomials of order $4p+3$ with GL nodes, and resemble exact integration for a cubic polynomial on a curvilinear grid. We consider overintegration because it is another tool used for stabilization [79] through polynomial dealiasing. Lastly, with our NSFR entropy conserving scheme that requires an uncollocated Hadamard product along with entropy projection techniques. We then, in dashed lines, run the same tests with an FR correction value of c_+ [54] to compare the additional cost of FR versus its DG equivalent. For the test, we evaluate the residual and apply the inverse of the weight-adjusted mass matrix 10 times sequentially and record the total CPU time. The test was run in parallel with 4 Intel i5-8600 CPUs with 4GB of DDR4 RAM. The CPU time presented is the sum across ranks of the CPU times on each processor.

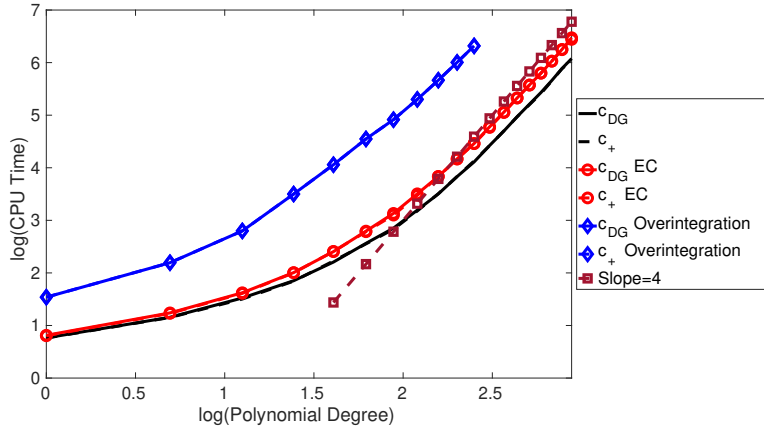


Figure 5.6: CPU time versus polynomial degree TGV.

From Figure 5.6, all three methods have the solver scale at order $\mathcal{O}(p^{d+1})$ in curvilinear coordinates because they exploit sum-factorization [40] for the matrix-vector products, and the NSFR-EC scheme uses our proposed sum-factorized Hadamard product evaluation [41]. The blue line representing the overintegrated conservative DG scheme took the most amount of CPU time and was run until $p = 20$ due to memory limitations. The conservative DG and NSFR-EC schemes took a comparable amount of CPU time in Fig. 5.6. This result is dependent on the

sum-factorized Hadamard product from Cicchino and Nadarajah [41]—the sum-factorized Hadamard product is evaluated in the same number of flops as the DG divergence of the flux with sum-factorization for the matrix-vector product. The computational cost difference between the DG conservative scheme and the NSFR-EC c_{DG} is in the evaluation of the two-point flux as compared to the convective flux at a single quadrature node. Also, there was a negligible computational cost difference between all c_{DG} versus c_+ schemes since the mass matrix inverse was approximated in a weight-adjusted form. From Fig. 5.6, it appears that using the algorithm in Cicchino and Nadarajah [41, Sec. 2], the entropy conserving scheme’s cost is more comparable to the conservative DG scheme rather than an overintegrated/exactly integrated DG scheme.

To further demonstrate the performance differences between the NSFR-EC- c_{DG} scheme using the “sum-factorized” Hadamard product evaluations detailed in Cicchino and Nadarajah [41, Sec. 2] and the conservative DG scheme in curvilinear coordinates, we run the inviscid TGV on a non-symmetrically warped curvilinear grid and compare the wall clock times. All schemes use an uncollocated, modal Lagrange basis, and are integrated on Gauss-Legendre quadrature nodes. The conservative DG scheme overintegrated by $2(p + 1)$ to resemble exact integration for a cubic polynomial on a curvilinear grid. We integrate in time with a 4-*th* order Runge-Kutta time-stepping scheme with an adaptive Courant-Friedrichs-Lewy value of 0.1 until a final time of $t_f = 14$ s. For NSFR-EC c_{DG} we use Chandrashekar’s flux [55] in the volume and surface with Ranocha’s pressure fix [76]. For the DG conservative scheme, we use the Roe [74] surface numerical flux. All of the tests were run on 1 node with 8 AMD Rome 7532 processors with 4GB of RAM on each CPU provided by the Digital-Alliance of Canada. Each test was run 4 times and we present the average of the 4-tests’ max wall clock time for a single processor and the average of the 4-tests’ total CPU time across the 8 processors.

p	Number of Elements	Scheme	Max Wall Clock (hours)	Total CPU Time (hours)
3	4^3	NSFR-EC- c_{DG}	0.1111	0.8713
		DG-cons	0.09416	0.7376
		DG-cons-overint	0.5033	3.816
	8^3	NSFR-EC- c_{DG}	1.530	12.06
		DG-cons	1.520	11.64
		DG-cons-overint	5.740	44.42
4	4^3	NSFR-EC- c_{DG}	0.2756	2.170
		DG-cons	0.2669	2.053
		DG-cons-overint	0.9977	7.767
	8^3	NSFR-EC- c_{DG}	3.873	30.55
		DG-cons	3.115	24.59
		DG-cons-overint	12.68	100.3
5	4^3	NSFR-EC- c_{DG}	0.5964	4.470
		DG-cons	Crashed	Crashed
		DG-cons-overint	2.013	15.10
	8^3	NSFR-EC- c_{DG}	7.052	52.58
		DG-cons	Crashed	Crashed
		DG-cons-overint	23.41	185.2

Table 5.4: TGV Comparison for CPU and Wall Clock Times.

From Table 5.4, averaging all of the tests, the NSFR-EC- c_{DG} scheme took about a 13% longer CPU time and 12% longer wall clock time as compared to conservative DG. On average, the overintegrated conservative DG scheme took 364% longer CPU time and 365% longer wall clock time than the NSFR-EC- c_{DG} scheme. This small percentage difference between DG conservative and NSFR-EC- c_{DG} demonstrates how the sum-factorized Hadamard product

algorithm in Cicchino and Nadarajah [41] has drastically reduced the computational cost of computing a two-point flux. The $p = 5$ DG conservative scheme diverged at $t = 9.06$ on the 4^3 mesh, and at $t = 6.70$ on the 8^3 mesh. This further demonstrates the advantage of the NSFR-EC scheme since it has provable guaranteed nonlinear stability for a reasonable computational cost trade-off. From both Fig. 5.6 and Table 5.4, it is clear that with the proposed sum-factorized Hadamard product, entropy conserving and stable methods are computationally competitive with classical DG schemes.

5.8 Conclusion

We demonstrated a novel, low-storage, weight-adjusted approach for NSFR schemes in curvilinear coordinates. In the context of an uncollocated case, both theoretical proof and numerical validation have demonstrated the attainability of discrete entropy conservation. Conversely, the preservation of discrete kinetic energy is achievable only for the collocated case on Gauss-Legendre-Lobatto quadrature nodes.

Additionally, in curvilinear coordinates, a unique, dense Gram matrix needs to be inverted within every element. This issue was circumvented by a weight-adjusted approach, where the operation cost was reduced to inverting a unique diagonal matrix storing the determinant of the metric Jacobian at each quadrature node. Coupled with sum-factorization, and the sum-factorized Hadamard product, our proposal greatly accelerates the run-time. For different FR schemes, the weight-adjusted framework maintained nonlinear stability for the inviscid Taylor-Green vortex problem on an extremely coarse, heavily warped curvilinear grid, making it an attractive implementation for FR in the high-performance computing context.

5.9 Acknowledgements

We would like to gratefully acknowledge the financial support of the Natural Sciences and Engineering Research Council of Canada (NSERC) Discovery Grant Program, NSERC

Postgraduate Scholarships – Doctoral program, and McGill University.

References

- [1] Jesse Chan. “On discretely entropy conservative and entropy stable discontinuous Galerkin methods”. In: *Journal of Computational Physics* 362 (2018), pp. 346–374.
- [2] Jesse Chan. “Skew-symmetric entropy stable modal discontinuous Galerkin formulations”. In: *Journal of Scientific Computing* 81.1 (2019), pp. 459–485.
- [3] Eitan Tadmor. “Numerical viscosity and the entropy condition for conservative difference schemes”. In: *Mathematics of Computation* 43.168 (1984), pp. 369–381.
- [4] Travis Calob Fisher. “High-order L2 stable multi-domain finite difference method for compressible flows”. PhD thesis. Purdue University, 2012.
- [5] Gregor J Gassner, Andrew R Winters, and David A Kopriva. “Split form nodal discontinuous Galerkin schemes with summation-by-parts property for the compressible Euler equations”. In: *Journal of Computational Physics* 327 (2016), pp. 39–66.
- [6] Jesse Chan and Lucas C Wilcox. “On discretely entropy stable weight-adjusted discontinuous Galerkin methods: Curvilinear meshes”. In: *Journal of Computational Physics* 378 (2019), pp. 366–393.
- [7] Heinz-Otto Kreiss and Joseph Oliger. “Comparison of accurate methods for the integration of hyperbolic equations”. In: *Tellus* 24.3 (1972), pp. 199–215.
- [8] Blair Swartz and Burton Wendroff. “The relative efficiency of finite difference and finite element methods. I: Hyperbolic problems and splines”. In: *SIAM Journal on Numerical Analysis* 11.5 (1974), pp. 979–993.
- [9] William H Reed and Thomas R Hill. *Triangular mesh methods for the neutron transport equation*. Tech. rep. Los Alamos Scientific Lab., N. Mex.(USA), 1973.

- [10] Jan S. Hesthaven and Tim Warburton. *Nodal discontinuous Galerkin methods algorithms, analysis and applications*. Springer, 2008.
- [11] H. T. Huynh. “A flux reconstruction approach to high-order schemes including discontinuous Galerkin methods”. In: American Institute of Aeronautics and Astronautics, 2007.
- [12] Peter E Vincent, Patrice Castonguay, and Antony Jameson. “A new class of high-order energy stable flux reconstruction schemes”. In: *Journal of Scientific Computing* 47.1 (2011), pp. 50–72.
- [13] Antony Jameson. “A proof of the stability of the spectral difference method for all orders of accuracy”. In: *Journal of Scientific Computing* 45.1-3 (2010), pp. 348–358.
- [14] Zhi Jian Wang and Haiyang Gao. “A unifying lifting collocation penalty formulation including the discontinuous Galerkin, spectral volume/difference methods for conservation laws on mixed grids”. In: *Journal of Computational Physics* 228.21 (2009), pp. 8161–8186.
- [15] Philip Zwanenburg and Siva Nadarajah. “Equivalence between the energy stable flux reconstruction and filtered discontinuous Galerkin schemes”. In: *Journal of Computational Physics* 306 (2016), pp. 343–369.
- [16] Yves Allaneau and Antony Jameson. “Connections between the filtered discontinuous Galerkin method and the flux reconstruction approach to high order discretizations”. In: *Computer Methods in Applied Mechanics and Engineering* 200.49–52 (2011), pp. 3628–3636.
- [17] Alexander Cicchino and Siva Nadarajah. “A new norm and stability condition for tensor product flux reconstruction schemes”. In: *Journal of Computational Physics* (2020), p. 110025.

- [18] Yen Liu, Marcel Vinokur, and Zhi J. Wang. “Spectral difference method for unstructured grids I: Basic formulation”. In: *Journal of Computational Physics* 216.2 (2006), pp. 780–801.
- [19] Eitan Tadmor. “Skew-self adjoint form for systems of conservation laws”. In: *Journal of Mathematical Analysis and Applications* 103.2 (1984), pp. 428–442.
- [20] Eitan Tadmor. “The numerical viscosity of entropy stable schemes for systems of conservation laws. I”. In: *Mathematics of Computation* 49.179 (1987), pp. 91–103.
- [21] Amiram Harten. “On the symmetric form of systems of conservation laws with entropy”. In: *Journal of Computational Physics* 49.1 (1983), pp. 151–164.
- [22] Philippe G LeFloch, Jean-Marc Mercier, and Christian Rohde. “Fully discrete, entropy conservative schemes of arbitrary order”. In: *SIAM Journal on Numerical Analysis* 40.5 (2002), pp. 1968–1992.
- [23] Philippe G LeFloch and Christian Rohde. “High-order schemes, entropy inequalities, and nonclassical shocks”. In: *SIAM Journal on Numerical Analysis* 37.6 (2000), pp. 2023–2060.
- [24] Gregor J Gassner. “A skew-symmetric discontinuous Galerkin spectral element discretization and its relation to SBP-SAT finite difference methods”. In: *SIAM Journal on Scientific Computing* 35.3 (2013), A1233–A1253.
- [25] Hendrik Ranocha, Philipp Öffner, and Thomas Sonar. “Summation-by-parts operators for correction procedure via reconstruction”. In: *Journal of Computational Physics* 311 (2016), pp. 299–328.
- [26] Yoshiaki Abe, Issei Morinaka, Takanori Haga, Taku Nonomura, Hisaichi Shibata, and Koji Miyaji. “Stable, non-dissipative, and conservative flux-reconstruction schemes in split forms”. In: *Journal of Computational Physics* 353 (2018), pp. 193–227.

- [27] David C Del Rey Fernández, Jason E Hicken, and David W Zingg. “Review of summation-by-parts operators with simultaneous approximation terms for the numerical solution of partial differential equations”. In: *Computers & Fluids* 95 (2014), pp. 171–196.
- [28] Jared Crean, Jason E Hicken, David C Del Rey Fernández, David W Zingg, and Mark H Carpenter. “Entropy-stable summation-by-parts discretization of the Euler equations on general curved elements”. In: *Journal of Computational Physics* 356 (2018), pp. 410–438.
- [29] David C Del Rey Fernández, Jared Crean, Mark H. Carpenter, and Jason E. Hicken. “Staggered-grid entropy-stable multidimensional summation-by-parts discretizations on curvilinear coordinates”. In: *Journal of Computational Physics* 392 (2019), pp. 161–186.
- [30] Travis C Fisher and Mark H Carpenter. “High-order entropy stable finite difference schemes for nonlinear conservation laws: Finite domains”. In: *Journal of Computational Physics* 252 (2013), pp. 518–557.
- [31] Lucas Friedrich, Gero Schnücke, Andrew R Winters, David C Del Rey Fernández, Gregor J Gassner, and Mark H Carpenter. “Entropy stable space–time discontinuous Galerkin schemes with summation-by-parts property for hyperbolic conservation laws”. In: *Journal of Scientific Computing* 80.1 (2019), pp. 175–222.
- [32] Matteo Parsani, Mark H Carpenter, and Eric J Nielsen. “Entropy stable wall boundary conditions for the three-dimensional compressible Navier–Stokes equations”. In: *Journal of Computational Physics* 292 (2015), pp. 88–113.
- [33] Rémi Abgrall, Elise le Meledo, and Phiipp Öffner. “On the connection between residual distribution schemes and flux reconstruction”. In: *arXiv preprint arXiv:1807.01261* (2018).

- [34] Rémi Abgrall. “A general framework to construct schemes satisfying additional conservation relations. Application to entropy conservative and entropy dissipative schemes”. In: *Journal of Computational Physics* 372 (2018), pp. 640–666.
- [35] Rémi Abgrall, Philipp Öffner, and Hendrik Ranocha. “Reinterpretation and extension of entropy correction terms for residual distribution and discontinuous Galerkin schemes: Application to structure preserving discretization”. In: *Journal of Computational Physics* 453 (2022), p. 110955.
- [36] Rémi Abgrall, Jan Nordström, Philipp Öffner, and Svetlana Tokareva. “Analysis of the SBP-SAT stabilization for finite element methods part II: Entropy stability”. In: *Communications on Applied Mathematics and Computation* (2021), pp. 1–23.
- [37] Alexander Cicchino, Siva Nadarajah, and David C. Del Rey Fernández. “Nonlinearly stable flux reconstruction high-order methods in split form”. In: *Journal of Computational Physics* (2022), p. 111094.
- [38] Alexander Cicchino, David C Del Rey Fernández, Siva Nadarajah, Jesse Chan, and Mark H Carpenter. “Provably stable flux reconstruction high-order methods on curvilinear elements”. In: *Journal of Computational Physics* 463 (2022), p. 111259.
- [39] Jesse Chan, Russell J Hewett, and Timothy Warburton. “Weight-adjusted discontinuous Galerkin methods: Curvilinear meshes”. In: *SIAM Journal on Scientific Computing* 39.6 (2017), A2395–A2421.
- [40] Steven A Orszag. “Spectral methods for problems in complex geometrics”. In: *Numerical methods for partial differential equations*. Elsevier, 1979, pp. 273–305.
- [41] Alexander Cicchino and Siva Nadarajah. “Scalable Evaluation of Hadamard Products with Tensor Product Basis for Entropy-Stable High-Order Methods”. In: *Accepted with minor modifications to the Journal of Computational Physics, arXiv preprint arXiv:2306.11665* (2023).

- [42] Michael S Mock. “Systems of conservation laws of mixed type”. In: *Journal of Differential equations* 37.1 (1980), pp. 70–88.
- [43] Lorenzo Botti. “Influence of reference-to-physical frame mappings on approximation properties of discontinuous piecewise polynomial spaces”. In: *Journal of Scientific Computing* 52.3 (2012), pp. 675–703.
- [44] David Moxey, Shankar P Sastry, and Robert M Kirby. “Interpolation error bounds for curvilinear finite elements and their implications on adaptive mesh refinement”. In: *Journal of Scientific Computing* 78.2 (2019), pp. 1045–1062.
- [45] Gregor J Gassner, Andrew R Winters, Florian J Hindenlang, and David A Kopriva. “The BR1 scheme is stable for the compressible Navier–Stokes equations”. In: *Journal of Scientific Computing* 77.1 (2018), pp. 154–200.
- [46] Juan Manzanero, Gonzalo Rubio, David A Kopriva, Esteban Ferrer, and Eusebio Valero. “Entropy–stable discontinuous Galerkin approximation with summation–by–parts property for the incompressible Navier–Stokes/Cahn–Hilliard system”. In: *Journal of Computational Physics* 408 (2020), p. 109363.
- [47] David A Kopriva. “Metric identities and the discontinuous spectral element method on curvilinear meshes”. In: *Journal of Scientific Computing* 26.3 (2006), p. 301.
- [48] Patrick D Thomas and Charles K Lombard. “Geometric conservation law and its application to flow computations on moving grids”. In: *AIAA journal* 17.10 (1979), pp. 1030–1037.
- [49] Marcel Vinokur and HC Yee. “Extension of efficient low dissipation high order schemes for 3-D curvilinear moving grids”. In: *Frontiers of Computational Fluid Dynamics 2002*. World Scientific, 2002, pp. 129–164.
- [50] David A Kopriva, Florian J Hindenlang, Thomas Bolemann, and Gregor J Gassner. “Free-Stream Preservation for Curved Geometrically Non-conforming Discontinuous

- Galerkin Spectral Elements”. In: *Journal of Scientific Computing* 79.3 (2019), pp. 1389–1408.
- [51] Patrice Castonguay, Peter E Vincent, and Antony Jameson. “A new class of high-order energy stable flux reconstruction schemes for triangular elements”. In: *Journal of Scientific Computing* 51.1 (2012), pp. 224–256.
- [52] D. M. Williams and A. Jameson. “Energy stable flux reconstruction schemes for advection–diffusion problems on tetrahedra”. In: *Journal of Scientific Computing* 59.3 (2014), pp. 721–759.
- [53] Abhishek Sheshadri and Antony Jameson. “On the stability of the flux reconstruction schemes on quadrilateral elements for the linear advection equation”. In: *Journal of Scientific Computing* 67.2 (2016), pp. 769–790.
- [54] Peter E Vincent, Patrice Castonguay, and Antony Jameson. “Insights from von Neumann analysis of high-order flux reconstruction schemes”. In: *Journal of Computational Physics* 230.22 (2011), pp. 8134–8154.
- [55] Praveen Chandrashekar. “Kinetic energy preserving and entropy stable finite volume schemes for compressible Euler and Navier-Stokes equations”. In: *Communications in Computational Physics* 14.5 (2013), pp. 1252–1286.
- [56] Farzad Ismail and Philip L Roe. “Affordable, entropy-consistent Euler flux functions II: Entropy production at shocks”. In: *Journal of Computational Physics* 228.15 (2009), pp. 5410–5436.
- [57] Hendrik Ranocha. *Generalised summation-by-parts operators and entropy stability of numerical methods for hyperbolic balance laws*. Ph.D. thesis, TU Braunschweig, 2018.
- [58] Patrice Castonguay. “High-order energy stable flux reconstruction schemes for fluid flow simulations on unstructured grids”. In: *Diss. Stanford University* (2012).

- [59] Tzanio Kolev, Paul Fischer, Misun Min, Jack Dongarra, Jed Brown, Veselin Dobrev, Tim Warburton, Stanimire Tomov, Mark S Shephard, Ahmad Abdelfattah, et al. “Efficient exascale discretizations: High-order finite element methods”. In: *The International Journal of High Performance Computing Applications* 35.6 (2021), pp. 527–552.
- [60] George Karniadakis and Spencer Sherwin. *Spectral/hp element methods for computational fluid dynamics*. Oxford University Press, 2013.
- [61] Chris D Cantwell, Spencer J Sherwin, Robert M Kirby, and Paul HJ Kelly. “From h to p efficiently: Strategy selection for operator evaluation on hexahedral and tetrahedral elements”. In: *Computers & Fluids* 43.1 (2011), pp. 23–28.
- [62] Martin Kronbichler and Wolfgang A Wall. “A performance comparison of continuous and discontinuous Galerkin methods with fast multigrid solvers”. In: *SIAM Journal on Scientific Computing* 40.5 (2018), A3423–A3448.
- [63] David Moxey, Roman Amici, and Mike Kirby. “Efficient matrix-free high-order finite element evaluation for simplicial elements”. In: *SIAM Journal on Scientific Computing* 42.3 (2020), pp. C97–C123.
- [64] Miguel R Visbal and Datta V Gaitonde. “On the use of higher-order finite-difference schemes on curvilinear and deforming meshes”. In: *Journal of Computational Physics* 181.1 (2002), pp. 155–185.
- [65] Yoshiaki Abe, Takanori Haga, Taku Nonomura, and Kozo Fujii. “On the freestream preservation of high-order conservative flux-reconstruction schemes”. In: *Journal of Computational Physics* 281 (2015), pp. 28–54.
- [66] David C Del Rey Fernández, Mark H Carpenter, Lisandro Dalcin, Stefano Zampini, and Matteo Parsani. “Entropy stable h/p-nonconforming discretization with the summation-by-parts property for the compressible Euler and Navier–Stokes equations”. In: *SN Partial Differential Equations and Applications* 1.2 (2020), pp. 1–54.

- [67] Magnus Svärd and Hatice Özcan. “Entropy-stable schemes for the Euler equations with far-field and wall boundary conditions”. In: *Journal of Scientific Computing* 58.1 (2014), pp. 61–89.
- [68] Sigrun Ortleb. “A Kinetic Energy Preserving DG Scheme Based on Gauss-Legendre Points.” In: *J. Sci. Comput.* 71.3 (2017), pp. 1135–1168.
- [69] Nail K Yamaleev and Mark H Carpenter. “A family of fourth-order entropy stable nonoscillatory spectral collocation schemes for the 1-D Navier–Stokes equations”. In: *Journal of Computational Physics* 331 (2017), pp. 90–107.
- [70] Mark H Carpenter, Matteo Parsani, Eric J Nielsen, and Travis C Fisher. “Towards an entropy stable spectral element framework for computational fluid dynamics”. In: *54th AIAA Aerospace Sciences Meeting*. 2016, p. 1058.
- [71] Patrice Castonguay, David M Williams, Peter E. Vincent, and Antony Jameson. “Energy stable flux reconstruction schemes for advection–diffusion problems”. In: *Computer Methods in Applied Mechanics and Engineering* 267 (2013), pp. 400–417.
- [72] H. T. Huynh. “A reconstruction approach to high-order schemes including discontinuous Galerkin for diffusion”. In: American Institute of Aeronautics and Astronautics, 2009.
- [73] Hendrik Ranocha, Philipp Öffner, and Thomas Sonar. “Extended skew-symmetric form for summation-by-parts operators and varying Jacobians”. In: *Journal of Computational Physics* 342 (2017), pp. 13–28.
- [74] Philip L Roe. “Approximate Riemann solvers, parameter vectors, and difference schemes”. In: *Journal of computational physics* 43.2 (1981), pp. 357–372.
- [75] Doug Shi-Dong and Siva Nadarajah. “Full-Space Approach to Aerodynamic Shape Optimization”. In: *Computers & Fluids* (2021), p. 104843.
- [76] Hendrik Ranocha and Gregor J Gassner. “Preventing pressure oscillations does not fix local linear stability issues of entropy-based split-form high-order schemes”. In: *Communications on Applied Mathematics and Computation* 4.3 (2022), pp. 880–903.

- [77] Gregor Gassner and David A Kopriva. “A comparison of the dispersion and dissipation errors of Gauss and Gauss–Lobatto discontinuous Galerkin spectral element methods”. In: *SIAM Journal on Scientific Computing* 33.5 (2011), pp. 2560–2579.
- [78] D. De Grazia, G. Mengaldo, D. Moxey, P. E. Vincent, and S. J. Sherwin. “Connections between the discontinuous Galerkin method and high-order flux reconstruction schemes”. In: *International Journal for Numerical Methods in Fluids* 75.12 (2014), pp. 860–877.
- [79] Andrew R Winters, Rodrigo C Moura, Gianmarco Mengaldo, Gregor J Gassner, Stefanie Walch, Joaquim Peiro, and Spencer J Sherwin. “A comparative study on polynomial dealiasing and split form discontinuous Galerkin schemes for under-resolved turbulence computations”. In: *Journal of Computational Physics* 372 (2018), pp. 1–21.

Chapter 6

General Discussion

For computational predictive science, discrete nonlinear stability serves as the bedrock that other powerful tools, such as overintegration, limiting, upwind dissipation, filtering, and artificial viscosity can be added to extend the field of flow regimes. The overarching goals of obtaining provably discretely nonlinearly stable flux reconstruction schemes, for any ESFR correction function, implemented in a low-storage and efficiently scalable manner was achieved for compressible flows on curvilinear meshes.

6.1 NSFR Modified Mass Matrix

The first research question addressed in Chapter 2 was: how can discrete nonlinear stability be achieved for flux reconstruction schemes with general ESFR correction functions? The challenge in this question was, that for ESFR correction functions other than the DG correction function, ESFR introduces a dense broken Sobolev-norm with influence on the nonlinear volume terms. In the linear setting, this term would vanish [24] but for a nonlinear flux in split form, it does not [73, 106, 107]. The paper from Cicchino *et al.* [119] in Chapter 2 re-envisioned FR specifically for the nonlinear setting. The successful result was to incorporate the ESFR correction functions on the nonlinear volume terms. This was accomplished by viewing ESFR as a DG scheme with a modified mass matrix [44, 45], recasting the discretization in variational

form, and embedding the split form within the stiffness operator. In this expression, a design order volume term was implicitly added to the discretization through the application of the ESFR filter operator. This additional term was derived in Lemma 2.3.1 and numerically shown to be design order in Sec. 2.4. The additional term can be viewed as a filter on the highest mode of the nonlinear flux in one-dimension.

In the final NSFR form in Chapter 5, this concept was abstracted to store all of the influence of the ESFR correction functions in the modified mass matrix. Then, by inverting the modified mass matrix and applying it to the residual, we are again applying a filter on the highest mode of all parts of its uncollocated, skew-symmetric DG entropy stable equivalent. The heart of ESFR and NSFR is that, by increasing the correction parameter c , from c_{DG} to c_+ , there is a larger allowable timestep [21, 29]. We provide an analytical reasoning for the increased timestep here.

Consider the NSFR modified mass matrix,

$$(\mathbf{M}_m + \mathbf{K}_m)_{ij} \approx \int_{\Omega_r} J_m^\Omega \chi_i(\boldsymbol{\xi}^r) \chi_j(\boldsymbol{\xi}^r) + \sum_{s,v,w} c_{(s,v,w)} J_m^\Omega \partial^{(s,v,w)} \chi_i(\boldsymbol{\xi}^r) \partial^{(s,v,w)} \chi_j(\boldsymbol{\xi}^r) d\Omega_r, \quad (6.1)$$

$$\forall i, j = 1, \dots, N_p.$$

Increasing c , with $c_{(s,v,w)}$ as its three-dimensional tensor product parameter from Chapters 3 and 5, improves the conditioning of the system matrix. In Chapters 2, 3, and 5, the NSFR spatial discretization at every timestep arrives at a system of ordinary differential equations (ODEs) for the modal coefficients of the solution in time,

$$(\mathbf{M}_m + \mathbf{K}_m) \frac{d}{dt} \hat{\mathbf{u}}_m(t)^T = \mathcal{L} \hat{\mathbf{u}}_m(t)^T + \mathcal{N}(\hat{\mathbf{u}}_m(t))^T, \quad t \in [t_n, t_n + \Delta t], \quad (6.2)$$

where we split the system of ODEs into a linear component \mathcal{L} and a nonlinear component \mathcal{N} with respect to the modal coefficients of the solution $\hat{\mathbf{u}}_m(t)$ at time t_n . The solution to

Eq. (6.2) is,

$$\begin{aligned} \hat{\mathbf{u}}_m(t_n + \Delta t)^T &= e^{((\mathbf{M}_m + \mathbf{K}_m)^{-1} \mathcal{L} \Delta t)} \hat{\mathbf{u}}_m(t_n)^T \\ &+ \int_0^{\Delta t} e^{((\mathbf{M}_m + \mathbf{K}_m)^{-1} \mathcal{L} (\Delta t - \tau))} (\mathbf{M}_m + \mathbf{K}_m)^{-1} \mathcal{N}(\hat{\mathbf{u}}_m(t_n + \tau))^T d\tau, \end{aligned} \quad (6.3)$$

via the matrix exponential. Letting $\mathbf{A}_m = (\mathbf{M}_m + \mathbf{K}_m)^{-1} \mathcal{L}$, then by Taylor series expansion the matrix exponential $e^{(\mathbf{A}_m \Delta t)}$ can be approximated by

$$\begin{aligned} e^{(\mathbf{A}_m \Delta t)} &\approx 1 + (\Delta t (\mathbf{M}_m + \mathbf{K}_m)^{-1} \mathcal{L}) + \frac{1}{2!} (\Delta t (\mathbf{M}_m + \mathbf{K}_m)^{-1} \mathcal{L})^2 + \frac{1}{3!} (\Delta t (\mathbf{M}_m + \mathbf{K}_m)^{-1} \mathcal{L})^3 \\ &+ \frac{1}{4!} (\Delta t (\mathbf{M}_m + \mathbf{K}_m)^{-1} \mathcal{L})^4 + \mathcal{O}(\Delta t)^5, \end{aligned} \quad (6.4)$$

for the 4-stage, 4-th order RK44 scheme.

In a von Neumann analysis, the maximum timestep corresponds to the largest value Δt while ensuring the spectral radius of the system matrix is less than 1, $\rho(e^{(\mathbf{A}_m \Delta t)}) < 1$. By observation of Eq. 6.4, the eigenvalues of $e^{(\mathbf{A}_m \Delta t)}$ are inversely proportional to the eigenvalues of $(\mathbf{M}_m + \mathbf{K}_m)$. Therefore, by increasing the value of c , the eigenvalues of $(\mathbf{M}_m + \mathbf{K}_m)$ increase as shown by Allaneau and Jameson for one-dimension [44] and Zwanenburg and Nadarajah for three-dimensions [45], and this results in a larger permissible timestep Δt with the same spectral radius $\rho(e^{(\mathbf{A}_m \Delta t)})$. The maximum value of c corresponds to a numerically found value c_+ and not $c_\infty \rightarrow \infty$, because for values beyond c_+ , the spatial discretization loses an order of accuracy for the linear setting and all orders of accuracy for the nonlinear setting [36]. Beyond c_+ we are no longer filtering the approximation, but rather altering the spatial discretization through the application of the Green's function on the nonlinear component \mathcal{N} .

6.2 NSFR Performance - Extension

From Chapter 5, in the low-storage weight-adjusted form, we capitalized on the increased timestep using c_+ without any additional computational cost. NSFR was developed to efficiently approximate the solution while maintaining free-stream preservation, conservation, and discrete nonlinear stability within a p -th order broken Sobolev-space. The trade-off for the increased timestep with c_+ was a larger error in the solution as compared to c_{DG} . Importantly, they both converged at the same high-order of $p + 1$. The last question that remains to be addressed in this thesis, is if the NSFR c_+ variant predicts the same flow features as the NSFR c_{DG} scheme in L2-space? Up to this point, the NSFR discrete nonlinear properties were always demonstrated within the p -th order broken Sobolev-norm, and conservation in the p -th order broken Sobolev-norm allows for oscillations within the L2-norm [24]. The extension is to consider a viscous problem with isotropic turbulent decay. The case highlights that there does not appear to be a significant difference within the flow features between the NSFR c_{DG} and c_+ variants thanks to the discrete nonlinear stability, conservation and free-stream preservation properties.

6.2.1 Viscous Problems: The Navier-Stokes Equations

The natural extension from Chapter 5 is to numerically solve the Navier-Stokes equations,

$$\begin{aligned}
& \frac{\partial \mathbf{W}^T}{\partial t} + \nabla \cdot \mathbf{f}_c(\mathbf{W})^T - \nabla \cdot \mathbf{f}_v(\mathbf{W}, \nabla \mathbf{W})^T = \mathbf{0}^T, \\
& \mathbf{W} = \begin{bmatrix} \rho, & \rho u, & \rho v, & \rho w, & \rho e \end{bmatrix}, \\
& \mathbf{f}_{c1} = \begin{bmatrix} \rho u, & \rho u^2 + p, & \rho uv, & \rho uw, & (\rho e + p)u \end{bmatrix}, \\
& \mathbf{f}_{c2} = \begin{bmatrix} \rho v, & \rho uv, & \rho v^2 + p, & \rho vw, & (\rho e + p)v \end{bmatrix}, \\
& \mathbf{f}_{c3} = \begin{bmatrix} \rho w, & \rho uw, & \rho vw, & \rho w^2 + p, & (\rho e + p)w \end{bmatrix}, \\
& \mathbf{f}_{v1} = \begin{bmatrix} 0, & \tau_{xx}, & \tau_{xy}, & \tau_{xz}, & u\tau_{xx} + v\tau_{xy} + w\tau_{xz} + \kappa \frac{\partial T}{\partial x} \end{bmatrix}, \\
& \mathbf{f}_{v2} = \begin{bmatrix} 0, & \tau_{yx}, & \tau_{yy}, & \tau_{yz}, & u\tau_{yx} + v\tau_{yy} + w\tau_{yz} + \kappa \frac{\partial T}{\partial y} \end{bmatrix}, \\
& \mathbf{f}_{v3} = \begin{bmatrix} 0, & \tau_{zx}, & \tau_{zy}, & \tau_{zz}, & u\tau_{zx} + v\tau_{zy} + w\tau_{zz} + \kappa \frac{\partial T}{\partial z} \end{bmatrix},
\end{aligned} \tag{6.5}$$

where $\rho e = \frac{p}{\gamma-1} + \frac{1}{2}\rho(u^2 + v^2 + w^2)$, and $\rho, u, v, w, p, e, \gamma$ are the density, velocity, pressure, specific total energy, and adiabatic coefficient respectively. Letting $\vec{\mathbf{u}} = [u, v, w]$, the viscous stress tensor is given by,

$$\boldsymbol{\tau} = \mu \left(\nabla \vec{\mathbf{u}} + \nabla \vec{\mathbf{u}}^T - \frac{2}{3} (\nabla \cdot \vec{\mathbf{u}}) \mathbf{I}_d \right). \tag{6.6}$$

Here, μ is the dynamic viscosity, which is obtained using Sutherland's law [120]. The thermal conductivity is determined by $\kappa = \frac{\mu c_p}{Pr}$, with $Pr = 0.72$ the Prandtl number and c_p is the specific heat coefficient at constant pressure.

To obtain the NSFR discretization for the Navier-Stokes equations in Eq. 6.5, alike Chapter 5, we let $\hat{\mathbf{u}}_m$ represent the modal coefficients of the solution for a single state in the

element m , and we introduce the auxiliary variable,

$$\mathbf{q}_m = \nabla \mathbf{u}_m \in \mathbb{R}^{d \times N_p}. \quad (6.7)$$

To solve for the auxiliary variable, we integrate Eq. 6.7 with respect to the basis function as the test function. Then, we apply integration-by-parts twice, and evaluate bilinear forms with quadrature rules to arrive at the strong form [13, 121]. For the primary equation, we use the NSFR discretization derived in Chapter 5 for the convective portion. For the primary equation's diffusive terms, we perform integration-by-parts twice, evaluate bilinear forms with quadrature rules, and arrive at the strong form. We let the subscript “ c ” refer to the convective portion and “ v ” refer to the viscous portion. The NSFR discretization for convective-viscous problems is,

$$\begin{aligned} \text{Auxiliary Equation: } & \left(\mathbf{M}_m + \tilde{\mathbf{K}}_m \right) \mathbf{q}_m^T = \chi(\boldsymbol{\xi}_v^r)^T \mathbf{W} \nabla^r \phi(\boldsymbol{\xi}_v^r) \hat{\mathbf{u}}_m^r(t)^T \\ & + \sum_{f=1}^{N_f} \sum_{k=1}^{N_{fp}} \chi(\boldsymbol{\xi}_{fk}^r)^T W_{fk} \hat{\mathbf{n}}^r \left(\mathbf{u}_m^{*,r} - \phi(\boldsymbol{\xi}_{fk}^r) \hat{\mathbf{u}}_m^r(t)^T \right), \\ \text{Primary Equation: } & \left(\mathbf{M}_m + \mathbf{K}_m \right) \frac{d}{dt} \hat{\mathbf{u}}_m(t)^T = - \left[\chi(\boldsymbol{\xi}_v^r)^T \chi(\boldsymbol{\xi}_f^r)^T \right] \left[\left(\tilde{\mathbf{Q}} - \tilde{\mathbf{Q}}^T \right) \odot \mathbf{F}_{m,c}^r \right] \mathbf{1}^T \\ & - \sum_{f=1}^{N_f} \sum_{k=1}^{N_{fp}} \chi(\boldsymbol{\xi}_{fk}^r)^T W_{fk} \hat{\mathbf{n}}^r \cdot \mathbf{f}_{m,c}^{*,r} \\ & + \chi(\boldsymbol{\xi}_v^r)^T \mathbf{W} \nabla^r \phi(\boldsymbol{\xi}_v^r) \cdot \hat{\mathbf{f}}_{m,v}^r(t)^T \\ & + \sum_{f=1}^{N_f} \sum_{k=1}^{N_{fp}} \chi(\boldsymbol{\xi}_{fk}^r)^T W_{fk} \hat{\mathbf{n}}^r \cdot \left(\mathbf{f}_{m,v}^{*,r} - \phi(\boldsymbol{\xi}_{f,k}^r) \hat{\mathbf{f}}_{m,v}^r(t)^T \right). \end{aligned} \quad (6.8)$$

For Eq. 6.8, we introduced an ESFR correction operator matrix $\tilde{\mathbf{K}}_m$ in the auxiliary equation to denote that it does not have to have the same correction parameter value as the primary equation's operator \mathbf{K}_m [122]. Note that for the auxiliary equation, there are no dot products in the volume or surface integrals because \mathbf{q}_m is a matrix of size d by N_p . Also, for the auxiliary

equation, $\hat{\mathbf{u}}_m^r(t)$ are the modal coefficients of the reference solution obtained by multiplication with the metric cofactor matrix, $\mathbf{u}_m^r = \mathbf{u}_m \mathbf{C}_m$, spanned by the flux-basis functions ϕ .

We consider the viscous TGV problem at Reynolds's number $\text{Re}_\infty = 1600$ from Chapter 5 with periodic boundary conditions in $[x, y, z] \in [0, 2\pi]^3$. We use the entropy conserving flux from Ismail and Roe [123] for the convective portion, and the interior penalty (IP) numerical flux [11] for the viscous terms. The penalty value for the IP flux used is $\frac{p(p+1)}{H^d}$, where H^d is the Hausdorff measure of the surface. The scheme uses a 4-th order Runge-Kutta time integrator, with a CFL = 0.1 and an adaptive timestep based on the maximum wavespeed in the domain. The solution nodes are Gauss-Lobatto-Legendre (LGL) quadrature nodes, the scheme is integrated on Gauss-Legendre quadrature nodes, and the basis functions are spanned by uncollocated Lagrange functions constructed on the LGL nodes. A Cartesian mesh is considered. For the cases below, $\tilde{\mathbf{K}}_m$ uses c_{DG} for the auxiliary equation [40, 41].

The physical quantities under investigation are the nondimensional kinetic energy K^* , dissipation rate ε , and enstrophy ζ^* ,

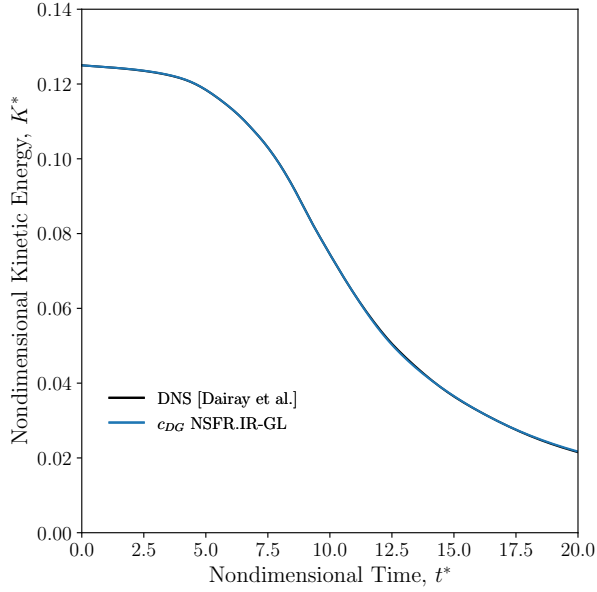
$$\begin{aligned} K^* &= \frac{1}{|\Omega|} \bigoplus_{m=1}^M \int_{\Omega_r} \frac{1}{2} J_m^\Omega \rho^* \vec{\mathbf{u}}^* \cdot \vec{\mathbf{u}}^* d\Omega_r, \\ \varepsilon &= -\frac{dK^*}{dt^*}, \\ \zeta^* &= \frac{1}{|\Omega|} \bigoplus_{m=1}^M \int_{\Omega_r} \frac{1}{2} J_m^\Omega \rho^* \boldsymbol{\omega}^* \cdot \boldsymbol{\omega}^* d\Omega_r, \end{aligned} \tag{6.9}$$

where $|\Omega| = (2\pi)^3$ is the total domain volume, ε is computed from K^* using finite-difference, and $\boldsymbol{\omega}^*$ is the vorticity vector. The “*” superscript refers to the values being nondimensionalized with respect to free-stream values. The computed quantities are compared to a reference spectral direct numerical simulation (DNS) data from Dairay [124] that used 512^3 DOFs.

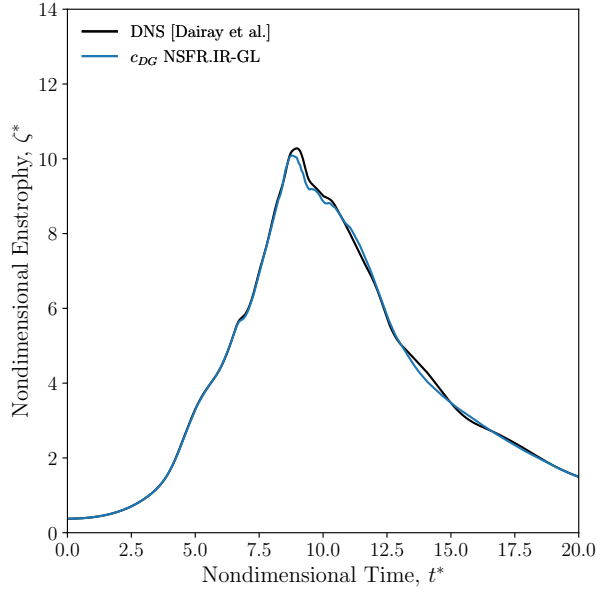
The results were obtained with the help of my colleague in the research group Julien Brillouin. Julien implemented the viscous stress tensor for the viscous flux, implemented the manufactured solution for the Navier-Stokes equations to verify the orders of accuracy, setup the viscous TGV test case, computed the unsteady quantities and the post-processing of

results. My contribution to this test was the implementation of the spatial discretization and evaluation for the auxiliary and primary equations in Eq. 6.8, and the subroutines therein. The goal of this test case is to evaluate the predictive performance of the spatial solver for a physically relevant turbulent problem.

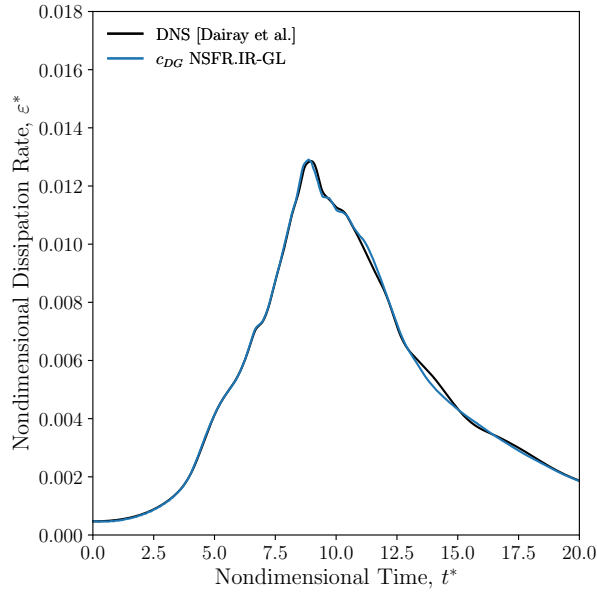
Firstly, we are interested in ensuring that the entropy conserving discretization recovers the physical quantities of the DNS result. For this, we ran the NSFV discretization with a value of c_{DG} with 256^3 DOFs. We used $p = 3$ and 64^3 elements.



(a) Kinetic Energy vs Time



(b) Enstrophy vs Time



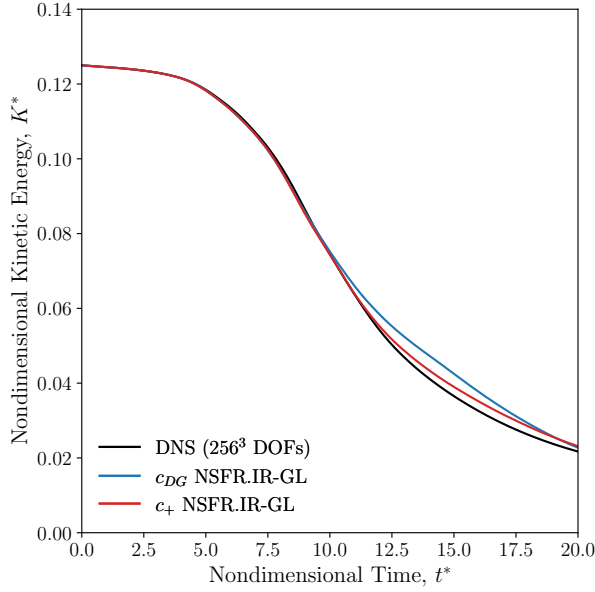
(c) Dissipation Rate vs Time

Figure 6.1: Viscous TGV at $Re_\infty = 1600$ using c_{DG} NSFR with 256^3 DOFs.

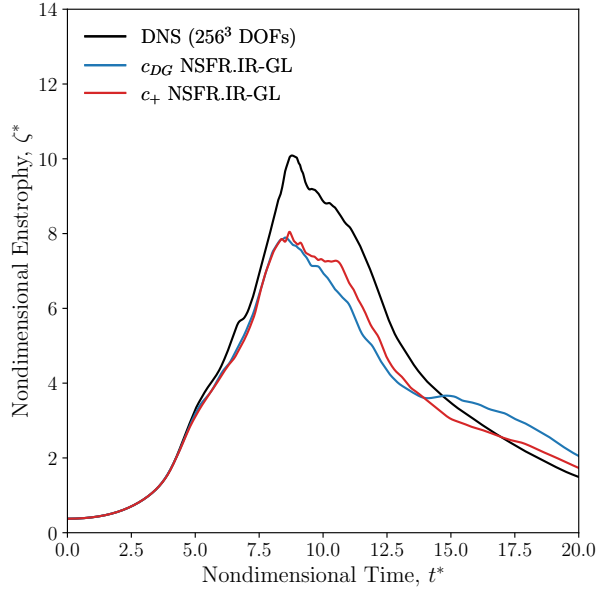
From Fig. 6.1, using $\frac{1}{23}$ the number of DOFs as compared to the reference DNS result, we obtained very reasonable results for the three physical quantities in all regions of the flow. This verifies that the spatial discretization recovers the expected turbulent quantities under high-resolution. It is to be noted that the conservative DG scheme with upwind dissipation

and overintegration also recovered the DNS result for this number of DOFs. For under-resolved turbulent flows, the conservative DG scheme fails without overintegration, and it passes with overintegration depending on the overintegration strength, final time of the simulation, and number of DOFs.

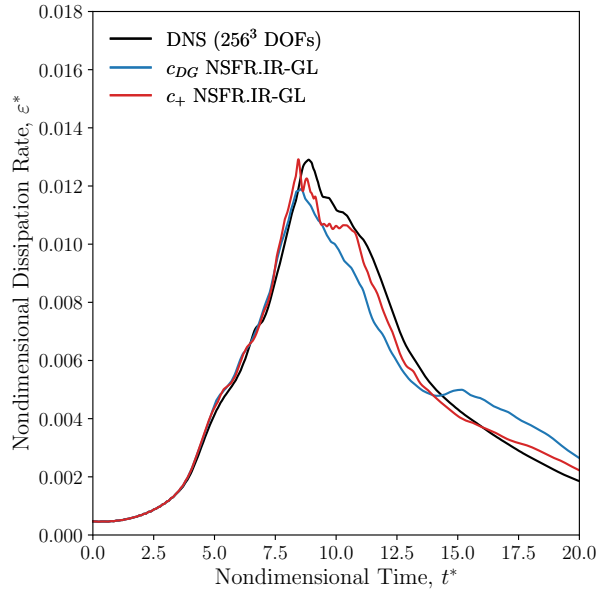
Next, we considered under-resolved turbulent flow, using 96^3 DOFs, and analyzed the difference between c_{DG} and c_+ . We used $p = 5$ and 16^3 elements.



(a) Kinetic Energy vs Time



(b) Enstrophy vs Time



(c) Dissipation Rate vs Time

Figure 6.2: Viscous TGV at $Re_\infty = 1600$ using c_{DG} and c_+ NSFR with 96^3 DOFs.

From Fig. 6.2, both c_{DG} and c_+ gave almost identical results in the laminar stage, then after the transitional stage, they differed for the isotropic turbulent decay. The c_+ variant was more dissipative than c_{DG} due to the filter it imposes on the highest mode of the scheme. There does not appear to be a clear disadvantage to using c_+ rather than c_{DG} for a viscous

turbulent problem, but rather an advantage with the increased timestep.

Importantly, this test case demonstrates that the NSFR c_+ scheme recovers the physically relevant flow properties for viscous isotropic turbulence. From the analysis in Sec. 6.1 and Equations (6.3) and (6.4), up to the limit of c_+ , the correction functions act as a low-pass filter improving the conditioning of the system matrix, and after c_+ , they alter the nonlinear properties of the scheme. Thus, by achieving discrete nonlinear stability through the modified mass matrix, we were able to exploit the timestep improvement with c_+ without corrupting the physical flow properties.

Chapter 7

Conclusion

The overarching goal of obtaining provable discrete nonlinearly stable flux reconstruction schemes, for any ESFR correction function, implemented in a low-storage and efficiently scalable manner was achieved for compressible flows on curvilinear meshes. Discrete nonlinear stability was achieved without the need for upwind dissipation. NSFR has the additional timestep benefit from the ESFR correction functions when compared to entropy stable schemes in the literature. By using sum-factorization for the matrix-vector products, and our proposed sum-factorized Hadamard product, NSFR is computationally competitive with the conservative DG scheme. NSFR was able to recover physically relevant quantities for compressible turbulent problems accurately.

The first novelty to NSFR was the incorporation of the ESFR correction functions on the nonlinear volume terms to achieve discrete nonlinear stability. This framework allowed for discrete entropy stable extensions from a scalar one-dimensional nonlinear PDE, to curvilinear coordinates, and finally to vector-valued systems of PDEs in curvilinear coordinates. To our knowledge, NSFR was the first to develop discrete nonlinearly stable schemes in dense norms beyond the L2-norm.

This thesis also had original contributions to the scalability and performance of high-order schemes. We developed a sum-factorized Hadamard product that scales at order $\mathcal{O}(n^{d+1})$.

This sum-factorized Hadamard product resolves the additional computational cost associated with entropy conserving two-point fluxes in high-order frameworks, and resulted in the NSFR discretization being computationally competitive with traditional high-order schemes. Additionally, we presented a novel weight-adjusted mass matrix inverse approximation for the NSFR modified mass matrix. The weight-adjusted approximation preserved the orders of convergence via the projection operator, that projects to the broken Sobolev-norm, and it effectively used sum-factorization in its application.

From the final form of NSFR, we concluded with an analytical reasoning as to why c_+ allowed for larger timesteps than c_{DG} —by improving the conditioning of the system matrix. The advancements in computational performance, with low memory and efficiently scalable techniques, coupled with the discrete nonlinear stability properties concluded in accurate high-order predictions for isotropic turbulent decay.

7.1 Future Work

This section will identify future topics that would extend the NSFR scheme to simulate a wider class of flow regimes as well as identify limitations in the current development.

7.1.1 Natural Extensions

Having established the NSFR scheme, natural extensions would include developing an equivalent entropy correction term for the p -th order broken Sobolev-norm, fully discrete implicit temporal integrators, and the application of NSFR to diffusive turbulent flows and shock-waves. To investigate an equivalent NSFR-residual distribution scheme, the entropy correction term would need to demonstrate stability in norms other than the L2-norm. This framework would allow for seamless extensions to the other finite element methods residual distribution schemes encompass.

For turbulent problems, high-order schemes excel in their application to implicit large eddy simulation. The strength that NSFR provides is that it disassociates stability from

dissipation. The removal of the upwind dissipation raises the prospect of developing novel dissipation mechanisms to model the dissipation range of isotropic turbulence. The role of classical turbulence models can be investigated in the absence of filtering and upwind dissipation to ensure stability.

The current computational limitation for large-scale test cases is the severe timestep restriction of explicit temporal integrators. For more industrially relevant problems, an implicit timestepping scheme is critical. Pairing an implicit timestepping scheme with a fully discrete entropy conserving framework could see significant improvements in total runtime. Another powerful extension of discretely nonlinearly stable methods is their application to shock-waves on extremely coarse meshes. For steep pressure gradients, a positivity-preserving limiter is essential to guarantee the positivity of density and pressure.

Novel approaches to establish positivity while accurately resolving shocks for high Reynolds turbulent flows would secure the future of nonlinearly stable schemes.

7.1.2 Limitations

One remaining open research question is whether entropy stability is sufficient to accurately capture the entropic solution. For linear problems, from the celebrated Lax–Richtmyer Theorem [125] or more popularly known as the Lax Equivalence Theorem, linear stability is sufficient for convergence. Unfortunately, for nonlinear problems, nonlinear stability is inadequate to imply convergence. The entropic solution satisfies the entropy inequality, but it is not necessarily the only discrete approximation that satisfies the entropy inequality [126]. While the entropy inequality enables the scheme to recover the correct shock speed [90], it does not guarantee that bounded spurious growth of errors does not corrupt the approximation. This is precisely the issue that motivated the development of total variation diminishing [127–129], total variation bounded [130], essentially non-oscillatory [128, 131], weighted essentially non-oscillatory [132–134], and maximum-principle preserving [135] schemes—to prove convergence [136]. NSFR as it is presented does not have a convergence proof to the entropic

solution.

We are also interested in the role anti-diffusive terms have on the discretization and we believe that there is a relationship to be established with convergence. The local energy stability problem introduced by Gassner and coauthors [137] explored the bounded growth of perturbations within entropy conserving schemes. The perturbation growth corrupted the solution approximation for smooth problems. This phenomenon is particularly of interest for turbulent and chaotic flows—it acts as a means to separate noise from the data.

A convergence proof and a discrete bound on the spurious growth of perturbation errors would provide chaotic problems with a quantification of the prediction’s uncertainty—rendering the algorithm truly predictive.

Bibliography

- [1] Heinz-Otto Kreiss and Joseph Oliger. “Comparison of accurate methods for the integration of hyperbolic equations”. In: *Tellus* 24.3 (1972), pp. 199–215.
- [2] Blair Swartz and Burton Wendroff. “The relative efficiency of finite difference and finite element methods. I: Hyperbolic problems and splines”. In: *SIAM Journal on Numerical Analysis* 11.5 (1974), pp. 979–993.
- [3] William H Reed and Thomas R Hill. *Triangular mesh methods for the neutron transport equation*. Tech. rep. Los Alamos Scientific Lab., N. Mex.(USA), 1973.
- [4] Jan S. Hesthaven and Tim Warburton. *Nodal discontinuous Galerkin methods algorithms, analysis and applications*. Springer, 2008.
- [5] HL Atkins and Chi-Wang Shu. “Quadrature-free implementation of discontinuous Galerkin method for hyperbolic equations”. In: *Institute for Computer Applications in Science and Engineering* (1996).
- [6] Sergei Konstantinovich Godunov. “A difference scheme for numerical solution of discontinuous solution of hydrodynamic equations”. In: *Math. Sbornik* 47 (1959), pp. 271–306.
- [7] Sergei K Godunov and I Bohachevsky. “Finite difference method for numerical computation of discontinuous solutions of the equations of fluid dynamics”. In: *Matematičeskij sbornik* 47.3 (1959), pp. 271–306.

- [8] Peter D Lax. “Weak solutions of nonlinear hyperbolic equations and their numerical computation”. In: *Communications on pure and applied mathematics* 7.1 (1954), pp. 159–193.
- [9] Philip L Roe. “Approximate Riemann solvers, parameter vectors, and difference schemes”. In: *Journal of computational physics* 43.2 (1981), pp. 357–372.
- [10] Antony Jameson. “Artificial diffusion, upwind biasing, limiters and their effect on accuracy and multigrid convergence in transonic and hypersonic flows”. In: *11th Computational Fluid Dynamics Conference*. 1993, p. 3359.
- [11] Douglas N. Arnold. “An interior penalty finite element method with discontinuous elements”. In: *SIAM Journal on Numerical Analysis* 19.4 (1982), pp. 742–760.
- [12] F. Bassi and S. Rebay. “A high-order accurate discontinuous finite element method for the numerical solution of the compressible Navier–Stokes equations”. In: *Journal of Computational Physics* 131.2 (1997), pp. 267–279.
- [13] Bernardo Cockburn and Chi-Wang Shu. “The local discontinuous Galerkin method for time-dependent convection-diffusion systems”. In: *SIAM Journal on Numerical Analysis* 35.6 (1998), pp. 2440–2463.
- [14] Jaime Peraire and Per-Olof Persson. “The compact discontinuous Galerkin (CDG) method for elliptic problems”. In: *SIAM Journal on Scientific Computing* 30.4 (2008), pp. 1806–1824.
- [15] S. Brdar, A. Dedner, and R. Klöfkorn. “Compact and stable discontinuous Galerkin methods for convection-diffusion problems”. In: *SIAM Journal on Scientific Computing* 34.1 (2012), A263–A282.
- [16] Zhi Jian Wang. “Spectral (finite) volume method for conservation laws on unstructured grids. Basic formulation: Basic formulation”. In: *Journal of computational physics* 178.1 (2002), pp. 210–251.

- [17] David A Kopriva and John H Kolas. “A conservative staggered-grid Chebyshev multidomain method for compressible flows”. In: *Journal of computational physics* 125.1 (1996), pp. 244–261.
- [18] Yen Liu, Marcel Vinokur, and Zhi J. Wang. “Spectral difference method for unstructured grids I: Basic formulation”. In: *Journal of Computational Physics* 216.2 (2006), pp. 780–801.
- [19] Antony Jameson. “A proof of the stability of the spectral difference method for all orders of accuracy”. In: *Journal of Scientific Computing* 45.1-3 (2010), pp. 348–358.
- [20] Zhi Jian Wang. “High-order methods for the Euler and Navier–Stokes equations on unstructured grids”. In: *Progress in Aerospace Sciences* 43.1-3 (2007), pp. 1–41.
- [21] H. T. Huynh. “A flux reconstruction approach to high-order schemes including discontinuous Galerkin methods”. In: American Institute of Aeronautics and Astronautics, 2007.
- [22] Zhi Jian Wang and Haiyang Gao. “A unifying lifting collocation penalty formulation including the discontinuous Galerkin, spectral volume/difference methods for conservation laws on mixed grids”. In: *Journal of Computational Physics* 228.21 (2009), pp. 8161–8186.
- [23] Antony Jameson, Peter E Vincent, and Patrice Castonguay. “On the non-linear stability of flux reconstruction schemes”. In: *Journal of Scientific Computing* 50.2 (2012), pp. 434–445.
- [24] Peter E Vincent, Patrice Castonguay, and Antony Jameson. “A new class of high-order energy stable flux reconstruction schemes”. In: *Journal of Scientific Computing* 47.1 (2011), pp. 50–72.
- [25] Patrice Castonguay. “High-order energy stable flux reconstruction schemes for fluid flow simulations on unstructured grids”. In: *Diss. Stanford University* (2012).

- [26] Zhi Jian Wang. *Adaptive high-order methods in computational fluid dynamics*. Vol. 2. World Scientific, 2011.
- [27] HT Huynh, Zhi J Wang, and Peter E Vincent. “High-order methods for computational fluid dynamics: A brief review of compact differential formulations on unstructured grids”. In: *Computers & fluids* 98 (2014), pp. 209–220.
- [28] Meilin Yu and Zhi Jian Wang. “On the connection between the correction and weighting functions in the correction procedure via reconstruction method”. In: *Journal of Scientific Computing* 54.1 (2013), pp. 227–244.
- [29] Peter E Vincent, Patrice Castonguay, and Antony Jameson. “Insights from von Neumann analysis of high-order flux reconstruction schemes”. In: *Journal of Computational Physics* 230.22 (2011), pp. 8134–8154.
- [30] D. M. Williams and A. Jameson. “Energy stable flux reconstruction schemes for advection–diffusion problems on tetrahedra”. In: *Journal of Scientific Computing* 59.3 (2014), pp. 721–759.
- [31] Peter E Vincent, Antony M Farrington, Freddie D Witherden, and Antony Jameson. “An extended range of stable-symmetric-conservative flux reconstruction correction functions”. In: *Computer Methods in Applied Mechanics and Engineering* 296 (2015), pp. 248–272.
- [32] Patrice Castonguay, Peter E Vincent, and Antony Jameson. “A new class of high-order energy stable flux reconstruction schemes for triangular elements”. In: *Journal of Scientific Computing* 51.1 (2012), pp. 224–256.
- [33] Patrice Castonguay, Peter E Vincent, and Antony Jameson. “A new class of high-order energy stable flux reconstruction schemes for triangular elements”. In: *Journal of Scientific Computing* 51.1 (2012), pp. 224–256.
- [34] FD Witherden, PE Vincent, and A Jameson. “High-order flux reconstruction schemes”. In: *Handbook of numerical analysis*. Vol. 17. Elsevier, 2016, pp. 227–263.

- [35] Freddie D Witherden, Antony M Farrington, and Peter E Vincent. “PyFR: An open source framework for solving advection–diffusion type problems on streaming architectures using the flux reconstruction approach”. In: *Computer Physics Communications* 185.11 (2014), pp. 3028–3040.
- [36] Erwan Lambert and Siva Nadarajah. “An L2-Error Estimate of Energy Stable Flux Reconstruction Method”. In: *arXiv preprint arXiv:2309.03801* (2023).
- [37] Ahmad Peyvan, Jonathan Komperda, Dongru Li, Zia Ghiasi, and Farzad Mashayek. “Flux reconstruction using Jacobi correction functions in discontinuous spectral element method”. In: *Journal of Computational Physics* 435 (2021), p. 110261.
- [38] Will Trojak and FD Witherden. “A new family of weighted one-parameter flux reconstruction schemes”. In: *Computers & Fluids* 222 (2021), p. 104918.
- [39] Patrice Castonguay, David M Williams, Peter E. Vincent, and Antony Jameson. “Energy stable flux reconstruction schemes for advection–diffusion problems”. In: *Computer Methods in Applied Mechanics and Engineering* 267 (2013), pp. 400–417.
- [40] Samuel Quaegebeur, Siva Nadarajah, Farshad Navah, and Philip Zwanenburg. “Stability of energy stable flux reconstruction for the diffusion problem using compact numerical fluxes”. In: *SIAM Journal on Scientific Computing* 41.1 (2019), A643–A667.
- [41] Samuel Quaegebeur and Siva Nadarajah. “Stability of energy stable flux reconstruction for the diffusion problem using the interior penalty and Bassi and Rebay II numerical fluxes for linear triangular elements”. In: *Journal of Computational Physics* 380 (2019), pp. 88–118.
- [42] Abhishek Sheshadri and Antony Jameson. “An analysis of stability of the flux reconstruction formulation on quadrilateral elements for the linear advection –diffusion equation”. In: *Journal of Scientific Computing* (2017), pp. 1–29.

- [43] Samuel Quaegebeur, Alexander Cicchino, and Sivakumaran Nadarajah. “Stability of Energy Stable Flux Reconstruction for the Diffusion Problem using Compact Numerical Fluxes on Quadrilateral Elements”. In: *AIAA Scitech 2020 Forum*. 2020, p. 1048.
- [44] Yves Allaneau and Antony Jameson. “Connections between the filtered discontinuous Galerkin method and the flux reconstruction approach to high order discretizations”. In: *Computer Methods in Applied Mechanics and Engineering* 200.49–52 (2011), pp. 3628–3636.
- [45] Philip Zwanenburg and Siva Nadarajah. “Equivalence between the energy stable flux reconstruction and filtered discontinuous Galerkin schemes”. In: *Journal of Computational Physics* 306 (2016), pp. 343–369.
- [46] Alexander Cicchino and Siva Nadarajah. “A new norm and stability condition for tensor product flux reconstruction schemes”. In: *Journal of Computational Physics* (2020), p. 110025.
- [47] David C Del Rey Fernández, Jason E Hicken, and David W Zingg. “Review of summation-by-parts operators with simultaneous approximation terms for the numerical solution of partial differential equations”. In: *Computers & Fluids* 95 (2014), pp. 171–196.
- [48] Magnus Svärd and Jan Nordström. “Review of summation-by-parts schemes for initial-boundary-value problems”. In: *Journal of Computational Physics* 268 (2014), pp. 17–38.
- [49] David C Del Rey Fernández, Pieter D Boom, and David W Zingg. “A generalized framework for nodal first derivative summation-by-parts operators”. In: *Journal of Computational Physics* 266 (2014), pp. 214–239.
- [50] Mark H Carpenter, David Gottlieb, and Saul Abarbanel. “Time-stable boundary conditions for finite-difference schemes solving hyperbolic systems: Methodology and

- application to high-order compact schemes”. In: *Journal of Computational Physics* 111.2 (1994), pp. 220–236.
- [51] Mark H Carpenter, Jan Nordström, and David Gottlieb. “A stable and conservative interface treatment of arbitrary spatial accuracy”. In: *Journal of Computational Physics* 148.2 (1999), pp. 341–365.
- [52] Jan Nordström and Mark H Carpenter. “Boundary and interface conditions for high-order finite-difference methods applied to the Euler and Navier–Stokes equations”. In: *Journal of Computational Physics* 148.2 (1999), pp. 621–645.
- [53] Jan Nordström and Mark H Carpenter. “High-order finite difference methods, multidimensional linear problems, and curvilinear coordinates”. In: *Journal of Computational Physics* 173.1 (2001), pp. 149–174.
- [54] Mark H Carpenter, Jan Nordström, and David Gottlieb. “Revisiting and extending interface penalties for multi-domain summation-by-parts operators”. In: *Journal of Scientific Computing* 45.1-3 (2010), pp. 118–150.
- [55] Magnus Svärd and Hatice Özcan. “Entropy-stable schemes for the Euler equations with far-field and wall boundary conditions”. In: *Journal of Scientific Computing* 58.1 (2014), pp. 61–89.
- [56] Matteo Parsani, Mark H Carpenter, and Eric J Nielsen. “Entropy stable discontinuous interfaces coupling for the three-dimensional compressible Navier-Stokes equations.” In: *J. Comput. Phys.* 290.1 (2015), pp. 132–138.
- [57] Matteo Parsani, Mark H Carpenter, and Eric J Nielsen. “Entropy stable wall boundary conditions for the three-dimensional compressible Navier–Stokes equations”. In: *Journal of Computational Physics* 292 (2015), pp. 88–113.
- [58] David C Del Rey Fernández, Mark H Carpenter, Lisandro Dalcin, Stefano Zampini, and Matteo Parsani. “Entropy stable h/p-nonconforming discretization with the summation-

- by-parts property for the compressible Euler and Navier–Stokes equations”. In: *SN Partial Differential Equations and Applications* 1.2 (2020), pp. 1–54.
- [59] Rémi Abgrall, Jan Nordström, Philipp Öffner, and Svetlana Tokareva. “Analysis of the SBP-SAT stabilization for finite element methods part II: Entropy stability”. In: *Communications on Applied Mathematics and Computation* (2021), pp. 1–23.
- [60] Travis Calob Fisher. “High-order L2 stable multi-domain finite difference method for compressible flows”. PhD thesis. Purdue University, 2012.
- [61] Travis C Fisher, Mark H Carpenter, Jan Nordström, Nail K Yamaleev, and Charles Swanson. “Discretely conservative finite-difference formulations for nonlinear conservation laws in split form: Theory and boundary conditions”. In: *Journal of Computational Physics* 234 (2013), pp. 353–375.
- [62] Travis C Fisher and Mark H Carpenter. “High-order entropy stable finite difference schemes for nonlinear conservation laws: Finite domains”. In: *Journal of Computational Physics* 252 (2013), pp. 518–557.
- [63] David C Del Rey Fernández, Pieter D Boom, Mark H Carpenter, and David W Zingg. “Extension of tensor-product generalized and dense-norm summation-by-parts operators to curvilinear coordinates”. In: *Journal of Scientific Computing* 80.3 (2019), pp. 1957–1996.
- [64] Matteo Parsani, Mark H Carpenter, Travis C Fisher, and Eric J Nielsen. “Entropy stable staggered grid discontinuous spectral collocation methods of any order for the compressible Navier–Stokes equations”. In: *SIAM Journal on Scientific Computing* 38.5 (2016), A3129–A3162.
- [65] Mark H Carpenter, Matteo Parsani, Eric J Nielsen, and Travis C Fisher. “Towards an entropy stable spectral element framework for computational fluid dynamics”. In: *54th AIAA Aerospace Sciences Meeting*. 2016, p. 1058.

- [66] Nail K Yamaleev and Mark H Carpenter. “A family of fourth-order entropy stable nonoscillatory spectral collocation schemes for the 1-D Navier–Stokes equations”. In: *Journal of Computational Physics* 331 (2017), pp. 90–107.
- [67] Jared Crean, Jason E Hicken, David C Del Rey Fernández, David W Zingg, and Mark H Carpenter. “Entropy-stable summation-by-parts discretization of the Euler equations on general curved elements”. In: *Journal of Computational Physics* 356 (2018), pp. 410–438.
- [68] Tianheng Chen and Chi-Wang Shu. “Entropy stable high order discontinuous Galerkin methods with suitable quadrature rules for hyperbolic conservation laws”. In: *Journal of Computational Physics* 345 (2017), pp. 427–461.
- [69] David C Del Rey Fernández, Jared Crean, Mark H. Carpenter, and Jason E. Hicken. “Staggered-grid entropy-stable multidimensional summation-by-parts discretizations on curvilinear coordinates”. In: *Journal of Computational Physics* 392 (2019), pp. 161–186.
- [70] Jesse Chan. “On discretely entropy conservative and entropy stable discontinuous Galerkin methods”. In: *Journal of Computational Physics* 362 (2018), pp. 346–374.
- [71] Lucas Friedrich, Gero Schnücke, Andrew R Winters, David C Del Rey Fernández, Gregor J Gassner, and Mark H Carpenter. “Entropy stable space–time discontinuous Galerkin schemes with summation-by-parts property for hyperbolic conservation laws”. In: *Journal of Scientific Computing* 80.1 (2019), pp. 175–222.
- [72] Magnus Svärd. “On coordinate transformations for summation-by-parts operators”. In: *Journal of Scientific Computing* 20.1 (2004), pp. 29–42.
- [73] Hendrik Ranocha, Philipp Öffner, and Thomas Sonar. “Extended skew-symmetric form for summation-by-parts operators and varying Jacobians”. In: *Journal of Computational Physics* 342 (2017), pp. 13–28.
- [74] Eitan Tadmor. “Skew-self adjoint form for systems of conservation laws”. In: *Journal of Mathematical Analysis and Applications* 103.2 (1984), pp. 428–442.

- [75] Amaury Johnen, J-F Remacle, and Christophe Geuzaine. “Geometrical validity of curvilinear finite elements”. In: *Journal of Computational Physics* 233 (2013), pp. 359–372.
- [76] Michael Turner, Joaquim Peiró, and David Moxey. “Curvilinear mesh generation using a variational framework”. In: *Computer-Aided Design* 103 (2018), pp. 73–91.
- [77] Lorenzo Botti. “Influence of reference-to-physical frame mappings on approximation properties of discontinuous piecewise polynomial spaces”. In: *Journal of Scientific Computing* 52.3 (2012), pp. 675–703.
- [78] David Moxey, Shankar P Sastry, and Robert M Kirby. “Interpolation error bounds for curvilinear finite elements and their implications on adaptive mesh refinement”. In: *Journal of Scientific Computing* 78.2 (2019), pp. 1045–1062.
- [79] Niklas Wintermeyer, Andrew R Winters, Gregor J Gassner, and David A Kopriva. “An entropy stable nodal discontinuous Galerkin method for the two dimensional shallow water equations on unstructured curvilinear meshes with discontinuous bathymetry”. In: *Journal of Computational Physics* 340 (2017), pp. 200–242.
- [80] Oskar Ålund and Jan Nordström. “Encapsulated high order difference operators on curvilinear non-conforming grids”. In: *Journal of Computational Physics* 385 (2019), pp. 209–224.
- [81] Patrick D Thomas and Charles K Lombard. “Geometric conservation law and its application to flow computations on moving grids”. In: *AIAA journal* 17.10 (1979), pp. 1030–1037.
- [82] David A Kopriva. “Metric identities and the discontinuous spectral element method on curvilinear meshes”. In: *Journal of Scientific Computing* 26.3 (2006), p. 301.
- [83] Yoshiaki Abe, Takanori Haga, Taku Nonomura, and Kozo Fujii. “On the freestream preservation of high-order conservative flux-reconstruction schemes”. In: *Journal of Computational Physics* 281 (2015), pp. 28–54.

- [84] Juan Manzanero, Gonzalo Rubio, David A Kopriva, Esteban Ferrer, and Eusebio Valero. “Entropy–stable discontinuous Galerkin approximation with summation–by–parts property for the incompressible Navier–Stokes/Cahn–Hilliard system”. In: *Journal of Computational Physics* 408 (2020), p. 109363.
- [85] Peter Lax and Burton Wendroff. *Systems of conservation laws*. Tech. rep. Los Alamos National Lab NM, 1959.
- [86] Peter D Lax. *Hyperbolic systems of conservation laws and the mathematical theory of shock waves*. SIAM, 1973.
- [87] Amiram Harten, James M Hyman, Peter D Lax, and Barbara Keyfitz. “On finite-difference approximations and entropy conditions for shocks”. In: *Communications on pure and applied mathematics* 29.3 (1976), pp. 297–322.
- [88] Olga Arsenévna Oleinik. “Discontinuous solutions of non-linear differential equations”. In: *Uspekhi Matematicheskikh Nauk* 12.3 (1957), pp. 3–73.
- [89] Eberhard Hopf. “On the right weak solution of the Cauchy problem for a quasilinear equation of first order”. In: *Journal of Mathematics and Mechanics* 19.6 (1969), pp. 483–487.
- [90] Peter Lax. “Shock Waves and Entropy”. In: *Contributions to Nonlinear Functional Analysis*. Academic Press, 1971, pp. 603–634.
- [91] S. N. Krushkov. “Results on the character of continuity of solutions of parabolic equations and some of their applications”. In: *Journal of Mathematics and Mechanics* 6 (1969), pp. 97–108.
- [92] John von Neumann and Robert D Richtmyer. “A method for the numerical calculation of hydrodynamic shocks”. In: *Journal of applied physics* 21.3 (1950), pp. 232–237.
- [93] Stanislav N Kružkov. “First order quasilinear equations in several independent variables”. In: *Mathematics of the USSR-Sbornik* 10.2 (1970), p. 217.

- [94] Kurt O Friedrichs and Peter D Lax. “Systems of conservation equations with a convex extension”. In: *Proceedings of the National Academy of Sciences* 68.8 (1971), pp. 1686–1688.
- [95] Sergei Konstantinovich Godunov. “An interesting class of quasi-linear systems”. In: *Doklady Akademii Nauk*. Vol. 139. 3. Russian Academy of Sciences. 1961, pp. 521–523.
- [96] Michael S Mock. “Systems of conservation laws of mixed type”. In: *Journal of Differential equations* 37.1 (1980), pp. 70–88.
- [97] Amiram Harten. “On the symmetric form of systems of conservation laws with entropy”. In: *Journal of Computational Physics* 49.1 (1983), pp. 151–164.
- [98] Björn Engquist and Stanley Osher. “Stable and entropy satisfying approximations for transonic flow calculations”. In: *Mathematics of Computation* 34.149 (1980), pp. 45–75.
- [99] Stanley Osher. “Riemann solvers, the entropy condition, and difference”. In: *SIAM Journal on Numerical Analysis* 21.2 (1984), pp. 217–235.
- [100] Eitan Tadmor. “The numerical viscosity of entropy stable schemes for systems of conservation laws. I”. In: *Mathematics of Computation* 49.179 (1987), pp. 91–103.
- [101] Philippe G LeFloch, Jean-Marc Mercier, and Christian Rohde. “Fully discrete, entropy conservative schemes of arbitrary order”. In: *SIAM Journal on Numerical Analysis* 40.5 (2002), pp. 1968–1992.
- [102] Philippe G LeFloch and Christian Rohde. “High-order schemes, entropy inequalities, and nonclassical shocks”. In: *SIAM Journal on Numerical Analysis* 37.6 (2000), pp. 2023–2060.
- [103] Gregor J Gassner. “A skew-symmetric discontinuous Galerkin spectral element discretization and its relation to SBP-SAT finite difference methods”. In: *SIAM Journal on Scientific Computing* 35.3 (2013), A1233–A1253.

- [104] Gregor J Gassner, Andrew R Winters, and David A Kopriva. “Split form nodal discontinuous Galerkin schemes with summation-by-parts property for the compressible Euler equations”. In: *Journal of Computational Physics* 327 (2016), pp. 39–66.
- [105] Jesse Chan. “Skew-symmetric entropy stable modal discontinuous Galerkin formulations”. In: *Journal of Scientific Computing* 81.1 (2019), pp. 459–485.
- [106] Hendrik Ranocha, Philipp Öffner, and Thomas Sonar. “Summation-by-parts operators for correction procedure via reconstruction”. In: *Journal of Computational Physics* 311 (2016), pp. 299–328.
- [107] Yoshiaki Abe, Issei Morinaka, Takanori Haga, Taku Nonomura, Hisaichi Shibata, and Koji Miyaji. “Stable, non-dissipative, and conservative flux-reconstruction schemes in split forms”. In: *Journal of Computational Physics* 353 (2018), pp. 193–227.
- [108] Rémi Abgrall. “A general framework to construct schemes satisfying additional conservation relations. Application to entropy conservative and entropy dissipative schemes”. In: *Journal of Computational Physics* 372 (2018), pp. 640–666.
- [109] Rémi Abgrall. “Some remarks about conservation for residual distribution schemes”. In: *Computational Methods in Applied Mathematics* 18.3 (2018), pp. 327–351.
- [110] Rémi Abgrall, Philipp Öffner, and Hendrik Ranocha. “Reinterpretation and extension of entropy correction terms for residual distribution and discontinuous Galerkin schemes: Application to structure preserving discretization”. In: *Journal of Computational Physics* 453 (2022), p. 110955.
- [111] Rémi Abgrall, Elise le Meledo, and Philipp Öffner. “On the connection between residual distribution schemes and flux reconstruction”. In: *arXiv preprint arXiv:1807.01261* (2018).
- [112] Steven A Orszag. “Spectral methods for problems in complex geometrics”. In: *Numerical methods for partial differential equations*. Elsevier, 1979, pp. 273–305.

- [113] Chris D Cantwell, Spencer J Sherwin, Robert M Kirby, and Paul HJ Kelly. “From h to p efficiently: Strategy selection for operator evaluation on hexahedral and tetrahedral elements”. In: *Computers & Fluids* 43.1 (2011), pp. 23–28.
- [114] Samuel Williams, Andrew Waterman, and David Patterson. “Roofline: an insightful visual performance model for multicore architectures”. In: *Communications of the ACM* 52.4 (2009), pp. 65–76.
- [115] George Karniadakis and Spencer Sherwin. *Spectral/hp element methods for computational fluid dynamics*. Oxford University Press, 2013.
- [116] Freddie D Witherden and Peter E Vincent. “An analysis of solution point coordinates for flux reconstruction schemes on triangular elements”. In: *Journal of Scientific Computing* 61.2 (2014), pp. 398–423.
- [117] Jesse Chan, Russell J Hewett, and Timothy Warburton. “Weight-adjusted discontinuous Galerkin methods: Curvilinear meshes”. In: *SIAM Journal on Scientific Computing* 39.6 (2017), A2395–A2421.
- [118] Jesse Chan and Lucas C Wilcox. “On discretely entropy stable weight-adjusted discontinuous Galerkin methods: Curvilinear meshes”. In: *Journal of Computational Physics* 378 (2019), pp. 366–393.
- [119] Alexander Cicchino, Siva Nadarajah, and David C. Del Rey Fernández. “Nonlinearly stable flux reconstruction high-order methods in split form”. In: *Journal of Computational Physics* (2022), p. 111094.
- [120] William Sutherland. “LII. The viscosity of gases and molecular force”. In: *The London, Edinburgh, and Dublin Philosophical Magazine and Journal of Science* 36.223 (1893), pp. 507–531.
- [121] F. Bassi and S. Rebay. “A high order discontinuous Galerkin method for compressible turbulent flows”. In: *Discontinuous Galerkin Methods*. Springer, Berlin, Heidelberg, 2000, pp. 77–88.

- [122] Samuel Quaegebeur, Sivakumaran Nadarajah, Farshad Navah, and Philip Zwanenburg. “Stability of energy stable flux reconstruction for the diffusion problem using compact numerical fluxes”. In: *SIAM Journal on Scientific Computing* 41.1 (2019), A643–A667.
- [123] Farzad Ismail and Philip L Roe. “Affordable, entropy-consistent Euler flux functions II: Entropy production at shocks”. In: *Journal of Computational Physics* 228.15 (2009), pp. 5410–5436.
- [124] Thibault Dairay, Eric Lamballais, Sylvain Laizet, and John Christos Vassilicos. “Numerical dissipation vs. subgrid-scale modelling for large eddy simulation”. In: *Journal of Computational Physics* 337 (2017), pp. 252–274.
- [125] Peter D Lax and Robert D Richtmyer. “Survey of the stability of linear finite difference equations”. In: *Communications on pure and applied mathematics* 9.2 (1956), pp. 267–293.
- [126] Brian T Hayes and Philippe G LeFloch. “Non-classical shocks and kinetic relations: Scalar conservation laws”. In: *Archive for Rational Mechanics and Analysis* 139 (1997), pp. 1–56.
- [127] Ami Harten. “On a class of high resolution total-variation-stable finite-difference schemes”. In: *SIAM Journal on Numerical Analysis* 21.1 (1984), pp. 1–23.
- [128] Ami Harten, Bjorn Engquist, Stanley Osher, and Sukumar R Chakravarthy. “Uniformly high order accurate essentially non-oscillatory schemes, III”. In: (1987), pp. 218–290.
- [129] Stanley Osher and Sukumar Chakravarthy. “High resolution schemes and the entropy condition”. In: *SIAM Journal on Numerical Analysis* 21.5 (1984), pp. 955–984.
- [130] Chi-Wang Shu. “TVB uniformly high-order schemes for conservation laws”. In: *Mathematics of Computation* 49.179 (1987), pp. 105–121.
- [131] Chi-Wang Shu and Stanley Osher. “Efficient implementation of essentially non-oscillatory shock-capturing schemes”. In: *Journal of computational physics* 77.2 (1988), pp. 439–471.

- [132] Xu-Dong Liu, Stanley Osher, and Tony Chan. “Weighted essentially non-oscillatory schemes”. In: *Journal of computational physics* 115.1 (1994), pp. 200–212.
- [133] Guang-Shan Jiang and Chi-Wang Shu. “Efficient implementation of weighted ENO schemes”. In: *Journal of computational physics* 126.1 (1996), pp. 202–228.
- [134] Chi-Wang Shu. “Essentially non-oscillatory and weighted essentially non-oscillatory schemes for hyperbolic conservation laws”. In: *Advanced numerical approximation of nonlinear hyperbolic equations* (1998), pp. 325–432.
- [135] Xiangxiong Zhang and Chi-Wang Shu. “On maximum-principle-satisfying high order schemes for scalar conservation laws”. In: *Journal of Computational Physics* 229.9 (2010), pp. 3091–3120.
- [136] Randall J LeVeque. *Numerical methods for conservation laws*. Vol. 214. Springer, 1992.
- [137] Gregor J Gassner, Magnus Svärd, and Florian J Hindenlang. “Stability Issues of Entropy-Stable and/or Split-form High-order Schemes”. In: *Journal of Scientific Computing* 90.3 (2022), pp. 1–36.